



HAL
open science

Immersed boundary methods for fluid-structure interaction with topological changes

Fannie Maria Gerosa

► **To cite this version:**

Fannie Maria Gerosa. Immersed boundary methods for fluid-structure interaction with topological changes. Numerical Analysis [math.NA]. Sorbonne Université, 2021. English. NNT: . tel-03240631v1

HAL Id: tel-03240631

<https://theses.hal.science/tel-03240631v1>

Submitted on 28 May 2021 (v1), last revised 23 Mar 2023 (v2)

HAL is a multi-disciplinary open access archive for the deposit and dissemination of scientific research documents, whether they are published or not. The documents may come from teaching and research institutions in France or abroad, or from public or private research centers.

L'archive ouverte pluridisciplinaire **HAL**, est destinée au dépôt et à la diffusion de documents scientifiques de niveau recherche, publiés ou non, émanant des établissements d'enseignement et de recherche français ou étrangers, des laboratoires publics ou privés.



IMMERSED BOUNDARY METHODS FOR
FLUID-STRUCTURE INTERACTION WITH
TOPOLOGICAL CHANGES

THÈSE DE DOCTORAT

présentée par

Fannie M. GEROSA

pour obtenir le grade de

DOCTEUR DE
SORBONNE UNIVERSITÉ

Spécialité : MATHÉMATIQUES APPLIQUÉES

Soutenue publiquement le 13 Avril 2021 devant le jury composé de :

Miguel Ángel FERNÁNDEZ	Directeur de thèse
Luca FORMAGGIA	Rapporteur
Lucia GASTALDI	Examinatrice
Céline GRANDMONT	Examinatrice
Laura GRIGORI	Examinatrice
Aline LEFEBVRE	Examinatrice
Patrick LE TALLEC	Rapporteur

Thèse préparée au sein de l'équipe-projet COMMEDIA
Centre de Recherche Inria de Paris
et Laboratoire Jacques-Louis Lions (Sorbonne Université et CNRS)

Ai miei nonni.

ACKNOWLEDGEMENTS

I would like to express my sincere gratitude to my advisor *Miguel Á. Fernández*, for all the support and advices. Always available to generously transmitting your enormous knowledge and passion for research. Thank you for your guidance and encouragement during these years. You have been a wonderful scientific father.

Special thank also to the REO-COMMEDIA members *Muriel Boulakia*, *Céline Grandmont*, *Damiano Lombardi* and *Olga Mula*. A particular thank to *Marina Vidrascu*, the quintessence of this team. I also wish to thank *Erik Burman* for his collaboration during my visiting period at the University College London.

I thank *Luca Formaggia* and *Patrick Le Tallec* for having accepted to review this manuscript and for all the constructive suggestions and remarks. I also thank *Lucia Gastaldi*, *Céline Grandmont*, *Laura Grigori* and *Aline Lefebvre* for agreeing to be part of the jury.

Thank to my Commedia's friends *Justine*, *Colette*, *Valeria*, *Sara*, *Fabien*, *Haibo*, *Oscar*, *Mihai* and *Marguerite*. To my office mates *Mocia*, *Vicente* and *Alexandre*. A special thank to *María* (nuestra profesora de salsa), *Ludovic* (l'aspirant mathématicien cuisinier, je n'oublierai jamais nos bavardages pendant la pause café), *Felipe* (músico, filósofo que compartió conmigo todas las fases del doctorado de principio a fin) and finally *Daniele* (mio testimone di nozze e miglior collaboratore sin dai lontani tempi del magico Poli).

Un grazie speciale alla mia famiglia, ai miei genitori, *Bruna e Federico*, ed al mio fratellino *Alessio*, per il loro costante sostegno. Vi voglio bene e non vedo l'ora di festeggiare insieme a voi (ovviamente anche con *Giorgia*).

Il mio ringraziamento più grande va a mio Marito *Florent*. Senza di te mi sentirei persa ovunque nella vita. Il tuo sostegno e la tua pazienza sono stati fondamentali durante questi ultimi mesi. Merci.

Paris, France
March 2021

Fannie Gerosa

MÉTHODES DE LA FRONTIÈRE IMMERGÉE POUR L'INTERACTIONS FLUIDE-STRUCTURE AVEC DES CHANGEMENTS DE TOPOLOGIE

Resumé: Cette thèse est dédiée à la modélisation, l'analyse numérique et à la simulation des problèmes d'interactions fluide-structure. Nous considérons des structures déformable à parois minces et immergées dans un fluide visqueux incompressible. La motivation sous-jacente de ce travail est la simulation des valves cardiaques.

Ce travail aborde des questions fondamentales qui vont du fractionnement efficace du temps avec des maillages non compatibles, à la modélisation de contact dans l'interaction fluide-structure et son approximation. Pour des raisons de robustesse et de solidité mathématique, l'approximation spatiale est basée sur le cadre de maillage non compatibles Nitsche-XFEM.

Dans la première partie, nous présentons et analysons un nouveau schéma semi-implicite, qui évite un couplage fort, sans compromettre la stabilité et la précision. Dans la deuxième partie, nous considérons la situation dans laquelle le contact se produit. Dans le contexte de Nitsche-XFEM, un modèle d'interaction fluide-structure-contact est également étendu dans le cas de contact avec plusieurs structures. Une procédure de duplication spécifique permet de préserver la consistance de la méthode également dans le cas du contact. Les inconsistances mécaniques traditionnelles de la formulation du contact relaxé dans l'interaction fluide-structure sont contournées en introduisant un modèle poreux de surface dans la paroi de contact. Cette couche décrit la rugosité de la surface, donnant un sens physique aux régions fluides infinitésimales, qui restent entre le solide et la surface au contact. Dans la dernière partie, nous développons l'extension 3D de la méthode de maillage Nitsche-XFEM, dans le cas de domaines fluides entièrement et partiellement intersectés.

Mots-clés: Interactions fluide-structure, Méthodes de maillages non compatibles, Schémas de couplage, Méthode de Nitsche, XFEM, Structures minces immergées, Contact.

IMMERSED BOUNDARY METHODS FOR FLUID-STRUCTURE INTERACTION WITH TOPOLOGICAL CHANGES

Abstract: This thesis is dedicated to the modeling, numerical analysis and simulation of fluid-structure interaction problems, involving thin-walled structures immersed in an incompressible viscous fluid. The underlying motivation of this work is the simulation of heart valves.

This work addresses fundamental issues which go from efficient time-splitting with unfitted meshes, to contact modeling in fluid-structure interaction and its approximation. For the sake of robustness and mathematical soundness, the spatial approximation is based on the Nitsche-XFEM unfitted mesh framework.

In the first part, we present and analyse a new semi-implicit scheme for Nitsche-XFEM, which avoids strong coupling, without compromising stability and accuracy. In the second part, we consider the situation in which contact occurs. In the context of Nitsche-XFEM, a fluid-structure-contact interaction model is extended also to the case of contact with multiple structures. A specific duplication procedure allows to extend the consistency of the method to the case of contact. Traditional mechanical inconsistencies of relaxed contact formulation in fluid-structure interaction are circumvented by introducing a surface porous model in the contact wall. This layer describes surface roughness, giving physical meaning to the infinitesimal fluid regions between the solid and the surface at contact. In the last part, we develop the 3D extension of the unfitted mesh Nitsche-XFEM method in case of fully and partially intersected fluid domains.

Keywords: Fluid-structure interaction, Unfitted mesh methods, Coupling schemes, Nitsche's method, XFEM, Immersed thin-walled structures, Contact.

Contents

INTRODUCTION	1
Thesis general context	3
Position of the thesis	3
Thesis outline and main contributions	4
Author's bibliography	5
1 Numerical methods for fluid-structure interaction	7
1.1 Introduction	7
1.2 Fluid-structure interaction	8
1.3 Numerical methods	18
<hr/>	
I TIME-SPLITTING SCHEMES FOR UNFITTED MESH APPROXIMATIONS OF FSI	23
<hr/>	
2 An unfitted mesh semi-implicit coupling scheme for fluid-structure interaction with immersed solids	25
2.1 Introduction	25
2.2 Linear model problem: static interfaces	27
2.3 Non-linear model: moving interface	40
2.4 Numerical experiments	43
2.5 Conclusion	56
3 Error analysis of an unfitted mesh semi-implicit coupling scheme for fluid-structure interaction	57
3.1 Introduction	57
3.2 Problem Setting	58
3.3 Numerical methods	60
3.4 Numerical analysis	65
3.5 Numerical experiments	83
3.6 Conclusion	87
<hr/>	
II MODELING AND APPROXIMATION OF FLUID-STRUCTURE-CONTACT INTERACTION	89
<hr/>	

4	An unfitted mesh fluid-structure-contact approximation with multiple thin-walled immersed solids	91
4.1	Introduction	91
4.2	Problem setting	92
4.3	Numerical methods	95
4.4	Numerical experiments	108
4.5	Conclusion	119
5	A mechanically consistent fluid-structure-contact interaction model	121
5.1	Introduction	122
5.2	Mathematical models	123
5.3	Numerical experiments	136
5.4	Conclusions	150
<hr/>		
III	3D NUMERICAL SIMULATIONS	151
<hr/>		
6	A 3D Nitsche-XFEM method for FSI with immersed thin-walled structures	153
6.1	Introduction	154
6.2	The linear model	155
6.3	The non-linear model	175
6.4	Numerical experiments	176
6.5	Conclusion	194
<hr/>		
GENERAL CONCLUSION AND PERSPECTIVES		197
<hr/>		
	References	201

INTRODUCTION

Thesis general context

The mechanical interaction of an incompressible viscous fluid with an immersed structure appears in a wide variety of engineering fields and is particularly ubiquitous in nature. The applications span from micro-encapsulation, biomechanics of cells deformation, birds flight, physiological flows, such as, heart dynamics and ciliary beating, to aeroelasticity of parachutes and sailing boats (see, e.g., [Liu and Liu \(2006\)](#); [Van Loon et al. \(2005\)](#); [Han and Peskin \(2018\)](#); [Nakata and Liu \(2012\)](#); [Weymouth et al. \(2006\)](#); [Takizawa and Tezduyar \(2012\)](#)).

Since the beginning of this century, impressive progress has been made in building efficient and accurate numerical methods, able to represent the physiological and pathological functionality of blood dynamics. Numerical simulations are effective tools, useful to physicians, as, e.g., support for design new devices, better understanding diseases or malfunctioning and they can become tools for quantity estimations, otherwise concretely inaccessible.

Position of the thesis

This thesis is devoted to the modeling, analysis and numerical simulations of fluid-structure interaction problems with immersed solids and contact. The work is mainly motivated by the numerical simulation of blood flow interacting with heart valves (see, e.g., [Kamensky et al. \(2015\)](#); [Lau et al. \(2010\)](#)), with particular focus on stability, accuracy and robustness. Given the ratio thickness/size of the leaflets, a common assumption is to model the heart valves as structures of co-dimension one (see, e.g., [Diniz dos Santos et al. \(2008\)](#); [Astorino et al. \(2009b\)](#)). This simplified, but realistic, reduced order problem is a fundamental ingredient of this thesis and we refer to as thin-walled solid model. With regard to efficiency, one possible way to gain in performance is to introduce a certain degrees of time-splitting between the fluid and solid problems, thus, avoid *strong coupling*. Standard *loosely coupled* schemes are known to exhibit stability and accuracy issues, since the interface coupling in incompressible fluid-structure interaction is extremely stiff. Indeed, they often require severe time-step restrictions and stability conditions, which are linked to the amount of *added-mass* effect (see Section 1.3.2).

The development of fluid-structure interaction numerical methods has been extensively investigated within the fitted and unfitted mesh frameworks. In the first strategy the fluid and solid meshes are fitted at their interface (see Section 1.3.1), thus, it is ideal for problems with moderate displacement and are usually treated with moving mesh techniques and an Arbitrary Lagrangian Eulerian description of the fluid problem. However, they becomes cumbersome within problems featuring large interface displacement and potential contact between solids.

In such situations, a favored numerical approach is the unfitted mesh based formulations, in which an Eulerian description of the fluid problem is combined with solid meshes which are freely to move independently of a background fluid mesh. However, the design and analysis of splitting schemes, which avoid strong coupling, in the unfitted framework, have been rarely addressed in the literature so far. In the first part of this thesis (Part I), we investigate the stability and accuracy of an unfitted mesh semi-implicit scheme, which avoids strong coupling. Therein, we will consider a consistent spatial discretization based on Nitsche mortaring, with unfitted mesh and cut-elements, named Nitsche-XFEM method.

Moreover, in applications where contact occurs, such as in heart valves dynamics, topological changes appear in the fluid domain. Modeling contact, in particular coupled with fluid-structure interaction, rises many issues, from the modeling and numerical points of view. The computational complexity is also an issue, in particular when a realistic contact (i.e, without relaxation of the contact conditions) is considered. Real topology changes can be avoided by relaxing the contact conditions (see Section 1.2.4). This approximation suffers, however, of mechanical consistency loss. In the second part of this thesis (Part II), we address some of these issues (see Section 1.2.4).

Furthermore, the development of efficient, accurate and robust methods is fundamental for 3D numerical simulations. This raises some issues that are addressed in Part III by extending the unfitted mesh, Nitsche's and cut-elements based method, to the 3D case. Indeed, the considered unfitted mesh method requires a specific track of the interface intersections which becomes cumbersome in 3D.

Thesis outline and main contributions

The main contributions of this work are listed here, chapter by chapter. For the sake of clarity, they are discussed at the beginning of each chapter.

Chapter 1. This is an introductory chapter. We present the essential models involved in fluid-structure interaction problems with thin-walled immersed solids. A review of the state-of-the-art on numerical methods is provided, by discussing the different available methods for the space and time discretization.

Part I: Time-splitting schemes for unfitted mesh approximations of FSI

Chapter 2. We introduce a new semi-implicit coupling scheme for the numerical approximation of incompressible fluid-structure interaction problems, involving thin-walled immersed solids. The method combines a Nitsche based unfitted mesh spatial approximation with a fractional-step time-marching in the fluid. The viscous part of the coupling is treated in an explicit fashion, while the remaining fluid pressure and solid contributions are treated implicitly. The presented scheme efficiently avoid strong coupling, without compromising stability and accuracy. A stability analysis is conducted in the chapter and the efficiency of the numerical scheme is illustrated via numerical experiments.

Chapter 3. This chapter is devoted to the error analysis of the numerical method presented in Chapter 2, for a linear fluid-structure coupled system, involving the transient Stokes equations (in a fixed domain) and a thin-walled solid elastodynamics model. Robust *a priori* error estimates are derived for two extrapolated variants of the solid velocity. Further, numerical evidences on the convergence properties of the methods is provided.

Part II: Modeling and approximation of fluid-structure-contact interaction

Chapter 4. We address the issues raised by the approximation of a basic fluid-structure-contact interaction model using the Nitsche-XFEM method. We illustrate that, for consistency reasons, further element duplication is needed in the fluid elements where contact between the structures occurs. The proposed method, for fluid-structure interaction with contact, is hence compared with the ALE and FD/Lagrange multipliers methods, exploiting the advantages and limitations of these strategies.

Chapter 5. We introduce a mechanically consistent mixed dimensional fluid-structure-contact interaction model. The fluid-structure-contact interaction problem is coupled to a thin-walled Darcy model on the contacting wall. The model gives a mechanical justification for the fluid-structure-contact interaction with a relaxed contact condition. The thin-walled porous layer introduces tangential creeping flow along the boundary and allows for the modelling of boundary flow due to surface roughness. Numerical examples are reported for both Stokes'-Darcy coupling alone, as well as fluid-structure-Darcy-contact at the porous boundary layer.

Part III: 3D numerical simulations

Chapter 6. In this chapter, we discuss the formulation and implementation aspects of the Nitsche-XFEM discretization method, to the three-dimensional case. A particular focus is made on the efficiency and robustness of the intersection and sub-triangulation algorithms without resorting to black-box meshing software. The performance and robustness of the presented method are explored via a series of numerical examples, involving moving interfaces, with partially and fully intersected fluid domains.

Author's bibliography

- Papers in peer reviewed journals:

1. M.A. Fernández and F.M. Gerosa, **An unfitted mesh semi-implicit coupling scheme for fluid-structure interaction with immersed solids.**

International Journal for Numerical Methods in Engineering, 2019, DOI: 10.1002/nme.6449. Available online: <https://hal.inria.fr/hal-02288723>.

- Papers in conference proceedings:

2. E. Burman, M. A. Fernández, S. Frei, and F. M. Gerosa, **3D-2D Stokes-Darcy coupling for the modelling of seepage with an application to fluid-structure interaction with contact**. *Chapter 20 of F. J. Vermolen, C. Vuik (eds.), Numerical Mathematics and Advanced Applications ENUMATH 2019, Lecture Notes in Computational Science and Engineering 139*. DOI: 10.1007/978-3-030-55874-1_20. Available online: <https://hal.inria.fr/hal-02417042>.

- Submitted papers:

3. E. Burman, M.A. Fernández and F.M. Gerosa, **Error analysis of an unfitted mesh semi-implicit coupling scheme for fluid-structure interaction**. Available online: <https://hal.inria.fr/hal-03065803>.
4. S. Frei, and F.M. Gerosa, E. Burman, M.A. Fernández, **A mechanically consistent model for fluid-structure interactions with contact including seepage**. Available online: <https://hal.archives-ouvertes.fr/hal-03174087>

- Papers in preparation:

5. F. Alauzet, D. Corti, M.A. Fernández and F.M. Gerosa, **A comparison of different strategies for fluid-structure-contact approximation with multiple thin-walled immersed solids**.
6. F. Alauzet, D. Corti, M.A. Fernández and F.M. Gerosa, **Three-dimensional Nitsche-XFEM method for the coupling of an incompressible fluid with immersed thin-walled structures**.

Numerical methods for fluid-structure interaction

In this chapter, we briefly review the basic models and numerical methods for fluid-structure interaction with immersed thin-walled solids. In particular, we present a review of the existing numerical methods, focusing, in particular, on the spatial discretization, the time splitting between the fluid and structure solvers and contact formulations.

Contents

1.1	Introduction	7
1.2	Fluid-structure interaction	8
1.2.1	Fluid models	8
1.2.2	Thin-walled solid model	10
1.2.3	Fluid-structure coupled problems	11
1.2.4	Contact modeling	14
1.3	Numerical methods	18
1.3.1	Spatial discretization	18
1.3.2	Time-splitting	19

1.1 Introduction

The content of this chapter serves as basic background of the work presented in the rest of this thesis. The reader interested in fundamentals of general continuum mechanics, is referred to [Gurtin \(1982\)](#); [Lai et al. \(2009\)](#). Material regarding fundamentals of solid mechanics can be found in [Ciarlet \(1988\)](#); [Chapelle and Bathe \(2011\)](#). The latter reference is related, in particular, to the mathematical models and their finite element approximation, in the context of thin-walled structures. The models commonly used for the mathematical modeling of fluid-structure interaction (FSI) problems are presented in the following sections. Starting from the description of the fluid equations, solid equations and, finally, considering the full FSI problem, adding the necessary coupling conditions. The fluid formalisms considered will be the Eulerian and Arbitrary Lagrangian Eulerian (ALE), while for the solid equation we restrict the discussion only to the Lagrangian description. As regards additional materials about basis and introduction to fluid-structure

interaction problems, we refer to [Formaggia et al. \(2009\)](#) and the references therein. Afterward, we describe the modeling in contact. In particular, for discussion on dry contact mechanics, we refer to [Wriggers and Zavarise \(2004\)](#), for contact treated via penalization to [Chouly and Hild \(2012\)](#), and via Augmented Lagrangian/Nitsche's approach to [Burman et al. \(2018, 2019\)](#). The latter approach can be seen as a consistent penalization method. For contact considered in the context of fluid-structure interaction, we refer to [Diniz dos Santos et al. \(2008\)](#); [Astorino et al. \(2009b\)](#); [Kamensky et al. \(2015\)](#); [Zonca et al. \(2020\)](#) and [Burman et al. \(2020a\)](#); [Mayer et al. \(2009, 2010\)](#); [Chouly et al. \(2017\)](#) for further examples of contact for FSI treated via Nitsche's approach.

Regarding the numerical approximation, we present a review of the existing numerical methods, discussing the possible spatial discretization strategies (distinguish fitted mesh from the unfitted mesh based approximations) and the degree of time splitting between the fluid and structure sub-problems (introducing the concept of strongly coupled and weakly-coupled schemes). Reviews on numerical methods for FSI can be found in [Hou et al. \(2012\)](#); [Formaggia et al. \(2009\)](#); [Fernández \(2011\)](#).

The rest of the chapter is organized as follows. In Section 1.2 we describe the general geometrical setting and we introduce the fundamental models involved in FSI problem. In particular, we present the fluid problems in Section 1.2.1, the solid problem in Section 1.2.2 and the coupled problems in Section 1.2.3. In Section 1.2.4, the main issues encountered considering contact modeling are described. Section 1.3 presents a review on the existing numerical methods regarding the space discretization (Section 1.3.1) and the splitting between the fluid and solid (Section 1.3.2).

1.2 Fluid-structure interaction

In this section, we consider the mechanical interaction between a deformable thin-walled structure and an incompressible viscous fluid. In the following, the structure domain and the fluid-structure coupling interface are identified by the solid mid-surface.

In continuum mechanics, the Lagrangian formalism is typically used when the interest is on following the material particles, while the Eulerian point of view describes the state of the system in a given control volume in the physical space. Depending on the context one formulation is preferred to the other (see [Formaggia et al. \(2009\)](#)). The classical choice is to consider the Eulerian representation for the fluid and the Lagrangian for the solid. Another possible formulation is the intermediate formalism, called Arbitrary Lagrangian Eulerian (ALE) and is often considered in hemodynamics simulations (see [Nobile \(2001\)](#); [Formaggia et al. \(2009\)](#)).

In the following paragraphs, we will first present the fluid equations in their Eulerian and ALE formalism, afterwards, the solid Lagrangian equations and finally the coupled FSI problem.

1.2.1 Fluid models

Blood is a complex non-Newtonian fluid characterized by a suspension of cells in a liquid (the plasma) made of water for its 90%. The constitutive particles are mainly

red blood cell, white blood cell and platelets. The red blood cell are responsible for the Non-Newtonian blood behavior, due to their highly deformable structure. The Non-Newtonian effects become significant when the vessel size is small (see, e.g., Fåhræus-Lindqvist effect in [Possenti et al. \(2019\)](#); [Pries et al. \(1994\)](#)), while they can be neglected for medium and large size arteries. In this work we will consider the numerical approximation of blood flow in large/medium size vessels, hence, it is reasonable to assume the blood as an *homogeneous, incompressible and Newtonian* fluid, governed by the Navier-Stokes equations. Let now introduce the Navier-Stokes equations in the different frameworks.

1.2.1.1 Eulerian Incompressible Navier-Stokes equations

In this paragraph we provide the necessary notations to describe the Navier-Stokes equations in their Eulerian framework. Let $\Omega^f(t) \in \mathbb{R}^d$, $d = 2, 3$, be a bounded time-dependent domain, with a Lipschitz boundary $\partial\Omega^f(t)$. We denote with \mathbf{n} the unit outward normal on $\partial\Omega^f(t)$. The previously discussed fluid assumptions translate to constant (in space and time) *fluid density* ρ^f and *dynamic viscosity* μ . The Incompressible Navier-Stokes equations in Eulerian framework read as follow: find the fluid velocity $\mathbf{u} : \Omega^f(t) \times \mathbb{R}^+ \rightarrow \mathbb{R}^d$ and pressure $p : \Omega^f(t) \times \mathbb{R}^+ \rightarrow \mathbb{R}$, such that for all $t \in \mathbb{R}^+$ we have

$$\begin{cases} \rho^f (\partial_t \mathbf{u} + (\mathbf{u} \cdot \nabla) \mathbf{u}) - \operatorname{div} \boldsymbol{\sigma}(\mathbf{u}, p) = 0 & \text{in } \Omega^f(t), \\ \operatorname{div} \mathbf{u} = 0 & \text{in } \Omega^f(t), \end{cases} \quad (1.1)$$

where $\boldsymbol{\sigma}(\mathbf{u}, p) \stackrel{\text{def}}{=} 2\mu\boldsymbol{\epsilon}(\mathbf{u}) - p\mathbf{I}$ is the Cauchy stress tensor and $\boldsymbol{\epsilon}(\mathbf{u}) \stackrel{\text{def}}{=} \frac{1}{2}(\nabla\mathbf{u} + \nabla\mathbf{u}^T)$ the strain rate tensor, in which \mathbf{I} denotes the identity tensor.

Problem (1.1) needs to be completed with proper initial condition $\mathbf{u}(0) = \mathbf{u}_0$ and boundary conditions on $\partial\Omega^f(t)$, namely

$$\begin{aligned} \mathbf{u} &= \mathbf{u}_D & \text{on } \Gamma_D(t), \\ \boldsymbol{\sigma}(\mathbf{u}, p)\mathbf{n} &= \mathbf{g}_N & \text{on } \Gamma_N(t), \end{aligned}$$

where \mathbf{u}_D and \mathbf{g}_N denote, respectively, a velocity and a pressure profile. Finally, Γ_D and Γ_N , are such that $\partial\Omega^f(t) = \Gamma_D(t) \cup \Gamma_N(t)$.

1.2.1.2 Arbitrary-Lagrangian-Eulerian Incompressible Navier-Stokes equations

In this paragraph we reformulate the Eulerian Navier-Stokes equation (1.1) in the ALE framework. Only the essential notions are presented. A more extensive presentation can be found in [Formaggia et al. \(2009\)](#) and [Nobile \(2001\)](#). Let $\hat{\Omega}^f = \Omega^f(0)$ be the reference fluid domain. The Arbitrary-Lagrangian-Eulerian description is based on the introduction of an appropriate one-to-one mapping $\mathcal{A} : \hat{\Omega}^f \times \mathbb{R}^+ \rightarrow \mathbb{R}^d$, defined in terms of the fluid domain displacement $\mathbf{d}^f : \hat{\Omega}^f \times \mathbb{R}^+ \rightarrow \mathbb{R}^d$, given by the following expression

$$\mathcal{A} \stackrel{\text{def}}{=} \mathbf{I}_{\hat{\Omega}^f \times \mathbb{R}^+} + \mathbf{d}^f.$$

The purpose of the ALE mapping \mathcal{A} is to parametrize the motion of fluid domain and facilitate the time discretization, when working with an evolving computational domain. The fluid domain velocity is hence defined as $\mathbf{w} \stackrel{\text{def}}{=} \partial_t \mathbf{d}^f$ and the initial configuration is such that $\widehat{\Omega}^f = \mathcal{A}(\widehat{\Omega}^f, 0)$. It should be noted that, the initial configuration coincides with the reference fluid domain. We will also introduce the notation $\mathcal{A}_t(\widehat{\mathbf{x}}) \stackrel{\text{def}}{=} \mathcal{A}(\widehat{\mathbf{x}}, t)$, by fixing $t > 0$ and with $\widehat{\mathbf{x}} \in \widehat{\Omega}^f$.

We recall that for a given functional defined on the ALE reference domain $\widehat{f} : \widehat{\Omega}^f \times \mathbb{R}^+$, we can define its Eulerian counterpart, by

$$f(\mathbf{x}, t) = \widehat{f}(\mathbf{x}, t) \circ \mathcal{A}_t^{-1} = \widehat{f}(\mathcal{A}_t^{-1}(\mathbf{x}), t), \quad \forall (\mathbf{x}, t) \in \Omega^f(t) \times \mathbb{R}^+,$$

and conversely

$$\widehat{f}(\widehat{\mathbf{x}}, t) = f(\mathcal{A}_t(\widehat{\mathbf{x}}), t), \quad \forall (\widehat{\mathbf{x}}, t) \in \widehat{\Omega}^f \times \mathbb{R}^+.$$

For instance, at each point of the current configuration, the Eulerian domain velocity is such that $\mathbf{w}(\mathbf{x}, t) = \widehat{\mathbf{w}}(\widehat{\mathbf{x}}, t)$. Notice that in general the fluid velocity and the domain velocity are different (if $\mathbf{w} = 0$ we retrieve the Eulerian formulation, while if $\mathbf{w} = \mathbf{u}$ the Lagrangian description).

The last necessary ingredient is the so-called ALE time-derivative. For a given Eulerian field \mathbf{q} , we define the ALE time-derivative as follows:

$$\left. \frac{\partial \mathbf{q}}{\partial t} \right|_{\mathcal{A}} \stackrel{\text{def}}{=} \partial_t |_{\mathcal{A}} \mathbf{q} = \mathbf{w} \cdot \nabla \mathbf{q} + \frac{\partial \mathbf{q}}{\partial t}.$$

Hence, the Arbitrary-Lagrangian-Eulerian description of the incompressible Navier-Stokes equations is obtained by introducing the ALE time derivative inside (1.1). The problem reads as follow:

find the velocity $\widehat{\mathbf{u}} = \widehat{\mathbf{u}}(\widehat{\mathbf{x}}, t) : \widehat{\Omega}^f \times \mathbb{R}^+ \rightarrow \mathbb{R}^d$ and pressure $\widehat{p} = \widehat{p}(\widehat{\mathbf{x}}, t) : \widehat{\Omega}^f \times \mathbb{R}^+ \rightarrow \mathbb{R}$, such that

$$\begin{cases} \rho^f (\partial_t |_{\mathcal{A}} \mathbf{u} + (\mathbf{u} - \mathbf{w} \cdot \nabla) \mathbf{u}) - \text{div } \boldsymbol{\sigma}(\mathbf{u}, p) = \mathbf{f} & \text{in } \Omega^f(t), \\ \text{div } \mathbf{u} = 0 & \text{in } \Omega^f(t), \end{cases} \quad (1.2)$$

As for the Eulerian description, problem (1.2) is similarly completed with initial condition on $\Omega^f(0)$ and boundary conditions on Γ_D and Γ_N .

1.2.2 Thin-walled solid model

For a full presentation of the theory of shell models we refer to [Chapelle and Bathe \(2011\)](#); [Bischoff et al. \(2018\)](#). Given the ratio thickness/size of the heart valve leaflets, a common assumption is to model the valves as co-dimensional one structures (i.e., $(d - 1)$ -dimensional models where d is the dimension of the problem under analysis, see, e.g., [Diniz dos Santos et al. \(2008\)](#); [Astorino et al. \(2009b\)](#)). These simplified (but still realistic) dimensionally reduced problems, that we refer to as thin-walled solid models, are those considered in the models presented in this work. Starting from a thick-walled solid description, with the assumption of ratio thickness/size of the solid structure small, we

define the solid equations on the solid mid-surface Σ and we refer to its thickness as ε . Note that Σ is at the same time the fluid-structure interface as well as the solid reference configuration. We will consider the *Reissner-Mindlin* kinematic assumption (see [Chapelle and Bathe \(2011\)](#)), which states that, a material line orthogonal to the reference mid-surface is assumed to remain straight and unstretched during deformation. The displacement is, hence, given in terms of a global displacement and a rotation vector around the normal to the mid-surface. Additionally we will consider a *shear-membrane-bending model* within a non-linear framework. This will be the model considered in the numerical examples of the next chapters, unless specified otherwise.

For sake of simplicity, the *shear-membrane-bending model* that we consider in the description of the methods reads as follow: find the solid displacement $\mathbf{d} : \Sigma \times \mathbb{R}^+ \rightarrow \mathbb{R}^d$ and velocity $\dot{\mathbf{d}} : \Sigma \times \mathbb{R}^+ \rightarrow \mathbb{R}^d$, such that

$$\begin{cases} \rho^s \varepsilon \partial_t \dot{\mathbf{d}} + \mathbf{L}(\mathbf{d}) = \mathbf{T} & \text{on } \Sigma, \\ \dot{\mathbf{d}} = \partial_t \mathbf{d} & \text{on } \Sigma, \end{cases} \quad (1.3)$$

where ρ^s represents the *solid density* and ε its *thickness*. Additionally, \mathbf{T} denotes a given source term, hence a force per unit area, and the surface operator \mathbf{L} represents the strong formulation of the thin-walled solid elastic contributions.

Finally, problem (1.3) must be completed with initial conditions, namely,

$$\begin{cases} \mathbf{d}(0) = \mathbf{d}_0 & \text{on } \Sigma, \\ \dot{\mathbf{d}}(0) = \dot{\mathbf{d}}_0 & \text{on } \Sigma, \end{cases} \quad (1.4)$$

as well as boundary conditions on $\partial\Sigma$.

1.2.3 Fluid-structure coupled problems

Considering the models presented previously, we can now describe the full fluid-structure interaction problem including the coupling/transmission conditions. Thus, we will couple the fluid equations introduced in Section 1.2.1 (considering both Eulerian and ALE formalism) with the thin-walled solid model presented in Section 1.2.2 in Lagrangian formalism.

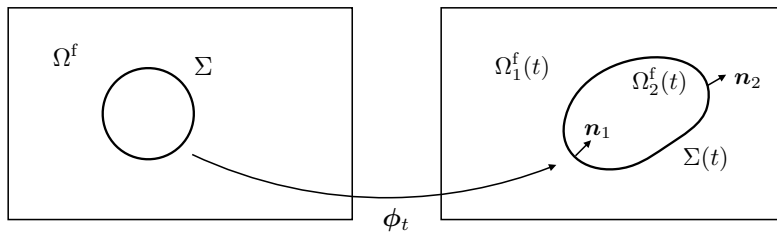


Figure 1.1: Geometrical configuration.

We consider $\Sigma \subset \mathbb{R}^d$, with $d = 2, 3$, the solid mid-surface and let $\Sigma(t)$ be the current position of the interface, given in terms of a deformation map $\phi : \Sigma \times \mathbb{R}^+ \rightarrow \mathbb{R}^d$ and

the solid displacement \mathbf{d} , namely $\phi \stackrel{\text{def}}{=} \mathbf{I}_{\Sigma \times \mathbb{R}^+} + \mathbf{d}$ and such that $\Sigma(t) = \phi(\Sigma, t)$. The geometric configuration is shown in Figure 1.1. The structure is allowed to move within a fixed domain $\Omega^f \subset \mathbb{R}^d$, with boundary $\Gamma \stackrel{\text{def}}{=} \partial\Omega^f$. The fluid time-dependent domain is then defined as $\Omega^f(t) \stackrel{\text{def}}{=} \Omega^f \setminus \Sigma(t)$ and with boundary $\partial\Omega^f = \Gamma \cup \Sigma(t)$. We also introduce the following notation $\phi_t \stackrel{\text{def}}{=} \phi(\cdot, t)$. The immersed interface $\Sigma(t)$ is oriented with unit normal \mathbf{n}_Σ and it divides the fluid domain $\Omega^f(t)$ into two subdomains, with normals respectively $\mathbf{n}_1 \stackrel{\text{def}}{=} \mathbf{n}_\Sigma$ and $\mathbf{n}_2 \stackrel{\text{def}}{=} -\mathbf{n}_\Sigma$.

For a given field f in $\Omega^f(t)$ (possibly discontinuous on $\Sigma(t)$), we define its sided-restrictions, denoted by f_1 and f_2 , as

$$f_1(\mathbf{x}) \stackrel{\text{def}}{=} \lim_{\xi \rightarrow 0^-} f(\mathbf{x} + \xi \mathbf{n}_1), \quad f_2(\mathbf{x}) \stackrel{\text{def}}{=} \lim_{\xi \rightarrow 0^-} f(\mathbf{x} + \xi \mathbf{n}_2),$$

for all $\mathbf{x} \in \Sigma(t)$, and the following jump and average operators across $\Sigma(t)$:

$$\llbracket f \rrbracket \stackrel{\text{def}}{=} f_1 - f_2 \quad \llbracket f \mathbf{n} \rrbracket \stackrel{\text{def}}{=} f_1 \mathbf{n}_1 + f_2 \mathbf{n}_2, \quad \{\!\!\{ f \}\!\!\} \stackrel{\text{def}}{=} \frac{1}{2}(f_1 + f_2).$$

In the coupling with a thin-walled solid the transmission conditions are applied directly to the solid mid-surface Σ , this means that the solid thickness effects are neglected in the interface coupling. This is a common assumption in the coupling of thin-walled solids with general 3D media (see, e.g., [Chapelle and Ferent \(2003\)](#)). The fluid and solid problems are coupled via the so-called kinematic and dynamic coupling conditions. The first is a no-slip condition, representing the fact that, due to its viscosity, the fluid sticks perfectly to the fluid-structure interface. The second accounts for the Newton's third law, hence, for the balance of stresses at the interface. Additionally a geometrical compatibility condition needs to be fulfilled between the fluid and solid domains $\Omega^f(t)$ and $\Sigma(t)$.

In the sequel, we introduce the Eulerian-Lagrangian and the ALE-Lagrangian description of the coupled FSI problem.

1.2.3.1 Eulerian-Lagrangian formalism

We can define the first coupled fluid-structure problem by considering the Eulerian Navier-Stokes equations of Section 1.2.1.1 and the membrane model of Section 1.2.2. The coupled problem reads as follows: find the fluid velocity $\mathbf{u} : \Omega^f \times \mathbb{R}^+ \rightarrow \mathbb{R}^d$ and pressure $p : \Omega^f \times \mathbb{R}^+ \rightarrow \mathbb{R}$, the solid displacement $\mathbf{d} : \Sigma \times \mathbb{R}^+ \rightarrow \mathbb{R}^d$ and velocity $\dot{\mathbf{d}} : \Sigma \times \mathbb{R}^+ \rightarrow \mathbb{R}^d$, such that

$$\begin{cases} \rho^f (\partial_t \mathbf{u} + \mathbf{u} \cdot \nabla \mathbf{u}) - \text{div } \boldsymbol{\sigma}(\mathbf{u}, p) = \mathbf{0} & \text{in } \Omega^f(t), \\ \text{div } \mathbf{u} = 0 & \text{in } \Omega^f(t), \\ \mathbf{u} = \mathbf{0} & \text{on } \Gamma, \end{cases} \quad (1.5)$$

$$\begin{cases} \rho^s \varepsilon \partial_t \dot{\mathbf{d}} + \mathbf{L}(\mathbf{d}) = \mathbf{T} & \text{on } \Sigma, \\ \dot{\mathbf{d}} = \partial_t \mathbf{d} & \text{on } \Sigma, \end{cases} \quad (1.6)$$

$$\left\{ \begin{array}{l} \phi = \mathbf{I}_{\Sigma \times \mathbb{R}^+} + \mathbf{d}, \quad \Sigma(t) = \phi(\Sigma, t), \quad \Omega^f(t) = \Omega^f \setminus \Sigma(t), \\ \mathbf{u} = \dot{\mathbf{d}} \circ \phi_t^{-1} \quad \text{on } \Sigma(t), \\ \int_{\Sigma} \mathbf{T} \cdot \mathbf{y} = - \int_{\Sigma(t)} \llbracket \boldsymbol{\sigma}(\mathbf{u}, p) \mathbf{n} \rrbracket \cdot \mathbf{y} \circ \phi_t^{-1} \quad \forall \text{ smooth } \mathbf{y} : \Sigma \rightarrow \mathbb{R}^d. \end{array} \right. \quad (1.7)$$

As previously, we complete the problem by adding initial and boundary conditions, which are inherited from problems (1.1) and (1.3).

The first equation in (1.7) represents the geometric coupling, which defines the time dependent fluid control volume following the motion of the interface. Equation (1.7)₂ enforces the kinematic coupling and the last equation (1.7)₃ the dynamic coupling, i.e., the balance of stresses at the interface $\Sigma(t)$.

As a consequence of the geometrical coupling condition, problem (1.5)-(1.7) is non-linear, since involves integrals defined on moving domains. In the following, we will refer to this as geometrical non-linearities.

1.2.3.2 ALE-Lagrangian formalism

In this section, we introduce an alternative formulation of problem (1.5)-(1.7), in which the fluid equations are formulated using the ALE formalism of Section 1.2.1.2.

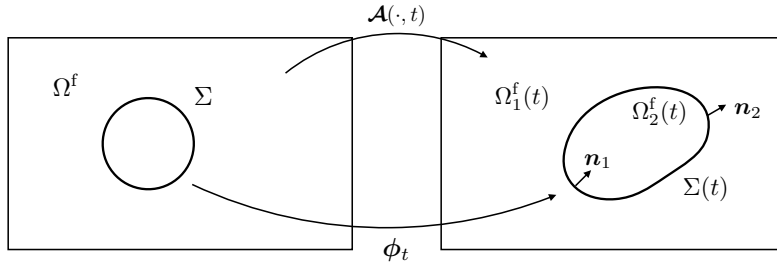


Figure 1.2: Geometrical configuration with for ALE-Lagrangian formalism.

We begin by recalling that the dynamics of the fluid domain is parametrized as $\Omega^f(t) = \mathcal{A}(\widehat{\Omega}^f, t)$, where \mathcal{A} is the ALE-one-to-one mapping defined in Section 1.2.1.2, in terms of the fluid domain displacement \mathbf{d}^f (see Figure 1.2). In the context of FSI, the fluid domain displacement is constrained to the solid displacement by a geometrical compatibility. Typically, the fluid domain displacement is described by a relation of the type $\mathbf{d}^f = \mathcal{L}(\mathbf{d})$, where $\mathcal{L}(\mathbf{d})$ represents a suitable lifting of \mathbf{d} from Σ to $\widehat{\Omega}^f$ which vanishes on Γ . Additionally, it should be noted that the fluid domain displacement is arbitrary in $\widehat{\Omega}^f \setminus \Sigma$. Here the terminology *Arbitrary* Lagrangian Eulerian. The choice for the mapping is arbitrary. However, the efficiency of the method is strongly connected to the effectiveness of the lifting operator, which has the objective of correctly deforming the fluid mesh while maintaining a reasonable elements quality. An harmonic lifting operator can be considered at first, even though, more involved operators based, for instance, on the resolution of elasticity problems are extensively used in the literature (see, e.g., [Stein et al. \(2003\)](#); [Landajuela et al. \(2017\)](#)).

The ALE-Lagrangian FSI coupled problem reads as follows: find the fluid domain displacement $\mathbf{d}^f : \widehat{\Omega}^f \times \mathbb{R}^+ \rightarrow \mathbb{R}^d$, the fluid velocity $\widehat{\mathbf{u}} : \widehat{\Omega}^f \times \mathbb{R}^+ \rightarrow \mathbb{R}^d$, the fluid pressure $\widehat{p} : \widehat{\Omega}^f \times \mathbb{R}^+ \rightarrow \mathbb{R}$, the solid mid-surface displacement $\mathbf{d} : \Sigma \times \mathbb{R}^+ \rightarrow \mathbb{R}^d$ and the solid mid-surface velocity $\dot{\mathbf{d}} : \Sigma \times \mathbb{R}^+ \rightarrow \mathbb{R}^d$, such that

$$\begin{cases} \rho^f \partial_t |_{\mathcal{A}} \mathbf{u} + \rho^f (\mathbf{u} - \mathbf{w}) \cdot \nabla \mathbf{u} - \operatorname{div} \boldsymbol{\sigma}(\mathbf{u}, p) = \mathbf{0} & \text{in } \Omega^f(t), \\ \operatorname{div} \mathbf{u} = 0 & \text{in } \Omega^f(t), \\ \mathbf{u} = \mathbf{0} & \text{on } \Gamma, \end{cases} \quad (1.8)$$

$$\begin{cases} \rho^s \varepsilon \partial_t \dot{\mathbf{d}} + \mathbf{L}(\mathbf{d}) = \mathbf{T} & \text{on } \Sigma, \\ \dot{\mathbf{d}} = \partial_t \mathbf{d} & \text{on } \Sigma, \end{cases} \quad (1.9)$$

$$\begin{cases} \mathbf{d}^f = \mathcal{L}(\mathbf{d}), \quad \mathbf{w} = \partial_t \mathbf{d}^f, \quad \mathcal{A} = \mathbf{I}_{\widehat{\Omega}^f \times \mathbb{R}^+} + \mathbf{d}^f, \quad \Omega^f(t) = \mathcal{A}(\widehat{\Omega}^f, t), \\ \phi = \mathbf{I}_{\Sigma \times \mathbb{R}^+} + \mathbf{d}, \quad \Sigma(t) = \phi(\Sigma, t), \\ \mathbf{u} = \dot{\mathbf{d}} \circ \phi_t^{-1} = \dot{\mathbf{d}} \circ \mathcal{A}_t^{-1} & \text{on } \Sigma(t), \\ \int_{\Sigma} \mathbf{T} \cdot \mathbf{y} = - \int_{\Sigma(t)} \llbracket \boldsymbol{\sigma}(\mathbf{u}, p) \mathbf{n} \rrbracket \cdot \mathbf{y} \circ \phi_t^{-1} = - \int_{\Sigma(t)} \llbracket \boldsymbol{\sigma}(\mathbf{u}, p) \mathbf{n} \rrbracket \cdot \mathbf{y} \circ \mathcal{A}_t^{-1}, \end{cases} \quad (1.10)$$

for all smooth function $\mathbf{y} : \Sigma \rightarrow \mathbb{R}^d$.

Compared to problem (1.5)-(1.7), the fluid domain motion is now fully parametrize by the map \mathcal{A} . Equations (1.10)_{2,3} and (1.10)₄ represent, respectively, the geometric, the kinematic, and the dynamic coupling conditions. Note that as a consequence of the geometrical coupling condition, the ALE \mathcal{A} mapping and the deformation map ϕ coincide on $\Sigma(t)$. Finally, problem (1.8)-(1.10) must be completed with appropriate initial and boundary conditions.

1.2.4 Contact modeling

Contact is an essential aspect of fluid-structure interaction problems, in particular, when we consider as target application heart valves hemodynamics. Building a fluid-structure-contact interaction model, which is, simultaneously, mechanically consistent and able to avoid penetration (between the contacting bodies), is a highly complicate and challenging problem. The computational complexity is also a issue, particularly in the case of real contact (i.e, without relaxation of the contact conditions). In the following, we will consider unilateral frictionless contact, where contact can occur between the solid and a rigid wall, but this can be generalized to the case of contact between multiple solids (see Section 4.2.1).

The distance between the solid and the contacting surface is called *gap* (see Figure 1.3) and solid penetration is typically avoided by adding a contact force to the solid problem when contact is detected. Usually, two exclusive status *gap* or *contact* are classically formulated by imposing an impermeability condition, a compression condition and a complementary condition. Let consider the solid model introduced in Section 1.2.2. Within the typical contact approaches, we can distinguish between *realistic* and *relaxed* contact models.

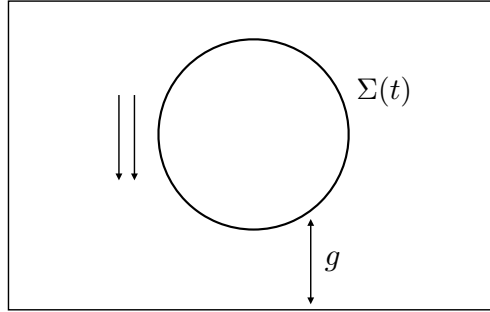


Figure 1.3: Geometric configuration in the non contact situation.

In the first setting, the solid is allowed to reach a zero gap distance, enabling a change in the fluid domain topology (see Figure 1.4). In this case the contact problem reads as follow: find the solid displacement $\mathbf{d} : \Sigma \times \mathbb{R}^+ \rightarrow \mathbb{R}^d$ and velocity $\dot{\mathbf{d}} : \Sigma \times \mathbb{R}^+ \rightarrow \mathbb{R}^d$, such that

$$\begin{cases} \rho^s \varepsilon \partial_t \dot{\mathbf{d}} + \mathbf{L}(\mathbf{d}) - \lambda \mathbf{n} = \mathbf{T} & \text{on } \Sigma, \\ \mathbf{d} \cdot \mathbf{n} - g \leq 0, \quad \lambda \leq 0, \quad \lambda(\mathbf{d} \cdot \mathbf{n} - g) = 0 & \text{on } \Sigma, \end{cases} \quad (1.11)$$

where \mathbf{n} denotes the outward normal vector of the contacting surface and λ represents the contact force in the normal direction. The first inequality in (1.11)₂ ensures that the solid can not pass through the contacting surface, the second inequality that the normal stress is zero (in the absence of contact) or negative (during contact) and the third condition is a complementarity condition that guarantees that at least one of the inequalities is activated. During contact state we have that $\mathbf{d} \cdot \mathbf{n} - g = 0$ and $\lambda < 0$, while $\lambda = 0$ if

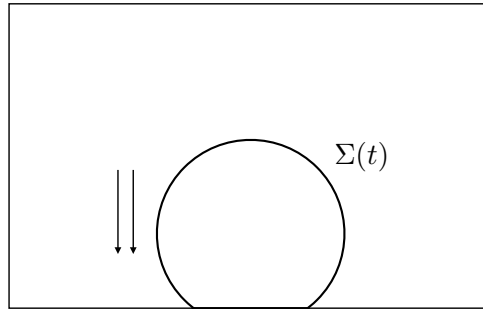


Figure 1.4: Geometric configuration for the realistic contact scenario.

$\mathbf{d} \cdot \mathbf{n} - g < 0$. As long as $\mathbf{d} \cdot \mathbf{n} - g < 0$, contact is not activated and no extra forces are added to the solid problem (see Figure 1.3).

Typically, at the discrete level the contacting nodes are removed from the FSI interface, hence, they are only in contact with the surface and, therefore, the Newton's third law is respected (the only force acting is the contact force, no fluid stresses are involved). This mechanical consistency at contact comes however at a price. Several difficulties have to be faced, such as, paradoxes at solid release (such as isolated vacuum

zone, see Figure 1.5) and FSI coupling interface which is, a priori, unknown, thus, the explicit treatment of geometrical non-linearities may be inappropriate. Additionally, at

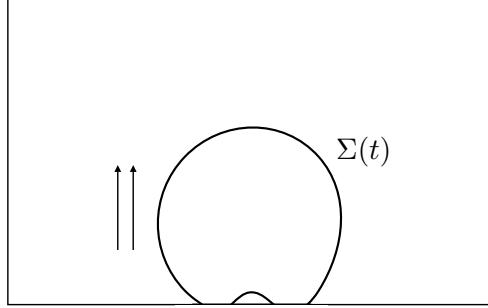


Figure 1.5: Geometric configuration for the realistic contact scenario with vacuum zone at release.

the discrete level, real contact between non matching meshes lead to small regions of fluid isolated from the rest of the fluid domain could appear. In [Ager et al. \(2019a\)](#), the authors propose an ad hoc approach by removing these isolated areas, when smaller than a specific size.

To overcome these difficulties, an alternative approach is to consider a *relaxed contact* formulation, which can also be seen as the insertion of a fictitious contact wall, only visible from the solid side. This formulation avoids real contact, by allowing a small separation between the structure and the contacting wall (see, e.g., [Burman et al. \(2020a\)](#)). In this approximation, the gap g is relaxed by a small fictitious gap ε_h , allowing an infinitesimal distance between the solid and the contacting surface at contact (see Figure 1.6). The

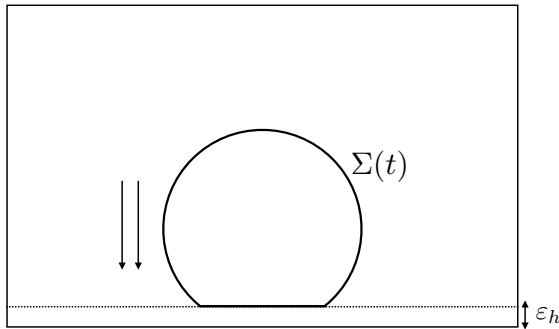


Figure 1.6: Geometric configuration for the relaxed contact scenario.

relaxed contact problem reads as follows: find the solid displacement $\mathbf{d} : \Sigma \times \mathbb{R}^+ \rightarrow \mathbb{R}^d$ and velocity $\dot{\mathbf{d}} : \Sigma \times \mathbb{R}^+ \rightarrow \mathbb{R}^d$, such that

$$\begin{cases} \rho^s \varepsilon \partial_t \dot{\mathbf{d}} + \mathbf{L}(\mathbf{d}) - \lambda \mathbf{n} = \mathbf{T} & \text{on } \Sigma, \\ \mathbf{d} \cdot \mathbf{n} - g_\varepsilon \leq 0, \quad \lambda \leq 0, \quad \lambda(\mathbf{d} \cdot \mathbf{n} - g_\varepsilon) = 0 & \text{on } \Sigma, \end{cases}$$

where $g_\varepsilon \stackrel{\text{def}}{=} g - \varepsilon_h$. Concretely, the no-penetration condition is imposed at ε_h -distance from the contacting surface. In the context of FSI with contact, a layer of fluid will always remain in between the solid and the surface, also at contact. Hence, the contacting structure feel both the contact force as well as the fluid stresses. The solid is at the same time in contact and coupled with the fluid, therefore, the balance of stresses is violated and the Newton's third law is broken. In other words, the contact relaxed formulation avoids the issues related to real topology change, but at the price of a loss of mechanical consistency.

A possible solution strategy to overcome this mechanical inconsistency has been introduced in [Ager et al. \(2019a\)](#). They propose to include, within a *real* contact fluid-structure model, a poroelastic medium over the surface, with the function of describe the solid asperities and eventually squeezing effect due to contact. Hence, the solid gets in contact with a poroelastic medium, which plays the role of an averaged representation between fluid and solid (see Figure 1.7). This approach solves, for instance, the problem

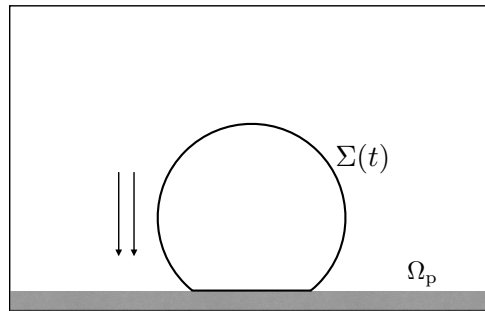


Figure 1.7: Geometric configuration for the realistic contact scenario with a poroelastic medium.

of possible fluid isolated region, that could be created at contact or at release, by enabling a fluid flux inside the poroelastic material. The drawbacks are the computational complexity and active switch between fluid-solid, fluid-porous and poroelastic-solid coupling conditions (due to the *real* contact approximation).

To overcome this additional issues, we will propose in Chapter 5 a reduced order porous model coupled with a relaxed contact formulation. Adding the porous layer over the contact surface is solving the problem of mechanical consistency loss in the relaxed contact problem, related to the Newton's third law rupture. In fact, the porous medium gives physical meaning to the fluid stresses of the infinitesimal fluid layer remaining at contact.

Regarding the contact algorithm considered in literature, we can find approaches based on the resolution of a constrained minimization problem (see, e.g., [Diniz dos Santos et al. \(2008\)](#); [Astorino et al. \(2009b\)](#)), penalization procedure, for instance, for contact treated via penalization we refer to [Chouly and Hild \(2012\)](#); [Kamensky et al. \(2015\)](#), via Augmented Lagrangian/Nitsche's approach to [Burman et al. \(2018, 2019, 2020a\)](#); [Mayer et al. \(2009, 2010\)](#); [Chouly et al. \(2017\)](#). In this work, we will consider a penalty-based ap-

proach, in which we assume contact to be frictionless and soft, characterized by the fact that only displacements in the normal direction are constrained. Moreover, no additional forces due to the lubrication of the structures by the surrounding fluid are considered.

1.3 Numerical methods

In this section, we draw an overview of the methods that are currently used for fluid-structure coupled problems with immersed solids. We will consider first the possible methodology related to the spatial discretization, in particular we will distinguish between fitted and unfitted meshes. Afterward, we consider the splitting in time of the fluid-structure coupling condition. We will discuss about monolithic/partitioned approaches and, within the latter class of coupling schemes, strongly coupled/weakly coupled schemes.

1.3.1 Spatial discretization

The numerical methods for fluid-structure interaction can be roughly divided between *fitted* and *unfitted* mesh based approaches. In the former methodology, the fluid and solid meshes match (see Figure 1.8(a)). Hence, accurate computation of the transmission condition are allowed since the fluid and solid meshes fit at their interface. Additionally, an exact representation of discontinuous quantities is easily embeddable, within the discrete problem, by simply duplicating the degrees of freedom on Σ . For contributions within the fitted meshes framework we refer to, e.g., [Formaggia et al. \(2009\)](#); [Nobile \(2001\)](#); [Boman and Ponthot \(2004\)](#); [Donea et al. \(1982\)](#); [Spühler et al. \(2018\)](#). When large displacements (specially contact) are considered the deformation procedure may fail. Advanced remeshing and moving meshes techniques are one way to circumvent these issues ([Wick \(2011\)](#); [Alauzet \(2014\)](#)).

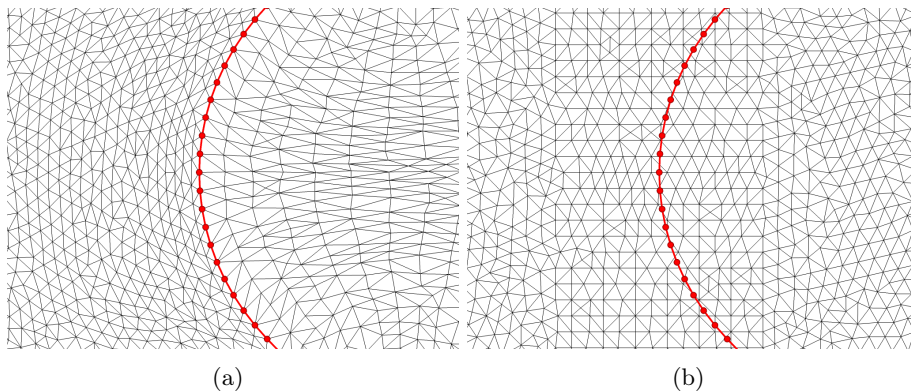


Figure 1.8: Fitted fluid and solid meshes (a), unfitted meshes (b).

In the unfitted mesh methodology (see Figure 1.8(b)), the solid mesh is free to move independently from the fluid mesh (often called background mesh). As a result, this method is quite appealing when FSI with large displacement and contact are considered,

but they consequently require a tracking of the interface. The position of the structure is typically tracked by displacing the solid mesh (see, e.g., [Boffi et al. \(2015\)](#)) or by capturing it through a level set method (see, e.g., [Legay et al. \(2006\)](#)). Among these methods, the most popular are the Immersed Boundary method (see, e.g., [Peskin \(2002\)](#); [Newren et al. \(2007\)](#); [Boffi et al. \(2011\)](#); [Kamensky et al. \(2015\)](#); [Griffith \(2012\)](#)), the Fictitious Domain method (see, e.g., [Glowinski et al. \(1999\)](#); [Baaijens \(2001\)](#); [De Hart et al. \(2003\)](#); [Astorino et al. \(2009b\)](#); [Boffi et al. \(2015\)](#); [Boffi and Gastaldi \(2017\)](#); [Baaijens \(2001\)](#)) and the fully Eulerian (see, e.g., [Cottet et al. \(2008\)](#); [Richter \(2013\)](#); [Frei \(2016\)](#)). In general, these unfitted mesh methods have the reputation of being inaccurate in space, since the fluid spatial discretization does not generally allow for discontinuities across the interface. This often yields severe interfacial mass loss (see, e.g., [Boilevin-Kayl et al. \(2019b\)](#)). The eXtended-FEM (XFEM) class of methods are able to overcome these issues. They are based on local duplication and a cut-FEM approach, but they introduce additional unknowns via Lagrange multipliers (see, e.g., [Zilian and Legay \(2008\)](#); [Gerstenberger and Wall \(2008a\)](#); [Sawada and Tezuka \(2011\)](#); [Gerstenberger and Wall \(2008b\)](#)). These issues are circumvented in an extension of the classical XFEM methods, based on Nitsche's treatment of the interface coupling, (see, e.g., [Burman and Fernández \(2014a\)](#); [Alauzet et al. \(2016\)](#); [Zonca et al. \(2018\)](#)), at the price of additional stabilization parameters, they require a specific evaluation of the interface and background mesh intersections (particularly involving in three dimensions as we will discuss in Chapter 6) and a loss of robustness with respect to how the interface intersects the fluid mesh (see, e.g., [Burman et al. \(2014\)](#); [Fries and Belytschko \(2010\)](#)).

The Nitsche-XFEM method of [Alauzet et al. \(2016\)](#) will be the basis of the spatial approximation considered in this thesis.

1.3.2 Time-splitting

In Section 1.2.3 we have introduced the full FSI models, in which the kinematic, dynamic and geometric conditions, couple the fluid and the structure sub-problems. Depending on how those conditions are imposed (at discrete level) in each problem we can distinguish between *implicit/strongly coupled*, *explicit* and *semi-implicit* coupling schemes.

In the literature, we often distinguish between *monolithic* and *partitioned* resolution strategies. Their peculiarities and differences can be summarized as follows:

Monolithic In this group of methods, the fluid and structure problems are solved simultaneously (in a single block) and in a unified solver (see, e.g., [Formaggia et al. \(2009\)](#); [Badia et al. \(2008c\)](#); [Richter and Wick \(2010\)](#); [Gee et al. \(2011\)](#); [Crosetto et al. \(2011\)](#)). Monolithic schemes are, by nature, *implicit* or *strongly coupled*. Hence, they deliver unconditional stability and optimal accuracy, but at the price of solving a computationally demanding coupled problem at each time-step. An illustration of the approach is presented in Figure 1.9.

Partitioned In the partitioned class of methods, the fluid and solid problems are solved separately, with their own solvers, and they are coupled via their transmission conditions (see, e.g., [Fernández and Moubachir \(2005\)](#); [Badia et al. \(2008a\)](#); [Van Brumme-](#)

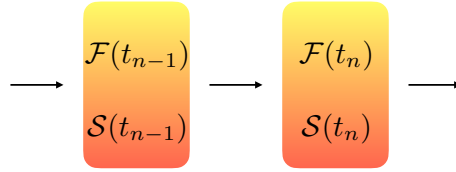


Figure 1.9: Monolithic solution of the coupled system.

len (2011); Nobile et al. (2013)). Their modular nature allows to include independent fluid and solid preexisting solver, at the price of losing some efficiency with respect to monolithic approaches (see, e.g., Badia et al. (2008c); Gee et al. (2011)).

In this thesis, we will consider partitioned schemes, in particular, the Dirichlet-Neumann approach. This implies that we impose the Dirichlet condition (kinematic coupling condition) in the fluid problem and the Neumann (dynamic coupling condition) in the solid problem (see, e.g., Toselli and Widlund (2006) for a general description on this the domain decomposition strategy). Among the partitioned methods, we can distinguish between *strongly*, *semi-implicit* and *weakly* coupled schemes, depending on the time-stepping splitting considered to impose the kinematic and dynamic conditions, inside each separate fluid and solid solvers. The main distinctive features are the following:

Strongly coupled Iterations between the fluid and solid problems are performed at each time iteration until convergence. Hence, the coupling condition is enforced exactly. The illustration of the approach is visible in Figure 1.10.

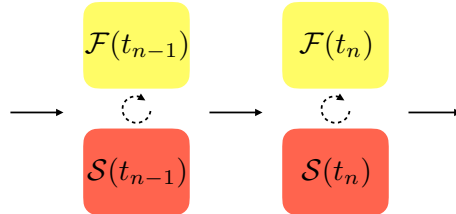


Figure 1.10: Strongly coupled solution of the coupled system.

Explicit Also called loosely coupled or weakly coupled schemes. In this class of schemes, the fluid and solid problems are solved only once per time step. Thus, no inner iteration are present between the fluid and solid solver within one time-step. They are less computationally demanding but might lead to stability and accuracy issues (see Figure 1.11).

Semi-implicit Here, the fluid problem is often divided in sub-problems (typically based in fractional-step strategy) and one part of the fluid problem is coupled explicitly with the solid, while the remaining part is strongly coupled with the solid problem (see Figure 1.12).

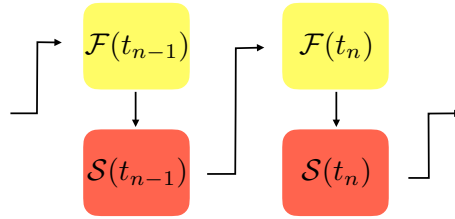


Figure 1.11: Loosely coupled solution of the coupled system.

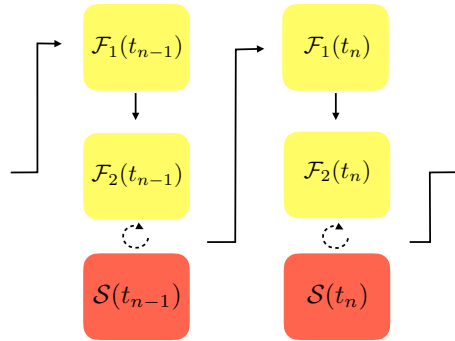


Figure 1.12: Semi-implicit solution of the coupled system.

The semi-implicit scheme that we will present in Chapter 2 is part of the last category. Additionally, it should be noted that, for the geometric coupling condition we will always consider an explicit treatment. This does not compromise stability and accuracy at a reduced computational cost.

Developing stable and accurate loosely-coupled schemes is very challenging problem in incompressible fluid-structure interaction, since the coupling can be extremely stiff. As explain in [Causin et al. \(2005\)](#), Dirichlet-Neumann explicit schemes become unconditionally unstable, as soon as the *added-mass effect* is large. This typically occurs when the fluid and solid density are of the same magnitude (classical situation in hemodynamics).

The majority of the works about not strongly coupled schemes existing in the literature, are based on fitted mesh approximation strategies (see, e.g., [Fernández et al. \(2007\)](#); [Quaini and Quarteroni \(2007\)](#); [Badia et al. \(2008b\)](#); [Astorino and Grandmont \(2010\)](#); [Fernández \(2013\)](#); [Bukac et al. \(2013\)](#); [Bukac and Muha \(2016\)](#)). On the contrary, fewer works exist which avoid strong coupling within the framework of unfitted meshes. The challenge is mainly related to weak treatment of the kinematic interface coupling, without compromising stability and/or accuracy. Note that with unfitted mesh based methods, no connection exist between the fluid and structure functional space. Examples of the loosely-coupled schemes within the unfitted framework are reported in [Boffi et al. \(2011\)](#); [Burman and Fernández \(2014a\)](#); [Alauzet et al. \(2016\)](#); [Kadapa et al. \(2018\)](#); [Kim and Lee \(2018\)](#). Unfortunately, they are known to enforce severe time-step restrictions for stability/accuracy or to be sensitive to the amount of added-mass effect. These issues are circumvented by the semi-implicit and loosely-coupled schemes reported in [Annese \(2017\)](#); [Fernández and Landajuela \(2015\)](#) and in [Boilevin-Kayl et al. \(2019a\)](#), respectively, in the

case of the coupling with thin-walled solids.

Part I

TIME-SPLITTING SCHEMES FOR
UNFITTED MESH APPROXIMATIONS OF
FSI

An unfitted mesh semi-implicit coupling scheme for fluid-structure interaction with immersed solids

Unfitted mesh finite element approximations of immersed incompressible fluid-structure interaction problems which efficiently avoid strong coupling without compromising stability and accuracy are rare in the literature. Moreover, most of the existing approaches introduce additional unknowns or are limited by penalty terms which yield ill-conditioning issues. In this chapter, we introduce a new unfitted mesh semi-implicit coupling scheme which avoids these issues. To this purpose, we provide a consistent generalization of the projection based semi-implicit coupling paradigm of [Int. J. Num. Meth. Engrg.,69(4):794-821, 2007] to the unfitted mesh Nitsche-XFEM framework.

Contents

2.1	Introduction	25
2.2	Linear model problem: static interfaces	27
2.2.1	Time-discretization: semi-implicit coupled scheme	29
2.2.2	Unfitted mesh approximation: fully discrete scheme	31
2.2.3	Partially intersected fluid domain	34
2.2.4	Energy based stability analysis	35
2.3	Non-linear model: moving interface	40
2.3.1	Problem setting	40
2.3.2	Numerical methods	41
2.4	Numerical experiments	43
2.4.1	Idealized valve without contact	44
2.4.2	Idealized valve with contact	47
2.4.3	Vesicle in lid-driven cavity flow	52
2.5	Conclusion	56

2.1 Introduction

Numerical methods for the approximation of mathematical models describing the mechanical interaction of an incompressible viscous fluid with an immersed elastic structure are an essential ingredient in the computer simulation of many living and engineering

systems (see, e.g., [Pozrikidis \(2010\)](#); [Hou et al. \(2012\)](#)). These coupled problems often feature large interface displacements, with potential contact between solids, so that the favored numerical approaches are mainly based on unfitted mesh approximations (the fluid mesh is not fitted to the fluid-solid interface). Among these methods, the most popular are the immersed boundary method (see, e.g., [Peskin \(2002\)](#); [Newren et al. \(2007\)](#); [Boffi et al. \(2011\)](#)) and the fictitious domain method (see, e.g., [Glowinski et al. \(1999\)](#); [Baaijens \(2001\)](#); [De Hart et al. \(2003\)](#); [Astorino et al. \(2009b\)](#); [Boffi et al. \(2015\)](#); [Boffi and Gastaldi \(2017\)](#)), which treat the solid in Lagrangian form. We can also mention the methods based on fully Eulerian descriptions of the coupled system (see, e.g., [Cottet et al. \(2008\)](#); [Richter \(2013\)](#)).

In general, unfitted mesh methods have the reputation of being inaccurate in space. This is due to the approximation of the interface conditions in an unfitted framework and to the fact that the fluid spatial discretization does not generally allow for discontinuities across the interface (which often yields severe interfacial mass loss). Mesh adaptation can improve the situation (see, e.g., [Hachem et al. \(2013\)](#)), but it does not cure the problem. The extended-FEM (XFEM) method, which combines a local duplication with a cut-FEM approach (see, e.g., [Zilian and Legay \(2008\)](#); [Gerstenberger and Wall \(2008a\)](#); [Sawada and Tezuka \(2011\)](#)), fixes these issues but at the expense of introducing Lagrange multipliers (additional unknowns) and deteriorating the robustness (ill-conditioning). The Nitsche-XFEM method (see [Burman and Fernández \(2014a\)](#); [Alauzet et al. \(2016\)](#); [Zonca et al. \(2018\)](#)) circumvents these difficulties through a Nitsche's treatment of the interface coupling (with overlapping meshes) and the addition of suitable stabilization in the vicinity of the interface. The superior accuracy of Nitsche-XFEM with respect to the traditional immersed boundary or fictitious domain methods (see [Boilevin-Kayl et al. \(2019b\)](#) for a recent comparative study) comes, however, at the price of introducing additional stabilization parameters, a much more involved computer implementation and a superior computational complexity. The latter is particularly due to the fact that accurate time-splitting schemes for Nitsche-XFEM are mainly of strongly coupled nature.

Time splitting is generally difficult to marry with unfitted meshes without compromising stability and/or accuracy. This is a direct consequence of the weak treatment of the kinematic interface coupling. To the best of our knowledge, the sole available approaches are the splitting methods introduced in [Boffi et al. \(2011\)](#); [Annese \(2017\)](#); [Kim and Lee \(2018\)](#); [Boilevin-Kayl et al. \(2019a\)](#) for the immersed boundary or fictitious domain methods, and in [Burman and Fernández \(2014a\)](#); [Alauzet et al. \(2016\)](#); [Kadapa et al. \(2018\)](#); [Fernández and Landajuela \(2015\)](#) for unfitted Nitsche based methods. The loosely coupled schemes reported in [Boffi et al. \(2011\)](#); [Burman and Fernández \(2014a\)](#); [Alauzet et al. \(2016\)](#); [Kadapa et al. \(2018\)](#); [Kim and Lee \(2018\)](#) are known to enforce severe time-step restrictions for stability/accuracy or to be sensitive to the amount of added-mass effect. In the case of the coupling with thin-walled solids, these issues are circumvented by the semi-implicit and loosely coupled schemes reported in [Annese \(2017\)](#); [Alauzet et al. \(2016\)](#); [Fernández and Landajuela \(2015\)](#) and in [Boilevin-Kayl et al. \(2019a\)](#), respectively. Nevertheless, the former introduces additional unknowns in the fluid sub-problem (intermediate solid velocity) and the accuracy of the latter relies on a grad-div penalty term (for enhanced mass conservation) which spoils the conditioning of the fluid problem.

In this chapter, we introduce and analyze a new semi-implicit coupling scheme for unfitted mesh approximations of fluid-structure interaction problems with immersed solids which overcomes the above mentioned drawbacks. To this purpose, we propose to generalize the projection based semi-implicit splitting paradigm reported in [Fernández et al. \(2007\)](#) with fitted meshes, to the unfitted Nitsche based framework of [Burman and Fernández \(2014a\)](#); [Alauzet et al. \(2016\)](#). The basic idea consists in the explicit treatment of the geometrical non-linearities, convective and viscous fluid contributions (which avoids strong coupling), whereas the remain fluid pressure and solid contributions are coupled in a fully implicit fashion (which guarantees added-mass free stability). In contrast to alternative immersed boundary and fictitious domain methods involving fractional-step time-marching in the fluid (see, e.g., [Newren et al. \(2007\)](#); [Roshchenko et al. \(2015\)](#)), the Nitsche-XFEM approximation guarantees the spatial consistency of the Laplacian operator in the projection step. For a model problem with static interface, we prove a stability result which states that the conditionally stability of the coupling scheme in the energy norm. Numerical evidence in a series of well-known two-dimensional examples, involving large interface displacements and solid contact, highlights the stability and accuracy properties of the proposed method.

The rest of the chapter is organized as follows. Section 2.2 presents the derivation of the proposed coupling scheme in a linear setting with static interfaces. The energy stability of this method is addressed in Section 2.2.4. In Section 2.3, the coupling scheme is formulated within a fully non-linear setting involving dynamic interfaces. The numerical experiments are reported in Section 2.4. Finally, a summary of the results of the present work are discussed in Section 2.5. Through this chapter and without loss of generality, the solid is assumed to be thin-walled, which corresponds to the most difficult case from the implementation point of view (e.g., discontinuous fluid pressure, interface with tip). The methods and theoretical results presented in this chapter remain valid in the case of the coupling with a thick-walled solid, by simply limiting the fluid problem to a single side of the interface.

2.2 Linear model problem: static interfaces

We first consider a linear fluid-structure interaction problem in which the fluid is described by the Stokes equations in a fixed domain and the structure by a linear immersed thin-walled solid model. We denote by $\Sigma \subset \mathbb{R}^d$, with $d = 2, 3$, the reference configuration of the solid mid-surface. The structure is supposed to be immersed within a fixed domain $\Omega \subset \mathbb{R}^d$, with boundary $\Gamma = \partial\Omega$ (see Figure 2.1). In this section, we assume that the solid undergoes infinitesimal displacements so that the fluid flows within the fixed domain $\Omega^f \stackrel{\text{def}}{=} \Omega \setminus \Sigma \subset \mathbb{R}^d$. The immersed interface Σ is supposed to divide Ω^f into two subdomains $\Omega^f = \Omega_1^f \cup \Omega_2^f$, with respective unit normals $\mathbf{n}_1 \stackrel{\text{def}}{=} \mathbf{n}_\Sigma$ and $\mathbf{n}_2 \stackrel{\text{def}}{=} -\mathbf{n}_\Sigma$. Here, \mathbf{n}_Σ the normal unit vector given by the orientation of the surface Σ . For a given field f defined in Ω^f (possibly discontinuous across the interface), we can then define its sided-restrictions,

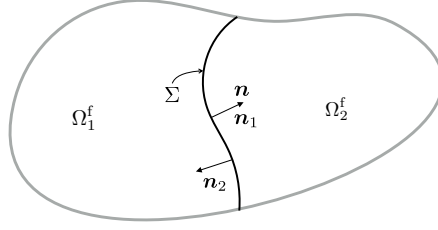


Figure 2.1: Geometric configuration of the fluid domain and the immersed solid.

denoted by f_1 and f_2 , as

$$f_1(\mathbf{x}) \stackrel{\text{def}}{=} \lim_{\xi \rightarrow 0^-} f(\mathbf{x} + \xi \mathbf{n}_1), \quad f_2(\mathbf{x}) \stackrel{\text{def}}{=} \lim_{\xi \rightarrow 0^-} f(\mathbf{x} + \xi \mathbf{n}_2),$$

for all $\mathbf{x} \in \Sigma$, and the following jump and average operators across Σ :

$$[[f]] \stackrel{\text{def}}{=} f_1 - f_2 \quad [[f\mathbf{n}]] \stackrel{\text{def}}{=} f_1 \mathbf{n}_1 + f_2 \mathbf{n}_2, \quad \{\{f\}\} \stackrel{\text{def}}{=} \frac{1}{2}(f_1 + f_2). \quad (2.1)$$

In this framework, the considered coupled problem reads as follow: find the fluid velocity and pressure $\mathbf{u} : \Omega^f \times \mathbb{R}^+ \rightarrow \mathbb{R}^d$, $p : \Omega^f \times \mathbb{R}^+ \rightarrow \mathbb{R}$, the solid displacement and velocity $\mathbf{d} : \Sigma \times \mathbb{R}^+ \rightarrow \mathbb{R}^d$, $\dot{\mathbf{d}} : \Sigma \times \mathbb{R}^+ \rightarrow \mathbb{R}^d$ such that for all $t \in \mathbb{R}^+$ we have

$$\begin{cases} \rho^f \partial_t \mathbf{u} - \text{div} \boldsymbol{\sigma}(\mathbf{u}, p) = \mathbf{0} & \text{in } \Omega^f, \\ \text{div} \mathbf{u} = 0 & \text{in } \Omega^f, \\ \mathbf{u} = \mathbf{0} & \text{on } \Gamma, \end{cases} \quad (2.2)$$

$$\begin{cases} \rho^s \varepsilon \partial_t \dot{\mathbf{d}} + \mathbf{L} \mathbf{d} = \mathbf{T} & \text{in } \Sigma, \\ \dot{\mathbf{d}} = \partial_t \mathbf{d} & \text{in } \Sigma, \\ \mathbf{d} = \mathbf{0} & \text{on } \partial \Sigma, \end{cases} \quad (2.3)$$

$$\begin{cases} \mathbf{u} = \dot{\mathbf{d}} & \text{on } \Sigma, \\ \mathbf{T} = -[[\boldsymbol{\sigma}(\mathbf{u}, p)\mathbf{n}]] & \text{on } \Sigma \end{cases} \quad (2.4)$$

with the initial conditions $\mathbf{u}(0) = \mathbf{u}_0$, $\mathbf{d}(0) = \mathbf{d}_0$ and $\dot{\mathbf{d}}(0) = \dot{\mathbf{d}}_0$. Here, the symbols ρ^f and ρ^s stand respectively the fluid and solid densities, the thickness of the solid is denoted by ε and the fluid Cauchy stress tensor is given by

$$\boldsymbol{\sigma}(\mathbf{u}, p) \stackrel{\text{def}}{=} 2\mu \boldsymbol{\epsilon}(\mathbf{u}) - p \mathbf{I}, \quad \boldsymbol{\epsilon}(\mathbf{u}) \stackrel{\text{def}}{=} \frac{1}{2}(\nabla \mathbf{u} + \nabla \mathbf{u}^T),$$

where μ denotes the fluid dynamic viscosity. The operator \mathbf{L} describes the elastic behavior of the solid. The relations in (2.4) enforce, respectively, the kinematic and dynamic interface coupling conditions. Note that the former enforces two conditions since it has to be seen as $\mathbf{u}_1 = \mathbf{u}_2 = \dot{\mathbf{d}}$ on Σ .

2.2.1 Time-discretization: semi-implicit coupled scheme

In what follows, we will use the following notation for the first-order backward difference: $\partial_\tau x^n \stackrel{\text{def}}{=} (x^n - x^{n-1})/\tau$, where $\tau > 0$ denotes the time-step length. For the time discretization of the coupled problem (2.2)-(2.4) we consider the projection based semi-implicit splitting scheme proposed in Fernández et al. (2007); Landajuéla et al. (2017) for the case of fitted-mesh spatial approximations (see also Quaini and Quarteroni (2007); Badia et al. (2008b); Astorino et al. (2009a); Astorino and Grandmont (2010)). The scheme avoids strong coupling without compromising stability and accuracy. The fundamental idea consists in combining a fractional-step time-marching in the fluid with a semi-implicit treatment of the interface coupling (2.4). The resulting time semi-discrete method reads as follows (see Fernández et al. (2007); Landajuéla et al. (2017)) for $n \geq 1$:

1. Explicit fluid viscous step: Find $\tilde{\mathbf{u}}^n : \Omega^f \rightarrow \mathbb{R}^d$ such that

$$\begin{cases} \frac{\rho^f}{\tau}(\tilde{\mathbf{u}}^n - \mathbf{u}^{n-1}) - \operatorname{div} \boldsymbol{\sigma}(\tilde{\mathbf{u}}^n, p^{n-1}) = \mathbf{0} & \text{in } \Omega^f, \\ \tilde{\mathbf{u}}^n = \mathbf{0} & \text{on } \Gamma, \\ \tilde{\mathbf{u}}^n = \dot{\mathbf{d}}^{n-1} & \text{on } \Sigma. \end{cases} \quad (2.5)$$

2. Implicit pressure-displacement step: Find $\mathbf{u}^n : \Omega^f \rightarrow \mathbb{R}^d$, $p^n : \Omega^f \rightarrow \mathbb{R}$, $\mathbf{d}^n : \Sigma \rightarrow \mathbb{R}^d$ and $\dot{\mathbf{d}}^n : \Sigma \rightarrow \mathbb{R}^d$ such that

$$\begin{cases} \frac{\rho^f}{\tau}(\mathbf{u}^n - \tilde{\mathbf{u}}^n) + \nabla(p^n - p^{n-1}) = \mathbf{0} & \text{in } \Omega^f, \\ \operatorname{div} \mathbf{u}^n = 0 & \text{in } \Omega^f, \\ \mathbf{u}^n \cdot \mathbf{n} = 0 & \text{on } \Gamma, \end{cases} \quad (2.6)$$

$$\begin{cases} \rho^s \varepsilon \partial_\tau \dot{\mathbf{d}}^n + \mathbf{L} \mathbf{d}^n = \mathbf{T}^n & \text{on } \Sigma, \\ \dot{\mathbf{d}}^n = \partial_\tau \mathbf{d}^n & \text{on } \Sigma, \\ \mathbf{d}^n = \mathbf{0} & \text{on } \partial \Sigma, \end{cases} \quad (2.7)$$

$$\begin{cases} \mathbf{u}_i^n \cdot \mathbf{n}_i = \dot{\mathbf{d}}^n \cdot \mathbf{n}_i & \text{on } \Sigma, \quad i = 1, 2, \\ \mathbf{T}^n = -\llbracket \boldsymbol{\sigma}(\tilde{\mathbf{u}}^n, p^n) \mathbf{n} \rrbracket & \text{on } \Sigma. \end{cases} \quad (2.8)$$

The viscous-step (2.5) is loosely coupled with the solid, which avoids strong coupling, whereas the step (2.6)-(2.8) guarantees added-mass free stability by the implicit treatment of the fluid pressure and solid inertia. From a computational point of view, the scheme (2.5)-(2.8) can be reformulated exclusively in terms of $\tilde{\mathbf{u}}^n$, p^n , \mathbf{d}^n and $\dot{\mathbf{d}}^n$ as shown in Algorithm 2.1. In the viscous step, the end-of-step velocity \mathbf{u}^{n-1} has been eliminated by inserting (2.6)₁, evaluated at time $n-1$, into (2.5)₁. This leads to a second-order extrapolation of the pressure, noted by $p^{n,*} \stackrel{\text{def}}{=} 2p^{n-1} - p^{n-2}$, in the viscous step. Finally, the projection step (2.6) can be rewritten in a Poisson-like problem by taking the divergence of (2.6)₁ and applying (2.6)₂ in each sub-domain Ω_i .

Algorithm 2.1 Time semi-discrete projection based semi-implicit scheme (from [Fernández et al. \(2007\)](#); [Landajuela et al. \(2017\)](#)).

For $n \geq 2$:

1. Fluid viscous step: Find $\tilde{\mathbf{u}}^n : \Omega^f \rightarrow \mathbb{R}^d$ such that

$$\begin{cases} \rho^f \partial_\tau \tilde{\mathbf{u}}^n - \operatorname{div} \boldsymbol{\sigma}(\tilde{\mathbf{u}}^n, p^{n,*}) = \mathbf{0} & \text{in } \Omega^f, \\ \tilde{\mathbf{u}}^n = \mathbf{0} & \text{on } \Gamma, \\ \tilde{\mathbf{u}}^n = \dot{\mathbf{d}}^{n-1} & \text{on } \Sigma. \end{cases} \quad (2.9)$$

2. Pressure-displacement step: Find $p^n : \Omega^f \rightarrow \mathbb{R}$, $\mathbf{d}^n : \Sigma \rightarrow \mathbb{R}^d$ and $\dot{\mathbf{d}}^n : \Sigma \rightarrow \mathbb{R}^d$ such that

$$\begin{cases} -\frac{\tau}{\rho^f} \Delta (p^n - p^{n-1}) = -\operatorname{div} \tilde{\mathbf{u}}^n & \text{in } \Omega^f, \\ \frac{\tau}{\rho^f} \nabla (p^n - p^{n-1}) \cdot \mathbf{n} = 0 & \text{on } \Gamma, \end{cases} \quad (2.10)$$

$$\begin{cases} \rho^s \varepsilon \partial_\tau \dot{\mathbf{d}}^n + \mathbf{L} \mathbf{d}^n = \mathbf{T}^n & \text{on } \Sigma, \\ \dot{\mathbf{d}}^n = \partial_\tau \mathbf{d}^n & \text{on } \Sigma, \\ \mathbf{d}^n = \mathbf{0} & \text{on } \partial \Sigma, \end{cases} \quad (2.11)$$

$$\begin{cases} \frac{\tau}{\rho^f} \nabla (p_i^n - p_i^{n-1}) \cdot \mathbf{n}_i = (\tilde{\mathbf{u}}_i^n - \dot{\mathbf{d}}^n) \cdot \mathbf{n}_i & \text{on } \Sigma, \quad i = 1, 2, \\ \mathbf{T}^n = -\llbracket \boldsymbol{\sigma}(\tilde{\mathbf{u}}^n, p^n) \mathbf{n} \rrbracket & \text{on } \Sigma. \end{cases} \quad (2.12)$$

An energy based stability result for the non-incremental version of (2.5)-(2.8) (i.e., with $p^{n-1} = 0$) with a fitted mesh based finite element approximation in space, has been reported in [Fernández et al. \(2007\)](#). Therein, stability is guaranteed under the CFL-like condition

$$\rho^f h^2 + 2\mu\tau \lesssim \rho^s \varepsilon h, \quad (2.13)$$

where $h > 0$ stands for the spatial grid parameter. It is also worth noting that unconditional stability was achieved in [Astorino et al. \(2009a\)](#) via a specific Nitsche's treatment of the viscous coupling. Unfortunately, the splitting error of the resulting scheme is known to be non uniform with respect to h , namely, to scales as $\mathcal{O}(\tau/h)$, so that suitable correction iterations are needed to enhance accuracy under restrictive constraints on the discretization parameters (as in [Alauzet et al. \(2016\)](#)).

Remark 2.2.1. Note that from the relation (2.12)₁ we get the continuity of flux on the pressure increment across Σ , namely,

$$\llbracket \nabla (p^n - p^{n-1}) \cdot \mathbf{n} \rrbracket = 0 \quad \text{on } \Sigma.$$

However, both the pressure p^n and the pressure increment $p^n - p^{n-1}$ are generally discontinuous across Σ , so that the pressure-Poisson equation (2.10)₁ is not valid across Σ , only

in Ω^f . Most of the immersed boundary and fictitious domain methods involving fractional-step time-marching in the fluid assume that this relation is valid in Ω (see, e.g., [Newren et al. \(2007\)](#); [Roshchenko et al. \(2015\)](#)). This is not the case of the unfitted mesh method considered in this chapter, which correctly enforces (2.10) in Ω^f rather than in Ω .

2.2.2 Unfitted mesh approximation: fully discrete scheme

In the following, the closed spaces $H_{\Gamma}^1(\omega)$, of functions in $H^1(\omega)$ with zero trace on Γ , and $L_0^2(\omega)$, of functions in $L^2(\omega)$ with zero mean in ω , will be considered. The scalar product in $L^2(\omega)$ is denoted by $(\cdot, \cdot)_{\omega}$. In this section, we introduce a consistent unfitted mesh spatial approximation of the time semi-discrete scheme given by Algorithm 2.1. The fluid fields $(\tilde{\mathbf{u}}^n, p^n)$ will hence be approximated in triangulations of Ω which are independent of Σ . To this purpose, it is important to note that:

- The velocity gradient $\nabla \tilde{\mathbf{u}}^n$ and the pressure p^n are discontinuous across Σ ;
- The bulk relations (2.9)₁ and (2.10)₁ are not valid across Σ , only in Ω^f (see Remark 2.2.1).

In the case of fitted mesh approximations, these discontinuous features of the solution can be introduced in the discrete approximation in simple fashion (e.g., by considering cracked meshes with duplicated nodes on the interface). However, if the fluid mesh does not have a geometrical representation of the interface Σ , guaranteeing consistency of the approximations requires a specific treatment. In this chapter, we build on the unfitted Nitsche's based method for incompressible fluid-structure interaction with overlapping meshes reported in [Burman and Fernández \(2014a\)](#); [Alauzet et al. \(2016\)](#). The fundamental reasons for this choice are: (i) it is Lagrange multipliers free and robust; (ii) it is mathematically sound (i.e., optimal error estimates are obtained for spatial semi-discrete approximations of linear model problems such as (2.2)-(2.4) under reasonable regularity assumptions (see, e.g., [Burman and Fernández \(2014a\)](#)); and (iii) it naturally provides a consistent form of the pressure-Poisson problem in step 2 of Algorithm 2.1.

In order to simplify the presentation, we assume that both Ω and Σ are polyhedral. Let be $\{\mathcal{T}_h^s\}_{0 < h < 1}$ a family of triangulations of Σ . We then consider the standard space of continuous piecewise affine functions:

$$X_h^s \stackrel{\text{def}}{=} \{v_h \in C^0(\bar{\Sigma}) \mid v_h|_K \in \mathbb{P}_1(K), \quad \forall K \in \mathcal{T}_h^s\}.$$

The weak form of the abstract solid elastic operator \mathbf{L} in (2.3) is assumed to be given by a positive and symmetric bi-linear form $a^s : \mathbf{W} \times \mathbf{W} \rightarrow \mathbb{R}$, where $\mathbf{W} = [H^1(\Sigma)]_0^d$ denotes the space of admissible displacements. The discrete space for the solid displacement and velocity approximations is hence defined as $\mathbf{W}_h = [X_h^s]^d \cap \mathbf{W}$. For the fluid, we consider a family of meshes $\{\mathcal{T}_h\}_{h>0}$ of Ω , fitted to its boundary Γ but not to the internal interface Σ . We can then define the two family of meshes $\{\mathcal{T}_{h,i}\}_{h>0}$, with $i = 1, 2$, such that $\mathcal{T}_{h,i} \subset \mathcal{T}_h$ covers the fluid region Ω_i . Each mesh $\mathcal{T}_{h,i}$ is fitted to the exterior boundary Γ but not to \mathcal{T}_h^s . Moreover, for every element $K \in \mathcal{T}_{h,1} \cap \mathcal{T}_{h,2}$ we have $K \cap \Sigma \neq \emptyset$.

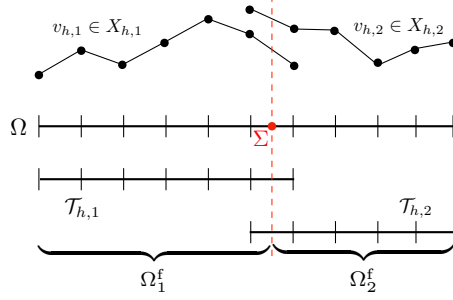


Figure 2.2: One dimensional illustration of the construction of the discrete spaces $X_{h,i}$.

We denote by $\Omega_{h,i}$ the domain covered by $\mathcal{T}_{h,i}$, viz.,

$$\Omega_{h,i} \stackrel{\text{def}}{=} \text{int} \left(\cup_{K \in \mathcal{T}_{h,i}} K \right).$$

We shall also make use of the following notation for the broken L^2 -product in the whole computational domain

$$(\cdot, \cdot)_h \stackrel{\text{def}}{=} \sum_{i=1}^2 \sum_{K \in \mathcal{T}_{h,i}} (\cdot, \cdot)_K.$$

For $i = 1, 2$, we can hence introduce the following spaces of continuous piecewise affine functions:

$$X_{h,i} \stackrel{\text{def}}{=} \{v_h \in C^0(\overline{\Omega_{h,i}}) \mid v_h|_K \in \mathbb{P}_1(K), \quad \forall K \in \mathcal{T}_{h,i}\},$$

Associated with $X_{h,i}$ we define the spaces

$$\mathbf{V}_{h,i} \stackrel{\text{def}}{=} [X_{h,i}]^d \cap [H_{\Gamma}^1(\Omega)]^d, \quad Q_{h,i} \stackrel{\text{def}}{=} X_{h,i} \cap L^2(\Omega)_0.$$

For the approximation of the fluid velocity and pressure we will consider the following discrete product spaces

$$\mathbf{V}_h \stackrel{\text{def}}{=} \mathbf{V}_{h,1} \times \mathbf{V}_{h,2}, \quad Q_h \stackrel{\text{def}}{=} Q_{h,1} \times Q_{h,2}, \quad (2.14)$$

which guarantee that interfacial (strong and weak) discontinuities are included in the discrete approximation of both the fluid velocity and pressure. Indeed, the functions of (2.14) are continuous in the physical fluid domain Ω^f but discontinuous across the interface Σ (see Figure 2.2). Since the discrete pair \mathbf{V}_h/Q_h is not inf-sup stable, we consider a symmetric stabilization operator, such as, the one given by Continuous Interior Penalty method (see [Burman and Hansbo \(2006\)](#)) over the whole computational domain:

$$s_h(p_h, q_h) = \frac{\gamma_p h^3}{\mu} \sum_{i=1}^2 \sum_{F \in \mathcal{F}_{h,i}} ([[\nabla p_h]]_F, [[\nabla q_h]]_F)_F,$$

where $\mathcal{F}_{h,i}$ denotes the set of interior edges or faces of $\mathcal{T}_{h,i}$. Finally, we introduce the fluid

discrete viscous bi-linear form

$$a_h^f(\mathbf{u}_h, \mathbf{v}_h) \stackrel{\text{def}}{=} 2\mu(\boldsymbol{\epsilon}(\mathbf{u}_h), \boldsymbol{\epsilon}(\mathbf{v}_h))_{\Omega^f} + g_h(\mathbf{u}_h, \mathbf{v}_h),$$

where the ghost-penalty operator is given by (see [Burman \(2010\)](#))

$$g_h(\mathbf{u}_h, \mathbf{v}_h) \stackrel{\text{def}}{=} \gamma_g \mu h \sum_{i=1}^2 \sum_{F \in \mathcal{F}_{i,h}^\Sigma} (\llbracket \nabla \mathbf{u}_{i,h} \rrbracket_F, \llbracket \nabla \mathbf{v}_{i,h} \rrbracket_F)_F \quad (2.15)$$

and where $\mathcal{F}_{i,h}^\Sigma$ denotes the set of interior edges or faces of the elements intersected by Σ , as shown in Figure 2.3. This operator guarantees robustness irrespectively to the way the interface is cutting the fluid mesh, by extending the coercivity of the viscous bi-linear form to the whole computational domain.

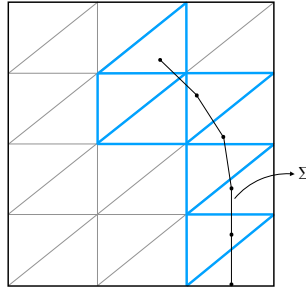


Figure 2.3: Illustration of the interior edges (highlighted in blue) where the ghost-penalty operator is applied.

For completeness and based on the above ingredients, a strongly coupled scheme for the unfitted mesh approximation of (2.2)-(2.4) is given in Algorithm 2.2. Note that, at each time step, the fluid and solid approximations are fully coupled. This guarantees unconditional stability and accuracy at the expense of computational complexity (see [Alauzet et al. \(2016\)](#)).

We can now introduce the unfitted mesh approximation of Algorithm 2.1 detailed in Algorithm 2.3. Its main ingredients are the following:

- Unfitted Nitsche's mortaring for the spatial discretization of the kinematic/dynamic viscous coupling in (2.9), (2.11) and (2.12), which is Lagrange multipliers free (i.e., without additional unknowns) and guarantees accuracy and robustness;
- For robustness, the Laplace operator in the projection-step (2.10) is integrated over the whole computational domain, whereas for consistency the remaining fluid bulk terms in (2.9) and in (2.10) are integrated in the whole physical domain.

Note that the price to pay for consistency in the last point is a specific track of the interface intersections and the integration over cut elements (see, e.g., [Massing et al. \(2013\)](#); [Alauzet et al. \(2016\)](#); [Zonca et al. \(2018\)](#) and the references therein). As regards the first point, it should be noted that in (2.17) the discrete interface stresses are exactly the variationally

Algorithm 2.2 Strongly coupled scheme with unfitted meshes (from [Alauzet et al. \(2016\)](#)).

For $n \geq 1$:

Find $(\mathbf{u}_h^n, p_h^n, \dot{\mathbf{d}}_h^n, \mathbf{d}_h^n) \in \mathbf{V}_h \times Q_h \times \mathbf{W}_h \times \mathbf{W}_h$ with $\dot{\mathbf{d}}_h^n = \partial_\tau \mathbf{d}_h^n$ and such that

$$\begin{aligned} & \rho^f (\partial_\tau \mathbf{u}_h^n, \mathbf{v}_h)_{\Omega^f} + a_h^f(\mathbf{u}_h^n, \mathbf{v}_h) - (p_h^n, \operatorname{div} \mathbf{v}_h)_{\Omega^f} + (q_h, \operatorname{div} \mathbf{u}_h^n)_{\Omega^f} + s_h(p_h, q_h) \\ & + \rho^s \varepsilon (\partial_\tau \dot{\mathbf{d}}_h^n, \mathbf{w}_h)_\Sigma + a^s(\mathbf{d}_h^n, \mathbf{w}_h) - \sum_{i=1}^2 (\boldsymbol{\sigma}(\mathbf{u}_{h,i}^n, p_{h,i}^n) \mathbf{n}_i, \mathbf{v}_{h,i} - \mathbf{w}_h)_\Sigma \\ & - \sum_{i=1}^2 (\mathbf{u}_{h,i}^n - \dot{\mathbf{d}}_h^n, \boldsymbol{\sigma}(\mathbf{v}_{h,i}, -q_{h,i})) \mathbf{n}_i)_\Sigma + \frac{\gamma \mu}{h} \sum_{i=1}^2 (\mathbf{u}_{h,i}^n - \dot{\mathbf{d}}_h^n, \mathbf{v}_{h,i} - \mathbf{w}_h)_\Sigma = 0 \end{aligned}$$

for all $(\mathbf{v}_h, q_h, \mathbf{w}_h) \in \mathbf{V}_h \times Q_h \times \mathbf{W}_h$.

consistent viscous stress of (2.9). This constitutes a fundamental difference with respect to the Robin based semi-implicit and explicit coupling schemes respectively reported in [Astorino et al. \(2009a\)](#); [Alauzet et al. \(2016\)](#) with fitted meshes. The main reason is to avoid the accuracy loss observed with this methods (see Section 2.2.1). The next section is devoted the energy based stability analysis of Algorithm 2.3.

2.2.3 Partially intersected fluid domain

In the case in which the interface has a boundary inside the fluid domain (the tip), we consider the construction of the fluid and solid spaces proposed in [Alauzet et al. \(2016\)](#), which basically consists in introduce a virtual interface $\tilde{\Sigma}$ which closes the fluid domain within the cut element. This virtual interface is defined as the segment connecting the interface tip with the fluid vertex opposite to the edge intersected by the interface (see Figure 2.4).

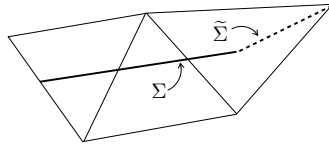


Figure 2.4: Case in which the Σ has a boundary inside the fluid domain.

Then, we enforce the kinematic/dynamic continuity of the fluid on $\tilde{\Sigma}$ in a discontinuous Galerkin fashion (see, e.g., [Di Pietro and Ern \(2012\)](#)). More precisely, the following terms are added

$$-(\{\{\boldsymbol{\sigma}(\tilde{\mathbf{u}}_h^n, 0)\}\mathbf{n}, \llbracket \tilde{\mathbf{v}}_h \rrbracket\})_{\tilde{\Sigma}} - (\{\{\boldsymbol{\sigma}(\tilde{\mathbf{v}}_h, 0)\}\mathbf{n}, \llbracket \tilde{\mathbf{u}}_h^n \rrbracket\})_{\tilde{\Sigma}} + \frac{\gamma \mu}{h} (\llbracket \tilde{\mathbf{u}}_h^n \rrbracket, \llbracket \tilde{\mathbf{v}}_h \rrbracket)_{\tilde{\Sigma}}, \quad (\llbracket p_h^{n,*} \rrbracket, \{\{\tilde{\mathbf{v}}_h\} \cdot \mathbf{n}\})_{\tilde{\Sigma}}, \quad (2.18)$$

Algorithm 2.3 Projection based semi-implicit scheme with unfitted meshes and static interface.

For $n \geq 1$:

1. Fluid viscous step: Find $\tilde{\mathbf{u}}_h^n \in \mathbf{V}_h$ such that

$$\begin{aligned} \rho^f (\partial_\tau \tilde{\mathbf{u}}_h^n, \tilde{\mathbf{v}}_h)_{\Omega^f} + a_h^f(\tilde{\mathbf{u}}_h^n, \tilde{\mathbf{v}}_h) - \sum_{i=1}^2 (\boldsymbol{\sigma}(\tilde{\mathbf{u}}_{h,i}^n, 0) \mathbf{n}_i, \tilde{\mathbf{v}}_{h,i})_\Sigma + \frac{\gamma\mu}{h} \sum_{i=1}^2 (\tilde{\mathbf{u}}_{h,i}^n - \dot{\mathbf{d}}_h^{n-1}, \tilde{\mathbf{v}}_{h,i})_\Sigma \\ - \sum_{i=1}^2 (\tilde{\mathbf{u}}_{h,i}^n - \dot{\mathbf{d}}_h^{n-1}, \boldsymbol{\sigma}(\tilde{\mathbf{v}}_{h,i}, 0) \mathbf{n}_i)_\Sigma = -(\nabla p_h^{n,*}, \tilde{\mathbf{v}}_h)_{\Omega^f} \end{aligned} \quad (2.16)$$

for all $\tilde{\mathbf{v}}_h \in \mathbf{V}_h$.

2. Pressure-displacement step: Find $(p_h^n, \mathbf{d}_h^n) \in Q_h \times \mathbf{W}_h$ with $\dot{\mathbf{d}}_h^n = \partial_\tau \mathbf{d}_h^n$, such that

$$\left\{ \begin{aligned} \frac{\tau}{\rho^f} (\nabla(p_h^n - p_h^{n-1}), \nabla q_h)_h + s_h(p_h^n, q_h) &= \sum_{i=1}^2 (\tilde{\mathbf{u}}_{h,i}^n - \dot{\mathbf{d}}_h^n, q_{h,i} \mathbf{n}_i)_\Sigma - (\operatorname{div} \tilde{\mathbf{u}}_h^n, q_h)_{\Omega^f}, \\ \rho^s \varepsilon (\partial_\tau \dot{\mathbf{d}}_h^n, \mathbf{w}_h)_\Sigma + a^s(\mathbf{d}_h^n, \mathbf{w}_h) &= \frac{\gamma\mu}{h} \sum_{i=1}^2 ((\tilde{\mathbf{u}}_{h,i}^n - \dot{\mathbf{d}}_h^{n-1}), \mathbf{w}_h)_\Sigma \\ &\quad - \sum_{i=1}^2 (\boldsymbol{\sigma}(\tilde{\mathbf{u}}_{h,i}^n, p_{h,i}^n) \mathbf{n}_i, \mathbf{w}_h)_\Sigma \end{aligned} \right. \quad (2.17)$$

for all $(q_h, \mathbf{w}_h) \in Q_h \times \mathbf{W}_h$.

into the left- and right-hand side of step (2.16), respectively, where as in (2.17)₁ we add

$$-\frac{\tau}{\rho^f} (\{\{\nabla p_h^n \cdot \mathbf{n}\}\}, \llbracket q_h \rrbracket)_{\tilde{\Sigma}} - \frac{\tau}{\rho^f} (\llbracket p_h^n \rrbracket, \{\{\nabla q_h \cdot \mathbf{n}\}\})_{\tilde{\Sigma}} + \frac{\tau}{\rho^f} \frac{\gamma}{h} (\llbracket p_h^n \rrbracket, \llbracket q_h \rrbracket)_{\tilde{\Sigma}}, \quad (\llbracket \tilde{\mathbf{u}}_h^n \rrbracket \cdot \mathbf{n}, \{\{\llbracket q_h \rrbracket\}\})_{\tilde{\Sigma}}, \quad (2.19)$$

to the left- and right-hand side, respectively.

2.2.4 Energy based stability analysis

For the purpose of the analysis below, we recall the following estimate from [Burman \(2010\)](#):

$$c_g (2\mu \|\boldsymbol{\epsilon}(\mathbf{v}_h)\|_{0,\Omega_h}^2 + g_h(\mathbf{v}_h, \mathbf{v}_h)) \leq 2\mu \|\boldsymbol{\epsilon}(\mathbf{v}_h)\|_{0,\Omega^f}^2 + g_h(\mathbf{v}_h, \mathbf{v}_h) \quad (2.20)$$

for all $\mathbf{v}_h \in \mathbf{V}_h$ with $c_g > 0$ and the notation

$$\|\cdot\|_{0,\Omega_h}^2 \stackrel{\text{def}}{=} (\cdot, \cdot)_h.$$

We shall also make use of the following (robust) discrete trace inequality

$$h\|\boldsymbol{\epsilon}(\mathbf{v}_h)\mathbf{n}\|_{0,\Sigma}^2 \leq C_T\|\boldsymbol{\epsilon}(\mathbf{v}_h)\|_{0,\Omega_h}^2 \quad (2.21)$$

for all $\mathbf{v}_h \in \mathbf{V}_h$. Let define the discrete total energy E_h^n by the following expression:

$$E_h^n \stackrel{\text{def}}{=} \frac{\rho^f}{2}\|\mathbf{u}_h^n\|_{0,\Omega^f}^2 + \frac{\rho^s\varepsilon}{2}\|\dot{\mathbf{d}}_h^n\|_{\Sigma}^2 + \frac{1}{2}a^s(\mathbf{d}_h^n, \mathbf{d}_h^n) + \frac{\tau^2}{2\rho^f}\|\nabla p_h^n\|_{0,\Omega_h}^2.$$

The following result states the conditional energy based stability of the approximation provided by Algorithm 2.3.

Theorem 2.2.1. *Let $\{(\mathbf{u}_h^n, p_h^n, \dot{\mathbf{d}}_h^n, \mathbf{d}_h^n)\}_{n \geq 1}$ be given by Algorithm 2.3. Under the following conditions*

$$\gamma \geq \frac{3 + 4\alpha}{\alpha} \frac{C_T}{c_g}, \quad (2.22)$$

$$\gamma\mu\tau \leq \frac{2}{1 + 4\alpha}\rho^s\varepsilon h, \quad (2.23)$$

with $\alpha > 0$, the discrete energy estimate presented below holds:

$$E_h^n \lesssim E_h^0, \quad (2.24)$$

for all $n \geq 1$. As a result, Algorithm 2.4 is conditionally stable in the energy norm.

Before proceeding with the proof of the above result, some remarks are in order. Note that condition (2.23) becomes less severe for small values of α and the opposite holds for condition (2.22). The parameter $\alpha > 0$ hence weighs the constraints of (2.23) and (2.22). It should be noted that the stability condition (2.23) provided by Theorem 2.2.1 is not exactly the same as the condition (2.13) obtained in Fernández et al. (2007) for Algorithm 2.1 with fitted meshes. In particular, condition (2.23) is independent of the fluid density. Both conditions share however a similar hyperbolic structure, $\tau = \mathcal{O}(h)$. For a given spatial mesh, the relation (2.23) provides an upper bound on $\gamma\tau$ below which the scheme is stable. The limit upper bound, as $\alpha \rightarrow 0$, is $2\rho^s\varepsilon h$. The numerical results of Section 2.4 indicate that this condition is necessary for stability.

Proof. We first introduce the L^2 -projection operator $\pi_h : [L^2(\Omega)]^d \rightarrow \mathbf{V}_h$ given by

$$(\pi_h \mathbf{s}, \mathbf{v}_h)_{\Omega^f} = (\mathbf{s}, \mathbf{v}_h)_{\Omega^f} \quad (2.25)$$

for all $\mathbf{v}_h \in \mathbf{V}_h^n$. Note that, depending on how the solid mesh \mathcal{T}_h^s intersects the fluid overlapping meshes $\mathcal{T}_{h,i}$, $\pi_h \mathbf{s}$ may not be uniquely defined in the whole computation domain. However, a simple argument show that $\pi_h \mathbf{s}$ is uniquely defined in the physical domain Ω^f (it suffices to remove the indetermination by blocking appropriate nodes outside the physical domain). This feature will be enough for the purpose of the present proof. In a

similar fashion, we introduce the intermediate velocity $\mathbf{u}_h^n \in \mathbf{V}_h^n$ given by

$$\frac{\rho^f}{\tau}(\mathbf{u}_h^n, \mathbf{v}_h)_{\Omega^f} = \frac{\rho^f}{\tau}(\tilde{\mathbf{u}}_h^n, \mathbf{v}_h)_{\Omega^f} - (\nabla(p_h^n - p_h^{n-1}), \mathbf{v}_h)_{\Omega^f} \quad (2.26)$$

for all $\mathbf{v}_h \in \mathbf{V}_h^n$, so that \mathbf{u}_h^n is uniquely defined in Ω^f . In particular, owing to (2.25) and (2.26), we have

$$\mathbf{u}_h^n = \tilde{\mathbf{u}}_h^n - \frac{\tau}{\rho^f} \pi_h \nabla (p_h^n - p_h^{n-1}) \quad \text{in } \Omega^f. \quad (2.27)$$

Now, since the fluid bulk terms of the viscous step (2.16) are integrated (only) in the physical domain and using (2.26), it can alternatively be written as

$$\begin{aligned} & \frac{\rho^f}{\tau}(\tilde{\mathbf{u}}_h^n, \tilde{\mathbf{v}}_h)_{\Omega} + a_h^{f,n}(\tilde{\mathbf{u}}_h^n, \tilde{\mathbf{v}}_h) - \sum_{i=1}^2 (\boldsymbol{\sigma}(\tilde{\mathbf{u}}_{h,i}^n, 0) \mathbf{n}_i, \tilde{\mathbf{v}}_{h,i})_{\Sigma} + \frac{\gamma\mu}{h} \sum_{i=1}^2 (\tilde{\mathbf{u}}_{h,i}^n - \dot{\mathbf{d}}_h^{n-1}, \tilde{\mathbf{v}}_{h,i})_{\Sigma} \\ & - \sum_{i=1}^2 (\tilde{\mathbf{u}}_{h,i}^n - \dot{\mathbf{d}}_h^{n-1}, \boldsymbol{\sigma}(\tilde{\mathbf{v}}_{h,i}, 0) \mathbf{n}_i)_{\Sigma} = \frac{\rho^f}{\tau}(\mathbf{u}_h^{n-1}, \tilde{\mathbf{v}}_h)_{\Omega} - (\nabla p_h^{n-1}, \tilde{\mathbf{v}}_h)_{\Omega} \end{aligned} \quad (2.28)$$

for all $\tilde{\mathbf{v}}_h \in \mathbf{V}_h^n$.

We then proceed by testing the relation (2.26) with $\mathbf{v}_h^n = \mathbf{u}_h^n$, which yields

$$\frac{\rho^f}{2\tau} [\|\mathbf{u}_h^n\|_{0,\Omega^f}^2 - \|\tilde{\mathbf{u}}_h^n\|_{0,\Omega^f}^2 + \|\mathbf{u}_h^n - \tilde{\mathbf{u}}_h^n\|_{0,\Omega^f}^2] + (\nabla(p_h^n - p_h^{n-1}), \mathbf{u}_h^n)_{\Omega^f} = 0. \quad (2.29)$$

By inserting (2.27) into the last equality and by rearranging the terms, we get

$$\frac{\rho^f}{2\tau} [\|\mathbf{u}_h^n\|_{0,\Omega^f}^2 - \|\tilde{\mathbf{u}}_h^n\|_{0,\Omega^f}^2 + (\nabla(p_h^n - p_h^{n-1}), \tilde{\mathbf{u}}_h^n)_{\Omega^f} - \frac{\tau}{2\rho^f} \|\pi_h \nabla(p_h^n - p_h^{n-1})\|_{0,\Omega^f}^2] = 0. \quad (2.30)$$

On the other hand, by testing (2.28) with $\tilde{\mathbf{v}}_h^n = \tilde{\mathbf{u}}_h^n$ and using (2.20), we have

$$\begin{aligned} & \frac{\rho^f}{2\tau} [\|\tilde{\mathbf{u}}_h^n\|_{0,\Omega^f}^2 - \|\mathbf{u}_h^{n-1}\|_{0,\Omega^f}^2 + \|\tilde{\mathbf{u}}_h^n - \mathbf{u}_h^{n-1}\|_{0,\Omega^f}^2] + 2c_g\mu \|\boldsymbol{\epsilon}(\tilde{\mathbf{u}}_h^n)\|_{0,\Omega_h}^2 + (\nabla p_h^{n-1}, \tilde{\mathbf{u}}_h^n)_{\Omega^f} \\ & + \frac{\gamma\mu}{h} \sum_{i=1}^2 (\tilde{\mathbf{u}}_{h,i}^n - \dot{\mathbf{d}}_h^{n-1}, \tilde{\mathbf{u}}_{h,i}^n)_{\Sigma} - 2\mu \sum_{i=1}^2 (\boldsymbol{\epsilon}(\tilde{\mathbf{u}}_{h,i}^n) \mathbf{n}_i, \tilde{\mathbf{u}}_{h,i}^n)_{\Sigma} \\ & - 2\mu \sum_{i=1}^2 (\boldsymbol{\epsilon}(\tilde{\mathbf{u}}_{h,i}^n) \mathbf{n}_i, \tilde{\mathbf{u}}_{h,i}^n - \dot{\mathbf{d}}_h^{n-1})_{\Sigma} \leq 0 \end{aligned} \quad (2.31)$$

and, by testing the fluid projection-step (2.17)₁ with $q_h = p_h^n$ and by integrating by parts the divergence term, we get

$$\begin{aligned} & \frac{\tau}{2\rho^f} [\|\nabla p_h^n\|_{0,\Omega_h}^2 - \|\nabla p_h^{n-1}\|_{0,\Omega_h}^2 + \|\nabla(p_h^n - p_h^{n-1})\|_{0,\Omega_h}^2] - (\nabla p_h^n, \tilde{\mathbf{u}}_h^n)_{\Omega^f} \\ & + \sum_{i=1}^2 (\dot{\mathbf{d}}_h^n, \mathbf{n}_i p_{h,i}^n)_{\Sigma} + s_h(p_h^n, p_h^n) = 0. \end{aligned} \quad (2.32)$$

Finally, by adding the relations (2.30)-(2.32) we get the following energy estimate for the fluid

$$\begin{aligned}
& \frac{\rho^f}{2} \partial_\tau \|\mathbf{u}_h^n\|_{0,\Omega^f}^2 + 2c_g \mu \|\boldsymbol{\epsilon}(\tilde{\mathbf{u}}_h^n)\|_{0,\Omega_h}^2 + \frac{\tau}{2\rho^f} [\|\nabla p_h^n\|_{0,\Omega_h}^2 - \|\nabla p_h^{n-1}\|_{0,\Omega_h}^2] \\
& + \frac{\tau}{2\rho^f} \|(\mathcal{I} - \pi_h) \nabla(p_h^n - p_h^{n-1})\|_{\Omega^f}^2 + \frac{\tau}{2\rho^f} \|\nabla(p_h^n - p_h^{n-1})\|_{\Omega_h \setminus \Omega^f}^2 + \sum_{i=1}^2 \left(\dot{\mathbf{d}}_h^n, \mathbf{n}_i p_{h,i}^n \right)_\Sigma \\
& + \frac{\gamma\mu}{h} \sum_{i=1}^2 \left(\tilde{\mathbf{u}}_{h,i}^n - \dot{\mathbf{d}}_h^{n-1}, \tilde{\mathbf{u}}_{h,i}^n \right)_\Sigma - 2\mu \sum_{i=1}^2 \left(\boldsymbol{\epsilon}(\tilde{\mathbf{u}}_{h,i}^n) \mathbf{n}_i, \tilde{\mathbf{u}}_{h,i}^n \right)_\Sigma \\
& - 2\mu \sum_{i=1}^2 \left(\boldsymbol{\epsilon}(\tilde{\mathbf{u}}_{h,i}^n) \mathbf{n}_i, \tilde{\mathbf{u}}_{h,i}^n - \dot{\mathbf{d}}_h^{n-1} \right)_\Sigma \leq 0. \quad (2.33)
\end{aligned}$$

We now proceed by testing the solid equation (2.17)₂ with $\mathbf{w}_h = \dot{\mathbf{d}}_h^n$, which yields

$$\begin{aligned}
& \frac{\rho^s \varepsilon}{2\tau} [\|\dot{\mathbf{d}}_h^n\|_{0,\Sigma}^2 - \|\dot{\mathbf{d}}_h^{n-1}\|_{0,\Sigma}^2 + \|\dot{\mathbf{d}}_h^n - \dot{\mathbf{d}}_h^{n-1}\|_{0,\Sigma}^2] \\
& + \frac{1}{2\tau} [a_s(\mathbf{d}_h^n, \mathbf{d}_h^n) - a_s(\mathbf{d}_h^{n-1}, \mathbf{d}_h^{n-1}) + a_s(\mathbf{d}_h^n - \mathbf{d}_h^{n-1}, \mathbf{d}_h^n - \mathbf{d}_h^{n-1})] \\
& + 2\mu \sum_{i=1}^2 \left(\boldsymbol{\epsilon}(\tilde{\mathbf{u}}_{h,i}^n) \mathbf{n}_i, \dot{\mathbf{d}}_h^n \right)_\Sigma - \sum_{i=1}^2 \left(p_{h,i}^n \mathbf{n}_i, \dot{\mathbf{d}}_h^n \right)_\Sigma - \frac{\gamma\mu}{h} \sum_{i=1}^2 \left(\tilde{\mathbf{u}}_{h,i}^n - \dot{\mathbf{d}}_h^{n-1}, \dot{\mathbf{d}}_h^n \right)_\Sigma = 0.
\end{aligned}$$

By adding this relation to (2.33) we get the following total energy estimate

$$\begin{aligned}
& \frac{\rho^f}{2} \partial_\tau \|\mathbf{u}_h^n\|_{0,\Omega^f}^2 + 2c_g \mu \|\boldsymbol{\epsilon}(\tilde{\mathbf{u}}_h^n)\|_{0,\Omega_h}^2 + \frac{\tau}{2\rho^f} [\|\nabla p_h^n\|_{0,\Omega_h}^2 - \|\nabla p_h^{n-1}\|_{0,\Omega_h}^2] \\
& \frac{\rho^s \varepsilon}{2\tau} [\|\dot{\mathbf{d}}_h^n\|_{0,\Sigma}^2 - \|\dot{\mathbf{d}}_h^{n-1}\|_{0,\Sigma}^2 + \|\dot{\mathbf{d}}_h^n - \dot{\mathbf{d}}_h^{n-1}\|_{0,\Sigma}^2] + \frac{1}{2\tau} [a_s(\mathbf{d}_h^n, \mathbf{d}_h^n) - a_s(\mathbf{d}_h^{n-1}, \mathbf{d}_h^{n-1})] \\
& \underbrace{- 2\mu \sum_{i=1}^2 \left(\boldsymbol{\epsilon}(\tilde{\mathbf{u}}_{h,i}^n) \mathbf{n}_i, \tilde{\mathbf{u}}_{h,i}^n - \dot{\mathbf{d}}_h^n \right)_\Sigma - 2\mu \sum_{i=1}^2 \left(\boldsymbol{\epsilon}(\tilde{\mathbf{u}}_{h,i}^n) \mathbf{n}_i, \tilde{\mathbf{u}}_{h,i}^n - \dot{\mathbf{d}}_h^{n-1} \right)_\Sigma}_{T_1} \\
& + \underbrace{\frac{\gamma\mu}{h} \sum_{i=1}^2 \left(\tilde{\mathbf{u}}_{h,i}^n - \dot{\mathbf{d}}_h^{n-1}, \tilde{\mathbf{u}}_{h,i}^n - \dot{\mathbf{d}}_h^n \right)_\Sigma}_{T_2} \leq 0. \quad (2.34)
\end{aligned}$$

Terms T_1 can be bounded from every side of the interface by adding and subtracting $\dot{\mathbf{d}}_h^n$,

using the Cauchy–Schwarz, Young’s and trace inequalities (2.21), as follows:

$$\begin{aligned}
T_1 &= -2\mu \left(\boldsymbol{\epsilon}(\tilde{\mathbf{u}}_{h,i}^n) \mathbf{n}_i, \dot{\mathbf{d}}_h^n - \dot{\mathbf{d}}_h^{n-1} \right)_\Sigma - 4\mu \left(\boldsymbol{\epsilon}(\tilde{\mathbf{u}}_{h,i}^n) \mathbf{n}_i, \tilde{\mathbf{u}}_{h,i}^n - \dot{\mathbf{d}}_h^n \right)_\Sigma \\
&\geq - \left(\frac{1}{\alpha_1} + \frac{2}{\alpha_2} \right) \frac{\mu C_{\text{TI}}}{\gamma} \|\boldsymbol{\epsilon}(\tilde{\mathbf{u}}_h^n)\|_{0,\Omega_h}^2 - \alpha_1 \frac{\gamma\mu}{h} \|\dot{\mathbf{d}}_h^n - \dot{\mathbf{d}}_h^{n-1}\|_{0,\Sigma}^2 \\
&\quad - 2\alpha_2 \frac{\gamma\mu}{h} \|\tilde{\mathbf{u}}_{h,i}^n - \dot{\mathbf{d}}_h^n\|_{0,\Sigma}^2,
\end{aligned} \tag{2.35}$$

with $\alpha_1, \alpha_2 > 0$. Similarly, for the second term, we have

$$\begin{aligned}
T_2 &= \frac{\gamma\mu}{h} \|\tilde{\mathbf{u}}_{h,i}^n - \dot{\mathbf{d}}_h^n\|_{0,\Sigma}^2 + \frac{\gamma\mu}{h} \left(\dot{\mathbf{d}}_h^n - \dot{\mathbf{d}}_h^{n-1}, \tilde{\mathbf{u}}_{h,i}^n - \dot{\mathbf{d}}_h^n \right)_\Sigma \\
&\geq \left(1 - \frac{1}{2\alpha_3} \right) \frac{\gamma\mu}{h} \|\tilde{\mathbf{u}}_{h,i}^n - \dot{\mathbf{d}}_h^n\|_{0,\Sigma}^2 - \frac{\alpha_3\gamma\mu}{2h} \|\dot{\mathbf{d}}_h^n - \dot{\mathbf{d}}_h^{n-1}\|_{0,\Sigma}^2
\end{aligned} \tag{2.36}$$

with $\alpha_3 > 0$. By inserting (2.35) and (2.36) into (2.34) we get

$$\begin{aligned}
&\frac{\rho^f}{2} \partial_\tau \|\mathbf{u}_h^n\|_{0,\Omega^f}^2 + \frac{\tau}{2\rho^f} \left[\|\nabla p_h^n\|_{0,\Omega_h}^2 - \|\nabla p_h^{n-1}\|_{0,\Omega_h}^2 \right] \\
&\quad + \frac{\rho^s \varepsilon}{2} \partial_\tau \|\dot{\mathbf{d}}_h^n\|_{0,\Sigma}^2 + \frac{1}{2\tau} \left[a_s(\mathbf{d}_h^n, \mathbf{d}_h^n) - a_s(\mathbf{d}_h^{n-1}, \mathbf{d}_h^{n-1}) \right] \\
&\quad + 2\mu \left[c_g - \frac{C_{\text{TI}}}{\gamma} \left(\frac{1}{2\alpha_1} + \frac{1}{\alpha_2} \right) \right] \|\boldsymbol{\epsilon}(\tilde{\mathbf{u}}_h^n)\|_{0,\Omega_h}^2 + \left[\frac{\rho^s \varepsilon}{2\tau} - \left(\alpha_1 + \frac{\alpha_3}{2} \right) \frac{\gamma\mu}{h} \right] \|\dot{\mathbf{d}}_h^n - \dot{\mathbf{d}}_h^{n-1}\|_{0,\Sigma}^2 \\
&\quad + \left(1 - \frac{1}{2\alpha_3} - 2\alpha_2 \right) \frac{\gamma\mu}{h} \sum_{i=1}^2 \|\tilde{\mathbf{u}}_{h,i}^n - \dot{\mathbf{d}}_h^n\|_{0,\Sigma}^2 \leq 0.
\end{aligned} \tag{2.37}$$

We now set

$$\alpha_1 = \frac{\alpha}{2}, \quad \alpha_2 = \frac{\alpha}{2(1+2\alpha)}, \quad \alpha_3 = \frac{1}{2} + \alpha, \quad \alpha > 0,$$

so that (2.37) yields

$$\begin{aligned}
&\frac{\rho^f}{2} \partial_\tau \|\mathbf{u}_h^n\|_{0,\Omega^f}^2 + \frac{\tau}{2\rho^f} \left[\|\nabla p_h^n\|_{0,\Omega_h}^2 - \|\nabla p_h^{n-1}\|_{0,\Omega_h}^2 \right] + \frac{\rho^s \varepsilon}{2} \partial_\tau \|\dot{\mathbf{d}}_h^n\|_{0,\Sigma}^2 \\
&\quad + \frac{1}{2\tau} \left[a_s(\mathbf{d}_h^n, \mathbf{d}_h^n) - a_s(\mathbf{d}_h^{n-1}, \mathbf{d}_h^{n-1}) \right] + \left[\frac{\rho^s \varepsilon}{2\tau} - \left(\frac{1}{4} + \alpha \right) \frac{\gamma\mu}{h} \right] \|\dot{\mathbf{d}}_h^n - \dot{\mathbf{d}}_h^{n-1}\|_{0,\Sigma}^2 \\
&\quad + 2\mu \left[c_g - \frac{C_{\text{TI}}}{\gamma} \frac{3+4\alpha}{\alpha} \right] \|\boldsymbol{\epsilon}(\tilde{\mathbf{u}}_h^n)\|_{0,\Omega_h}^2 + \frac{\alpha}{1+2\alpha} \frac{\gamma\mu}{h} \sum_{i=1}^2 \|\tilde{\mathbf{u}}_{h,i}^n - \dot{\mathbf{d}}_h^n\|_{0,\Sigma}^2 \leq 0.
\end{aligned} \tag{2.38}$$

Finally, the energy estimate (2.24) follows from (2.38) under the assumption (2.23), which completes the proof. \square

2.3 Non-linear model: moving interface

In this section, we propose an extension of the semi-implicit coupling scheme given by Algorithm 2.3 to the case of non-linear fluid–structure interaction problems involving an incompressible viscous fluid and a moving immersed thin-walled structure. The fluid is described by the Navier-Stokes equations (in Eulerian form) and the structure by a possibly non-linear (beam or shell) solid model (in Lagrangian form).

2.3.1 Problem setting

Let $\Omega \subset \mathbb{R}^d$ be the reference configuration of the fluid domain with boundary $\Gamma \stackrel{\text{def}}{=} \partial\Omega$, and $\Sigma \subset \mathbb{R}^2$ be the reference solid mid-surface. In contrast to Section 2.2, the structure is now supposed to move within the fluid domain. The current position of the interface $\Sigma(t)$ is described in terms of a deformation map $\phi : \Sigma \times \mathbb{R}^+ \rightarrow \mathbb{R}^d$ as $\Sigma(t) = \phi(\Sigma, t)$, with $\phi \stackrel{\text{def}}{=} \mathbf{I}_\Sigma + \mathbf{d}$ and where \mathbf{d} denotes the solid displacement. To simplify the notation we will refer to $\phi_t \stackrel{\text{def}}{=} \phi(\cdot, t)$, so that we also have $\Sigma(t) = \phi_t(\Sigma)$. Note that the fluid control volume is now time-dependent, namely $\Omega^f(t) \stackrel{\text{def}}{=} \Omega \setminus \Sigma(t) \subset \mathbb{R}^d$ with boundary $\partial\Omega(t) = \Sigma(t) \cup \Gamma$. The notations introduced in Section 2.2 for the surface normal vector \mathbf{n}_Σ , jumps and average operators remain valid with the sole difference that they refer to the current interface position $\Sigma(t)$. The considered coupled problem reads therefore as follow: find the fluid velocity and pressure $\mathbf{u} : \Omega \times \mathbb{R}^+ \rightarrow \mathbb{R}^d$, $p : \Omega \times \mathbb{R}^+ \rightarrow \mathbb{R}$, the solid displacement and velocity $\mathbf{d} : \Sigma \times \mathbb{R}^+ \rightarrow \mathbb{R}^d$, $\dot{\mathbf{d}} : \Sigma \times \mathbb{R}^+ \rightarrow \mathbb{R}^d$ such that for all $t \in \mathbb{R}^+$ we have

$$\begin{cases} \rho^f(\partial_t \mathbf{u} + \mathbf{u} \cdot \nabla \mathbf{u}) - \operatorname{div} \boldsymbol{\sigma}(\mathbf{u}, p) = \mathbf{0} & \text{in } \Omega^f(t), \\ \operatorname{div} \mathbf{u} = 0 & \text{in } \Omega^f(t), \\ \mathbf{u} = \mathbf{0} & \text{on } \Gamma, \end{cases} \quad (2.39)$$

$$\begin{cases} \rho^s \varepsilon \partial_t \dot{\mathbf{d}} + \mathbf{L}(\mathbf{d}) = \mathbf{T} & \text{on } \Sigma, \\ \dot{\mathbf{d}} = \partial_t \mathbf{d} & \text{on } \Sigma, \\ \mathbf{d} = \mathbf{0} & \text{on } \partial\Sigma, \end{cases} \quad (2.40)$$

$$\begin{cases} \phi = \mathbf{I}_\Sigma + \mathbf{d}, \quad \Sigma(t) = \phi_t(\Sigma), \quad \Omega^f(t) = \Omega \setminus \Sigma(t), \\ \mathbf{u} = \dot{\mathbf{d}} \circ \phi_t^{-1} & \text{on } \Sigma(t), \\ \int_\Sigma \mathbf{T} \cdot \mathbf{w} = - \int_{\Sigma(t)} \llbracket \boldsymbol{\sigma}(\mathbf{u}, p) \mathbf{n} \rrbracket \cdot \mathbf{w} \circ \phi_t^{-1} \quad \forall \mathbf{w} \in \mathbf{W}. \end{cases} \quad (2.41)$$

The relations in (2.41) respectively enforce the geometrical compatibility, the kinematic and the dynamic coupling at the interface between the fluid and the solid. In the next section, we propose a numerical method for the coupled system (2.39)-(2.41) based on

Algorithm 2.3.

2.3.2 Numerical methods

With the purpose of avoiding geometrical non-linearities in the fluid, we will discretize the geometric compatibility condition (2.41)₁, namely $\Omega^f(t) = \Omega \setminus \Sigma(t)$, in an explicit fashion. For a given displacement approximation $\mathbf{d}_h^n \in \mathbf{W}_h$, we define by ϕ_h^n its associated deformation map as $\phi_h^n \stackrel{\text{def}}{=} \mathbf{I}_\Sigma + \mathbf{d}_h^n$. This map characterizes the interface position, at time level n , as $\Sigma^n \stackrel{\text{def}}{=} \phi_h^n(\Sigma)$. We hence propose to explicitly update the physical fluid domain as

$$\Omega^{f,n} \stackrel{\text{def}}{=} \Omega \setminus \Sigma^{n-1}. \quad (2.42)$$

For the fluid discrete spaces, \mathbf{V}_h^n and Q_h^n , we proceed as in Section 2.2.2, with the difference that they are now given in term of the time-dependent overlapping meshes $\mathcal{T}_{h,i}^n$ covering each side of $\Omega^{f,n}$. We recall that this functional spaces are made of functions that are continuous in each side of $\Omega^{f,n}$ but discontinuous across Σ^{n-1} . Finally, we introduce the broken L^2 -product in the moving computational domain as

$$(\cdot, \cdot)_{n,h} \stackrel{\text{def}}{=} \sum_{i=1}^2 \sum_{K \in \mathcal{T}_{h,i}^n} (\cdot, \cdot)_K.$$

The approximation space for the solid \mathbf{W}_h is the same as in Section 2.2.2.

For the spatial approximation of the fluid, we introduce the following discrete tri-linear form associated to the convective term

$$\begin{aligned} c^n(\mathbf{z}_h, \mathbf{u}_h, \mathbf{v}_h) &\stackrel{\text{def}}{=} \rho^f (\mathbf{z}_h \cdot \nabla \mathbf{u}_h, \mathbf{v}_h)_{\Omega^{f,n}} + \frac{\rho^f}{2} ((\text{div} \mathbf{z}_h) \mathbf{u}_h, \mathbf{v}_h)_{\Omega^{f,n}} \\ &\quad - \rho^f (\{\{\mathbf{z}_h\}\} \cdot \mathbf{n} \llbracket \mathbf{u}_h \rrbracket, \{\{\mathbf{v}_h\}\})_{\Sigma^{n-1}} - \frac{\rho^f}{2} (\llbracket \mathbf{z}_h \cdot \mathbf{n} \rrbracket, \{\{\mathbf{u}_h \cdot \mathbf{v}_h\}\})_{\Sigma^{n-1}}, \end{aligned} \quad (2.43)$$

where the three last terms are added in order to guarantee that $c^n(\mathbf{v}_h, \mathbf{z}_h, \mathbf{z}_h) = 0$ for all $\mathbf{z}_h \in \mathbf{V}_h^n$ (see Alauzet et al. (2016)). Numerical instabilities, due to the lack of inf–sup compatibility of the discrete spaces and to large local Reynolds number, will be handled by the continuous interior penalty stabilization method (CIP) of Burman et al. (2006); Burman and Fernández (2007). The associated symmetric velocity and pressure stabilization operators are given by:

$$\begin{aligned} s_{v,h}^n(\mathbf{z}_h; \mathbf{u}_h, \mathbf{v}_h) &\stackrel{\text{def}}{=} \gamma_v h^2 \sum_{i=1}^2 \sum_{F \in \mathcal{F}_{h,i}^n} \xi(\text{Re}_F(\mathbf{z}_h)) \|\mathbf{z}_h \cdot \mathbf{n}\|_{L^\infty(F)} (\llbracket \nabla \mathbf{u}_h \rrbracket_F, \llbracket \nabla \mathbf{v}_h \rrbracket_F)_F, \\ s_{p,h}^n(\mathbf{z}_h; p_h, q_h) &\stackrel{\text{def}}{=} \gamma_p h^2 \sum_{i=1}^2 \sum_{F \in \mathcal{F}_{h,i}^n} \frac{\xi(\text{Re}_F(\mathbf{z}_h))}{\|\mathbf{z}_h\|_{L^\infty(F)}} (\llbracket \nabla p_h \rrbracket_F, \llbracket \nabla q_h \rrbracket_F)_F, \end{aligned}$$

where $\mathcal{F}_{h,i}^n$ denotes the set of interior edges or faces of $\mathcal{T}_{h,i}^n$, $\text{Re}_F(\mathbf{z}_h) \stackrel{\text{def}}{=} \rho^f \|\mathbf{z}_h\|_{L^\infty(F)} h \mu^{-1}$

denotes the local Reynolds number, $\xi(x) \stackrel{\text{def}}{=} \min\{1, x\}$ is a cut-off function and $\gamma_p, \gamma_v > 0$ are user-defined parameters. In order to guarantee robustness with respect to the way the interface Σ^n is cutting the fluid domain Ω , we introduce the time-dependent ghost-penalty operator, given by

$$g_h^n(\mathbf{u}_h, \mathbf{v}_h) \stackrel{\text{def}}{=} \gamma_g \mu h \sum_{i=1}^2 \sum_{F \in \mathcal{F}_{i,h}^{\Sigma^{n-1}}} (\llbracket \nabla \mathbf{u}_{i,h} \rrbracket_F, \llbracket \nabla \mathbf{v}_{i,h} \rrbracket_F)_F,$$

where $\mathcal{F}_{i,h}^{\Sigma^{n-1}}$ denotes the set of interior edges or faces of the elements intersected by Σ^{n-1} . Finally, we collect all the above terms in a single contribution

$$a_h^{\text{f},n}(\mathbf{z}_h; \mathbf{u}_h, \mathbf{v}_h) \stackrel{\text{def}}{=} c^n(\mathbf{z}_h, \mathbf{u}_h, \mathbf{v}_h) + 2\mu(\boldsymbol{\epsilon}(\mathbf{u}_h), \boldsymbol{\epsilon}(\mathbf{v}_h))_{\Omega^{\text{f},n}} + s_{v,h}^n(\mathbf{z}_h; \mathbf{u}_h, \mathbf{v}_h) + g_h^n(\mathbf{u}_h, \mathbf{v}_h). \quad (2.44)$$

With all the above ingredients, we propose to approximate (2.39)-(2.41) by the semi-implicit coupling scheme reported in Algorithm 2.4. The basic idea consists in combining the interface kinematic/dynamic coupling of Algorithm 2.3 with the explicit treatment of the geometrical compatibility (2.42).

Note that steps (2.45) and (2.46) of Algorithm 2.4 involves integrals of functions associated with different time levels, namely,

$$(\tilde{\mathbf{u}}_h^{n-1}, \tilde{\mathbf{v}}_h)_{\Omega^n}, \quad (\nabla p_h^{n-1}, \tilde{\mathbf{v}}_h)_{\Omega^n}, \quad (\nabla p_h^{n-2}, \tilde{\mathbf{v}}_h)_{\Omega^n}, \quad (\nabla p_h^{n-1}, \nabla q_h)_{n,h}.$$

with $\tilde{\mathbf{u}}_h^n \in \mathbf{V}_h^n$, $p_h^{n-1} \in Q_h^{n-1}$ and $p_h^{n-2} \in Q_h^{n-2}$. This requires the integration of products of functions that might be discontinuous at different locations in the same element. In order avoid the simultaneous intersection of different interface locations with the same fluid element, we consider the approach introduced in [Alauzet et al. \(2016\)](#) (see also [Fries and Zilian \(2009\)](#)), which basically consists in locally shifting the discontinuity at time t^* to the structure location at time t^n , where t^* refers to t^{n-1} and t^{n-2} respectively. In the case where the discontinuities are located in different elements, the quadrature is performed in a standard fashion since we keep track of the (previous) intersections at different times and we can treat each discontinuity separately.

Remark 2.3.1. *In the case of partially intersected fluid domain with dynamic interface, we proceed as in Remark 2.2.3. The terms in (2.18) and (2.19) are now evaluated on $\tilde{\Sigma}^{n-1}$ and we add the following convective Discontinuous Galerkin contributions (see, e.g., [Di Pietro and Ern \(2012\)](#)) to the tri-linear form (2.43):*

$$-\rho^{\text{f}}(\{\{z_h\}\} \cdot \mathbf{n} \llbracket \mathbf{u}_h \rrbracket, \{\{v_h\}\})_{\tilde{\Sigma}^{n-1}} - \frac{\rho^{\text{f}}}{2}(\llbracket z_h \cdot \mathbf{n} \rrbracket, \{\{u_h \cdot v_h\}\})_{\tilde{\Sigma}^{n-1}}.$$

Remark 2.3.2. *Note that whenever $\dot{\mathbf{d}}_h^n$, $\dot{\mathbf{d}}_h^{n-1}$ and \mathbf{w}_h are integrated on Σ^{n-1} , one has to understand $\dot{\mathbf{d}}_h^n \circ (\phi_h^{n-1})^{-1}$, $\dot{\mathbf{d}}_h^{n-1} \circ (\phi_h^{n-1})^{-1}$ and $\mathbf{w}_h \circ (\phi_h^{n-1})^{-1}$ respectively. This abuse of notation is simply made to ease the presentation.*

Algorithm 2.4 Projection based semi-implicit scheme with unfitted meshes and moving interfaces.

For $n \geq 1$:

1. Interface update:

$$\Sigma^{n-1} = \phi_h^{n-1}(\Sigma), \quad \Omega^{f,n} = \Omega \setminus \Sigma^{n-1}.$$

2. Fluid viscous step: Find $\tilde{\mathbf{u}}_h^n \in \mathbf{V}_h^n$ such that

$$\begin{aligned} \rho^f (\partial_\tau \tilde{\mathbf{u}}_h^n, \tilde{\mathbf{v}}_h)_{\Omega^{f,n}} + a_h^{f,n}(\tilde{\mathbf{u}}_h^{n-1}; \tilde{\mathbf{u}}_h^n, \tilde{\mathbf{v}}_h) - \sum_{i=1}^2 (\boldsymbol{\sigma}(\tilde{\mathbf{u}}_{h,i}^n, 0) \mathbf{n}_i, \tilde{\mathbf{v}}_{h,i})_{\Sigma^{n-1}} \\ + \frac{\gamma\mu}{h} \sum_{i=1}^2 (\tilde{\mathbf{u}}_{h,i}^n - \dot{\mathbf{d}}_h^{n-1}, \tilde{\mathbf{v}}_{h,i})_{\Sigma^{n-1}} \\ - \sum_{i=1}^2 (\tilde{\mathbf{u}}_{h,i}^n - \dot{\mathbf{d}}_h^{n-1}, \boldsymbol{\sigma}(\tilde{\mathbf{v}}_{h,i}, 0) \mathbf{n}_i)_{\Sigma^{n-1}} = -(\nabla p_h^{n,*}, \tilde{\mathbf{v}}_h)_{\Omega^{f,n}} \end{aligned} \quad (2.45)$$

for all $\tilde{\mathbf{v}}_h \in \mathbf{V}_h^n$.

3. Pressure-displacement step: Find $(p_h^n, \mathbf{d}_h^n) \in Q_h^n \times \mathbf{W}_h$ with $\dot{\mathbf{d}}_h^n = \partial_\tau \mathbf{d}_h^n$, such that

$$\left\{ \begin{aligned} & \frac{\tau}{\rho^f} (\nabla(p_h^n - p_h^{n-1}), \nabla q_h)_{n,h} + s_{p,h}^n(\tilde{\mathbf{u}}_h^n; p_h^n, q_h) \\ & = \sum_{i=1}^2 (\tilde{\mathbf{u}}_{h,i}^n - \dot{\mathbf{d}}_h^n, q_{h,i} \mathbf{n}_i)_{\Sigma^{n-1}} - (\operatorname{div} \tilde{\mathbf{u}}_h^n, q_h)_{\Omega^{f,n}}, \\ & \rho^s \varepsilon (\partial_\tau \dot{\mathbf{d}}_h^n, \mathbf{w}_h)_\Sigma + a^s(\mathbf{d}_h^n, \mathbf{w}_h) = \frac{\gamma\mu}{h} \sum_{i=1}^2 (\tilde{\mathbf{u}}_{h,i}^n - \dot{\mathbf{d}}_h^{n-1}, \mathbf{w}_h)_{\Sigma^{n-1}} \\ & - \sum_{i=1}^2 (\boldsymbol{\sigma}(\tilde{\mathbf{u}}_{h,i}^n, p_{h,i}^n) \mathbf{n}_i, \mathbf{w}_h)_{\Sigma^{n-1}} \end{aligned} \right. \quad (2.46)$$

for all $(q_h, \mathbf{w}_h) \in Q_h^n \times \mathbf{W}_h$. Then, set $\phi_h^n = \mathbf{I}_\Sigma + \mathbf{d}_h^n$.

2.4 Numerical experiments

In this section we illustrate the stability and accuracy of the proposed semi-implicit scheme (Algorithm 2.4) in different 2D test cases motivated by the simulation of heart valves and of micro-encapsulation. To this purpose we compare the results obtained with Algorithm 2.4 and those obtained with the strongly coupled and loosely coupled (stabilized explicit coupling) schemes proposed in [Alauzet et al. \(2016\)](#). The implicit step in Algorithm 2.4 is solved in a partitioned fashion by a Dirichlet-Neumann based Newton-GMRES iterative algorithm. In all the tests, the solid is described by a non-linear Reissner–Mindlin curved beam model with a MITC spacial discretization. All the units

are given in the CGS units system. In all the numerical tests, the ghost penalty parameters has been set to $\gamma_g = 1$ and the CIP stabilization parameters to $\gamma_v = \gamma_p = 10^{-2}$.

2.4.1 Idealized valve without contact

The first example is the heart-valve-inspired benchmark proposed in Gil et al. (2013); Hesch et al. (2012); Wick (2013); Kamensky et al. (2015); Boilevin-Kayl et al. (2019b). The considered geometry is shown in Figure 2.5(a). The fluid domain is a rectangle $\Omega = [0, 8] \times [0, 0.805]$, while the immersed solid reference configuration Σ is the straight segment AB , with $A = (2, 0)$ and $B = (2, 0.7)$.

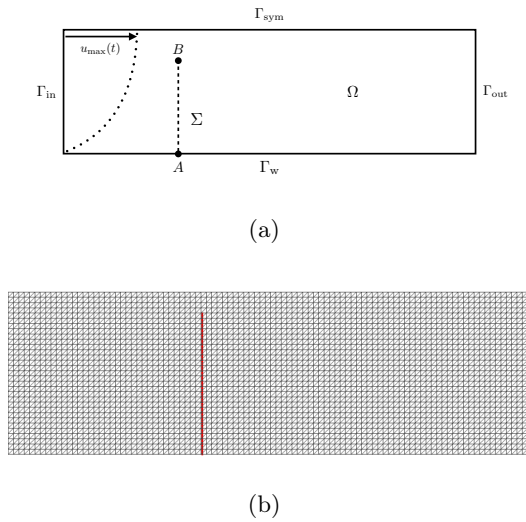


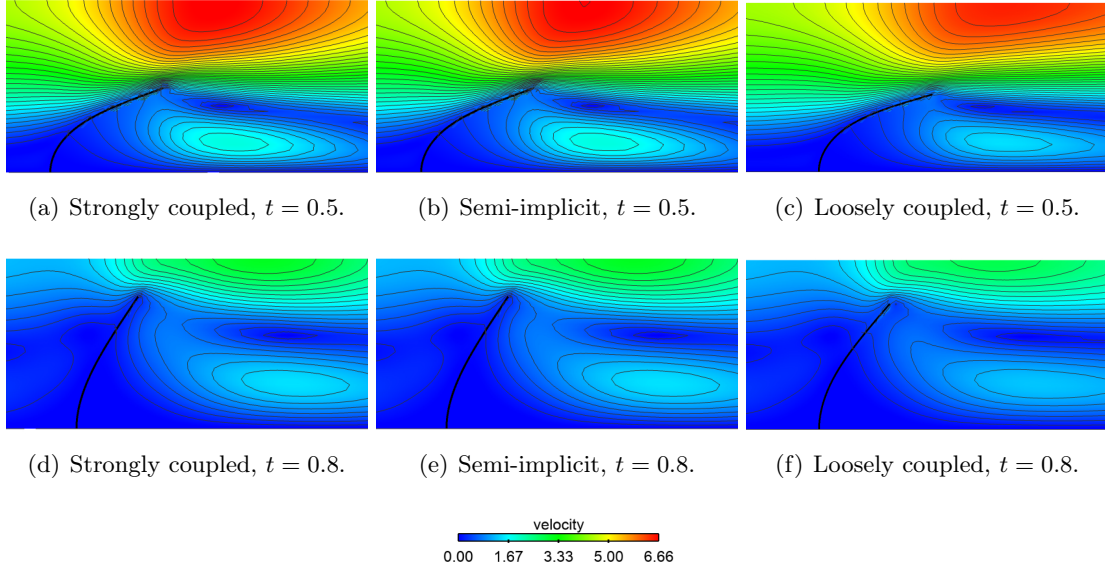
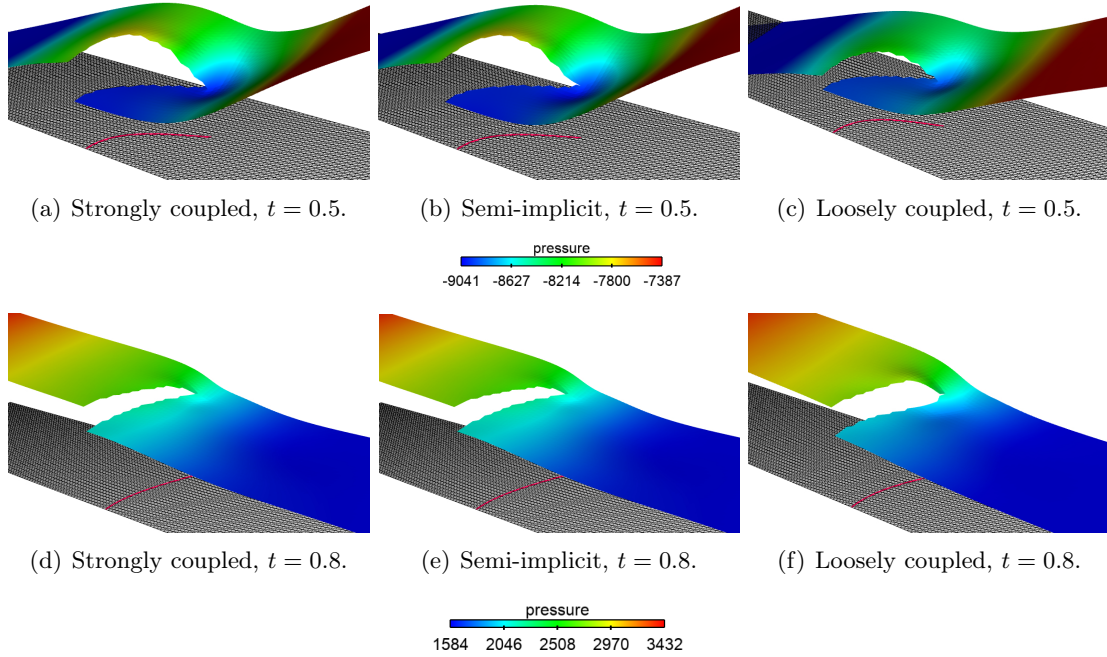
Figure 2.5: (a) Geometric configuration of the idealized valve without contact, (b) Zoom of the fluid and solid meshes.

The physical parameters used for the fluid in this test are $\rho^f = 100$, $\mu = 10$. While for the solid we have $\rho^s = 100$, $\varepsilon = 0.0212$, the Young's modulus $E = 5.6 \cdot 10^7$ and Poisson's ratio $\nu = 0.4$. Concerning the boundary conditions, no-slip boundary condition is apply on Γ_w , a symmetry condition is imposed on Γ_{sym} , zero traction on Γ_{out} and finally on Γ_{in} the following half parabolic profile is applied:

$$u_{max}(t) = 5(0.805)^2 (\sin(2\pi t) + 1.1), \quad t \in \mathbb{R}^+.$$

The solid rotation and displacement are set to zero at the bottom endpoint A and zero initial conditions are considered for both fluid and solid.

The solid mesh is made of 64 edges while the fluid unfitted mesh is made of 18662 triangles (see Figure 2.5(b)). We have $h \approx 0.037$. Three different levels of time-step refinement, $\tau \in \{(10^{-3}/2^i)\}_{i=0}^2$, are considered in order to compare results from Algorithms 2.4 and the loosely coupled and strongly coupled schemes. The final time is $T = 3$, which corresponds to 3 full oscillations cycles for the structure. The Nitsche penalty parameter is set to $\gamma = 10$. With the above physical and discretization parameters, the relation (2.23)

Figure 2.6: Velocity magnitude snapshots at $\tau = 10^{-3}$.Figure 2.7: Pressure snapshots at $\tau = 10^{-3}$.

provides the limit upper bound $\gamma \leq 2\rho^s \varepsilon h / (\mu \tau) \approx 15.6$ for stability. Numerical evidence, not reported here, suggests that larger values yield indeed numerical instability.

For illustration purposes, snapshots of the fluid velocity magnitude and the position of

the interface, computed with $\tau = 10^{-3}$, are shown in Figure 2.6 at time $t = 0.5$ and $t = 0.8$ respectively. A very good agreement is obtained for the three methods already with the larger time step and all algorithms reproduce very well the vortex induced after the leaflet. The two times selected correspond to a situation of opening of the valve at $t = 0.5$ and closing at $t = 0.8$. At opening state, there is an increasing velocity magnitude on top of the channel, while the velocity is decreasing at closing state. Figure 2.7 presents the pressure elevation computed with the coarsest time step, $\tau = 10^{-3}$, obtained with the semi-implicit coupling scheme (Algorithm 2.4), the loosely coupled and the strongly coupled schemes at the same time instants as before. The discontinuity of the pressure is well captured with all methods. A very good agreement can be observed between Algorithm 2.4 and the strongly coupled scheme, while some differences are clear visible in the loosely coupled scheme.

Figures 2.8 and 2.9 report the displacement history of the upper structure endpoint B as function of time, in terms of x -displacement and y -displacement respectively. Algorithm 2.4 delivers practically the same results as the strongly coupled scheme (the two curves are indistinguishable already with the larger time step), whereas some differences are clearly visible with the loosely coupled scheme. This mismatch is reduced with the time-step refinement.

A quantitative comparison is given in Table 2.1 which shows the difference, in the $\ell^\infty(0, T; \ell^2(\Sigma))$ norm, of the displacement obtained with the strongly coupled scheme and Algorithm 2.4. We can observe that this quantity decreases with the time-step length τ . Dimensionless runtimes for the strongly coupled and the semi-implicit coupling scheme are reported in Table 2.2. The observed computational time reduction using the semi-implicit scheme is on average of 27.4%. It should be noted that this corresponds to the worst-case scenario, in which no specific preconditioners for the fluid linear systems involved in steps 2 and 3 of Algorithm 2.4 are considered.

τ	$\ell^\infty(0, T; \ell^2(\Sigma))$ norm
10^{-3}	$1.03 \cdot 10^{-2}$
$5 \cdot 10^{-4}$	$5 \cdot 10^{-3}$
$2.5 \cdot 10^{-4}$	$2.76 \cdot 10^{-3}$

Table 2.1: Measure of the difference of the displacement between the strongly coupled and the semi-implicit schemes.

τ	Strongly coupled	Semi-implicit
10^{-3}	1.35	1
$5 \cdot 10^{-4}$	2.7	1.93
$2.5 \cdot 10^{-4}$	4.83	3.4

Table 2.2: Dimensionless runtimes for the strongly coupled and semi-implicit schemes.

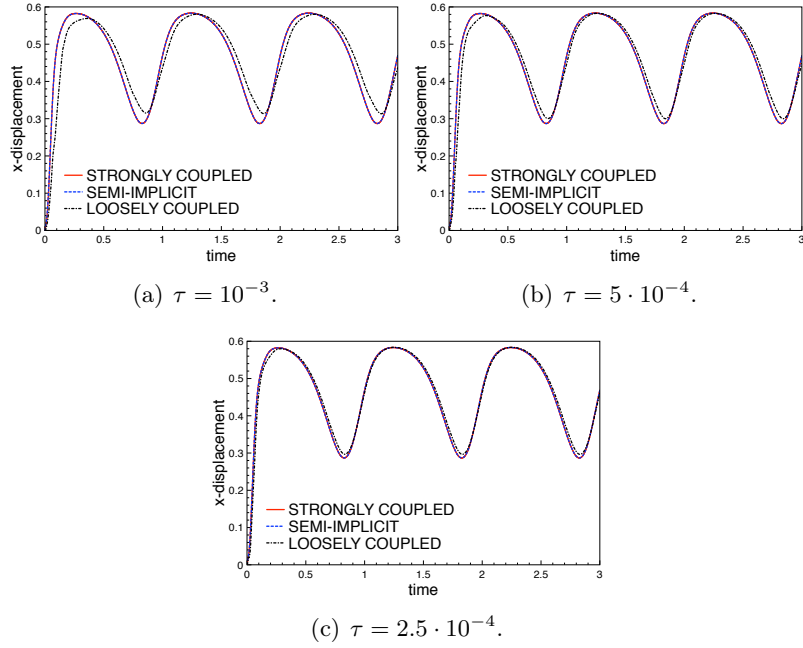


Figure 2.8: Time evolution of the x -displacement for the structure endpoint B .

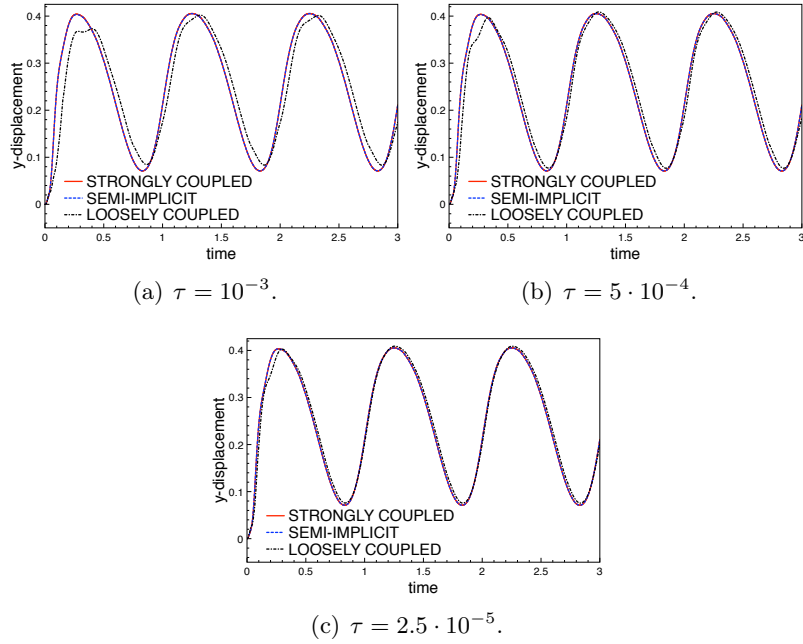


Figure 2.9: Time evolution of the y -displacement for the structure endpoint B .

2.4.2 Idealized valve with contact

The second numerical example corresponds to the idealized valve test with contact introduced in [Boilevin-Kayl et al. \(2019a\)](#). It is an extension of the previous one in which

the structure is sufficiently long to get in contact with Γ_{sym} . The geometry is shown in Figure 2.10(a). The fluid domain Ω is the same as in the previous example, while as reference configuration for the solid, Σ , we consider a curve segment of extreme $A = (4, 0)$ and $B = (5.112, 0.483)$, parametrized by the analytical function

$$y(x) = \frac{1}{2} \sqrt{1 - \frac{(x - 11/2)^2}{(3/2)^2}}, \quad x \in [4, 5.112].$$

The physical parameters used for the fluid in this test are $\rho^f = 1$, $\mu = 0.03$. While for the solid we have $\rho^s = 1.2$, $\varepsilon = 0.065$, the Young's modulus $E = 10^7$ and the Poisson's ratio $\nu = 0.4$.

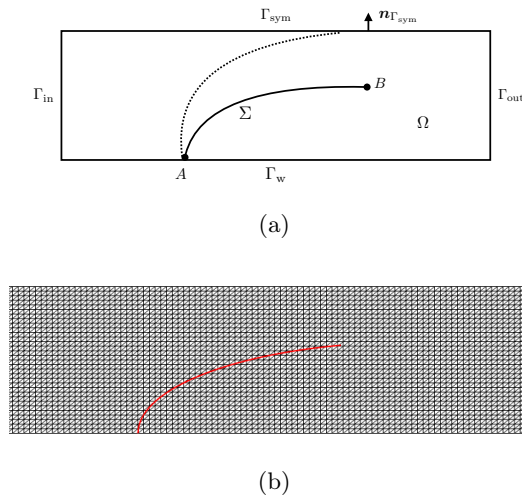


Figure 2.10: (a) Geometric configuration of the idealized valve with contact, (b) Zoom of the leaflet mesh and fluid mesh.

Regarding the boundary condition, a symmetry condition is enforced on Γ_{sym} , a no-slip condition on Γ_w , zero traction on the outflow boundary Γ_{out} and a traction condition is imposed on Γ_{in} in terms of the following time-dependent pressure:

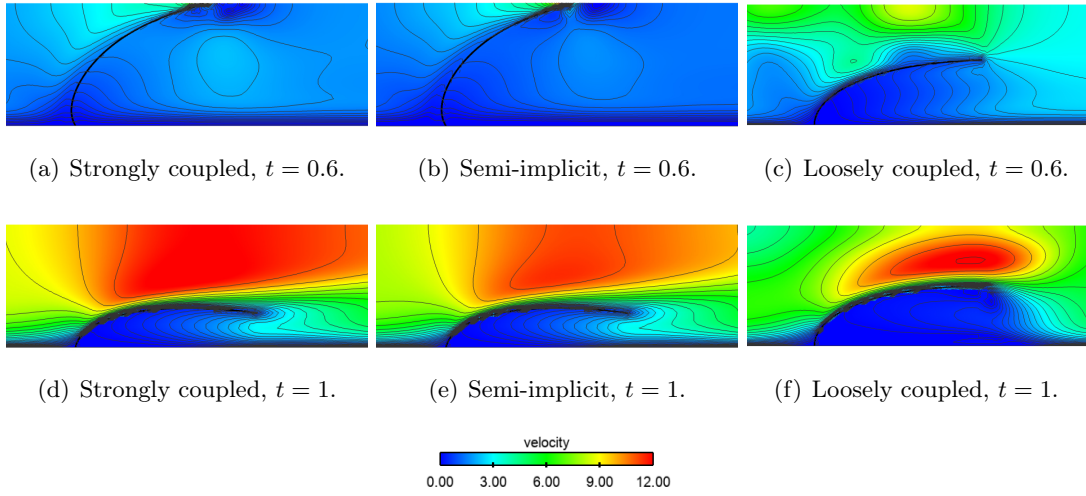
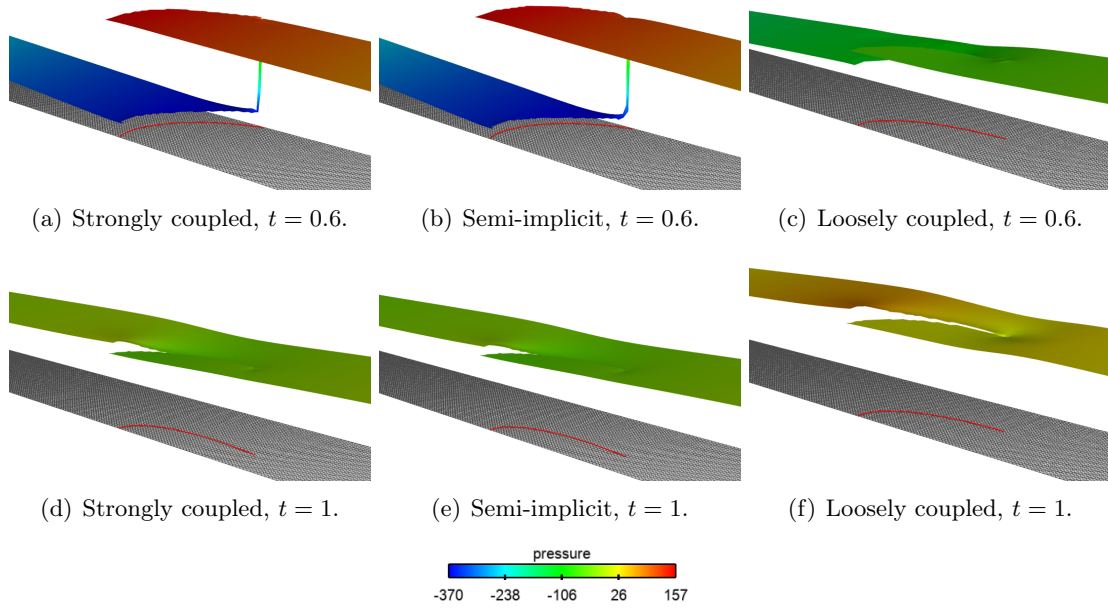
$$p_{\text{in}}(t) = \begin{cases} -200 \operatorname{atanh}(100t) & \text{if } 0 < t < 0.7, \\ 200 & \text{if } t \geq 0.7. \end{cases}$$

The final time is $T = 1$ and it corresponds to one full valve oscillation cycle. The fluid and the solid are initially at rest and the beam is pinched at the bottom tip A .

In order to avoid penetration on Γ_{top} , we enforce the following contact condition:

$$\mathbf{d} \cdot \mathbf{n}_{\Gamma_{\text{sym}}} - g \leq 0 \quad \text{on } \Sigma, \quad (2.47)$$

where $\mathbf{n}_{\Gamma_{\text{sym}}}$ denotes the exterior unit normal to Γ_{sym} (see Figure 2.10 (a)) and $g : \Sigma \rightarrow \mathbb{R}^+$ refer to the gap function between Σ and Γ_{sym} , defined as the initial distance of a point on Σ to the wall Γ_{sym} in the direction of $\mathbf{n}_{\Gamma_{\text{sym}}}$, namely $g = y_{\Gamma_{\text{sym}}} - y(x)$. The inequality

Figure 2.11: Velocity magnitude snapshots with $\tau = 10^{-3}$.Figure 2.12: Pressure snapshots with $\tau = 10^{-3}$.

constraint (2.47) is approximated via a penalty method (see, e.g., [Scholz \(1984\)](#)), by inserting the following term in the solid discrete problem:

$$\frac{\gamma_c E \varepsilon}{h^2} ([\mathbf{d}_h^n \cdot \mathbf{n}_{\Gamma_{\text{sym}}} - g + \varepsilon_h]_+, \mathbf{w}_h)_\Sigma, \quad (2.48)$$

where $[x]_+ \stackrel{\text{def}}{=} \max\{0, x\}$, $\gamma_c > 0$ is a (dimensionless) user-defined parameter and $\varepsilon_h > 0$

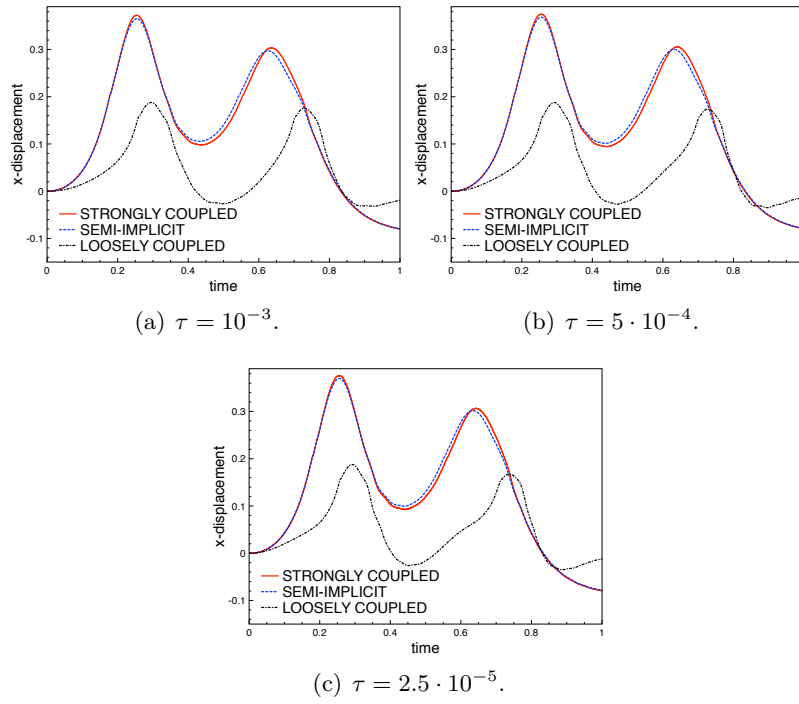


Figure 2.13: Time evolution of the x -displacement for the structure endpoint B .

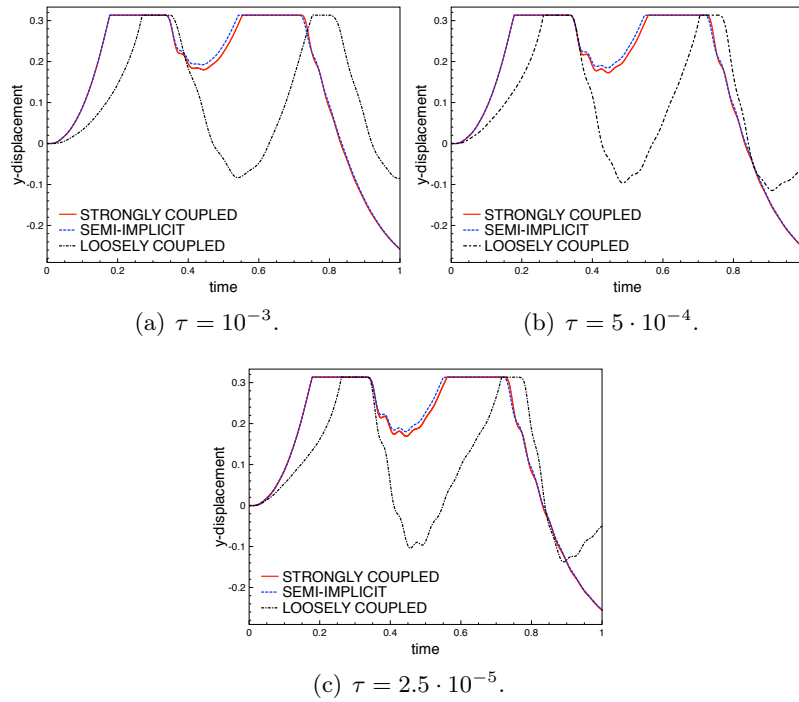


Figure 2.14: Time evolution of the y -displacement for the structure endpoint B .

is a contact tolerance. The contact parameters are given by $\varepsilon_h = 0.01$ and $\gamma_c = 5 \cdot 10^{-3}$ as in Boilevin-Kayl et al. (2019a). The relaxation parameter ε_h is chosen in such a way that the generated artificial gap is below h . The penalty parameter γ_c (independent of h) is chosen to avoid penetration (i.e., not very small) and in such a way that the term (2.48) does not perturb the convergence of the Newton solver in the solid (the operator $[\cdot]_+$ is not differentiable at 0).

The fluid mesh has 16384 triangles and the solid 50 edges. We have $h \approx 0.04$. The zoom on the both meshes is presented in Figure 2.10(b). As in the previous example, we consider three levels of time refinement $\tau \in \{(10^{-3}/2^i)\}_{i=0}^2$ for the comparisons. The Nitsche parameter is set to $\gamma = 100$. With the above set of physical and discretization parameters, the relation (2.23) provides the limit bound $\gamma \leq 2\rho^s \varepsilon_h / (\mu\tau) \approx 208.6$ for stability. As in the previous example, numerical evidence (not reported here) indicates that larger values yield numerical instability.

For illustration purposes, we report in Figure 2.11 the velocity magnitude, with the corresponding contour lines, at two different instants. In Figures 2.11 (a), (b) and (c) are reported the solutions obtained at time $t = 0.6$, when the valve is supposed to get into contact with the upper wall and the fluid velocity decreases globally as consequence of the closing of the valve. The same comparison is performed at time $t = 1$ in Figures 2.11 (d), (e) and (f) in a situation where the valve is open and far from contact. In this case the flux is reestablishes and the velocity increases in the channel. Again, a good agreement is observed between Algorithm 2.4 and the strongly coupled scheme, even though at $t = 1$ slightly differences in the velocity are visible. On the contrary, the loosely coupled scheme delivers an approximation that is far from the previous ones. Similar observations can be made from Figure 2.12, where we compare the pressure at the same instants the pressure. We can see the high pressure jump when the valve is getting in contact with the wall (Figures 2.12(a) and (b)), while at $t = 1$ the discontinuity between the two sides of the interface is weaker (see Figures 2.12(d) and (e)). Algorithm 2.4 reproduces very well the pressure jump obtained with the strongly coupled scheme, though a small difference is visible at $t = 0.6$. Figure 2.12 (c) and (f) show the results obtained with the loosely coupled algorithm, which is unable to deliver reasonable approximations.

Finally, Figures 2.13 and 2.14 present the time history of the horizontal and vertical displacement, respectively, at the upper solid point B for the different levels of time refinement. The contact condition with the wall can be seen in Figures 2.14, whereas Figures 2.13 shows that the structure is sliding and bouncing over the top wall. These results clearly show that Algorithm 2.4 is able to capture the dynamics of the interface before and after contact with the upper wall. Only slightly differences are observed, in particular close to the contact instant, but which decrease with the time refinement. On the contrary, the loosely coupled is not able to reproduce the dynamics obtained with the strongly coupled scheme, even with finest time refinement. This illustrates the limitations of the loosely coupled scheme.

A more quantitative comparison of the strongly coupled and semi-implicit schemes is given in Table 2.3 which shows the $\ell^\infty(0, T; \ell^2(\Sigma))$ norm of the difference of the displacement obtained with each method. We can observe that the difference reduces with the time refinement, but less than in the previous example. This is probably due to the ex-

τ	$\ell^\infty(0, T, \ell^2(\Sigma))$ norm
10^{-3}	$1.34 \cdot 10^{-1}$
$5 \cdot 10^{-4}$	$1.28 \cdot 10^{-1}$
$2.5 \cdot 10^{-4}$	$1.22 \cdot 10^{-1}$

Table 2.3: Measure of the difference of the displacement between the strongly coupled and the semi-implicit schemes.

τ	Strongly coupled	Semi-implicit
10^{-3}	1.32	1
$5 \cdot 10^{-4}$	2.57	2
$2.5 \cdot 10^{-4}$	5.35	4

Table 2.4: Dimensionless runtimes for the strongly coupled and semi-implicit schemes.

treme singularity of the problem with contact. Table 2.4 displays the computational times (dimensionless) of the strongly coupled and the semi-implicit (Algorithm 2.4) schemes. The scaling is similar with the different time-steps and the semi-implicit scheme provides on average a computational cost reduction of 24.2%.

2.4.3 Vesicle in lid-driven cavity flow

The last example is an adaptation of the well-known lid-driven cavity test with an immersed elastic disk (see, e.g., Roy et al. (2013); Wang and Zhang (2010); E Griffith (2012); Griffith and Luo (2017)). The fluid geometry is shown in Figure 2.15 (a) and consists in three rigid walls Γ_w and a lid Γ_{top} moving with tangential velocity. The domain Ω is the unit square given by $[0, 1] \times [0, 1]$. The reference solid configuration is a circle of center $(0.6, 0.5)$ and radius 0.2. The physical parameters used for the fluid in this test are $\rho^f = 100$, $\mu = 10$. For the solid we have $\rho^s = 100$, $\varepsilon = 0.0212$, the Young's modulus $E = 5.6 \cdot 10^3$ and Poisson's ratio $\nu = 0.4$. Both the fluid and the solid are initially at rest. For the boundary conditions, we impose zero velocity on Γ_w and tangential velocity of magnitude $\bar{u} = 1$ on Γ_{top} .

Since the fluid is entirely enclosed by Dirichlet-type boundary conditions, standard Dirichlet–Neumann partitioned procedures for the solution of the implicit step (2.46) are known to diverge. This is due to the ill-posedness of the fluid system which enforces a volumetric constraint on the interfacial solid velocity. In order to avoid this issue, we consider the approach proposed in Küttler et al. (2006) which consists in enforcing the volumetric constraint into the structure equation using a scalar Lagrange multiplier, in order to avoid the incompressibility incompatibilities with the subsequent fluid problem. More precisely, in step (2.46) of Algorithm 2.4 the solid problem is replaced by the following

mixed system

$$\left\{ \begin{array}{l} \rho^s \varepsilon (\partial_\tau \dot{\mathbf{d}}_h^n, \mathbf{w}_h)_\Sigma + a^s(\dot{\mathbf{d}}_h^n, \mathbf{w}_h) + \lambda^n \int_{\Sigma^{n-1}} \widehat{\mathbf{w}}_h \cdot \mathbf{n} = \\ \frac{\gamma \mu}{h} \sum_{i=1}^2 ((\tilde{\mathbf{u}}_{h,i}^n - \dot{\mathbf{d}}_h^{n-1}), \widehat{\mathbf{w}}_h)_{\Sigma^{n-1}} - \sum_{i=1}^2 (\boldsymbol{\sigma}(\tilde{\mathbf{u}}_{h,i}^n, p_{h,i}^n) \mathbf{n}_i, \widehat{\mathbf{w}}_h)_{\Sigma^{n-1}}, \\ \int_{\Sigma^{n-1}} \dot{\mathbf{d}}_h^n \cdot \mathbf{n} = 0 \end{array} \right.$$

for all $\mathbf{w}_h \in \mathbf{W}_h$. The scalar Lagrange multiplier $\lambda^n \in \mathbb{R}$ represents the unknown constant pressure in the fluid.

The fluid mesh has 3200 triangles while the solid mesh is composed by 80 edges. We have $h \approx 0.035$. Both meshes are presented in Figure 2.15 (b). The chosen time-step lengths are $\tau \in \{(5 \cdot 10^{-3}/2^i)\}_{i=0}^2$ and the final time is $T = 10$. We take as Nitsche parameter $\gamma = 1$. With the above physical and discretization parameters, the relation (2.23) provides approximately the limit bound $\gamma \leq 2\rho^s \varepsilon h / (\mu \tau) \approx 3$ for stability. Numerical evidence, not reported here, indicates that larger values yield numerical instability.

For illustration purposes, Figure 2.16 shows the snapshots of the fluid magnitude for both schemes and at different time, i.e., two different positions of the structure. At $t = 2$, Figures 2.16(a) and (b), the vesicle is starting the upper region of the cavity, while at $t = 5$, Figures 2.16(d) and (e), is moving away this region. Even with the coarsest time step, Algorithm 2.4 is able to predict the same location as the strongly coupled scheme. Figures 2.16(c) and (f) show the results of the loosely coupled scheme, which is clearly unable to reproduce the previous dynamics. Similar observations can be made from Figure 2.17 which shows the elevation of the pressure for the same time instants. No notable differences can be seen between Algorithm 2.4 and the strongly coupled scheme, whereas a major mismatch is obtained with the loosely coupled algorithm, particularly at time $t = 5$.

In Figure 2.18 we present the trajectory of the vesicle rightmost node obtained with

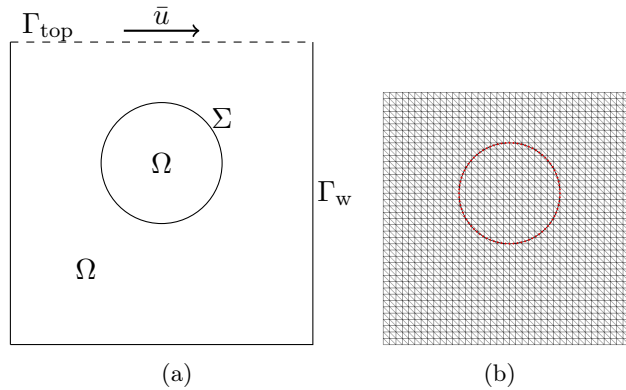


Figure 2.15: (a) Geometric configuration and external boundary condition, (b) Fluid and solid meshes at time $t = 0$.

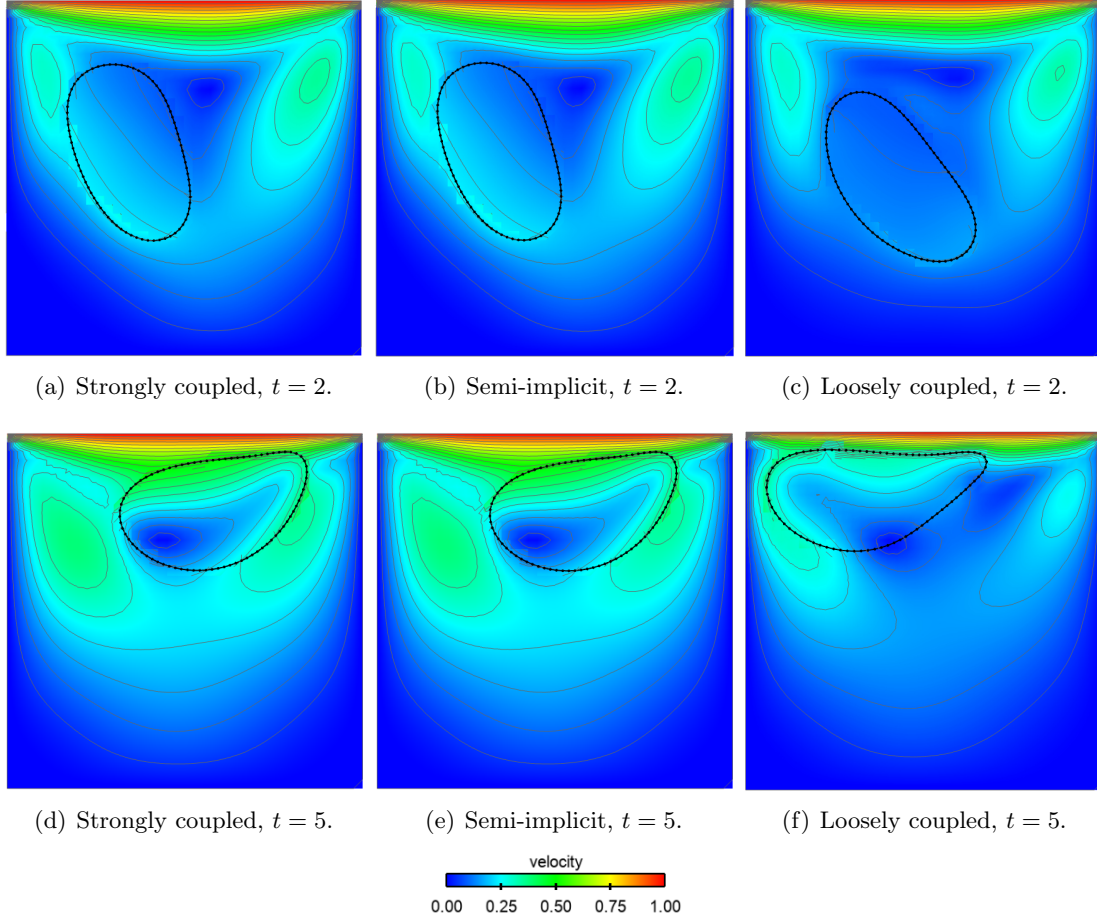


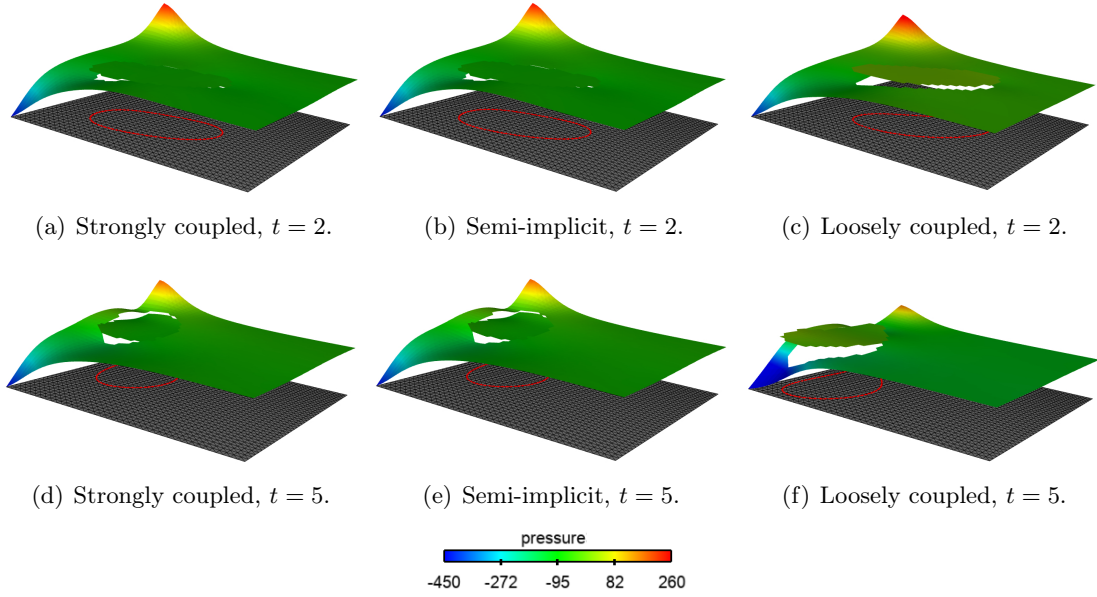
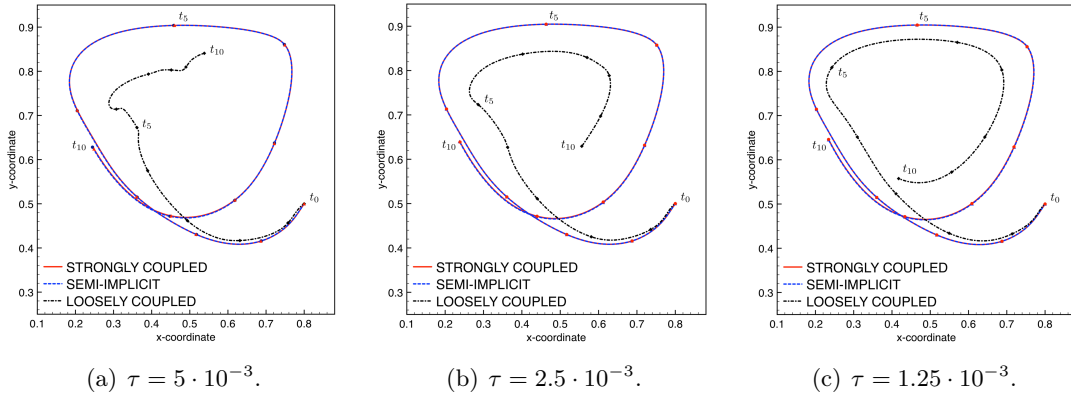
Figure 2.16: Velocity magnitude snapshots with $\tau = 5 \cdot 10^{-3}$.

the three numerical methods for the different levels of time refinement. Time markers have been depicted in order to facilitate the comparison of the results. Algorithm 2.4 is able to capture the dynamics of the strongly coupled scheme at all the discretization levels (time markers t_5 and t_{10} are practically indistinguishable), whereas the loosely coupled scheme requires a sufficiently small time-step to deliver a minimally reasonable approximation (time markers t_5 and t_{10} get closer after time refinement, but still yield poor approximations).

τ	$\ell^\infty(0, T, \ell^2(\Sigma))$ norm
$5 \cdot 10^{-3}$	$6.70 \cdot 10^{-2}$
$2.5 \cdot 10^{-3}$	$1.97 \cdot 10^{-2}$
$1.25 \cdot 10^{-3}$	$7.76 \cdot 10^{-3}$

Table 2.5: Measure of the difference of the displacement between the strongly coupled and the semi-implicit schemes.

Table 2.5 shows a quantitative measure of the difference between the approximations

Figure 2.17: Pressure snapshots with $\tau = 5 \cdot 10^{-3}$.Figure 2.18: Trajectory of the extreme right node of the vesicle from $t = 0$ to $t = 10$.

τ	Strongly coupled	Semi-implicit
$5 \cdot 10^{-3}$	1.4	1
$2.5 \cdot 10^{-3}$	2.3	1.9
$1.25 \cdot 10^{-3}$	4	3.1

Table 2.6: Dimensionless runtimes for the strongly coupled and semi-implicit schemes.

provided by the strongly coupled and Algorithm 2.4, for each level of time refinement. As in the idealized valve without contact, no stagnation phenomena are visible. Finally, dimensionless runtimes are provided in Table 2.6, showing that the semi-implicit algorithm shows on average computational cost reduction of 23.3%, consistently with the previous examples.

2.5 Conclusion

In this chapter, we have introduced a new semi-implicit coupling scheme for the numerical approximations of incompressible fluid-structure interaction problems involving immersed solids. The proposed method generalizes the projection based semi-implicit coupling paradigm of [Fernández et al. \(2007\)](#) to the Nitsche-XFEM framework, with the following main ingredients:

- The traditional accuracy issues of previous splitting schemes based on a Nitsche's interface treatment (see [Astorino et al. \(2009a\)](#); [Alauzet et al. \(2016\)](#)) are circumvented through a variationally consistent transfer of the fluid viscous stresses to the solid problem;
- Consistent spatial approximation of the pressure-Poisson problem through the Nitsche-XFEM unfitted framework.

Moreover, Theorem 2.2.1 has shown that the method preserves the stability properties of the original splitting in the fitted mesh framework (see [Fernández et al. \(2007\)](#)). The comprehensive numerical study reported in Section 2.4 confirmed these findings and showed a very good performance, in terms of stability and accuracy, with respect to the previous strongly coupled and loosely coupled schemes reported in [Alauzet et al. \(2016\)](#). As a result, the present semi-implicit coupling scheme can be considered as a robust approach to avoid strong coupling in unfitted meshes without compromising stability and accuracy.

Ongoing work focuses on the implementation of the present approach with 3D unstructured meshes. The main difficulty lies on the formulation of a robust and efficient algorithm for mesh intersection and integration over the cut-elements (see [Massing et al. \(2013\)](#); [Zonca et al. \(2018\)](#), Chapter 6), as well as the management of contact between several solids, which we address in Chapter 4.

Error analysis of an unfitted mesh semi-implicit coupling scheme for fluid-structure interaction

3.1 Introduction

This chapter is devoted to the error analysis of the numerical method described in Chapter 2, for a linear fluid-structure coupled system involving the transient Stokes equations (in a fixed domain) and a thin-walled solid elastodynamics model. This system is often used as model problem for the analysis of time-splitting schemes for incompressible fluid-structure interaction (see, e.g., [Astorino and Grandmont \(2010\)](#); [Fernández \(2013\)](#); [Burman and Fernández \(2014a\)](#); [Fernández and Mullaert \(2016\)](#); [Bukac and Muha \(2016\)](#); [Boffi and Gastaldi \(2017\)](#)). Indeed, it retains the fundamental numerical difficulties that have to be faced also in general incompressible fluid-structure systems. A large amount of added-mass in the system is known to severely compromise stability and accuracy in standard explicit coupling schemes (i.e., those which invoke the fluid and solid solvers only once per time-step, see, e.g., [Le Tallec and Mouro \(2001\)](#); [Causin et al. \(2005\)](#); [Förster et al. \(2007\)](#); [van Brummelen \(2009\)](#)). The simplest approach to overcome these issues is to resort to a strongly coupled scheme (i.e., one in which the interface coupling is implicitly discretized in time), but at the expense of a higher computational complexity.

The development and the analysis of time splitting schemes which avoid strong coupling without compromising stability and accuracy has been a very active field of research during the last fifteen years. The vast majority of the studies have been devoted to the case of spatial approximations based on fluid meshes which are fitted to the interface (see, e.g., [Fernández et al. \(2007\)](#); [Quaini and Quarteroni \(2007\)](#); [Badia et al. \(2008b\)](#); [Astorino and Grandmont \(2010\)](#); [Fernández \(2013\)](#); [Bukac et al. \(2013\)](#); [Bukac and Muha \(2016\)](#)). For many applications, such a mesh compatibility can however be cumbersome to maintain in practice (see, e.g., [Peskin \(2002\)](#); [Gerstenberger and Wall \(2008a\)](#); [Sawada and Tezuka \(2011\)](#); [Boffi et al. \(2011\)](#); [Burman and Fernández \(2014a\)](#); [Kadapa et al. \(2018\)](#); [Kim and Lee \(2018\)](#)).

The earliest explicit coupling schemes with unfitted meshes have been reported in [Boffi et al. \(2011\)](#); [Kim and Lee \(2018\)](#), using the immersed boundary method, and in [Burman and Fernández \(2014a\)](#); [Kadapa et al. \(2018\)](#), using unfitted Nitsche approximations with overlapping meshes. Nevertheless, these methods suffer from major stability/accuracy

issues which either require severe time-step restrictions (see [Boffi et al. \(2011\)](#); [Burman and Fernández \(2014a\)](#)) or are limited by the amount of added-mass in the system (see [Kadapa et al. \(2018\)](#); [Kim and Lee \(2018\)](#)). A new class of semi-implicit schemes with unfitted meshes has been recently reported in [Fernández and Landajuola \(2019\)](#); [Annese et al.](#) for the case of the coupling with thin-walled solids. These methods robustly avoid strong coupling but at the expense of introducing additional unknowns in the fluid sub-problem (intermediate solid velocity). Fully explicit variants of these approaches have been derived in [Fernández and Landajuola \(2019\)](#) and in [Boilevin-Kayl et al. \(2019a\)](#). Nevertheless, the formulation of the former in the case of immersed solids remains open and the accuracy of the latter relies on a grad-div penalty stabilization (for enhanced mass conservation) which spoils the conditioning of the fluid subsystem.

This chapter is devoted to the numerical analysis of the unfitted mesh semi-implicit coupling scheme recently introduced in Chapter 2. The method combines a Nitsche based unfitted mesh spatial approximation with a fractional-step time-marching in the fluid. The viscous part of the coupling is treated in an explicit fashion (which avoids strong coupling), while the remaining fluid pressure and solid contributions are treated implicitly (which guarantees added-mass free stability). Robust *a priori* error estimates are derived for two extrapolated variants ($r = 1, 2$ stands for the extrapolation of the solid velocity). The analysis highlights the fundamental role played by the time discretization of the Nitsche's penalty term in the stability and accuracy of the splitting. In particular, an $\mathcal{O}(\tau^r/h^{\frac{1}{2}})$ splitting error is obtained instead of the standard $\mathcal{O}(\tau/h)$ for the stabilized explicit coupling scheme of [Burman and Fernández \(2014a\)](#). The superior accuracy of the method is also supported by numerical experiments in an academic benchmark.

The rest of the chapter is organized as follows. Section 3.2 presents the continuous setting. Its numerical approximation is discussed in Section 3.3. The numerical analysis of the semi-implicit scheme is reported in Section 3.4. Numerical evidence on the convergence properties of the methods is given in Section 3.5. Finally, Section 3.6 summarizes the main conclusions of this work.

3.2 Problem Setting

We consider a linear fluid-structure interaction problem in which the fluid is described by the Stokes equations in a fixed polyhedral bounded domain $\Omega^f \subset \mathbb{R}^d$, with $d = 2, 3$ and the structure by a linear thin-walled solid model with mid-surface given by Σ , also assumed polyhedral. Let the boundary of Ω^f be partitioned as $\partial\Omega^f = \Sigma \cup \Gamma$ and denote the outward unit normal to $\partial\Omega^f$ by \mathbf{n} . In this framework, the considered coupled problem reads as follow: find the fluid velocity and pressure $\mathbf{u} : \Omega^f \times \mathbb{R}^+ \rightarrow \mathbb{R}^d$, $p : \Omega^f \times \mathbb{R}^+ \rightarrow \mathbb{R}$, the solid displacement and velocity $\mathbf{d} : \Sigma \times \mathbb{R}^+ \rightarrow \mathbb{R}^d$, $\dot{\mathbf{d}} : \Sigma \times \mathbb{R}^+ \rightarrow \mathbb{R}^d$ such that for all $t \in \mathbb{R}^+$ we have

$$\begin{cases} \rho^f \partial_t \mathbf{u} - \operatorname{div} \boldsymbol{\sigma}(\mathbf{u}, p) = \mathbf{0} & \text{in } \Omega^f \times \mathbb{R}^+, \\ \operatorname{div} \mathbf{u} = 0 & \text{in } \Omega^f \times \mathbb{R}^+, \\ \mathbf{u} = \mathbf{0} & \text{on } \Gamma \times \mathbb{R}^+, \end{cases} \quad (3.1)$$

$$\begin{cases} \rho^s \varepsilon \partial_t \dot{\mathbf{d}} + \mathbf{L}\mathbf{d} = \mathbf{T} & \text{in } \Sigma \times \mathbb{R}^+, \\ \dot{\mathbf{d}} = \partial_t \mathbf{d} & \text{in } \Sigma \times \mathbb{R}^+, \\ \mathbf{d} = \mathbf{0} & \text{on } \partial\Sigma \times \mathbb{R}^+, \end{cases} \quad (3.2)$$

$$\begin{cases} \mathbf{u} = \dot{\mathbf{d}} & \text{on } \Sigma \times \mathbb{R}^+, \\ \mathbf{T} = -\boldsymbol{\sigma}(\mathbf{u}, p)\mathbf{n} & \text{on } \Sigma \times \mathbb{R}^+, \end{cases} \quad (3.3)$$

with the initial conditions $\mathbf{u}(0) = \mathbf{u}_0$, $\mathbf{d}(0) = \mathbf{d}_0$ and $\dot{\mathbf{d}}(0) = \dot{\mathbf{d}}_0$. Here, the symbols ρ^f and ρ^s stand, respectively, for the fluid and solid densities. The thickness of the solid is denoted by ε and the fluid Cauchy stress tensor is given by

$$\boldsymbol{\sigma}(\mathbf{u}, p) \stackrel{\text{def}}{=} 2\mu\boldsymbol{\epsilon}(\mathbf{u}) - p\mathbf{I}, \quad \boldsymbol{\epsilon}(\mathbf{u}) \stackrel{\text{def}}{=} \frac{1}{2}(\nabla\mathbf{u} + \nabla\mathbf{u}^T),$$

where μ denotes the fluid dynamic viscosity and \mathbf{I} is the identity matrix. The relations in (3.3) enforce, respectively, the kinematic and dynamic interface coupling conditions. The abstract differential operator \mathbf{L} in (3.2) describes the elastic behavior of the solid.

In the following, we will make use of the usual Sobolev's spaces $H^m(\Omega)$ ($m \geq 0$), with norm $\|\cdot\|_{m,\Omega}$ and seminorm $|\cdot|_{m,\Omega}$, along with the closed spaces $H_\Gamma^1(\Omega)$, of functions in $H^1(\Omega)$ with zero trace on Γ , and $L_0^2(\Omega)$, of functions in $L^2(\Omega)$ with zero mean in Ω . The scalar product in $L^2(\Omega)$ is denoted by $(\cdot, \cdot)_\Omega$.

For the weak formulation of the fluid problem we consider $V = [H_\Gamma^1(\Omega^f)]^d$ and $Q = L^2(\Omega^f)$ as the fluid velocity and pressure functional spaces, respectively. The standard Stokes bilinear forms are given by

$$a(\mathbf{u}, \mathbf{v}) \stackrel{\text{def}}{=} 2\mu(\boldsymbol{\epsilon}(\mathbf{u}), \boldsymbol{\epsilon}(\mathbf{v}))_{\Omega^f}, \quad b(q, \mathbf{v}) \stackrel{\text{def}}{=} -(q, \text{div}\mathbf{v})_{\Omega^f}.$$

For the solid weak problem we suppose that $\mathbf{W} \subset [H_{\partial\Sigma}^1(\Sigma)]^d$ is the space of admissible displacements and we assume that $\mathbf{L}: \mathbf{D} \subset [L^2(\Sigma)]^d \rightarrow [L^2(\Sigma)]^d$ is a self-adjoint second-order differential operator symmetric, coercive and continuous on \mathbf{W} . Associated to the operator \mathbf{L} , we define the elastic bilinear form

$$a^s(\mathbf{d}, \mathbf{w}) \stackrel{\text{def}}{=} (\mathbf{L}\mathbf{d}, \mathbf{w})_\Sigma \quad (3.4)$$

for all $\mathbf{d} \in \mathbf{D}$ and $\mathbf{w} \in \mathbf{W}$. We define the following elastic energy norm on

$$\|\mathbf{w}\|_s^2 \stackrel{\text{def}}{=} a^s(\mathbf{w}, \mathbf{w})$$

and we assume that the following continuity estimate holds

$$\|\mathbf{w}\|_s^2 \leq \beta^s \|\mathbf{w}\|_{1,\Sigma}^2 \quad (3.5)$$

for all $\mathbf{w} \in \mathbf{W}$, with $\beta^s > 0$.

3.3 Numerical methods

In this section, we discuss three numerical methods for the approximations of the coupled problem (3.1)-(3.3). These methods involve an unfitted mesh spatial discretization and different levels of fluid-solid time splitting.

3.3.1 Unfitted mesh spatial approximation

In a standard conforming finite element approximation, typically based on fitted meshes (see, e.g., Du et al. (2004); Fernández (2013)), the kinematic coupling condition (3.3)₁ is strongly enforced. This is no longer feasible in the unfitted mesh setting. We consider the robust and optimal unfitted mesh method with overlapping meshes proposed in Burman and Fernández (2014a). Therein, the interfacial fluid-solid coupling is treated in a fully weak fashion via a Nitsche's type mortaring.

Let be $\{\mathcal{T}_h^s\}_{0 < h < 1}$ a family of triangulations of Σ , such that $\Sigma = \bigcup_{K \in \mathcal{T}_h^s} K$. We then consider the standard space of continuous piecewise affine functions associated to \mathcal{T}_h^s , namely,

$$X_h^s \stackrel{\text{def}}{=} \{v_h \in C^0(\bar{\Sigma}) \mid v_h|_K \in \mathbb{P}_1(K), \quad \forall K \in \mathcal{T}_h^s\}.$$

For the approximation of the solid discrete space for the displacement and velocity we consider the following space $\mathbf{W}_h = [X_h^s]^d \cap \mathbf{W}$.

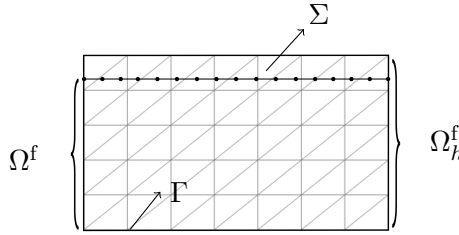


Figure 3.1: Unfitted meshes.

We denote with $\{\mathcal{T}_h^f\}_{0 < h < 1}$ a family of triangulations that cover the fluid domain Ω^f such that:

1. Every \mathcal{T}_h^f is fitted to Γ but, in general, not to Σ ;
2. For every simplex $K \in \mathcal{T}_h^f$, we have $K \cap \Omega^f \neq \emptyset$.

In what follows, Ω_h^f stands for the domain covered by \mathcal{T}_h^f (i.e., the fluid computational domain). We denote by \mathcal{G}_h the set of elements of \mathcal{T}_h^f intersected by Σ , by \mathcal{F}_h the set of the internal edges or faces of \mathcal{T}_h^f , and by $\mathcal{F}_{\mathcal{G}_h}$ the set of edges or faces of the elements of \mathcal{G}_h that do not lie on $\partial\Omega_h^f$, namely,

$$\Omega_h^f \stackrel{\text{def}}{=} \text{int}(\cup_{K \in \mathcal{T}_h^f} K), \quad \mathcal{G}_h \stackrel{\text{def}}{=} \{K \in \mathcal{T}_h^f \mid K \cap \Sigma \neq \emptyset\},$$

$$\mathcal{F}_h \stackrel{\text{def}}{=} \{F \in \partial K \mid K \in \mathcal{T}_h^f, \quad F \cap \partial\Omega_h^f \neq F\}, \quad \mathcal{F}_{\mathcal{G}_h} \stackrel{\text{def}}{=} \{F \in \partial K \mid K \in \mathcal{G}_h, \quad F \cap \partial\Omega_h^f \neq F\}.$$

We consider the following space of continuous piecewise affine functions defined over \mathcal{T}_h^f

$$X_h^f \stackrel{\text{def}}{=} \left\{ v_h \in C^0(\overline{\Omega}_h) \mid v_h|_K \in \mathbb{P}_1(K) \quad \forall K \in \mathcal{T}_h^f \right\}. \quad (3.6)$$

For the approximation of the fluid velocity and pressure, we consider the following spaces

$$\mathbf{V}_h \stackrel{\text{def}}{=} \left\{ \mathbf{v}_h \in [X_h^f]^d \mid \mathbf{v}_h|_\Gamma = \mathbf{0} \right\}, \quad Q_h \stackrel{\text{def}}{=} X_h^f.$$

Since the discrete pair \mathbf{V}_h/Q_h lacks inf-sup stability, we consider the classical Brezzi-Pitkäranta symmetric pressure stabilization (see, e.g., [Brezzi and Pitkäranta \(1984\)](#)):

$$s_h(p_h, q_h) \stackrel{\text{def}}{=} \gamma_p \int_{\Omega_h^f} \frac{h^2}{\mu} \nabla p_h \cdot \nabla q_h, \quad \gamma_p > 0 \quad (3.7)$$

Note that the pressure stabilization is defined over the computational fluid domain Ω_h^f . In order to guarantee robustness of the method with respect to the way the interface is cutting the fluid mesh, we consider the following ghost-penalty operator (see [Burman \(2010\)](#)):

$$g_h(\mathbf{u}_h, \mathbf{v}_h) \stackrel{\text{def}}{=} \gamma_g \mu h \sum_{F \in \mathcal{F}_{\mathcal{G}_h}} (\llbracket \nabla \mathbf{u}_h \rrbracket_F, \llbracket \nabla \mathbf{v}_h \rrbracket_F)_F. \quad (3.8)$$

We can hence introduce the following total stabilization operator S_h and associated semi-norm:

$$\begin{aligned} S_h((\mathbf{u}_h, p_h), (\mathbf{v}_h, q_h)) &\stackrel{\text{def}}{=} s_h(p_h, q_h) + g_h(\mathbf{u}_h, \mathbf{v}_h), \\ |(\mathbf{u}_h, p_h)|_S &\stackrel{\text{def}}{=} S_h((\mathbf{u}_h, p_h), (\mathbf{u}_h, p_h))^{\frac{1}{2}}, \end{aligned} \quad (3.9)$$

so that the fluid discrete bi-linear form is given by

$$a_h^f((\mathbf{u}_h, p_h), (\mathbf{v}_h, q_h)) \stackrel{\text{def}}{=} a^f((\mathbf{u}_h, p_h), (\mathbf{v}_h, q_h)) + S_h((\mathbf{u}_h, p_h), (\mathbf{v}_h, q_h)).$$

Finally, the considered space semi-discrete unfitted mesh approximation of (3.1)–(3.3) reads as follows: for $t > 0$, find $(\mathbf{u}_h(t), p_h(t), \dot{\mathbf{d}}_h(t), \mathbf{d}_h(t)) \in \mathbf{V}_h \times Q_h \times \mathbf{W}_h \times \mathbf{W}_h$, such that $\dot{\mathbf{d}}_h = \partial_t \mathbf{d}_h$ and

$$\begin{cases} \rho^f (\partial_t \mathbf{u}_h, \mathbf{v}_h)_\Omega + a_h^f((\mathbf{u}_h, p_h), (\mathbf{v}_h, q_h)) + \rho^s \varepsilon (\partial_t \dot{\mathbf{d}}_h, \mathbf{w}_h)_\Sigma + a^s(\mathbf{d}_h, \mathbf{w}_h) \\ - (\boldsymbol{\sigma}(\mathbf{u}_h, p_h) \mathbf{n}, \mathbf{v}_h - \mathbf{w}_h)_\Sigma - (\mathbf{u}_h - \dot{\mathbf{d}}_h, \boldsymbol{\sigma}(\mathbf{v}_h, -q_h) \mathbf{n})_\Sigma + \frac{\gamma \mu}{h} (\mathbf{u}_h - \dot{\mathbf{d}}_h, \mathbf{v}_h - \mathbf{w}_h)_\Sigma = 0 \end{cases} \quad (3.10)$$

for all $(\mathbf{v}_h, q_h, \mathbf{w}_h) \in \mathbf{V}_h \times Q_h \times \mathbf{W}_h$. Here, $\gamma > 0$ denotes the Nitsche's penalty parameter.

Remark 3.3.1. *In the numerical experiments of Section 3.5, the second assumption on \mathcal{T}_h^f , that is, all the elements of Ω_h^f intersect the physical domain Ω^f is relaxed. This is achieved by extending the ghost-penalty operator (3.8) to \mathcal{F}_h (all internal edges or faces of \mathcal{T}_h^f), i.e.,*

$$g_h(\mathbf{u}_h, \mathbf{v}_h) \stackrel{\text{def}}{=} \gamma_g \mu h \sum_{F \in \mathcal{F}_h} (\llbracket \nabla \mathbf{u}_h \rrbracket_F, \llbracket \nabla \mathbf{v}_h \rrbracket_F)_F. \quad (3.11)$$

This ensures the invertibility of the fluid stiffness matrix. It should be noted that the results of the numerical analysis reported in Section 3.4 below also hold in this case.

3.3.2 Time splitting schemes

This section is devoted to the time-discretization of (3.10). We first discuss the strongly coupled and the stabilized explicit coupling schemes reported in [Burman and Fernández \(2014a\)](#). Particular attention is paid to the well-known accuracy issues of the latter. We then discuss the semi-implicit projection based coupling scheme reported in Chapter 2, whose purpose was precisely to circumvent such difficulties without resorting to strong coupling.

In the following, the parameter $\tau > 0$ denotes the time-step length, $\partial_\tau x^n$ stands for the first-order backward difference formula and $x^{*,r}$ represents the r -th order explicit extrapolations to x^n , viz.,

$$\partial_\tau x^n \stackrel{\text{def}}{=} \frac{1}{\tau} (x^n - x^{n-1}), \quad x^{*,r} \stackrel{\text{def}}{=} \begin{cases} x^{n-1} & \text{if } r = 1, \\ 2x^{n-1} - x^{n-2} & \text{if } r = 2. \end{cases} \quad (3.12)$$

3.3.2.1 Strongly coupled scheme

Traditionally, the natural way to achieve numerical stability has been to consider a strongly coupled scheme, that is, a fully implicit time-discretization of (3.10). An example of such an approach is reported in Algorithm 3.1. The method is also known to deliver an optimal $O(\tau) + O(h)$ accuracy in the energy norm (see [Fernández and Landajuela \(2019\)](#)). The price to pay for this robustness is the resolution (at each time-step) of the hybrid coupled system (3.13), which can be computationally demanding in practice, particularly, due to its hybrid nature. Indeed, this monolithic system often yields ill-conditioned matrices which require dedicated solvers.

Algorithm 3.1 Strongly coupled scheme (from [Burman and Fernández \(2014a\)](#)).

For $n \geq 1$:

find $(\mathbf{u}_h^n, p_h^n, \dot{\mathbf{d}}_h^n, \mathbf{d}_h^n) \in \mathbf{V}_h \times Q_h \times \mathbf{W}_h \times \mathbf{W}_h$ with $\dot{\mathbf{d}}_h^n = \partial_\tau \mathbf{d}_h^n$ and such that

$$\begin{aligned} & \rho^f (\partial_\tau \mathbf{u}_h^n, \mathbf{v}_h)_{\Omega^f} + a_h^f((\mathbf{u}_h^n, p_h^n), (\mathbf{v}_h, q_h)) + \rho^s \varepsilon (\partial_\tau \dot{\mathbf{d}}_h^n, \mathbf{w}_h)_\Sigma + a^s(\mathbf{d}_h^n, \mathbf{w}_h) \\ & - (\boldsymbol{\sigma}(\mathbf{u}_h^n, p_h^n) \mathbf{n}, \mathbf{v}_h - \mathbf{w}_h)_\Sigma - (\mathbf{u}_h^n - \dot{\mathbf{d}}_h^n, \boldsymbol{\sigma}(\mathbf{v}_h, -q_h) \mathbf{n})_\Sigma + \frac{\gamma \mu}{h} (\mathbf{u}_h^n - \dot{\mathbf{d}}_h^n, \mathbf{v}_h - \mathbf{w}_h)_\Sigma = 0 \end{aligned} \quad (3.13)$$

for all $(\mathbf{v}_h, q_h, \mathbf{w}_h) \in \mathbf{V}_h \times Q_h \times \mathbf{W}_h$.

3.3.2.2 Stabilized explicit coupling scheme

The stabilized explicit coupling scheme reported in Algorithm 3.2 enables a fully sequential decoupled time-marching of (3.10). Energy stability is achieved under a mild CFL-like condition (see [Burman and Fernández \(2014a\)](#)), thanks to the specific explicit

treatment of the Nitsche penalty interface term and to the addition of an interface pressure stabilization in time (weakly consistent interfacial compressibility). The stability of the method is independent of the added-mass effect and of the considered local fluid and solid time-marching schemes. These features come however at a price: the sub-optimality of the splitting error, whose leading term scales as $\mathcal{O}(\tau/h)$ (see Remark 3.4.3 and Burman and Fernández (2014b)). Correction iterations are thus needed to enhance accuracy, under restrictive constraints on the discretization parameters.

Algorithm 3.2 Stabilized explicit coupling scheme (from Burman and Fernández (2014a)).

For $n \geq 1$:

- Solid sub-step: find $(\dot{\mathbf{d}}_h^n, \mathbf{d}_h^n) \in \mathbf{W}_h \times \mathbf{W}_h$ with $\dot{\mathbf{d}}_h^n = \partial_\tau \mathbf{d}_h^n$ and such that

$$\begin{aligned} \rho^s \varepsilon(\partial_\tau \dot{\mathbf{d}}_h^n, \mathbf{w}_h)_\Sigma + a^s(\mathbf{d}_h^n, \mathbf{w}_h) + \frac{\gamma\mu}{h}(\dot{\mathbf{d}}_h^n, \mathbf{w}_h)_\Sigma = \\ \frac{\gamma\mu}{h}(\mathbf{u}_h^{n-1}, \mathbf{w}_h)_\Sigma - (\boldsymbol{\sigma}(\mathbf{u}_h^{n-1}, p_h^{n-1})\mathbf{n}, \mathbf{w}_h)_\Sigma \end{aligned} \quad (3.14)$$

for all $\mathbf{w}_h \in \mathbf{W}_h$.

- Fluid sub-step: find $(\mathbf{u}_h^n, p_h^n) \in \mathbf{V}_h \times Q_h$, such that

$$\begin{aligned} \rho^f(\partial_\tau \mathbf{u}_h^n, \mathbf{v}_h)_{\Omega^f} + a_h^f((\mathbf{u}_h, p_h), (\mathbf{v}_h, q_h)) + \frac{\gamma_0 h}{\gamma\mu}(p_h^n - p_h^{n-1}, q_h)_\Sigma \\ - (\mathbf{u}_h^n - \dot{\mathbf{d}}_h^n, q_h \mathbf{n})_\Sigma + \frac{\gamma\mu}{h}(\mathbf{u}_h^n, \mathbf{v}_h)_\Sigma = \frac{\gamma\mu}{h}(\dot{\mathbf{d}}_h^n, \mathbf{v}_h)_\Sigma + (\boldsymbol{\sigma}(\mathbf{u}_h^{n-1}, p_h^{n-1})\mathbf{n}, \mathbf{v}_h)_\Sigma \end{aligned} \quad (3.15)$$

for all $(\mathbf{v}_h, q_h) \in \mathbf{V}_h \times Q_h$.

Roughly speaking, the lack of spatial uniformity in the splitting error of Algorithm 3.2 can be explained as follows. After spatial refinement, i.e., whenever $h \rightarrow 0$, the solid sub-problem (3.14) forces the solid velocity $\dot{\mathbf{d}}_h^n$ to be close to $\mathbf{u}_h^{n-1}|_\Sigma$, whereas in the fluid sub-problem (3.15) the fluid velocity $\mathbf{u}_h^n|_\Sigma$ approximates $\dot{\mathbf{d}}_h^n$. In summary, the spatial discretization forces $\|\mathbf{u}_h^n - \mathbf{u}_h^{n-1}\|_{0,\Sigma}$ to be small as $h \rightarrow 0$, by amplifying the time-splitting error. This is an essential ingredient of the scheme that guarantees numerical stability but it degrades accuracy.

3.3.2.3 Projection based semi-implicit coupling scheme

Algorithm 3.3 reports the projection based semi-implicit scheme of Chapter 2. The fundamental idea of this method, borrowed from Fernández et al. (2007) in the case of fitted mesh approximations, consists in combining a fractional-step time-marching in the fluid (3.1) (see, e.g., Guermond et al. (2006)) with a semi-implicit treatment of the interface coupling (3.3). In Algorithm 3.3, the fluid is discretized in time with an incremental pressure-correction method and a backward-Euler method is considered for the solid. We

introduce the fluid discrete viscous bi-linear form

$$a_h^f(\mathbf{u}_h, \mathbf{v}_h) \stackrel{\text{def}}{=} 2\mu(\boldsymbol{\epsilon}(\mathbf{u}_h), \boldsymbol{\epsilon}(\mathbf{v}_h))_{\Omega^f}.$$

Note that the fluid viscous-step (3.16) is explicitly coupled with the solid, hence avoiding strong coupling (i.e., reducing computational complexity), whereas the coupled pressure-displacement system (3.17) guarantees added-mass free stability through the implicit treatment of the fluid incompressibility and solid inertial effects. For $r = 2$, the Algorithm 3.3 can be initialized with one step of the scheme with $r = 1$.

Algorithm 3.3 Projection-based semi-implicit scheme (from Chapter 2).

For $n \geq r$:

1. Fluid viscous step: find $\tilde{\mathbf{u}}_h^n \in \mathbf{V}_h$ such that

$$\begin{aligned} & \frac{\rho^f}{\tau} (\tilde{\mathbf{u}}_h^n - \mathbf{u}_h^{n-1}, \tilde{\mathbf{v}}_h)_{\Omega^f} + a_h^f(\tilde{\mathbf{u}}_h^n, \tilde{\mathbf{v}}_h) + g_h(\tilde{\mathbf{u}}_h^n, \mathbf{v}_h) + (\nabla p_h^{n-1}, \tilde{\mathbf{v}}_h)_{\Omega^f} \\ & - (\boldsymbol{\sigma}(\tilde{\mathbf{u}}_h^n, 0)\mathbf{n}, \tilde{\mathbf{v}}_h)_{\Sigma} + \frac{\gamma\mu}{h} (\tilde{\mathbf{u}}_h^n - \dot{\mathbf{d}}_h^{*,r}, \tilde{\mathbf{v}}_h)_{\Sigma} - (\tilde{\mathbf{u}}_h^n - \dot{\mathbf{d}}_h^{*,r}, \boldsymbol{\sigma}(\tilde{\mathbf{v}}_h, 0)\mathbf{n})_{\Sigma} = 0 \end{aligned} \quad (3.16)$$

for all $\tilde{\mathbf{v}}_h \in \mathbf{V}_h$.

2. Pressure-displacement step: find $(p_h^n, \mathbf{d}_h^n) \in Q_h \times \mathbf{W}_h$ with $\dot{\mathbf{d}}_h^n = \partial_{\tau} \mathbf{d}_h^n$, such that

$$\begin{cases} \frac{\tau}{\rho^f} (\nabla(p_h^n - p_h^{n-1}), \nabla q_h)_{\Omega_h^f} + s_h(p_h^n, q_h) = (\tilde{\mathbf{u}}_h^n - \dot{\mathbf{d}}_h^n, q_h \mathbf{n})_{\Sigma} - (\operatorname{div} \tilde{\mathbf{u}}_h^n, q_h)_{\Omega^f}, \\ \rho^s \varepsilon(\partial_{\tau} \dot{\mathbf{d}}_h^n, \mathbf{w}_h)_{\Sigma} + a^s(\mathbf{d}_h^n, \mathbf{w}_h) = \frac{\gamma\mu}{h} (\tilde{\mathbf{u}}_h^n - \dot{\mathbf{d}}_h^{*,r}, \mathbf{w}_h)_{\Sigma} - (\boldsymbol{\sigma}(\tilde{\mathbf{u}}_h^n, p_h^n)\mathbf{n}, \mathbf{w}_h)_{\Sigma} \end{cases} \quad (3.17)$$

for all $(q_h, \mathbf{w}_h) \in Q_h \times \mathbf{W}_h$.

3. Intermediate velocity step: find $\mathbf{u}_h^n \in \mathbf{V}_h$ such that

$$\frac{\rho^f}{\tau} (\mathbf{u}_h^n, \mathbf{v}_h)_{\Omega^f} = \frac{\rho^f}{\tau} (\tilde{\mathbf{u}}_h^n, \mathbf{v}_h)_{\Omega^f} - (\nabla(p_h^n - p_h^{n-1}), \mathbf{v}_h)_{\Omega^f} \quad (3.18)$$

for all $\mathbf{v}_h \in \mathbf{V}_h$.

It is worth noting that the discrete interface stresses in the (3.17)₂ involve the same penalty term as in (3.16). In other words, the viscous stresses in (3.17)₂ correspond to the variationally consistent residual of (3.16). This constitutes a fundamental difference with respect to Algorithm 3.2 (and also with respect to [Astorino et al. \(2009a\)](#) with fitted meshes).

The next section provides an error estimate for Algorithm 3.3 which shows superior accuracy with respect to Algorithm 3.2, namely: $\mathcal{O}(\tau^r/h^{\frac{1}{2}})$, with $r = 1, 2$, instead of $\mathcal{O}(\tau/h)$. Furthermore, the numerical evidence reported in Section 3.5 suggests Algorithm 3.3 delivers practically the same accuracy as Algorithm 3.1, which is uniform with respect to h . The price to pay for this superior accuracy with respect to Algorithm 3.2 is threefold:

- An additional CFL-like condition for stability (see Theorem 2.2.1 and Theorem 3.4.1 below);
- The solution of the coupled pressure-displacement system (3.17);
- A limited flexibility in the choice of the time-stepping for the fluid and solid sub-systems.

Remark 3.3.2. *In practice, we can avoid solving the third step, by inserting (3.18) into the viscous step (3.16), obtaining*

$$\begin{aligned} & \rho^f (\partial_\tau \tilde{\mathbf{u}}_h^n, \tilde{\mathbf{v}}_h)_{\Omega^f} + a_h^f(\tilde{\mathbf{u}}_h^n, \tilde{\mathbf{v}}_h) + g_h(\tilde{\mathbf{u}}_h^n, \mathbf{v}_h) + (\nabla(2p^{n-1} - p^{n-2}), \tilde{\mathbf{v}}_h)_{\Omega^f} \\ & - (\boldsymbol{\sigma}(\tilde{\mathbf{u}}_h^n, 0)\mathbf{n}, \tilde{\mathbf{v}}_h)_\Sigma + \frac{\gamma\mu}{h}(\tilde{\mathbf{u}}_h^n - \dot{\mathbf{d}}_h^{*,r}, \tilde{\mathbf{v}}_h)_\Sigma - (\tilde{\mathbf{u}}_h^n - \dot{\mathbf{d}}_h^{*,r}, \boldsymbol{\sigma}(\tilde{\mathbf{v}}_{h,i}, 0)\mathbf{n}_i)_\Sigma = 0 \end{aligned}$$

for all $\tilde{\mathbf{v}}_h \in \mathbf{V}_h$.

3.4 Numerical analysis

This section is devoted to the numerical analysis of Algorithm 3.3. We first recall the main ingredients for the energy stability of the method reported in Chapter 2 and extend the proof to cover the case of a second-order extrapolation ($r = 2$). An a priori error estimate is derived in Section 3.4.2.

3.4.1 Energy stability

We assume (see, e.g., [Hansbo and Hansbo \(2004\)](#); [Burman and Hansbo \(2012\)](#)) that the following trace inequality holds

$$\|v\|_{0,\Sigma \cap K}^2 \leq C_T (h^{-1}\|v\|_{0,K}^2 + h\|\nabla v\|_{0,K}^2) \quad (3.19)$$

for all $v \in H^1(K)$, $K \in \mathcal{T}_h^f$ and C_T depending only on Σ . By combining (3.19) with a discrete inverse inequality, it follows

$$\begin{aligned} \|\boldsymbol{\varepsilon}(\mathbf{v}_h)\mathbf{n}\|_{0,\Sigma}^2 & \leq \sum_{K \in \mathcal{G}_h} \|\boldsymbol{\varepsilon}(\mathbf{v}_h)\|_{0,\Sigma \cap K}^2 \\ & \leq C_T \sum_{K \in \mathcal{G}_h} \left(h^{-1} \|\boldsymbol{\varepsilon}(\mathbf{v}_h)\|_{0,K}^2 + h \|\nabla \boldsymbol{\varepsilon}(\mathbf{v}_h)\|_{0,K}^2 \right) \\ & \leq \frac{C_{\text{TI}}}{h} \sum_{K \in \mathcal{G}_h} \|\boldsymbol{\varepsilon}(\mathbf{v}_h)\|_{0,K}^2 \end{aligned} \quad (3.20)$$

for all $\mathbf{v}_h \in \mathbf{V}_h$. Hence,

$$h \|\boldsymbol{\varepsilon}(\mathbf{v}_h)\mathbf{n}\|_{0,\Sigma}^2 \leq C_{\text{TI}} \|\boldsymbol{\varepsilon}(\mathbf{v}_h)\|_{0,\Omega_h^f}^2 \quad (3.21)$$

for all $\mathbf{v}_h \in \mathbf{V}_h$. These estimates are fundamental for the energy stability of the method.

Let define the discrete total energy E_h^n by the following expression:

$$E_h^n \stackrel{\text{def}}{=} \frac{\rho^f}{2} \|\mathbf{u}_h^n\|_{0,\Omega^f}^2 + \frac{\rho^s \varepsilon}{2} \|\dot{\mathbf{d}}_h^n\|_{\Sigma}^2 + \frac{1}{2} \|\mathbf{d}_h^n\|_s^2 + \frac{\tau^2}{2\rho^f} \|\nabla p_h^n\|_{0,\Omega_h^f}^2. \quad (3.22)$$

The following result states the conditional energy based stability of the approximation provided by Algorithm 3.3.

Theorem 3.4.1. *Let $\{(\mathbf{u}_h^n, p_h^n, \dot{\mathbf{d}}_h^n, \mathbf{d}_h^n)\}_{n \geq 1}$ be given by Algorithm 3.3 with $r = 1, 2$. Under the following conditions*

$$\gamma \geq \frac{2(3 + 4\alpha)}{\alpha} \frac{C_{\text{TI}}}{c_g}, \quad (3.23)$$

$$\gamma \mu \tau \leq \frac{2^{2-r}}{1 + 4\alpha} \rho^s \varepsilon h, \quad (3.24)$$

with $\alpha > 0$, the discrete energy estimate presented below holds:

$$E_h^n \lesssim E_h^0, \quad (3.25)$$

for all $n \geq 1$. As a result, Algorithm 3.3 is conditionally stable in the energy norm (3.22).

Proof. The proof for $r = 1$ is reported in Chapter 2. We recall here some of the steps and provide some details that include also the case $r = 2$, which follows similarly. We proceed by testing (3.16)-(3.18) with $(\mathbf{v}_h, \tilde{\mathbf{v}}_h, q_h, \mathbf{w}_h) = (\mathbf{u}_h^n, \tilde{\mathbf{u}}_h^n, p_h^n, \dot{\mathbf{d}}_h^n)$. By proceeding like in the derivation of (2.34) in Chapter 2 (the sole difference lies in the choice of $\dot{\mathbf{d}}_h^{*,r}$ and the inclusion of the seminorm associated to the stabilization operator S_h), we get the following energy estimate

$$\begin{aligned} & \frac{\rho^f}{2} \partial_\tau \|\mathbf{u}_h^n\|_{0,\Omega^f}^2 + 2c_g \mu \|\boldsymbol{\epsilon}(\tilde{\mathbf{u}}_h^n)\|_{0,\Omega_h^f}^2 + \frac{\tau}{2\rho^f} [\|\nabla p_h^n\|_{0,\Omega_h^f}^2 - \|\nabla p_h^{n-1}\|_{0,\Omega_h^f}^2] + \|(\tilde{\mathbf{u}}_h^n, p_h^n)\|_S^2 \\ & \frac{\rho^s \varepsilon}{2\tau} [\|\dot{\mathbf{d}}_h^n\|_{0,\Sigma}^2 - \|\dot{\mathbf{d}}_h^{n-1}\|_{0,\Sigma}^2 + \|\dot{\mathbf{d}}_h^n - \dot{\mathbf{d}}_h^{n-1}\|_{0,\Sigma}^2] + \frac{1}{2\tau} (\|\mathbf{d}_h^n\|_s^2 - \|\mathbf{d}_h^{n-1}\|_s^2) \\ & \underbrace{-2\mu \left(\boldsymbol{\epsilon}(\tilde{\mathbf{u}}_h^n) \mathbf{n}, \tilde{\mathbf{u}}_h^n - \dot{\mathbf{d}}_h^n \right)_\Sigma - 2\mu \left(\boldsymbol{\epsilon}(\tilde{\mathbf{u}}_h^n) \mathbf{n}, \tilde{\mathbf{u}}_h^n - \dot{\mathbf{d}}_h^{*,r} \right)_\Sigma}_{T_1} \\ & \quad + \underbrace{\frac{\gamma \mu}{h} \left(\tilde{\mathbf{u}}_h^n - \dot{\mathbf{d}}_h^{*,r}, \tilde{\mathbf{u}}_h^n - \dot{\mathbf{d}}_h^n \right)_\Sigma}_{T_2} \leq 0 \quad (3.26) \end{aligned}$$

for $n \geq r$. Term T_1 can be bounded by adding and subtracting $\dot{\mathbf{d}}_h^n$, using the

Cauchy–Schwarz, Young’s and trace inequalities (3.20), as follows:

$$\begin{aligned}
T_1 &= -2\mu \left(\boldsymbol{\epsilon}(\tilde{\mathbf{u}}_h^n) \mathbf{n}, \dot{\mathbf{d}}_h^n - \dot{\mathbf{d}}_h^{*,r} \right)_\Sigma - 4\mu \left(\boldsymbol{\epsilon}(\tilde{\mathbf{u}}_h^n) \mathbf{n}, \tilde{\mathbf{u}}_h^n - \dot{\mathbf{d}}_h^n \right)_\Sigma \\
&\geq - \left(\frac{1}{\alpha_1} + \frac{2}{\alpha_2} \right) \frac{\mu C_{\text{TI}}}{\gamma} \|\boldsymbol{\epsilon}(\tilde{\mathbf{u}}_h^n)\|_{0,\Omega_h^f}^2 - r\alpha_1 \frac{\gamma\mu}{h} \|\dot{\mathbf{d}}_h^n - \dot{\mathbf{d}}_h^{n-1}\|_{0,\Sigma}^2 \\
&\quad - 2(r-1)\alpha_1 \frac{\gamma\mu}{h} \|\dot{\mathbf{d}}_h^{n-1} - \dot{\mathbf{d}}_h^{n-2}\|_{0,\Sigma}^2 - 2\alpha_2 \frac{\gamma\mu}{h} \|\tilde{\mathbf{u}}_h^n - \dot{\mathbf{d}}_h^n\|_{0,\Sigma}^2,
\end{aligned} \tag{3.27}$$

with $\alpha_1, \alpha_2 > 0$. Similarly, for the second term, we have

$$\begin{aligned}
T_2 &= \frac{\gamma\mu}{h} \|\tilde{\mathbf{u}}_h^n - \dot{\mathbf{d}}_h^n\|_{0,\Sigma}^2 + \frac{\gamma\mu}{h} \left(\dot{\mathbf{d}}_h^n - \dot{\mathbf{d}}_h^{*,r}, \tilde{\mathbf{u}}_h^n - \dot{\mathbf{d}}_h^n \right)_\Sigma \\
&\geq \left(1 - \frac{1}{2\alpha_3} \right) \frac{\gamma\mu}{h} \|\tilde{\mathbf{u}}_h^n - \dot{\mathbf{d}}_h^n\|_{0,\Sigma}^2 - r \frac{\alpha_3 \gamma \mu}{2h} \|\dot{\mathbf{d}}_h^n - \dot{\mathbf{d}}_h^{n-1}\|_{0,\Sigma}^2 \\
&\quad - (r-1) \frac{\alpha_3 \gamma \mu}{h} \|\dot{\mathbf{d}}_h^{n-1} - \dot{\mathbf{d}}_h^{n-2}\|_{0,\Sigma}^2
\end{aligned} \tag{3.28}$$

with $\alpha_3 > 0$. By inserting (3.27) and (3.28) into (3.26) we get

$$\begin{aligned}
&\frac{\rho^f}{2} \partial_\tau \|\mathbf{u}_h^n\|_{0,\Omega^f}^2 + \frac{\tau}{2\rho^f} \left[\|\nabla p_h^n\|_{0,\Omega_h^f}^2 - \|\nabla p_h^{n-1}\|_{0,\Omega_h^f}^2 \right] + \frac{\rho^s \varepsilon}{2} \partial_\tau \|\dot{\mathbf{d}}_h^n\|_{0,\Sigma}^2 \\
&\quad + \frac{1}{2\tau} (\|\mathbf{d}_h^n\|_s^2 - \|\mathbf{d}_h^{n-1}\|_s^2) + 2\mu \left[c_g - \frac{C_{\text{TI}}}{\gamma} \left(\frac{1}{2\alpha_1} + \frac{1}{\alpha_2} \right) \right] \|\boldsymbol{\epsilon}(\tilde{\mathbf{u}}_h^n)\|_{0,\Omega_h^f}^2 \\
&\quad + \left[\frac{\rho^s \varepsilon}{2\tau} - r \left(\alpha_1 + \frac{\alpha_3}{2} \right) \frac{\gamma\mu}{h} \right] \|\dot{\mathbf{d}}_h^n - \dot{\mathbf{d}}_h^{n-1}\|_{0,\Sigma}^2 + \left(1 - \frac{1}{2\alpha_3} - 2\alpha_2 \right) \frac{\gamma\mu}{h} \|\tilde{\mathbf{u}}_h^n - \dot{\mathbf{d}}_h^n\|_{0,\Sigma}^2 \\
&\quad - (r-1) (2\alpha_1 + \alpha_3) \frac{\gamma\mu}{h} \|\dot{\mathbf{d}}_h^{n-1} - \dot{\mathbf{d}}_h^{n-2}\|_{0,\Sigma}^2 \leq 0 \tag{3.29}
\end{aligned}$$

for $n \geq r$. We now set

$$\alpha_1 = \frac{\alpha}{2}, \quad \alpha_2 = \frac{\alpha}{2(1+2\alpha)}, \quad \alpha_3 = \frac{1}{2} + \alpha, \quad \alpha > 0,$$

so that (3.29) yields

$$\begin{aligned}
&\frac{\rho^f}{2} \partial_\tau \|\mathbf{u}_h^n\|_{0,\Omega^f}^2 + \frac{\tau}{2\rho^f} \left[\|\nabla p_h^n\|_{0,\Omega_h^f}^2 - \|\nabla p_h^{n-1}\|_{0,\Omega_h^f}^2 \right] + \frac{\rho^s \varepsilon}{2} \partial_\tau \|\dot{\mathbf{d}}_h^n\|_{0,\Sigma}^2 + \frac{1}{2\tau} (\|\mathbf{d}_h^n\|_s^2 - \|\mathbf{d}_h^{n-1}\|_s^2) \\
&\quad + \left[\frac{\rho^s \varepsilon}{2\tau} - r \left(\frac{1}{4} + \alpha \right) \frac{\gamma\mu}{h} \right] \|\dot{\mathbf{d}}_h^n - \dot{\mathbf{d}}_h^{n-1}\|_{0,\Sigma}^2 - (r-1) \left(\frac{1}{2} + 2\alpha \right) \frac{\gamma\mu}{h} \|\dot{\mathbf{d}}_h^{n-1} - \dot{\mathbf{d}}_h^{n-2}\|_{0,\Sigma}^2 \\
&\quad + 2\mu \left[c_g - \frac{C_{\text{TI}}}{\gamma} \frac{3+4\alpha}{\alpha} \right] \|\boldsymbol{\epsilon}(\tilde{\mathbf{u}}_h^n)\|_{0,\Omega_h^f}^2 + \frac{\alpha}{1+2\alpha} \frac{\gamma\mu}{h} \|\tilde{\mathbf{u}}_h^n - \dot{\mathbf{d}}_h^n\|_{0,\Sigma}^2 \leq 0 \tag{3.30}
\end{aligned}$$

for $n \geq r$. We now replace the upper index n by m and sum over $m = r \dots n$ and multiply by τ . This yields

$$\begin{aligned}
& \frac{\rho^f}{2} \|\mathbf{u}_h^n\|_{0,\Omega^f}^2 + \frac{\tau^2}{2\rho^f} \|\nabla p_h^n\|_{0,\Omega_h^f}^2 + \frac{\rho^s \varepsilon}{2} \|\dot{\mathbf{d}}_h^n\|_{0,\Sigma}^2 + \frac{1}{2\tau} \|\mathbf{d}_h^n\|_s^2 \\
& + \left[\frac{\rho^s \varepsilon}{2} - \tau r \left(\frac{1}{4} + \alpha \right) \frac{\gamma \mu}{h} \right] \sum_{m=1}^n \|\dot{\mathbf{d}}_h^m - \dot{\mathbf{d}}_h^{m-1}\|_{0,\Sigma}^2 - \tau(r-1) \left(\frac{1}{2} + 2\alpha \right) \frac{\gamma \mu}{h} \sum_{m=2}^n \|\dot{\mathbf{d}}_h^{m-1} - \dot{\mathbf{d}}_h^{m-2}\|_{0,\Sigma}^2 \\
& + 2\tau\mu \left[c_g - \frac{C_{\text{TI}}}{\gamma} \frac{3+4\alpha}{\alpha} \right] \sum_{m=2}^n \|\epsilon(\tilde{\mathbf{u}}_h^m)\|_{0,\Omega_h^f}^2 + \tau \frac{\alpha}{1+2\alpha} \frac{\gamma \mu}{h} \sum_{m=2}^n \|\tilde{\mathbf{u}}_h^m - \dot{\mathbf{d}}_h^m\|_{0,\Sigma}^2 \\
& \leq \frac{\rho^f}{2} \|\mathbf{u}_h^{r-1}\|_{0,\Omega^f}^2 + \frac{\tau^2}{2\rho^f} \|\nabla p_h^{r-1}\|_{0,\Omega_h^f}^2 + \frac{\rho^s \varepsilon}{2} \|\dot{\mathbf{d}}_h^{r-1}\|_{0,\Sigma}^2 + \frac{1}{2} \|\mathbf{d}_h^{r-1}\|_s^2
\end{aligned}$$

for $n \geq r$. By rearranging the terms in the first sums, we get

$$\begin{aligned}
& \frac{\rho^f}{2} \|\mathbf{u}_h^n\|_{0,\Omega^f}^2 + \frac{\tau^2}{2\rho^f} \|\nabla p_h^n\|_{0,\Omega_h^f}^2 + \frac{\rho^s \varepsilon}{2} \|\dot{\mathbf{d}}_h^n\|_{0,\Sigma}^2 + \frac{1}{2\tau} \|\mathbf{d}_h^n\|_s^2 \\
& + \left[\frac{\rho^s \varepsilon}{2} - \tau 4^{r-1} \left(\frac{1}{4} + \alpha \right) \frac{\gamma \mu}{h} \right] \sum_{m=2}^n \|\dot{\mathbf{d}}_h^m - \dot{\mathbf{d}}_h^{m-1}\|_{0,\Sigma}^2 - \tau(r-1) \left(\frac{1}{2} + 2\alpha \right) \frac{\gamma \mu}{h} \|\dot{\mathbf{d}}_h^1 - \dot{\mathbf{d}}_h^0\|_{0,\Sigma}^2 \\
& + 2\tau\mu \left[c_g - \frac{C_{\text{TI}}}{\gamma} \frac{3+4\alpha}{\alpha} \right] \sum_{m=2}^n \|\epsilon(\tilde{\mathbf{u}}_h^m)\|_{0,\Omega_h^f}^2 + \tau \frac{\alpha}{1+2\alpha} \frac{\gamma \mu}{h} \sum_{m=2}^n \|\tilde{\mathbf{u}}_h^m - \dot{\mathbf{d}}_h^m\|_{0,\Sigma}^2 \\
& \leq \frac{\rho^f}{2} \|\mathbf{u}_h^{r-1}\|_{0,\Omega^f}^2 + \frac{\tau^2}{2\rho^f} \|\nabla p_h^{r-1}\|_{0,\Omega_h^f}^2 + \frac{\rho^s \varepsilon}{2} \|\dot{\mathbf{d}}_h^{r-1}\|_{0,\Sigma}^2 + \frac{r}{2} \|\mathbf{d}_h^{r-1}\|_s^2 \quad (3.31)
\end{aligned}$$

for $n \geq r$.

In the case $r = 1$, the previous bound yields the energy estimate provided in Chapter 2. For $r = 2$, we need to control the contributions coming from the initialization step, namely,

$$\frac{\rho^f}{2} \|\mathbf{u}_h^1\|_{0,\Omega^f}^2 + \frac{\tau^2}{2\rho^f} \|\nabla p_h^1\|_{0,\Omega_h^f}^2 + \frac{\rho^s \varepsilon}{2} \|\dot{\mathbf{d}}_h^1\|_{0,\Sigma}^2 + \frac{1}{2} \|\mathbf{d}_h^1\|_s^2,$$

which are obtained from one step of Algorithm 3.3 with $r = 1$. We hence consider (3.31) with $(n = 1, r = 1)$, which yields

$$\begin{aligned}
& \frac{\rho^f}{2} \|\mathbf{u}_h^1\|_{0,\Omega^f}^2 + \frac{\tau^2}{2\rho^f} \|\nabla p_h^1\|_{0,\Omega_h^f}^2 + \frac{\rho^s \varepsilon}{2} \|\dot{\mathbf{d}}_h^1\|_{0,\Sigma}^2 + \frac{1}{2} \|\mathbf{d}_h^1\|_s^2 \\
& + \left[\frac{\rho^s \varepsilon}{2} - \tau \left(\frac{1}{4} + \alpha \right) \frac{\gamma \mu}{h} \right] \|\dot{\mathbf{d}}_h^1 - \dot{\mathbf{d}}_h^0\|_{0,\Sigma}^2 + 2\tau\mu \left[c_g - \frac{C_{\text{TI}}}{\gamma} \frac{3+4\alpha}{\alpha} \right] \|\epsilon(\tilde{\mathbf{u}}_h^1)\|_{0,\Omega_h^f}^2 \\
& + \tau \frac{\alpha}{1+2\alpha} \frac{\gamma \mu}{h} \|\tilde{\mathbf{u}}_h^1 - \dot{\mathbf{d}}_h^1\|_{0,\Sigma}^2 \leq \frac{\rho^f}{2} \|\mathbf{u}_h^0\|_{0,\Omega^f}^2 + \frac{\tau^2}{2\rho^f} \|\nabla p_h^0\|_{0,\Omega_h^f}^2 + \frac{\rho^s \varepsilon}{2} \|\dot{\mathbf{d}}_h^0\|_{0,\Sigma}^2 + \frac{1}{2} \|\mathbf{d}_h^0\|_s^2.
\end{aligned}$$

Hence, by adding this expression to (3.31), we finally get

$$\begin{aligned}
& \frac{\rho^f}{2} \|\mathbf{u}_h^n\|_{0,\Omega^f}^2 + \frac{\tau^2}{2\rho^f} \|\nabla p_h^n\|_{0,\Omega_h^f}^2 + \frac{\rho^s \varepsilon}{2} \|\dot{\mathbf{d}}_h^n\|_{0,\Sigma}^2 + \frac{1}{2} \|\mathbf{d}_h^n\|_s^2 \\
& + \left[\frac{\rho^s \varepsilon}{2} - \tau(1+4\alpha) \frac{\gamma \mu}{h} \right] \sum_{m=1}^n \|\dot{\mathbf{d}}_h^m - \dot{\mathbf{d}}_h^{m-1}\|_{0,\Sigma}^2
\end{aligned}$$

$$\begin{aligned}
& + 2\tau\mu \left[c_g - \frac{C_{\text{TI}}}{\gamma} \frac{3 + 4\alpha}{\alpha} \right] \sum_{m=1}^n \|\epsilon(\tilde{\mathbf{u}}_h^m)\|_{0,\Omega_h^f}^2 + \tau \frac{\alpha}{1 + 2\alpha} \frac{\gamma\mu}{h} \sum_{m=1}^n \|\tilde{\mathbf{u}}_h^m - \dot{\mathbf{d}}_h^m\|_{0,\Sigma}^2 \\
& \leq \frac{\rho^f}{2} \|\mathbf{u}_h^0\|_{0,\Omega^f}^2 + \frac{\tau^2}{2\rho^f} \|\nabla p_h^0\|_{0,\Omega_h^f}^2 + \frac{\rho^s \varepsilon}{2} \|\dot{\mathbf{d}}_h^0\|_{0,\Sigma}^2 + \frac{1}{2} \|\mathbf{d}_h^0\|_s^2 \quad (3.32)
\end{aligned}$$

for $n \geq 1$. The energy estimate (3.22) hence follows from (3.32) under the conditions (3.23)-(3.24), which completes the proof. \square

Remark 3.4.1. *A similar stability analysis can be derived in the case of a thick-walled solid. The solid quantities appearing on the interface Σ , such as $\dot{\mathbf{d}}_h^n - \dot{\mathbf{d}}_h^{n-1}$, are controlled on the whole solid domain using element-wise trace inequalities. This yields to a parabolic CFL-type stability condition, namely,*

$$\gamma\mu\tau \lesssim \rho^s h^2,$$

which is more restrictive than in the case of a thin-walled solid. An analogous stability result is reported in [Fernández et al. \(2007\)](#) for the non-incremental version of Algorithm 3.3 within the framework of fitted mesh. Stability is guaranteed under the CFL-like condition $\rho^f h^2 + 2\mu\tau \lesssim \rho^s \varepsilon h$ for a thin-walled solid and $\rho^f h^2 + 2\mu\tau \lesssim \rho^s h^2$ in the case of thick-walled solid.

3.4.2 A priori error estimate

In the following we use the notation $v^n \stackrel{\text{def}}{=} v(t_n)$ for a given time dependent function v . For conciseness, an abuse of notation will be committed by denoting $(\partial_t v)^n$ with $\partial_t v^n$. Furthermore, the symbol \lesssim indicates inequalities up to a multiplicative constant (independent of the discretization parameter h and of the physical parameters). We consider the following mesh-dependent seminorms for functions defined on the interface Σ :

$$\|f\|_{\frac{1}{2},h,\Sigma}^2 = \sum_{K \in \mathcal{G}_h} h^{-1} \|f\|_{0,\Sigma_K}^2, \quad \|f\|_{-\frac{1}{2},h,\Sigma}^2 = \sum_{K \in \mathcal{G}_h} h \|f\|_{0,\Sigma_K}^2$$

where Σ_K denotes the part of the interface intersecting the simplex K , i.e., $\Sigma_K \stackrel{\text{def}}{=} K \cap \Sigma$.

For the sake of simplicity, in the error analysis we assume that the interface Σ is flat. Furthermore, the elements of the solid mesh are supposed to be grouped in disjoint macropatches P_i , with $\text{meas}(P_i) = \mathcal{O}(h^d)$. Each $(d-1)$ -dimensional macro patch P_i is assumed to contain at least one interior node and the union of the P_i is assumed to cover Σ , viz., $\cup_i P_i = \Sigma$.

The discrete interpolation operators are those introduced in [Burman and Fernández \(2014a\)](#) (see also [Fernández and Landajuela \(2019\)](#)). For the solid displacement, we consider the elastic Ritz-projection operator $\pi_h^s : \mathbf{W} \rightarrow \mathbf{W}_h$ defined by the relation

$$a^s(\mathbf{w} - \pi_h^s \mathbf{w}, \mathbf{w}_h) = 0 \quad (3.33)$$

for all $\mathbf{w}_h \in \mathbf{W}_h$, and for which there holds

$$\|\mathbf{w} - \pi_h^s \mathbf{w}\|_{0,\Sigma} + h \|\nabla (\mathbf{w} - \pi_h^s \mathbf{w})\|_{0,\Sigma} \lesssim h^2 |\mathbf{w}|_{2,\Sigma} \quad (3.34)$$

for all $\mathbf{w} \in [H^2(\Sigma)]^d \cap \mathbf{W}$. For the solid velocity, we consider the operator $\mathbf{I}_h : \mathbf{W} \rightarrow \mathbf{W}_h$ which is defined as a correction of the operator π_h^s by the relation

$$\mathbf{I}_h \mathbf{w} \stackrel{\text{def}}{=} \pi_h^s \mathbf{w} + \sum_i \alpha_i \varphi_i,$$

with $\alpha_i \in \mathbb{R}$ to be fixed with a constraint detailed below. The φ_i are functions with support in the macropatches P_i , such that

$$0 \leq \varphi_i \leq 1, \quad \|\varphi_i\|_{0,P_i} \lesssim h^{\frac{d-1}{2}}$$

and take the value 1, component-wise, in the interior nodes of the associated patch P_i . The scalars α_i are chosen so that the following condition holds:

$$\int_{P_i} (\mathbf{w} - \mathbf{I}_h \mathbf{w}) \cdot \mathbf{n} = 0. \quad (3.35)$$

This orthogonality condition is used in the error analysis to control the interface terms coupling the fluid pressure and the solid velocity. We refer to [Becker et al. \(2009\)](#) for the detailed construction of such an operator. It can be shown (see ([Burman and Fernández, 2014a](#), Lemma 3.3)) that

$$\|\mathbf{w} - \mathbf{I}_h \mathbf{w}\|_{0,\Sigma} + h \|\nabla (\mathbf{w} - \mathbf{I}_h \mathbf{w})\|_{0,\Sigma} \lesssim h^2 |\mathbf{w}|_{2,\Sigma} \quad (3.36)$$

for all $\mathbf{w} \in [H^2(\Sigma)]^d \cap \mathbf{W}$.

Since the physical solution and the discrete one, are defined on different domains, namely Ω^f and Ω_h^f , with $\Omega^f \subset \Omega_h^f$, we assume that there exist two linear continuous lifting operators $E_2 : H^2(\Omega^f) \rightarrow H^2(\mathbb{R}^d)$ and $E_1 : H^1(\Omega^f) \rightarrow H^1(\mathbb{R}^d)$, satisfying the bounds $\|E_1 v\|_{H^1(\mathbb{R}^d)} \lesssim \|v\|_{H^1(\Omega^f)}$ for all $v \in H^1(\Omega^f)$ and $\|E_2 v\|_{H^2(\mathbb{R}^d)} \lesssim \|v\|_{H^2(\Omega^f)}$ for all $v \in H^2(\Omega^f)$, (see, e.g., [Evans \(2002\)](#); [Salsa \(2009\)](#)). To interpolate the resulting extended fluid solution we consider the Scott–Zhang operator i_{sz} , see [Ern and Guermond \(2004\)](#) for extra details. Then it holds (see ([Burman and Fernández, 2014a](#), Lemma 3.3)):

$$\begin{aligned} \|\mathbf{v} - i_{sz} E_2 \mathbf{v}\|_{0,\Omega^f} + h \|\nabla (\mathbf{v} - i_{sz} E_2 \mathbf{v})\|_{0,\Omega^f} &\lesssim h^2 |\mathbf{v}|_{2,\Omega^f}, \\ \|q - i_{sz} E_1 q\|_{0,\Omega^f} + h \|\nabla (q - i_{sz} E_1 q)\|_{0,\Omega^f} &\lesssim h |q|_{1,\Omega^f}, \\ \|\boldsymbol{\sigma}(\mathbf{v} - i_{sz} E_2 \mathbf{v}, q - i_{sz} E_1 q) \mathbf{n}\|_{-\frac{1}{2},h,\Sigma} &\lesssim h (\|\mathbf{v}\|_{2,\Omega^f} + \|q\|_{1,\Omega^f}), \\ \|\mathbf{v} - i_{sz} E_2 \mathbf{v}\|_{\frac{1}{2},h,\Sigma} &\lesssim h \|\mathbf{v}\|_{2,\Omega^f}, \\ \|\mathbf{w} - \mathbf{I}_h \mathbf{w}\|_{\frac{1}{2},h,\Sigma} &\lesssim h^{\frac{3}{2}} \|\mathbf{w}\|_{2,\Sigma} \end{aligned} \quad (3.37)$$

for all $\mathbf{v} \in [H^2(\Omega^f)]^d$, $q \in H^1(\Omega^f)$ and $\mathbf{w} \in [H^2(\Sigma)]^d \cap \mathbf{W}$. Moreover, using an inverse

inequality, (3.37) and the stability of the extension operator we have the following stability result for the gradient projection

$$\|\nabla i_{sz} E_1 q\|_{0, \Omega_h^f}^2 \leq h^{-1} \|i_{sz} E_1 q - E_1 q\|_{0, \Omega_h^f}^2 + \|\nabla E_1 q\|_{0, \Omega_h^f}^2 \lesssim \|q\|_{1, \Omega^f}^2. \quad (3.38)$$

For the pressure and ghost-penalty stabilization operators (3.7)-(3.8), the following consistency properties hold (see, e.g., [Burman and Fernández \(2014a\)](#); [Burman and Hansbo \(2014\)](#)):

$$s_h (i_{sz} E_1 q, i_{sz} E_1 q)^{\frac{1}{2}} \lesssim \mu^{-\frac{1}{2}} h |q|_{1, \Omega^f} \quad (3.39)$$

and

$$g_h (i_{sz} E_2 \mathbf{v}, i_{sz} E_2 \mathbf{v})^{\frac{1}{2}} \lesssim h \mu^{\frac{1}{2}} |v|_{2, \Omega^f}. \quad (3.40)$$

In the following we will make use of the discrete Gronwall lemma (see, e.g., [Heywood and Rannacher \(1990\)](#)), which we collect here without a proof.

Lemma 3.4.2. *Let τ, B and a_m, b_m, c_m, η_m (for integers $m \geq 1$) be non-negative numbers such that*

$$a_n + \tau \sum_{m=1}^n b_m \leq \tau \sum_{m=1}^n \eta_m a_m + \tau \sum_{m=1}^n c_m + B$$

for $n \geq 1$. Suppose that $\tau \eta_m < 1$ for all $m \geq 1$. Then there holds

$$a_n + \tau \sum_{m=1}^n b_m \leq \exp\left(\tau \sum_{m=1}^n \frac{\eta_m}{1 - \tau \eta_m}\right) \left(\tau \sum_{m=1}^n c_m + B\right)$$

for $n \geq 1$.

For the a priori error estimate, we assume that the exact solution of problem (3.1)-(3.3) has the following regularity, for a given final time $T \geq \tau$:

$$\begin{aligned} \mathbf{u} &\in [H^1(0, T; H^2(\Omega))]^d, \quad \mathbf{u}|_{\Sigma} \in [H^1(0, T; H^2(\Sigma))]^d, \\ \partial_{tt} \mathbf{u} &\in [L^2(0, T; L^2(\Omega))]^d, \quad \partial_{tt} \mathbf{u}|_{\Sigma} \in [L^2(0, T; L^2(\Sigma))]^d, \\ p &\in H^1(0, T; H^1(\Omega)), \quad \mathbf{u}|_{\Sigma} \in [H^2(0, T; H^2(\Sigma))]^d, \\ \partial_t^{(r)} \mathbf{u}|_{\Sigma} &\in [L^2(0, T; L^2(\Sigma))]^d, \quad \mathbf{d} \in [H^1(0, T; H^2(\Sigma))]^d. \end{aligned} \quad (3.41)$$

We define the energy norm of the error at time t_n as

$$\begin{aligned} \mathcal{Z}_h^n &\stackrel{\text{def}}{=} (\rho^f)^{\frac{1}{2}} \|\mathbf{u}^n - \mathbf{u}_h^n\|_{0, \Omega^f} + \frac{\tau}{(\rho^f)^{\frac{1}{2}}} \|\nabla(p^n - p_h^n)\|_{0, \Omega_h^f} + (\rho^s \varepsilon)^{\frac{1}{2}} \|\dot{\mathbf{d}}^n - \dot{\mathbf{d}}_h^n\|_{0, \Sigma} + \|\mathbf{d}^n - \mathbf{d}_h^n\|_s \\ &+ \left(\sum_{m=1}^n \tau \frac{\alpha}{1 + 2\alpha} \gamma \mu \|\tilde{\mathbf{u}}_h^m - \dot{\mathbf{d}}_h^m\|_{\frac{1}{2}, h, \Sigma}^2 \right)^{\frac{1}{2}} + \left(\sum_{m=1}^n \tau |(\tilde{\mathbf{u}}_h^m, p_h^m)|_S^2 \right)^{\frac{1}{2}}. \end{aligned}$$

We can then state the following a priori error estimate.

Theorem 3.4.3. *Let $(\mathbf{u}, p, \mathbf{d}, \dot{\mathbf{d}})$ be the solution of (3.1)-(3.2) and, $\{(\mathbf{u}_h^n, \tilde{\mathbf{u}}_h^n, p_h^n, \mathbf{d}_h^n, \dot{\mathbf{d}}_h^n)\}_{n \geq r}$ be given by Algorithm 3.3, with initial data*

$$(\tilde{\mathbf{u}}_h^{r-1}, p_h^{r-1}, \mathbf{d}_h^{r-1}, \dot{\mathbf{d}}_h^{r-1}) = (i_{sz}E_2\mathbf{u}^{r-1}, i_{sz}E_1p^{r-1}, \boldsymbol{\pi}_h^s\mathbf{d}^{r-1}, \mathbf{I}_h\dot{\mathbf{d}}^{r-1})$$

for $r = 1, 2$. Suppose that the exact solution has the regularity (3.41) and that the stability conditions (3.23)-(3.24) hold. Then, for $n \geq r$ and $n\tau < T$, we have the following discrete error estimate:

$$\mathcal{Z}_h^n \lesssim c_1 h + c_2 \tau + c_3 \frac{\tau^r}{h^{\frac{1}{2}}}, \quad (3.42)$$

where $\{c_i\}_{i=1}^3$ denote positive constants independent of h and τ , but which depend on the physical parameters and on the regularity of the exact solution.

Proof. The proof combines some of the arguments reported in [Burman et al. \(2017\)](#); [Burman and Fernández \(2014a\)](#). Note however that analysis of [Burman and Fernández \(2014a\)](#) focuses on the spatial semi-discrete problem (3.10) and the work of [Burman et al. \(2017\)](#) is limited to a pure fluid problem. Multiplying (3.1)-(3.2) by $(\mathbf{v}_h, q_h) \in \mathbf{V}_h \times Q_h$ and $\mathbf{w}_h \in \mathbf{W}_h$, integrating by parts over Ω^f and using (3.1)₃ and (3.3)₂ we obtain

1. Fluid sub-problem:

$$\begin{cases} \rho^f (\partial_t \mathbf{u}, \mathbf{v}_h)_{\Omega^f} + 2\mu (\boldsymbol{\epsilon}(\mathbf{u}), \boldsymbol{\epsilon}(\mathbf{v}_h))_{\Omega^f} + (\nabla p, \mathbf{v}_h)_{\Omega^f} - (\boldsymbol{\sigma}(\mathbf{u}, 0) \mathbf{n}, \mathbf{v}_h)_{\Sigma} = 0, \\ (q_h, \operatorname{div} \mathbf{u})_{\Omega^f} = 0. \end{cases} \quad (3.43)$$

2. Solid sub-problem:

$$\rho^s \varepsilon (\partial_t \dot{\mathbf{d}}, \mathbf{w}_h)_{\Sigma} + a^s (\mathbf{d}, \mathbf{w}_h) + (\boldsymbol{\sigma}(\mathbf{u}, p) \mathbf{n}, \mathbf{w}_h)_{\Sigma} = 0.$$

Note that only the viscous term has been integrated by parts in the fluid.

On the other hand, owing to the kinematic coupling condition (3.3)₁, we also have

1. Fluid sub-problem:

$$\begin{cases} \rho^f (\partial_t \mathbf{u}, \mathbf{v}_h)_{\Omega^f} + 2\mu (\boldsymbol{\epsilon}(\mathbf{u}), \boldsymbol{\epsilon}(\mathbf{v}_h))_{\Omega^f} + (\nabla p, \mathbf{v}_h)_{\Omega^f} - (\boldsymbol{\sigma}(\mathbf{u}, 0) \mathbf{n}, \mathbf{v}_h)_{\Sigma} \\ \quad + \frac{\gamma\mu}{h} (\mathbf{u} - \dot{\mathbf{d}}, \mathbf{v}_h)_{\Sigma} - (\mathbf{u} - \dot{\mathbf{d}}, \boldsymbol{\sigma}(\mathbf{v}_h, -q_h) \mathbf{n})_{\Sigma} = 0, \\ (q_h, \operatorname{div} \mathbf{u})_{\Omega^f} = 0 \end{cases} \quad (3.44)$$

for all $(\mathbf{v}_h, q_h) \in \mathbf{V}_h \times Q_h$.

2. Solid sub-problem:

$$\rho^s \varepsilon (\partial_t \dot{\mathbf{d}}, \mathbf{w}_h)_{\Sigma} + a^s (\mathbf{d}, \mathbf{w}_h) + \frac{\gamma\mu}{h} (\dot{\mathbf{d}} - \mathbf{u}, \mathbf{w}_h)_{\Sigma} + (\boldsymbol{\sigma}(\mathbf{u}, p) \mathbf{n}, \mathbf{w}_h)_{\Sigma} = 0 \quad (3.45)$$

for all $\mathbf{w}_h \in \mathbf{W}_h$.

Thereafter, using the lifting operators (component-wise) we introduce the following decomposition of the errors for the fluid:

$$\begin{aligned}
E_2 \mathbf{u}^n - \mathbf{u}_h^n &= \underbrace{E_2 \mathbf{u}^n - i_{sz} E_2 \mathbf{u}^n}_{\stackrel{\text{def}}{=} \boldsymbol{\theta}_\pi^n} + \underbrace{i_{sz} E_2 \mathbf{u}^n - \mathbf{u}_h^n}_{\stackrel{\text{def}}{=} \boldsymbol{\theta}_h^n} & \text{in } \Omega_h^f, \\
E_2 \mathbf{u}^n - \tilde{\mathbf{u}}_h^n &= \underbrace{E_2 \mathbf{u}^n - i_{sz} E_2 \mathbf{u}^n}_{\stackrel{\text{def}}{=} \boldsymbol{\theta}_\pi^n} + \underbrace{i_{sz} E_2 \mathbf{u}^n - \tilde{\mathbf{u}}_h^n}_{\stackrel{\text{def}}{=} \tilde{\boldsymbol{\theta}}_h^n} & \text{in } \Omega_h^f, \\
E_1 p^n - p_h^n &= \underbrace{E_1 p^n - i_{sz} E_1 p^n}_{\stackrel{\text{def}}{=} y_\pi^n} + \underbrace{i_{sz} E_1 p^n - p_h^n}_{\stackrel{\text{def}}{=} y_h^n} & \text{in } \Omega_h^f
\end{aligned} \tag{3.46}$$

and for the solid:

$$\begin{aligned}
\mathbf{d}^n - \mathbf{d}_h^n &= \underbrace{\mathbf{d}^n - \pi_h^s \mathbf{d}^n}_{\stackrel{\text{def}}{=} \boldsymbol{\xi}_\pi^n} + \underbrace{\pi_h^s \mathbf{d}^n - \mathbf{d}_h^n}_{\stackrel{\text{def}}{=} \boldsymbol{\xi}_h^n} & \text{in } \Sigma, \\
\dot{\mathbf{d}}^n - \dot{\mathbf{d}}_h^n &= \underbrace{\dot{\mathbf{d}}^n - I_h \dot{\mathbf{d}}^n}_{\stackrel{\text{def}}{=} \dot{\boldsymbol{\xi}}_\pi^n} + \underbrace{I_h \dot{\mathbf{d}}^n - \dot{\mathbf{d}}_h^n}_{\stackrel{\text{def}}{=} \dot{\boldsymbol{\xi}}_h^n} & \text{in } \Sigma.
\end{aligned} \tag{3.47}$$

By adding and subtracting $\partial_\tau \pi_h^s \mathbf{d}^n$, we can rewrite $\dot{\boldsymbol{\xi}}_h^n$ as

$$\dot{\boldsymbol{\xi}}_h^n = \mathcal{I}_h \dot{\mathbf{d}}^n - \dot{\mathbf{d}}_h^n = \underbrace{\mathcal{I}_h \dot{\mathbf{d}}^n - \partial_\tau \pi_h^s \mathbf{d}^n}_{\stackrel{\text{def}}{=} \mathbf{z}_h^n} + \underbrace{\partial_\tau \pi_h^s \mathbf{d}^n - \partial_\tau \mathbf{d}_h^n}_{\stackrel{\text{def}}{=} \partial_\tau \boldsymbol{\xi}_h^n} = \mathbf{z}_h^n + \partial_\tau \boldsymbol{\xi}_h^n. \tag{3.48}$$

We also introduce the following notations:

$$\dot{\boldsymbol{\chi}}_\pi^{*,r} \stackrel{\text{def}}{=} \dot{\mathbf{d}}^n - I_h \dot{\mathbf{d}}^{*,r} = \begin{cases} \dot{\mathbf{d}}^n - I_h \dot{\mathbf{d}}^{n-1} & \text{if } r = 1, \\ \dot{\mathbf{d}}^n - 2I_h \dot{\mathbf{d}}^{n-1} + I_h \dot{\mathbf{d}}^{n-2} & \text{if } r = 2, \end{cases} \tag{3.49}$$

$$\psi_h^{n-1} \stackrel{\text{def}}{=} y_h^{n-1} + i_{sz} E_1 p^n - i_{sz} E_1 p^{n-1}. \tag{3.50}$$

In particular, owing to (3.49), we have

$$\mathbf{u}^n - \tilde{\mathbf{u}}_h^n - (\dot{\mathbf{d}}^n - \dot{\mathbf{d}}_h^{*,r}) = \boldsymbol{\theta}_\pi^n + \tilde{\boldsymbol{\theta}}_h^n - (\dot{\boldsymbol{\chi}}_\pi^{*,r} + \mathcal{I}_h \dot{\mathbf{d}}^{*,r} - \dot{\mathbf{d}}_h^{*,r}) = \boldsymbol{\theta}_\pi^n + \tilde{\boldsymbol{\theta}}_h^n - (\dot{\boldsymbol{\chi}}_\pi^{*,r} + \dot{\boldsymbol{\xi}}_h^{n,r}), \tag{3.51}$$

Similar, from (3.50), one straightforwardly gets the following useful relations:

$$\begin{aligned}
p^n - p_h^{n-1} &= \psi_h^{n-1} + y_\pi^n, \\
p_h^n - p_h^{n-1} &= \psi_h^{n-1} - y_h^n.
\end{aligned} \tag{3.52}$$

The essential part of the proof focuses on deriving an a priori estimate for the discrete errors

$$\{(\boldsymbol{\theta}_h^n, \tilde{\boldsymbol{\theta}}_h^n, y_h^n, \boldsymbol{\xi}_h^n, \dot{\boldsymbol{\xi}}_h^n)\}_{n \geq r},$$

in terms of the following energy norm

$$\begin{aligned} \mathcal{E}_h^n &\stackrel{\text{def}}{=} (\rho^f)^{\frac{1}{2}} \|\boldsymbol{\theta}_h^n\|_{0,\Omega^f} + \left(\frac{\tau}{\rho^f}\right)^{\frac{1}{2}} \|\nabla \mathbf{y}_h^n\|_{0,\Omega_h^f} + (\rho^s \varepsilon)^{\frac{1}{2}} \|\dot{\boldsymbol{\xi}}_h^n\|_{0,\Sigma} + \|\boldsymbol{\xi}_h^n\|_s \\ &+ \left(\sum_{m=r}^n \tau \mu \|\nabla \tilde{\boldsymbol{\theta}}_h^m\|_{0,\Omega_h^f}^2\right)^{\frac{1}{2}} + \left(\sum_{m=r}^n \tau \frac{\alpha}{1+2\alpha} \gamma \mu \|\tilde{\boldsymbol{\theta}}_h^m - \dot{\boldsymbol{\xi}}_h^m\|_{\frac{1}{2},h,\Sigma}^2\right)^{\frac{1}{2}} + \left(\sum_{m=r}^n \tau c_g |(\tilde{\boldsymbol{\theta}}_h^m, \mathbf{y}_h^m)|_S^2\right)^{\frac{1}{2}}. \end{aligned}$$

To this purpose, we first focus on the fluid subsystem. By subtracting (3.16) from the momentum equation of (3.44) at $t = t_n$, with $n \geq r$, we get

$$\begin{aligned} \rho^f (\partial_t \mathbf{u}^n, \tilde{\mathbf{v}}_h)_{\Omega^f} - \frac{\rho^f}{\tau} (\tilde{\mathbf{u}}_h^n - \mathbf{u}_h^{n-1}, \tilde{\mathbf{v}}_h)_{\Omega^f} + 2\mu (\boldsymbol{\epsilon}(\mathbf{u}^n - \tilde{\mathbf{u}}_h^n), \boldsymbol{\epsilon}(\tilde{\mathbf{v}}_h))_{\Omega^f} + (\nabla(p^n - p_h^{n-1}), \tilde{\mathbf{v}}_h)_{\Omega^f} \\ + \frac{\gamma \mu}{h} ((\mathbf{u}^n - \tilde{\mathbf{u}}_h^n) - (\dot{\mathbf{d}}^n - \dot{\mathbf{d}}_h^{*,r}), \tilde{\mathbf{v}}_h)_{\Sigma} - (\mathbf{u}^n - \dot{\mathbf{d}}^n, \boldsymbol{\sigma}(\tilde{\mathbf{v}}_h, -q_h) \mathbf{n})_{\Sigma} + (\tilde{\mathbf{u}}_h^n - \dot{\mathbf{d}}_h^{*,r}, \boldsymbol{\sigma}(\tilde{\mathbf{v}}_h, 0) \mathbf{n})_{\Sigma} \\ - (\boldsymbol{\sigma}(\mathbf{u}^n - \tilde{\mathbf{u}}_h^n, 0) \mathbf{n}, \tilde{\mathbf{v}}_h)_{\Sigma} - g_h(\tilde{\mathbf{u}}_h^n, \mathbf{v}_h^n) = 0. \quad (3.53) \end{aligned}$$

Owing to the error decompositions (3.46) -(3.47) and using (3.51)-(3.52), the identity (3.53) can be rewritten as

$$\begin{aligned} \frac{\rho^f}{\tau} (\tilde{\boldsymbol{\theta}}_h^n - \boldsymbol{\theta}_h^{n-1}, \tilde{\mathbf{v}}_h)_{\Omega^f} + 2\mu (\boldsymbol{\epsilon}(\tilde{\boldsymbol{\theta}}_h^n), \boldsymbol{\epsilon}(\tilde{\mathbf{v}}_h))_{\Omega^f} + (\nabla \psi_h^{n-1}, \tilde{\mathbf{v}}_h)_{\Omega^f} \\ + \frac{\gamma \mu}{h} (\tilde{\boldsymbol{\theta}}_h^n - \dot{\boldsymbol{\xi}}_h^{*,r}, \tilde{\mathbf{v}}_h)_{\Sigma} - (\tilde{\boldsymbol{\theta}}_h^n - \dot{\boldsymbol{\xi}}_h^{*,r}, \boldsymbol{\sigma}(\tilde{\mathbf{v}}_h, 0) \mathbf{n})_{\Sigma} - (\boldsymbol{\sigma}(\tilde{\boldsymbol{\theta}}_h^n, 0) \mathbf{n}, \tilde{\mathbf{v}}_h)_{\Sigma} + g_h(\tilde{\boldsymbol{\theta}}_h^n, \mathbf{v}_h^n) \\ = \rho^f (-\partial_t \mathbf{u}^n + \partial_{\tau} \mathbf{u}^n - \partial_{\tau} \boldsymbol{\theta}_{\pi}^n, \tilde{\mathbf{v}}_h)_{\Omega^f} - 2\mu (\boldsymbol{\epsilon}(\boldsymbol{\theta}_{\pi}^n), \boldsymbol{\epsilon}(\tilde{\mathbf{v}}_h))_{\Omega^f} - (\nabla y_{\pi}^n, \tilde{\mathbf{v}}_h)_{\Omega^f} \\ - \frac{\gamma \mu}{h} (\boldsymbol{\theta}_{\pi}^n - \dot{\boldsymbol{\chi}}_{\pi}^{*,r}, \tilde{\mathbf{v}}_h)_{\Sigma} + (\boldsymbol{\theta}_{\pi}^n - \dot{\boldsymbol{\chi}}_{\pi}^{*,r}, \boldsymbol{\sigma}(\tilde{\mathbf{v}}_h, 0) \mathbf{n})_{\Sigma} + (\boldsymbol{\sigma}(\boldsymbol{\theta}_{\pi}^n, 0) \mathbf{n}, \tilde{\mathbf{v}}_h)_{\Sigma} + g_h(i_{sz} E_2 \mathbf{u}^n, \mathbf{v}_h^n) \end{aligned} \quad (3.54)$$

for $n \geq r$.

For the pressure, subtracting the pressure-projection step of (3.17) from the mass conservation equation (3.44) at $t = t_n$, with $n \geq r$, we get the following relation

$$(\operatorname{div}(\mathbf{u}^n - \tilde{\mathbf{u}}_h^n), q_h)_{\Omega^f} - \frac{\tau}{\rho^f} (\nabla(p_h^n - p_h^{n-1}), \nabla q_h)_{\Omega_h^f} - s_h(p_h^n, q_h) + (\tilde{\mathbf{u}}_h^n - \dot{\mathbf{d}}_h^n, q_h \mathbf{n})_{\Sigma} = 0. \quad (3.55)$$

Again, using the definition of error decomposition (3.46)-(3.47), the coupling kinematic condition (3.3)₁ and (3.52), from (3.55) we obtain

$$\begin{aligned} \frac{\tau}{\rho^f} (\nabla(y_h^n - \psi_h^{n-1}), \nabla q_h)_{\Omega_h^f} + (\operatorname{div} \tilde{\boldsymbol{\theta}}_h^n, q_h)_{\Omega^f} + s_h(y_h^n, q_h) - (\tilde{\boldsymbol{\theta}}_h^n - \dot{\boldsymbol{\xi}}_h^n, q_h \mathbf{n})_{\Sigma} \\ = -(\operatorname{div} \boldsymbol{\theta}_{\pi}^n, q_h)_{\Omega^f} + s_h(i_{sz} E_1 p^n, q_h) + (\boldsymbol{\theta}_{\pi}^n - \dot{\boldsymbol{\xi}}_{\pi}^n, q_h \mathbf{n})_{\Sigma} \end{aligned} \quad (3.56)$$

for $n \geq r$.

Finally, adding and subtracting $i_{sz} E_2 \mathbf{u}^n$, $i_{sz} E_1 p^n$, $i_{sz} E_1 p^{n-1}$ in (3.18) and using (3.52),

we obtain the following relation for the end-of-step velocity error

$$\frac{\rho^f}{\tau}(\boldsymbol{\theta}_h^n - \tilde{\boldsymbol{\theta}}_h^n, \mathbf{v}_h)_{\Omega^f} + (\nabla(y_h^n - \psi_h^{n-1}), \mathbf{v}_h)_{\Omega^f} = 0 \quad (3.57)$$

for $n \geq r$.

Subtracting the solid problem of (3.17) from (3.45) $t = t_n$, with $n \geq r$, and using the relation (3.51), we obtain

$$\begin{aligned} \rho^s \varepsilon (\partial_t \dot{\mathbf{d}}^n - \partial_\tau^* \dot{\mathbf{d}}_h^n, \mathbf{w}_h)_\Sigma + a^s(\mathbf{d}^n - \mathbf{d}_h^n, \mathbf{w}_h) - \frac{\gamma\mu}{h}(\mathbf{u}^n - \tilde{\mathbf{u}}_h^n - (\dot{\mathbf{d}}^n - \dot{\mathbf{d}}_h^{*,r}), \mathbf{w}_h)_\Sigma \\ + (\boldsymbol{\sigma}(\mathbf{u}^n - \tilde{\mathbf{u}}_h^n, p^n - p_h^n) \mathbf{n}, \mathbf{w}_h)_\Sigma = 0. \end{aligned}$$

Thus, using (3.46) -(3.47) and (3.51), we finally get the equation for the solid discrete errors:

$$\begin{aligned} \rho^s \varepsilon (\partial_\tau \dot{\boldsymbol{\xi}}_h^n, \mathbf{w}_h)_\Sigma + a^s(\boldsymbol{\xi}_h^n, \mathbf{w}_h) - \frac{\gamma\mu}{h}(\tilde{\boldsymbol{\theta}}_h^n - \dot{\boldsymbol{\xi}}_h^{*,r}, \mathbf{w}_h)_\Sigma + (\boldsymbol{\sigma}(\tilde{\boldsymbol{\theta}}_h^n, y_h^n) \mathbf{n}, \mathbf{w}_h)_\Sigma \\ = \rho^s \varepsilon (\partial_\tau \dot{\mathbf{d}}^n - \partial_t \dot{\mathbf{d}}^n - \partial_\tau \dot{\boldsymbol{\xi}}_\pi^n, \mathbf{w}_h)_\Sigma - \underbrace{a^s(\boldsymbol{\xi}_\pi^n, \mathbf{w}_h)}_{=0} + \frac{\gamma\mu}{h}(\boldsymbol{\theta}_\pi^n - \dot{\boldsymbol{\chi}}_\pi^{*,r}, \mathbf{w}_h)_\Sigma - (\boldsymbol{\sigma}(\boldsymbol{\theta}_\pi^n, y_\pi^n) \mathbf{n}, \mathbf{w}_h)_\Sigma \end{aligned} \quad (3.58)$$

for $n \geq r$. Note that term $a^s(\boldsymbol{\xi}_\pi^n, \mathbf{w}_h)$ vanishes due to the definition of the solid velocity projection operator (3.33).

Owing to (3.54), (3.56), (3.57) and (3.58), we have that the the discrete errors $(\boldsymbol{\theta}_h^n, \tilde{\boldsymbol{\theta}}_h^n, y_h^n, \boldsymbol{\xi}_h^n, \dot{\boldsymbol{\xi}}_h^n)$ satisfy a time-stepping scheme similar to Algorithm 3.3, but with a modified right-hand side and pressure increment (i.e., we have $y_h^n - \psi_h^{n-1}$ instead of $p_h^n - p_h^{n-1}$). Therefore, we can leverage the stability arguments of Theorem 3.4.1 to derive an a priori error estimate. We proceed by testing (3.54), (3.56), (3.57) and (3.58) with

$$(\tilde{\mathbf{v}}_h, \mathbf{v}_h, q_h, \mathbf{w}_h) = \tau(\tilde{\boldsymbol{\theta}}_h^n, \boldsymbol{\theta}_h^n, y_h^n, \dot{\boldsymbol{\xi}}_h^n).$$

By adding the resulting expressions, using the equivalent steps considered for (3.30) in Theorem 3.4.1, we obtain the following energy inequality for the discrete errors:

$$\begin{aligned} \frac{\rho^f}{2} \left(\|\boldsymbol{\theta}_h^n\|_{0,\Omega^f}^2 - \|\boldsymbol{\theta}_h^{n-1}\|_{0,\Omega^f}^2 \right) + \frac{\tau^2}{2\rho^f} \left(\|\nabla y_h^n\|_{0,\Omega_h^f}^2 - \|\nabla \psi_h^{n-1}\|_{0,\Omega_h^f}^2 \right) + \frac{\rho^s \varepsilon}{2} \left(\|\dot{\boldsymbol{\xi}}_h^n\|_{0,\Sigma}^2 - \|\dot{\boldsymbol{\xi}}_h^{n-1}\|_{0,\Sigma}^2 \right) \\ + \frac{1}{2} \left(\|\boldsymbol{\xi}_h^n\|_s^2 - \|\boldsymbol{\xi}_h^{n-1}\|_s^2 \right) + \left[\frac{\rho^s \varepsilon}{2} - \tau \left(\frac{r}{4} + r\alpha \right) \frac{\gamma\mu}{h} \right] \|\dot{\boldsymbol{\xi}}_h^n - \dot{\boldsymbol{\xi}}_h^{n-1}\|_{0,\Sigma}^2 \\ - \tau(r-1) \left(\frac{1}{2} + 2\alpha \right) \frac{\gamma\mu}{h} \|\dot{\boldsymbol{\xi}}_h^{n-1} - \dot{\boldsymbol{\xi}}_h^{n-2}\|_{0,\Sigma}^2 + \tau \|\tilde{\boldsymbol{\theta}}_h^n, y_h^n\|_S^2 \\ + 2\mu\tau \left(c_g - \frac{C_{\text{TI}}}{\gamma} \frac{3+4\alpha}{\alpha} \right) \|\boldsymbol{\epsilon}(\tilde{\boldsymbol{\theta}}_h^n)\|_{0,\Omega_h^f}^2 + \tau \frac{\alpha}{1+2\alpha} \frac{\gamma\mu}{h} \|\tilde{\boldsymbol{\theta}}_h^n - \dot{\boldsymbol{\xi}}_h^n\|_{0,\Sigma}^2 \leq \mathcal{G}_h^{*,r} \end{aligned} \quad (3.59)$$

for $n \geq r$, and with the right-hand side $\mathcal{G}_h^{*,r}$ defined by

$$\begin{aligned}
\mathcal{G}_h^{*,r} \stackrel{\text{def}}{=} & \underbrace{\tau \rho^f (-\partial_t \mathbf{u}^n + \partial_\tau \mathbf{u}^n - \partial_\tau \boldsymbol{\theta}_\pi^n, \tilde{\boldsymbol{\theta}}_h^n)}_{\stackrel{\text{def}}{=} T_1} + \underbrace{\tau (y_\pi^n, \operatorname{div} \tilde{\boldsymbol{\theta}}_h^n)}_{\stackrel{\text{def}}{=} T_2} \underbrace{- 2\tau \mu (\boldsymbol{\epsilon}(\boldsymbol{\theta}_\pi^n), \boldsymbol{\epsilon}(\tilde{\boldsymbol{\theta}}_h^n))}_{\stackrel{\text{def}}{=} T_3} \\
& + \underbrace{\tau (\boldsymbol{\theta}_\pi^n - \dot{\boldsymbol{\chi}}_\pi^{*,r}, \boldsymbol{\sigma}(\tilde{\boldsymbol{\theta}}_h^n, 0) \mathbf{n})}_\Sigma}_{\stackrel{\text{def}}{=} T_4} \underbrace{- \tau \frac{\gamma \mu}{h} (\boldsymbol{\theta}_\pi^n - \dot{\boldsymbol{\chi}}_\pi^{*,r}, \tilde{\boldsymbol{\theta}}_h^n - \dot{\boldsymbol{\xi}}_h^n)}_\Sigma}_{\stackrel{\text{def}}{=} T_5} \underbrace{+ \tau (\boldsymbol{\sigma}(\boldsymbol{\theta}_\pi^n, y_\pi^n) \mathbf{n}, \tilde{\boldsymbol{\theta}}_h^n - \dot{\boldsymbol{\xi}}_h^n)}_\Sigma}_{\stackrel{\text{def}}{=} T_6} \\
& - \underbrace{\tau (\operatorname{div} \boldsymbol{\theta}_\pi^n, y_h^n)}_{\Omega^f} + \underbrace{\tau (\boldsymbol{\theta}_\pi^n - \dot{\boldsymbol{\xi}}_\pi^n, y_h^n \mathbf{n})}_\Sigma + \underbrace{\tau S_h ((i_{sz} E_2 \mathbf{u}^n, i_{sz} E_1 p^n), (\tilde{\boldsymbol{\theta}}_h^n, y_h^n))}_{\stackrel{\text{def}}{=} T_8} \\
& \underbrace{\tau \rho^s \varepsilon (\partial_\tau \dot{\mathbf{d}}^n - \partial_t \dot{\mathbf{d}}(t_n) - \partial_\tau \dot{\boldsymbol{\xi}}_\pi^n, \dot{\boldsymbol{\xi}}_h^n)}_\Sigma}_{\stackrel{\text{def}}{=} T_9} \underbrace{- \tau a^s (\boldsymbol{\xi}_h^n, z_h^n)}_{\stackrel{\text{def}}{=} T_{10}}
\end{aligned} \tag{3.60}$$

Considering condition (3.23), equation (3.59) can be written as:

$$\begin{aligned}
& \frac{\rho^f}{2} \left(\|\boldsymbol{\theta}_h^n\|_{0,\Omega^f}^2 - \|\boldsymbol{\theta}_h^{n-1}\|_{0,\Omega^f}^2 \right) + \frac{\tau^2}{2\rho^f} \left(\|\nabla y_h^n\|_{0,\Omega_h^f}^2 - \|\nabla y_h^{n-1}\|_{0,\Omega_h^f}^2 \right) + \frac{\rho^s \varepsilon}{2} \left(\|\dot{\boldsymbol{\xi}}_h^n\|_{0,\Sigma}^2 - \|\dot{\boldsymbol{\xi}}_h^{n-1}\|_{0,\Sigma}^2 \right) \\
& + \frac{1}{2} \left(\|\boldsymbol{\xi}_h^n\|_s^2 - \|\boldsymbol{\xi}_h^{n-1}\|_s^2 \right) + \left[\frac{\rho^s \varepsilon}{2} - \tau \left(\frac{r}{4} + r\alpha \right) \frac{\gamma \mu}{h} \right] \|\dot{\boldsymbol{\xi}}_h^n - \dot{\boldsymbol{\xi}}_h^{n-1}\|_{0,\Sigma}^2 \\
& - \tau(r-1) \left(\frac{1}{2} + 2\alpha \right) \frac{\gamma \mu}{h} \|\dot{\boldsymbol{\xi}}_h^{n-1} - \dot{\boldsymbol{\xi}}_h^{n-2}\|_{0,\Sigma}^2 \\
& + \tau \|\tilde{\boldsymbol{\theta}}_h^n, y_h^n\|_S^2 + \mu c_g \tau \|\boldsymbol{\epsilon}(\tilde{\boldsymbol{\theta}}_h^n)\|_{0,\Omega_h^f}^2 + \tau \frac{\alpha}{1+2\alpha} \frac{\gamma \mu}{h} \|\tilde{\boldsymbol{\theta}}_h^n - \dot{\boldsymbol{\xi}}_h^n\|_{0,\Sigma}^2 \leq \mathcal{G}_h^{*,r}.
\end{aligned}$$

The lack of telescoping sum on the pressure terms $\|\nabla y_h^n\|_{0,\Omega_h^f}^2 - \|\nabla y_h^{n-1}\|_{0,\Omega_h^f}^2$ is not an issue (see, e.g., [Burman et al. \(2017\)](#)). Indeed, using (3.38) we have

$$\begin{aligned}
\|\nabla y_h^{n-1}\|_{0,\Omega_h^f}^2 &= \|\nabla y_h^{n-1} + \tau \nabla \partial_\tau i_{sz} E_1 p^n\|_{0,\Omega_h^f}^2 \\
&\leq \left(1 + \frac{\tau}{T}\right) \|\nabla y_h^{n-1}\|_{0,\Omega_h^f}^2 + \left(1 + \frac{T}{\tau}\right) \tau^2 \|\nabla \partial_\tau i_{sz} E_1 p^n\|_{0,\Omega_h^f}^2 \\
&\lesssim \left(1 + \frac{\tau}{T}\right) \|\nabla y_h^{n-1}\|_{0,\Omega_h^f}^2 + (\tau + T) \|\partial_t p\|_{L^2(t_{n-1}, t_n; H^1(\Omega^f))}^2,
\end{aligned}$$

so that by inserting this expression into (3.59), we have

$$\begin{aligned}
& \frac{\rho^f}{2} \left(\|\boldsymbol{\theta}_h^n\|_{0,\Omega^f}^2 - \|\boldsymbol{\theta}_h^{n-1}\|_{0,\Omega^f}^2 \right) + \frac{\tau^2}{2\rho^f} \left(\|\nabla y_h^n\|_{0,\Omega_h^f}^2 - \|\nabla y_h^{n-1}\|_{0,\Omega_h^f}^2 \right) + \frac{\rho^s \varepsilon}{2} \left(\|\dot{\boldsymbol{\xi}}_h^n\|_{0,\Sigma}^2 - \|\dot{\boldsymbol{\xi}}_h^{n-1}\|_{0,\Sigma}^2 \right) \\
& + \frac{1}{2} \left(\|\boldsymbol{\xi}_h^n\|_s^2 - \|\boldsymbol{\xi}_h^{n-1}\|_s^2 \right) + \left[\frac{\rho^s \varepsilon}{2} - \tau \left(\frac{r}{4} + r\alpha \right) \frac{\gamma \mu}{h} \right] \|\dot{\boldsymbol{\xi}}_h^n - \dot{\boldsymbol{\xi}}_h^{n-1}\|_{0,\Sigma}^2 \\
& - \tau(r-1) \left(\frac{1}{2} + 2\alpha \right) \frac{\gamma \mu}{h} \|\dot{\boldsymbol{\xi}}_h^{n-1} - \dot{\boldsymbol{\xi}}_h^{n-2}\|_{0,\Sigma}^2 + \tau \|\tilde{\boldsymbol{\theta}}_h^n, y_h^n\|_S^2 + \mu c_g \tau \|\boldsymbol{\epsilon}(\tilde{\boldsymbol{\theta}}_h^n)\|_{0,\Omega_h^f}^2
\end{aligned}$$

$$+\tau \frac{\alpha}{1+2\alpha} \frac{\gamma\mu}{h} \|\tilde{\boldsymbol{\theta}}_h^n - \dot{\boldsymbol{\xi}}_h^n\|_{0,\Sigma}^2 \lesssim \mathcal{G}_h^{*,r} + \frac{\tau^3}{2\rho^f T} \|\nabla y_h^{n-1}\|_{0,\Omega_h^f}^2 + (\tau + T) \frac{\tau^2}{2\rho^f} \|\partial_t p\|_{L^2(t_{n-1}, t_n; H^1(\Omega^f))}^2$$

for $n \geq r$. We now replace the upper index n by m and sum over $m = r \dots n$, this yields

$$\begin{aligned} & \frac{\rho^f}{2} \|\boldsymbol{\theta}_h^n\|_{0,\Omega^f}^2 + \frac{\tau^2}{2\rho^f} \|\nabla y_h^n\|_{0,\Omega_h^f}^2 + \frac{\rho^s \varepsilon}{2} \|\dot{\boldsymbol{\xi}}_h^n\|_{0,\Sigma}^2 + \frac{1}{2} \|\boldsymbol{\xi}_h^n\|_s^2 + \mu c_g \sum_{m=r}^n \tau \|\boldsymbol{\epsilon}(\tilde{\boldsymbol{\theta}}_h^m)\|_{0,\Omega_h^f}^2 \\ & \quad + \frac{\alpha}{1+2\alpha} \frac{\gamma\mu}{h} \sum_{m=r}^n \tau \|\tilde{\boldsymbol{\theta}}_h^m - \dot{\boldsymbol{\xi}}_h^m\|_{0,\Sigma}^2 + \sum_{m=r}^n \tau \|\tilde{\boldsymbol{\theta}}_h^m, y_h^m\|_S^2 \\ & + \left[\frac{\rho^s \varepsilon}{2} - \tau 4^r \left(\frac{1}{4} + \alpha \right) \frac{\gamma\mu}{h} \right] \sum_{m=r}^n \|\dot{\boldsymbol{\xi}}_h^m - \dot{\boldsymbol{\xi}}_h^{m-1}\|_{0,\Sigma}^2 - \tau(r-1) \left(\frac{1}{2} + 2\alpha \right) \frac{\gamma\mu}{h} \|\dot{\boldsymbol{\xi}}_h^{r-1} - \dot{\boldsymbol{\xi}}_h^{r-2}\|_{0,\Sigma}^2 \\ & \lesssim \frac{\tau^2}{2\rho^f T} \sum_{m=r-1}^{n-1} \tau \|\nabla y_h^m\|_{0,\Omega_h^f}^2 + \frac{\rho^f}{2} \|\boldsymbol{\theta}_h^{r-1}\|_{0,\Omega^f}^2 + \frac{\tau^2}{2\rho^f} \|\nabla y_h^{r-1}\|_{0,\Omega_h^f}^2 \\ & \quad + \frac{\rho^s \varepsilon}{2} \|\dot{\boldsymbol{\xi}}_h^{r-1}\|_{0,\Sigma}^2 + \frac{1}{2} \|\boldsymbol{\xi}_h^{r-1}\|_s^2 + \sum_{m=r}^n \mathcal{G}_h^{m,r} + (\tau + T) \frac{\tau^2}{2\rho^f} \|\partial_t p\|_{L^2(t_{r-1}, T; H^1(\Omega^f))}^2 \quad (3.61) \end{aligned}$$

for $n \geq r$.

We proceed by estimating $\mathcal{G}_h^{*,r}$, by treating each term in (3.60) separately. The first term can be bound in a standard fashion using a Taylor expansion, (3.37), the Cauchy–Schwarz and the Poincaré’s inequalities with constant C_P . This yields

$$\begin{aligned} T_1 & \leq \rho^f \tau (\|\partial_t \mathbf{u}^n - \partial_\tau \mathbf{u}^n\|_{0,\Omega^f} + \|\partial_\tau \boldsymbol{\theta}_\pi^n\|_{0,\Omega^f}) \|\tilde{\boldsymbol{\theta}}_h^n\|_{0,\Omega^f} \\ & \leq \rho^f \tau (\tau^{\frac{1}{2}} \|\partial_{tt} \mathbf{u}^n\|_{L^2(t_{n-1}, t_n; L^2(\Omega^f))} + \tau^{-\frac{1}{2}} \|\partial_t \boldsymbol{\theta}_\pi\|_{L^2(t_{n-1}, t_n; L^2(\Omega^f))}) \|\tilde{\boldsymbol{\theta}}_h^n\|_{0,\Omega^f} \\ & \leq \frac{(\rho^f C_P)^2}{2\varepsilon_1 \mu} (\tau^2 \|\partial_{tt} \mathbf{u}\|_{L^2(t_{n-1}, t_n; L^2(\Omega^f))}^2 + \|\partial_t \boldsymbol{\theta}_\pi\|_{L^2(t_{n-1}, t_n; L^2(\Omega^f))}^2) + \varepsilon_1 \tau \mu \|\nabla \tilde{\boldsymbol{\theta}}_h^n\|_{0,\Omega_h^f}^2 \\ & \lesssim \frac{(\rho^f C_P)^2}{2\varepsilon_1 \mu} \tau^2 \|\partial_{tt} \mathbf{u}\|_{L^2(t_{n-1}, t_n; L^2(\Omega^f))}^2 + \frac{(\rho^f C_P)^2}{2\varepsilon_1 \mu} h^2 \|\partial_t \mathbf{u}\|_{L^2(t_{n-1}, t_n; H^2(\Omega^f))}^2 \\ & \quad + \varepsilon_1 \tau \mu \|\nabla \tilde{\boldsymbol{\theta}}_h^n\|_{0,\Omega_h^f}^2 \quad (3.62) \end{aligned}$$

with $\varepsilon_1 > 0$. Observe that the last term can be absorbed in the left-hand side of (3.61) with ε_1 small enough. For term T_9 we proceed in a similar fashion. Using (3.37), we get

$$\begin{aligned} T_9 & \leq \tau \rho^s \varepsilon (\|(\partial_t - \partial_\tau) \dot{\mathbf{d}}^n\|_{0,\Sigma} + \|\partial_\tau \dot{\boldsymbol{\xi}}_\pi^n\|_{0,\Sigma}) \|\dot{\boldsymbol{\xi}}_h^n\|_{0,\Sigma} \\ & \leq \rho^s \varepsilon \tau (\tau^{\frac{1}{2}} \|\partial_{tt} \mathbf{u}\|_{L^2(t_{n-1}, t_n; L^2(\Sigma))} + \tau^{-\frac{1}{2}} \|\partial_t \dot{\boldsymbol{\xi}}_\pi^n\|_{L^2(t_{n-1}, t_n; L^2(\Sigma))}) \|\dot{\boldsymbol{\xi}}_h^n\|_{0,\Sigma} \\ & \leq \frac{\rho^s \varepsilon T}{2\varepsilon_9} (\tau^2 \|\partial_{tt} \mathbf{u}\|_{L^2(t_{n-1}, t_n; L^2(\Sigma))}^2 + h^2 \|\partial_t \mathbf{u}\|_{L^2(t_{n-1}, t_n; H^2(\Sigma))}^2) + \tau \frac{\varepsilon_9 \rho^s \varepsilon}{2T} \|\dot{\boldsymbol{\xi}}_h^n\|_{0,\Sigma}^2, \quad (3.63) \end{aligned}$$

with $\varepsilon_9 > 0$ and where the last term can be controlled in (3.61) using a Grönwall argument (Lemma 3.4.2).

For term T_2 , using (3.37), we have

$$T_2 = \tau(y_\pi^n, \operatorname{div} \tilde{\boldsymbol{\theta}}_h^n)_{\Omega^f} \leq \tau h^2 \frac{1}{2\varepsilon_2 \mu} \|p^n\|_{1, \Omega^f}^2 + \tau \frac{\varepsilon_2}{2} \mu \|\nabla \tilde{\boldsymbol{\theta}}_h^n\|_{0, \Omega_h^f}^2. \quad (3.64)$$

The second term can be absorbed in the left-hand side of (3.61) for $\varepsilon_2 > 0$ small enough.

$$T_3 \lesssim \tau \frac{\mu}{\varepsilon_3} h^2 \|\mathbf{u}^n\|_{2, \Omega}^2 + \tau \varepsilon_3 \mu \|\nabla \tilde{\boldsymbol{\theta}}_h^n\|_{0, \Omega_h^f}^2. \quad (3.65)$$

The last term can be, once again, absorbed in the left-hand side of (3.61), for $\varepsilon_3 > 0$ sufficiently small.

Terms T_4 and T_5 involve the Nitsche splitting error, namely $\|\boldsymbol{\theta}_\pi^n - \dot{\boldsymbol{\chi}}_\pi^{*,r}\|_{\frac{1}{2}, h, \Sigma}$. Using (3.36), (3.37) and a Taylor expansion we have

$$\begin{aligned} \|\boldsymbol{\theta}_\pi^n - \dot{\boldsymbol{\chi}}_\pi^{*,r}\|_{\frac{1}{2}, h, \Sigma} &\leq \|\boldsymbol{\theta}_\pi^n - \dot{\boldsymbol{\xi}}_\pi^n\|_{\frac{1}{2}, h, \Sigma} + \|\mathbf{I}_h \dot{\mathbf{d}}^n - \mathbf{I}_h \dot{\mathbf{d}}^{*,r}\|_{\frac{1}{2}, h, \Sigma} \\ &\lesssim h \|\mathbf{u}^n\|_{2, \Omega^f} + h^{\frac{3}{2}} \left(\|\dot{\mathbf{d}}^n\|_{2, \Sigma} + \sum_{i=1}^r \|\dot{\mathbf{d}}^{n-r}\|_{2, \Sigma} \right) + \frac{\tau^{\frac{2r-1}{2}}}{h^{\frac{1}{2}}} \|\partial_t^r \dot{\mathbf{d}}\|_{L^2(t_{n-r}, t_n; L^2(\Sigma))}. \end{aligned} \quad (3.66)$$

To estimate T_4 , we follow the same idea of [Burman and Fernández \(2014a\)](#). Using the robust trace inequality (3.21) combined with (3.66), we get

$$\begin{aligned} T_4 &\leq \tau \frac{\mu}{\varepsilon_4} \|\boldsymbol{\theta}_\pi^n - \dot{\boldsymbol{\chi}}_\pi^{*,r}\|_{\frac{1}{2}, h, \Sigma}^2 + \tau \mu \varepsilon_4 \|\boldsymbol{\epsilon}(\tilde{\boldsymbol{\theta}}_h^n) \mathbf{n}\|_{-\frac{1}{2}, h, \Sigma}^2 \\ &\lesssim \tau \frac{\mu}{\varepsilon_4} h^2 \left(\|\mathbf{u}^n\|_{2, \Omega}^2 + \sum_{i=1}^r \|\dot{\mathbf{d}}^{n-r}\|_{2, \Sigma} \right) + \frac{\mu}{\varepsilon_4} \frac{\tau^{2r}}{h} \|\partial_t^r \dot{\mathbf{d}}\|_{L^2(t_{n-r}, t_n; L^2(\Sigma))}^2 + \tau \varepsilon_4 \mu \|\nabla \tilde{\boldsymbol{\theta}}_h^n\|_{0, \Omega_h^f}^2. \end{aligned} \quad (3.67)$$

Once more, the last term can be absorbed in the left-hand side of (3.61), for $\varepsilon_4 > 0$ sufficiently small. Similarly, for T_5 we have

$$\begin{aligned} T_5 &\leq \frac{\tau}{2\varepsilon_5} \gamma \mu \|\boldsymbol{\theta}_\pi^n - \dot{\boldsymbol{\chi}}_\pi^{*,r}\|_{\frac{1}{2}, h, \Sigma}^2 + \frac{\tau \varepsilon_5}{2} \gamma \mu \|\tilde{\boldsymbol{\theta}}_h^n - \dot{\boldsymbol{\xi}}_h^n\|_{\frac{1}{2}, h, \Sigma}^2 \\ &\lesssim \tau \frac{\gamma \mu}{\varepsilon_5} h^2 \left(\|\mathbf{u}^n\|_{2, \Omega}^2 + \sum_{i=1}^r \|\dot{\mathbf{d}}^{n-r}\|_{2, \Sigma} \right) + \frac{\gamma \mu}{\varepsilon_6} \frac{\tau^{2r}}{h} \|\partial_t^r \dot{\mathbf{d}}\|_{L^2(t_{n-r}, t_n; L^2(\Sigma))}^2 \\ &\quad + \frac{\tau \varepsilon_5}{2} \gamma \mu \|\tilde{\boldsymbol{\theta}}_h^n - \dot{\boldsymbol{\xi}}_h^n\|_{\frac{1}{2}, h, \Sigma}^2. \end{aligned} \quad (3.68)$$

Note that the last term can be included in the left-hand side of (3.61) for $\varepsilon_5 > 0$ small enough.

Term T_6 can be handled using (3.37) as follows:

$$\begin{aligned} T_6 &\leq \tau \frac{1}{2\varepsilon_6} \frac{1}{\gamma \mu} \|\boldsymbol{\sigma}(\boldsymbol{\theta}_\pi^n, y_\pi^n) \mathbf{n}\|_{-\frac{1}{2}, h, \Sigma}^2 + \tau \frac{\varepsilon_6}{2} \gamma \mu \|\tilde{\boldsymbol{\theta}}_h^n - \dot{\boldsymbol{\xi}}_h^n\|_{\frac{1}{2}, h, \Sigma}^2 \\ &\leq \tau h^2 \frac{1}{2\varepsilon_6 \gamma \mu} (\|\mathbf{u}^n\|_{2, \Omega^f}^2 + \|p^n\|_{1, \Omega^f}^2) + \tau \frac{\varepsilon_6}{2} \gamma \mu \|\tilde{\boldsymbol{\theta}}_h^n - \dot{\boldsymbol{\xi}}_h^n\|_{\frac{1}{2}, h, \Sigma}^2. \end{aligned} \quad (3.69)$$

Again, the last term can be absorbed in the left-hand side of (3.61), for $\varepsilon_6 > 0$ small enough.

Integrating by parts in T_7 , we have

$$T_7 = \underbrace{\tau(\boldsymbol{\theta}_\pi^n, \nabla \mathbf{y}_h^n)_{\Omega^f}}_{\stackrel{\text{def}}{=} T_{7,1}} + \underbrace{\tau(\dot{\boldsymbol{\xi}}_\pi^n, \tau \mathbf{y}_h^n \mathbf{n})_\Sigma}_{\stackrel{\text{def}}{=} T_{7,2}}. \quad (3.70)$$

Term $T_{7,1}$ can be easily handled by using (3.37) as follows:

$$T_{7,1} \leq \tau \frac{1}{2\varepsilon_7} \|\boldsymbol{\theta}_\pi^n\|_{0,\Omega^f}^2 + \tau \frac{\varepsilon_7}{2} \|\nabla \mathbf{y}_h^n\|_{0,\Omega^f}^2 \lesssim \tau h^2 \frac{\mu}{2\varepsilon_7} \|\mathbf{u}^n\|_{0,\Omega^f}^2 + \tau \frac{\varepsilon_7}{2} |(0, \mathbf{y}_h^n)|_S^2. \quad (3.71)$$

The second term can be absorbed in the left-hand side of (3.61), for $\varepsilon_7 > 0$ sufficiently small. For the second term of (3.70), we proceed as in [Burman and Fernández \(2014a\)](#) (see also [Fernández and Landajuela \(2019\)](#)). We denote by $\bar{y}_i^n \in \mathbb{R}$ the average of y_h^n over the interface patch P_i . Combining the trace inequality (3.19) with the orthogonality property (3.35) of the interpolation operator \mathbf{I}_h and the standard estimate

$$\|y_h^n - \bar{y}_i^n\|_{0,P_i} \lesssim h \|\nabla y_h^n\|_{0,P_i},$$

term $T_{7,2}$ can be estimated as follow:

$$\begin{aligned} T_{7,2} &= -\tau \sum_i (y_h^n - \bar{y}_i^n, \dot{\boldsymbol{\xi}}_\pi^n \cdot \mathbf{n})_{P_i} \lesssim \tau \sum_i h \|\nabla y_h^n\|_{0,P_i} \|\dot{\boldsymbol{\xi}}_\pi^n\|_{0,P_i} \\ &\lesssim \tau h^3 \frac{\mu}{2\varepsilon_7} \|\dot{\mathbf{d}}^n\|_{2,\Sigma}^2 + \tau h^2 \frac{\varepsilon_7}{2\mu} \|\nabla \mathbf{y}_h^n\|_{0,\Omega_h}^2 \lesssim \tau h^3 \frac{\mu}{2\varepsilon_7} \|\dot{\mathbf{d}}^n\|_{2,\Sigma}^2 + \tau \frac{\varepsilon_7}{2} |(0, \mathbf{y}_h^n)|_S^2. \end{aligned} \quad (3.72)$$

It should be noted here we have assumed that the solid mesh step has an asymptotic regime similar to the fluid mesh step, namely, $h^s = \mathcal{O}(h^f)$. As for $T_{7,1}$, the last term in (3.72) can be, once again, absorbed in the left-hand side of (3.61), for $\varepsilon_7 > 0$ sufficiently small.

For term T_8 , using the weak consistency of the stabilization operators (3.39) and (3.40), we have

$$\begin{aligned} T_8 &\leq \tau \frac{1}{2\varepsilon_8} |(i_{sz} E_2 \mathbf{u}^n, i_{sz} E_1 p^n)|_S^2 + \tau \frac{\varepsilon_8}{2} |(\tilde{\boldsymbol{\theta}}_h^n, \mathbf{y}_h^n)|_S^2 \\ &\lesssim \tau h^2 \frac{1}{\varepsilon_8 \mu} \left(\mu \|\mathbf{u}^n\|_{2,\Omega^f}^2 + \mu^{-1} \|p^n\|_{1,\Omega^f}^2 \right) + \tau \frac{\varepsilon_8}{2} |(\tilde{\boldsymbol{\theta}}_h^n, \mathbf{y}_h^n)|_S^2. \end{aligned} \quad (3.73)$$

Again, the last term can be absorbed in the left-hand side of (3.61), for $\varepsilon_8 > 0$ small enough.

Term T_{10} can be bounded using the continuity estimate for the elastic bilinear form

(3.5), (3.33), (3.37) and a triangular inequality. This yields

$$\begin{aligned}
T_{10} &= -\tau a^s \left(\boldsymbol{\xi}_h^n, \mathbf{I}_h \dot{\mathbf{d}}^n - \partial_\tau \pi_h^s \mathbf{d}^n \right) \\
&= -\tau a^s \left(\boldsymbol{\xi}_h^n, \mathbf{I}_h \dot{\mathbf{d}}_s^n - \partial_\tau \mathbf{d}^n \right) \\
&\leq \tau \|\boldsymbol{\xi}_h^n\|_s \|\mathbf{I}_h \dot{\mathbf{d}}^n - \partial_\tau \mathbf{d}^n\|_s \\
&\leq \tau \|\boldsymbol{\xi}_h^n\|_s \left(\|\mathbf{I}_h \dot{\mathbf{d}}^n - \dot{\mathbf{d}}^n\|_s + \|\dot{\mathbf{d}}^n - \partial_\tau \mathbf{d}^n\|_s \right) \\
&\leq \frac{\tau \varepsilon_{11}}{2T} \|\boldsymbol{\xi}_h^n\|_s^2 + \tau \frac{h^2 \beta^s T}{2\varepsilon_{10}} \|\mathbf{u}^n\|_{2,\Sigma}^2 + \tau^2 \frac{\beta^s T}{2\varepsilon_{10}} \|\partial_t \mathbf{u}\|_{L^2(t_{n-1}, t_n; H^1(\Sigma))}^2.
\end{aligned} \tag{3.74}$$

Note that the first term can be controlled via Lemma 3.4.2 in (3.61).

In summary, the term $\sum_{m=r}^n \mathcal{G}_h^{m,r}$ in the right-hand side of (3.61) can be estimated by collecting the estimates (3.62)-(3.74) and by inserting them into (3.60), for $n \geq r$. The desired estimate (3.42) hence follows from (3.61) together with the stability condition (3.24) and Lemma 3.4.2 with

$$a_m = \frac{\rho^f}{2} \|\boldsymbol{\theta}_h^m\|_{0,\Omega^f}^2 + \frac{\tau^2}{2\rho^f} \|\nabla y_h^m\|_{0,\Omega_h^f}^2 + \frac{\rho^s \varepsilon}{2} \|\dot{\boldsymbol{\xi}}_h^m\|_{0,\Sigma}^2 + \frac{1}{2} \|\boldsymbol{\xi}_h^m\|_s^2, \quad \eta_m = \frac{1}{T} \tag{3.75}$$

and by noting that, owing to the initial data, we have

$$\boldsymbol{\theta}_h^{r-1} = \mathbf{0}, \quad \tilde{\boldsymbol{\theta}}_h^{r-1} = \mathbf{0}, \quad y_h^{r-1} = 0, \quad \boldsymbol{\xi}_h^{r-1} = \mathbf{0}, \quad \dot{\boldsymbol{\xi}}_h^{r-1} = \mathbf{0} \tag{3.76}$$

for $r = 1, 2$. This completes proof. \square

Corollary 3.4.3.1. *Assume that Algorithm 3.3 with $r = 2$ is initialized with one step of the method with $r = 1$. Then, under the assumptions of Theorem 3.4.3, for $n \geq 1$ and $n\tau < T$, the following discrete error estimate holds for the scheme with $r = 2$:*

$$\mathcal{Z}_h^n \lesssim c_1 h + c_2 \tau + c_3 \frac{\tau^2}{h^{\frac{1}{2}}} + c_4 \frac{\tau^{\frac{3}{2}}}{h^{\frac{1}{2}}}, \tag{3.77}$$

where $\{c_i\}_{i=1}^4$ denote positive constants independent of h and τ , but which depend on the physical parameters and on the regularity of the exact solution.

Proof. For $r = 2$, we have to bound the contributions from the initialization step in the right-hand side of (3.61), namely,

$$\frac{\rho^f}{2} \|\boldsymbol{\theta}_h^1\|_{0,\Omega^f}^2 + \frac{\tau^2}{2\rho^f} \|\nabla y_h^1\|_{0,\Omega_h^f}^2 + \frac{\rho^s \varepsilon}{2} \|\dot{\boldsymbol{\xi}}_h^1\|_{0,\Sigma}^2 + \frac{1}{2} \|\boldsymbol{\xi}_h^1\|_s^2. \tag{3.78}$$

To this purpose, we use the fact that the initialization of Algorithm 3.3 with $r = 2$ is provided by the first step of the scheme with $r = 1$. We can hence use the estimate provided by (3.61) with $r = 1$ and $n = 1$ to control (3.78). More precisely, using (3.76), this yields

$$\begin{aligned}
& \frac{\rho^f}{2} \|\boldsymbol{\theta}_h^1\|_{0,\Omega^f}^2 + \frac{\tau^2}{2\rho^f} \|\nabla y_h^1\|_{0,\Omega_h^f}^2 + \frac{\rho^s \varepsilon}{2} \|\dot{\boldsymbol{\xi}}_h^1\|_{0,\Sigma}^2 + \frac{1}{2} \|\boldsymbol{\xi}_h^1\|_s^2 + \mu c_g \tau \left\| \boldsymbol{\epsilon}(\tilde{\boldsymbol{\theta}}_h^1) \right\|_{0,\Omega_h^f}^2 \\
& + \frac{\alpha}{1+2\alpha} \frac{\gamma\mu}{h} \tau \|\tilde{\boldsymbol{\theta}}_h^1 - \dot{\boldsymbol{\xi}}_h^1\|_{0,\Sigma}^2 + \tau \|(\tilde{\boldsymbol{\theta}}_h^1, y_h^1)\|_S^2 + \left[\frac{\rho^s \varepsilon}{2} - \tau \left(\frac{1}{4} + \alpha \right) \frac{\gamma\mu}{h} \right] \|\dot{\boldsymbol{\xi}}_h^1 - \dot{\boldsymbol{\xi}}_h^0\|_{0,\Sigma}^2 \\
& \lesssim \mathcal{G}_h^{1,1} + \frac{\tau^3}{2\rho^f} \|\partial_t p\|_{L^2(0,\tau;H^1(\Omega^f))}^2.
\end{aligned}$$

Hence, by inserting this estimate in (3.61), we get

$$\begin{aligned}
& \frac{\rho^f}{2} \|\boldsymbol{\theta}_h^n\|_{0,\Omega^f}^2 + \frac{\tau^2}{2\rho^f} \|\nabla y_h^n\|_{0,\Omega_h^f}^2 + \frac{\rho^s \varepsilon}{2} \|\dot{\boldsymbol{\xi}}_h^n\|_{0,\Sigma}^2 + \frac{1}{2} \|\boldsymbol{\xi}_h^n\|_s^2 + \mu c_g \sum_{m=1}^n \tau \left\| \boldsymbol{\epsilon}(\tilde{\boldsymbol{\theta}}_h^m) \right\|_{0,\Omega_h^f}^2 \\
& + \frac{\alpha}{1+2\alpha} \frac{\gamma\mu}{h} \sum_{m=1}^n \tau \|\tilde{\boldsymbol{\theta}}_h^m - \dot{\boldsymbol{\xi}}_h^m\|_{0,\Sigma}^2 + \sum_{m=1}^n \tau \|(\tilde{\boldsymbol{\theta}}_h^m, y_h^m)\|_S^2 \\
& + \left[\frac{\rho^s \varepsilon}{2} - \tau (1+4\alpha) \frac{\gamma\mu}{h} \right] \sum_{m=1}^n \|\dot{\boldsymbol{\xi}}_h^m - \dot{\boldsymbol{\xi}}_h^{m-1}\|_{0,\Sigma}^2 \\
& \lesssim \frac{\tau^2}{2\rho^f T} \sum_{m=1}^{n-1} \tau \|\nabla y_h^m\|_{0,\Omega_h^f}^2 + \mathcal{G}_h^{1,1} + \sum_{m=2}^n \mathcal{G}_h^{m,2} + (\tau + T) \frac{\tau^2}{2\rho^f} \|\partial_t p\|_{L^2(0,T;H^1(\Omega^f))}^2 \quad (3.79)
\end{aligned}$$

for $n \geq 1$. Owing to the initialization procedure, the bounds provided in (3.67)-(3.68) for terms T_4 and T_5 of $\mathcal{G}_h^{1,1}$ yield a $\mathcal{O}(\tau^3/h)$ splitting error, by noting that

$$\gamma\mu \frac{\tau^2}{h} \|\partial_t \dot{\boldsymbol{d}}\|_{L^2(0,\tau;L^2(\Sigma))}^2 \leq \gamma\mu \frac{\tau^3}{h} \|\partial_t \dot{\boldsymbol{d}}\|_{L^\infty(0,\tau;L^2(\Sigma))}^2. \quad (3.80)$$

The estimate (3.42) for $r = 2$ hence follows from (3.79) together with the stability condition (3.24) and Lemma 3.4.2 with (3.75). This completes proof. \square

We conclude this section with a series of remarks.

Remark 3.4.2. For $r = 2$, the last term in (3.42) comes from the bound of the first step of Algorithm 3.3 with $r = 1$, that is, the estimate given by (3.80). This bound is quasi-optimal in time because the Taylor expansions are evaluated in $L^2(0,T)$ instead of $L^1(0,T)$. Alternatively, one could avoid this term by initializing Algorithm 3.3 with the first-step of Algorithm 3.1.

Remark 3.4.3. Note that Algorithm 3.2 introduces the following perturbations terms in the discrete error equation

$$\frac{\gamma\mu}{h} (\mathbf{u}_h^n - \mathbf{u}_h^{n-1}, \mathbf{w}_h)_{0,\Sigma} + (\boldsymbol{\sigma}(\mathbf{u}_h^n, p_h^n) \mathbf{n} - \boldsymbol{\sigma}(\mathbf{u}_h^{n-1}, p_h^{n-1}) \mathbf{n}, \mathbf{v}_h - \mathbf{w}_h)_{0,\Sigma},$$

with $\mathbf{w}_h = \tau \dot{\boldsymbol{\xi}}_h^n$. The first term leads to the following bound:

$$\tau \frac{\gamma\mu}{h} (\mathbf{u}^n - \mathbf{u}^{n-1}, \dot{\boldsymbol{\xi}}_h^n)_{0,\Sigma} \leq \frac{(\gamma\mu)^2}{2} \frac{\tau^2}{h^2} \|\partial_t \mathbf{u}\|_{L^2(t_{n-1}, t_n; L^2(\Sigma))}^2 + \frac{\tau}{2} \|\dot{\boldsymbol{\xi}}_h^n\|_{0,\Sigma}^2.$$

The second term can be controlled via Lemma 3.4.2 while the first yields the above mentioned $\mathcal{O}(\tau/h)$ sub-optimal splitting error.

Remark 3.4.4. As shown in Theorem 3.4.3, the discrete error estimates of Algorithm 3.3 contains terms of order $\mathcal{O}(\tau^r/h^{1/2})$, which are not visible numerically (see Section 3.5). To fully understand the impact of selecting the same penalty term in the viscous step as in the solid sub-step in Algorithm 3.3, we consider the coupling of a parabolic equation with and an hyperbolic one. The considered coupled problem reads as follow: find $u : \Omega^f \times \mathbb{R}^+ \rightarrow \mathbb{R}$, $d : \Sigma \times \mathbb{R}^+ \rightarrow \mathbb{R}$, $\dot{d} : \Sigma \times \mathbb{R}^+ \rightarrow \mathbb{R}$, such that for all $t \in \mathbb{R}^+$ we have

$$\begin{cases} \partial_t u - \Delta u = 0 & \text{in } \Omega^f \times \mathbb{R}^+, \\ u = 0 & \text{on } \Gamma \times \mathbb{R}^+, \end{cases} \quad \begin{cases} \partial_t \dot{d} - \Delta d = T & \text{in } \Sigma \times \mathbb{R}^+, \\ \dot{d} = \partial_t d & \text{in } \Sigma \times \mathbb{R}^+, \\ d = 0 & \text{on } \partial\Sigma \times \mathbb{R}^+, \end{cases}$$

$$\begin{cases} u = \dot{d} & \text{on } \Sigma \times \mathbb{R}^+, \\ T = -\frac{\partial u}{\partial n} & \text{on } \Sigma \times \mathbb{R}^+, \end{cases}$$

with the respective initial conditions. We propose to discretize the problem via a loosely coupled scheme, inspired by the semi-implicit scheme of Algorithm 3.3. The fully discrete approximation results in the following (explicit) scheme:

For $n \geq 1$:

- Parabolic step: find $u_h^n \in V_h$, such that

$$(\partial_\tau u_h^n, v_h)_{\Omega^f} + (\nabla u_h^n, \nabla v_h)_{\Omega^f} + \frac{\gamma}{h} (u_h^n - \dot{d}_h^{n-1}, v_h)_\Sigma - \left(\frac{\partial u_h^n}{\partial n}, v_h \right)_\Sigma = 0$$

for all $v_h \in V_h$.

- Hyperbolic step: find $(d_h^n, \dot{d}_h^n) \in W_h \times W_h$ with $\dot{d}_h^n = \partial_\tau d_h^n$ and such that

$$(\partial_\tau \dot{d}_h^n, w_h)_\Sigma + (\nabla d_h^n, \nabla w_h)_\Sigma - \frac{\gamma}{h} (u_h^n - \dot{d}_h^{n-1}, w_h)_\Sigma + \left(\frac{\partial u_h^n}{\partial n}, w_h \right)_\Sigma = 0$$

for all $w_h \in W_h$.

When considering loosely coupled schemes with Nitsche's coupling, the sub-optimal terms come typically from the fact that we introduce a time-splitting error inside the Nitsche's penalty term, which is scaled with an h^{-1} . A possible way to overcome this issue, is to remove the time-splitting error from the Nitsche's penalty term, by introducing an error in time within the definition of the projection errors. Thus, considering the following

decomposition of the errors for the parabolic-hyperbolic explicit scheme:

$$\begin{aligned}
E_2 u^n - u_h^n &= \underbrace{E_2 u^n - i_{sz} E_2 u^n}_{\stackrel{\text{def}}{=} \theta_\pi^n} + \underbrace{i_{sz} E_2 u^n - u_h^n}_{\stackrel{\text{def}}{=} \theta_h^n} \quad \text{in } \Omega_h^f, \\
d^n - d_h^n &= \underbrace{d^n - \pi_h d^n}_{\stackrel{\text{def}}{=} \xi_\pi^n} + \underbrace{\pi_h d^n - d_h^n}_{\stackrel{\text{def}}{=} \xi_h^n} \quad \text{in } \Sigma, \\
\dot{d}^n - \dot{d}_h^n &= \underbrace{\dot{d}^n - \pi_h \dot{d}^n}_{\stackrel{\text{def}}{=} \dot{\xi}_\pi^n} + \underbrace{\pi_h \dot{d}^n - \pi_h \dot{d}^{n+1}}_{\stackrel{\text{def}}{=} \dot{\xi}_\tau^n} + \underbrace{\pi_h \dot{d}^{n+1} - \dot{d}_h^n}_{\stackrel{\text{def}}{=} \dot{\xi}_h^n} \quad \text{in } \Sigma,
\end{aligned} \tag{3.81}$$

it can be proven that the scheme delivers optimal space and time accuracy. More in detail, using similar arguments of the proof of Theorem 3.4.3, we will get the following terms inside the Nitsche's penalty part:

$$u^n - u_h^n - (\dot{d}^n - \dot{d}_h^{n-1}) = \theta_\pi^n + \theta_h^n - \underbrace{(\dot{d}^n - \pi_h \dot{d}^n)}_{\dot{\xi}_\pi^n} + \underbrace{(\pi_h \dot{d}^n - \dot{d}_h^{n-1})}_{\dot{\xi}_h^{n-1}},$$

which does not contain error in time, in fact the arising terms involving $\theta_h^n - \dot{\xi}_h^{n-1}$ are controlled via the stability result and terms involving $\theta_\pi^n - \dot{\xi}_\pi^n$ have optimal convergence order. The only terms which contain $\dot{\xi}_\tau^n$ are the corresponding T_9 and T_{10} terms of (3.60) and their optimality can be proved.

A similar strategy fails when considered for the semi-implicit scheme of Algorithm 3.3. In particular we will retrieve terms of order $\mathcal{O}(\tau/h^{1/2})$ when controlling the pressure term $T_{7,2}$ of (3.60).

3.5 Numerical experiments

In this section, we illustrate via numerical experiments the convergence properties of Algorithm 3.3 with $r = 1, 2$ (semi-implicit scheme) in an academic numerical example. The obtained results are compared with those of Algorithms 3.1 (strongly coupled scheme) and Algorithm 3.2 (stabilized explicit coupling scheme).

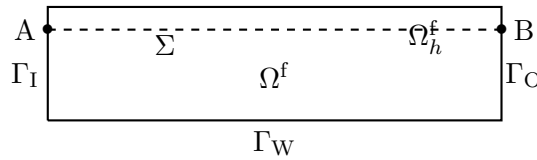


Figure 3.2: Geometric configuration.

The considered test case is the well-known fluid-structure interaction benchmark describing the propagation of a pressure wave within a straight two-dimensional elastic tube (see, e.g., Formaggia et al. (2001); Burman and Fernández (2009, 2014a)). In the following, all the units are given in the CGS system.

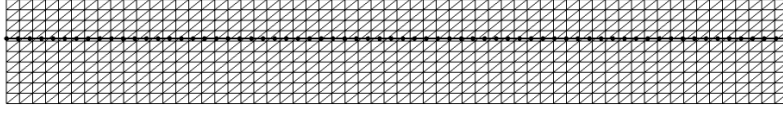
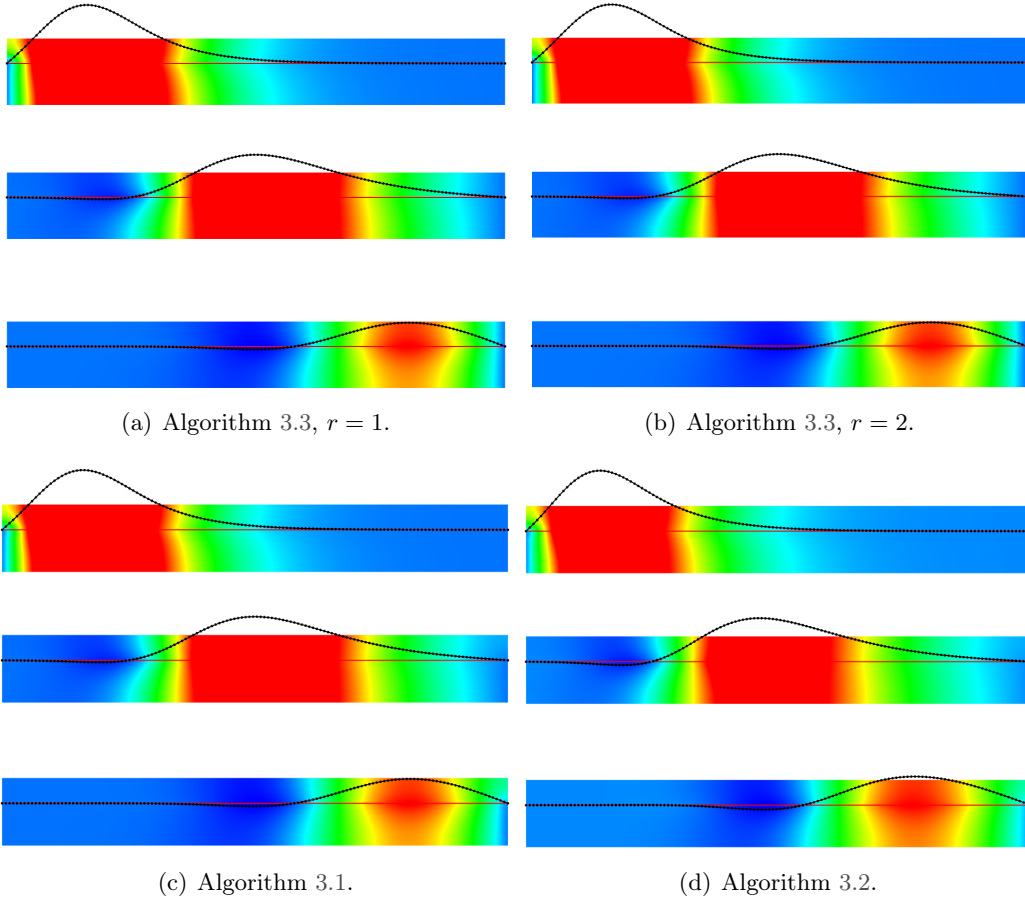
Figure 3.3: Fluid and solid meshes for $h = 0.1$.

Figure 3.4: Snapshots of the fluid pressure and deformation (magnified) at different time instants.

The fluid domain is defined as $\Omega^f = [0, L] \times [0, R]$, with $L = 6$ and $R = 0.5$, while the fluid computational domain is given by $\Omega_h^f = [0, 6] \times [0, 0.8]$. The solid domain is $\Sigma = [0, L] \times \{R\}$, as shown in Figure 3.2. In the sequel, the solid is described by a one-dimensional string model, viz.,

$$\mathbf{d} = \begin{pmatrix} 0 \\ \eta \end{pmatrix}, \quad \mathbf{Ld} = \begin{pmatrix} 0 \\ -\lambda_1 \partial_{xx} \eta + \lambda_0 \eta \end{pmatrix}, \quad \lambda_1 \stackrel{\text{def}}{=} \frac{E\varepsilon}{2(1+\nu)}, \quad \lambda_0 \stackrel{\text{def}}{=} \frac{E\varepsilon}{R^2(1-\nu^2)},$$

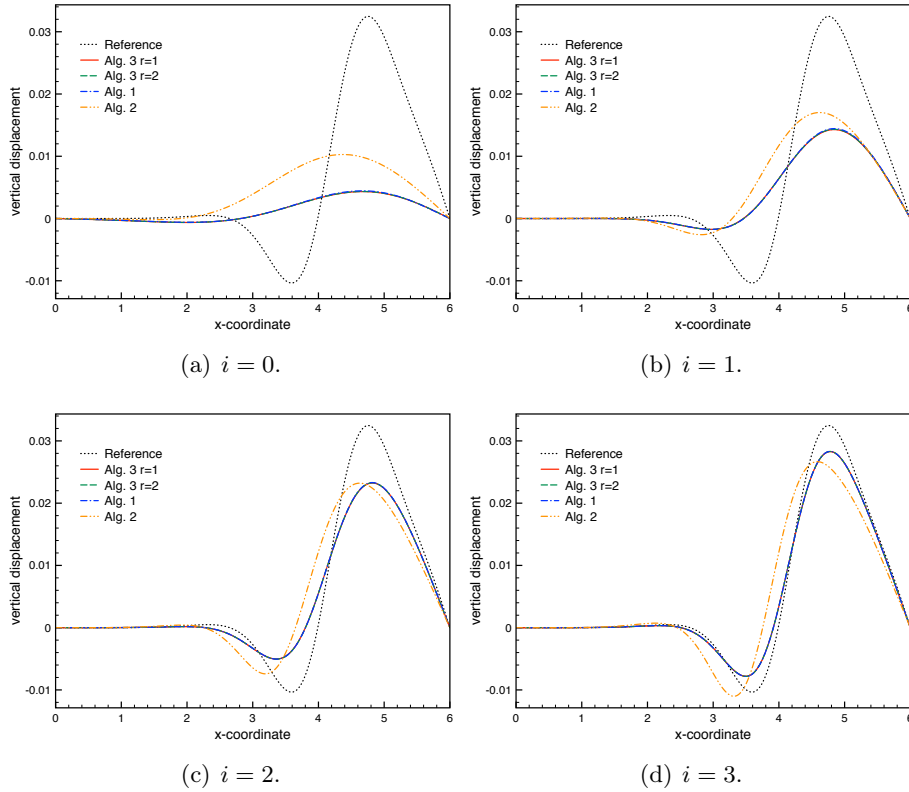


Figure 3.5: Comparison of the solid displacements at $t = 1.5 \times 10^{-2}$ for different levels of (τ, h) -refinement, given by (3.82) with $i = 0, \dots, 3$.

hence in (3.4), taking $\mathbf{w} = (0, w)^T$, we have

$$a^s(\mathbf{d}, \mathbf{w}) \stackrel{\text{def}}{=} \lambda_1(\partial_x \eta, \partial_x w)_\Sigma + \lambda_0(\eta, w)_\Sigma.$$

The fluid physical parameters are given by $\rho^f = 1.0, \mu = 0.035$. For the solid we have $\rho^s = 1.1$ and $\varepsilon = 0.1$, with Young's modulus $E = 0.75 \times 10^6$ and Poisson's ratio $\nu = 0.5$. Regarding the boundary conditions, we consider both fluid and structure to be initially at rest and we impose a sinusoidal normal traction of maximal amplitude 2×10^4 for 5×10^{-3} time instants at the inlet Γ_I . A symmetry condition is applied on the lower wall Γ_W and zero traction is enforced at Γ_O . All the computations have been performed with FreeFem++ Hecht (2012). An example of the unfitted meshes is shown in Figure 3.3 with fluid space discretization parameter $h = 0.1$. The Nitsche parameter is set to $\gamma = 10^3$ and for the pressure and ghost-penalty stabilization terms (3.7)-(3.8) we consider $\gamma_p = 10^{-3}$ and $\gamma_g = 1$, respectively.

As expected, all the considered methods deliver a numerical solution with a stable pressure-wave propagation. For illustration purposes, Figure 3.4 provides the snapshots of the fluid pressure and solid deformation at time $t = 5 \times 10^{-3}, 10^{-2}$ and 1.5×10^{-2} , obtained with $\tau = 10^{-4}$ and $h = 0.05$ using respectively Algorithms 3.1-3.3.

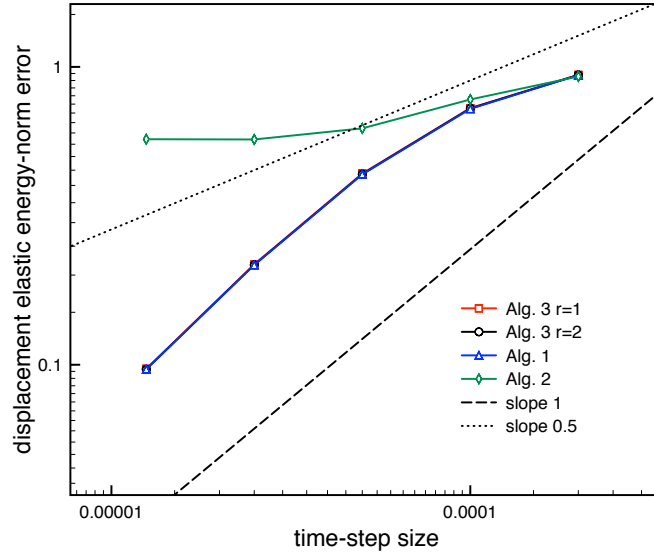


Figure 3.6: Convergence history of the solid displacements at $t = 1.5 \times 10^{-2}$ in the elastic-energy norm.

The solid displacement has been amplified by a factor 20. A very good agreement between Algorithm 3.1 and Algorithm 3.3 ($r = 1, 2$) is clearly visible, while a difference on the solid displacement is noticeable with Algorithm 3.2.

In order to quantify the accuracy properties of each coupling scheme we have evaluated the convergence histories by uniformly refining in space and in time

$$(h, \tau) \in \{0.1/2^i, 2 \times 10^{-4}/2^i\}_{i=0}^4. \quad (3.82)$$

Figure 3.5 shows the corresponding solid displacement at $t = 1.5 \times 10^{-2}$ for $i = 0, \dots, 3$ and the different coupling schemes. As in Figure 3.4, a very good fit is observed between Algorithm 3.1 and Algorithm 3.3 ($r = 1, 2$), while a degradation of accuracy is visible for Algorithm 3.2 under space-time refinement. The depicted reference solution has been generated using the strongly coupled fitted method with a high space-time grid resolution ($h = 3.125 \times 10^{-3}$ and $\tau = 10^{-6}$).

Figure 3.6 reports the convergence history of the solid displacement at time $t = 1.5 \times 10^{-2}$, in the relative elastic energy-norm. Note that by the choice of space and time discretization parameters we have $\tau = \mathcal{O}(h)$. The results show that Algorithm 3.3 with $r = 1, 2$ and Algorithm 3.1 retrieve the overall optimal first-order accuracy $\mathcal{O}(h)$ of Algorithm 3.1. As expected, Algorithm 3.2 shows a non-convergent behavior. This points out the sub-optimal $\mathcal{O}(\tau/h)$ splitting error (see Remark 3.4.3). Finally, it is worth noting that no effect from the $\mathcal{O}(\tau/h^{\frac{1}{2}})$ and $\mathcal{O}(\tau^2/h^{\frac{1}{2}})$ anticipated by Theorem 3.4.3 is visible on the convergence history of Algorithm 3.3.

3.6 Conclusion

In this chapter we have analyzed the unfitted mesh based semi-implicit coupling scheme introduced in Chapter 2 in the context of linear-fluid structure interaction with thin-walled solid. The investigated method combines a Nitsche based unfitted mesh spatial approximation with a fractional-step time-splitting in the fluid. The strong coupling is avoided by treating explicitly the fluid viscous part, while the added-mass free stability (see Theorem 2.2.1 and Theorem 3.4.1) is achieved by treating implicitly the fluid incompressibility and the solid inertia.

We have extended the stability analysis, previously carried out in Chapter 2, for first order extrapolation in the solid velocity, namely $r = 1$, to the case of second order extrapolation, $r = 2$. An additional CFL-like condition is obtained, which limits the choice of the time-step, subordinated to the space discretization and the Nitsche's penalty parameters. An *a priori* convergence analysis is derived in Section 3.4.2, for the two extrapolated variants, $r = 1, 2$. A superior accuracy is shown, namely $\mathcal{O}(\tau^r/h^{\frac{1}{2}})$, $r = 1, 2$, with respect to the stabilized explicit scheme of [Burman and Fernández \(2014a\)](#), which is $\mathcal{O}(\tau/h)$.

The numerical evidence of Section 3.5 indicates that the semi-implicit algorithm and the strongly coupled (from [Burman and Fernández \(2014a\)](#)) deliver the same accuracy behavior. Future extensions of this work could consider, for instance, curved and moving interfaces.

Part II

MODELING AND APPROXIMATION OF
FLUID-STRUCTURE-CONTACT
INTERACTION

An unfitted mesh fluid-structure-contact approximation with multiple thin-walled immersed solids

In this chapter we address some of the difficulties that arise in the treatment of contact within the Nitsche-XFEM framework. In order to guarantee consistency, further element duplication is introduced in the fluid elements where contact between the solid occurs. The proposed Nitsche-XFEM method for fluid-structure-contact interaction is then compared with alternative fitted (ALE based) and unfitted (fictitious domain) mesh methods. The advantages and limitations of all this approaches are discussed in an academic test case.

Contents

4.1	Introduction	91
4.2	Problem setting	92
4.2.1	Contact model	93
4.2.2	Fluid-structure-contact model	94
4.3	Numerical methods	95
4.3.1	Solid contact approximation via penalty	96
4.3.2	Unfitted mesh Nitsche-XFEM method	97
4.3.3	Fitted mesh ALE method	104
4.3.4	Unfitted mesh Fictitious Domain method	106
4.4	Numerical experiments	108
4.5	Conclusion	119

4.1 Introduction

In this chapter, we address the problem of fluid-structure interaction with contact between multiple thin-walled immersed structures, starting from the Nitsche-XFEM methodology proposed in [Alauzet et al. \(2016\)](#). Specific duplication and intersection procedures allow to extend the consistency of the method to the case of contact.

The immersed interfaces separate each intersected fluid element into two, or more (when multiple structures enter the same fluid element), physical regions. Here, we propose to enrich the discrete spaces as many times as needed, in order to well reproduce all the

physical regions belonging to each fluid element. This approach is a natural extension of the procedure proposed in [Alauzet et al. \(2016\)](#), even though, to our knowledge, no previous works combining contact, XFEM, fluid-structure interaction with multiple thin-walled structures and unfitted mesh are available.

In order to avoid penetration between the solids, we consider an unbiased contact formulation which does not distinguish between master and slave surfaces (see, e.g., [Mlika et al. \(2017\)](#); [Poulios and Renard \(2015\)](#)). Additionally, issues related to real contact (such as, changing in time of the FSI interface, creation of vacuum zones at solid release) are circumvented considering a relaxed contact formulation. The relaxed contact formulation suffers of mechanical inconsistencies at contact. This subject will be considered in Chapter 5. For discussion on dry contact mechanics, we refer to [Wriggers and Zavarise \(2004\)](#). Additionally, for contact treated via penalization we refer to [Chouly and Hild \(2012\)](#); [Kamensky et al. \(2015\)](#), via Augmented Lagrangian/Nitsche's approach to [Burman et al. \(2018, 2019\)](#). The latter approach can be seen as a consistent penalization method. We also refer to [Burman et al. \(2020a\)](#); [Mayer et al. \(2009, 2010\)](#); [Chouly et al. \(2017\)](#) for further examples of contact for FSI with Nitsche. In this chapter, we will compare the Nitsche-XFEM method with FD and ALE numerical methods.

The rest of the chapter is organized as follows. Section 4.2 recalls the geometrical setting for the models considered. In particular, we introduce in Section 4.2.1 the non-linear contact model and in Section 4.2.2 the fluid-structure-contact model. The numerical methods are presented in Section 4.3, in particular, Section 4.3.1 describes the penalty-based contact algorithm considered, the new Nitsche-XFEM method is introduced in Section 4.3.2, together with the new intersection and duplication procedures. Additionally, we exhibit in Section 4.3.3 the ALE fitted method and in Section 4.3.4 the FD/Lagrange multipliers method. In Section 4.4 we compare the previously introduced methods on an academic numerical example and, finally, a summary of the conclusion are given in Section 4.5.

4.2 Problem setting

In what follows, the fluid is modeled by the incompressible Navier-Stokes equations in the ALE or Eulerian formalisms. We refer to Section 1.2.1 for a description of these mathematical formalisms. For the solid, we consider a non-linear thin-walled solid model in Lagrangian form (details on Section 1.2.2). The considered geometric configurations are those presented in Section 2.3.1, except for the fact that we consider multiple moving thin-walled structures immersed within the fluid domain Ω^f . The current configuration of the solid $\Sigma(t)$ is hence made of $m \in \mathbb{N}$ connected components, $\Sigma(t) = \bigcup_{i=1, \dots, m} \Sigma_i(t)$. Similarly, for the reference configuration we have $\Sigma = \bigcup_{i=1, \dots, m} \Sigma_i$. The time-dependent fluid domain is $\Omega^f(t) = \Omega^f \setminus \Sigma(t)$. Additionally, the thin-walled structures are assumed to divide the fluid domain into $m + 1$ disconnected domains $\Omega_i^f(t)$, $i = 1, \dots, m + 1$. Without loss of generality, the model presented in this chapter will consider only two structures, but it can be derived for $m \in \mathbb{N}$ immersed structures. Hence, we have $\Sigma(t) = \Sigma_1(t) \cup \Sigma_2(t)$ and $\Omega^f(t) = \Omega_1^f(t) \cup \Omega_2^f(t) \cup \Omega_3^f(t)$. The considered geometry is shown in Figure 4.1. We

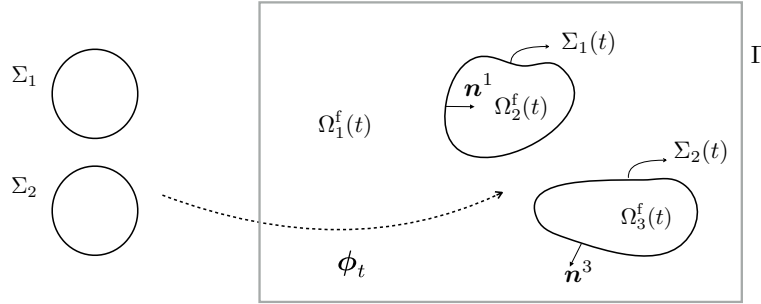


Figure 4.1: Geometric configuration of the fluid domain and the immersed solids.

now describe, separately, the considered contact and fluid-structure-contact interaction models.

4.2.1 Contact model

For simplicity, we assume that the thin-walled solid is made of two connected components $\Sigma = \Sigma_1 \cup \Sigma_2$. We have $\Sigma_i(t) = \phi_t(\Sigma)$. Each surface is oriented with a unit normal vector $\mathbf{n}_{\Sigma_i(t)}$ pointing outwards, with respect to the enclosed fluid domain (see Figure 4.1). Following [Mlika et al. \(2017\)](#), we consider an unbiased contact formulation which does not distinguish between master and slave surfaces. The formulation of the non-penetration conditions, in the deformed configuration, requires the introduction of a map which detects the potential contacts between opposed surfaces, namely, a vector-valued function

$$\boldsymbol{\pi} : \Sigma(t) \longrightarrow \mathbb{R}^d.$$

A standard method to define the map $\boldsymbol{\pi}$ is the closest-point projection algorithm, but this is known to yield complicated tangent expressions for the contact terms (see, e.g., [Poulios and Renard \(2015\)](#)). Here, we consider a simpler approach, the so-called ray-tracing method of [Poulios and Renard \(2015\)](#), which for each point $\mathbf{y} \in \Sigma_i(t) \subset \Sigma(t)$, the target $\boldsymbol{\pi}(\mathbf{y}) \in \Sigma_j(t)$ is defined as the closest intersection of a opposite surface $\Sigma_j(t) \subset \Sigma(t)$ with the line passing through point \mathbf{y} and having as direction $\mathbf{n}_{\Sigma_i(t)}$ (see Figure 4.2). Here $i, j \in \{1, 2\}$ are such that $i \neq j$, but self contact could also be considered. Note that the ray intersection might not exist. In that case, it suffices to simply define the target as a point along the positive part of the ray and sufficiently far away from a given bounding box. We can hence define the gap function $g : \Sigma \longrightarrow \mathbb{R}$ as

$$g(\mathbf{x}) \stackrel{\text{def}}{=} (\boldsymbol{\pi}(\phi_t(\mathbf{x})) - \phi_t(\mathbf{x})) \cdot \mathbf{n}_{\Sigma_i(t)}$$

for all $\mathbf{x} \in \Sigma_i \subset \Sigma$. Note that g depends non-linearly on ϕ_t and thus on \mathbf{d} , i.e., $g = g(\mathbf{d})$ with a little abuse of notation.

The solid equilibrium with the non penetration conditions is then given by the following

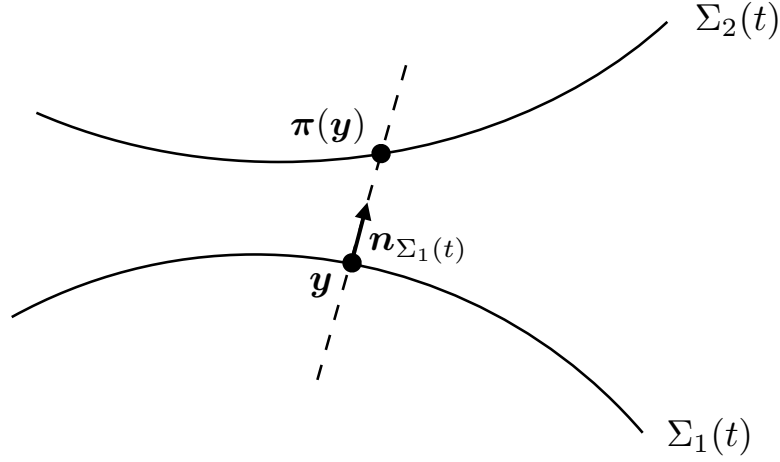


Figure 4.2: Definition of the map π using the ray-tracing approach.

system:

$$\begin{cases} \rho^s \varepsilon \partial_t \dot{\mathbf{d}} + \mathbf{L}(\mathbf{d}) - \lambda \mathbf{n}_{\Sigma(t)} = \mathbf{T} & \text{in } \Sigma, \\ g(\mathbf{d}) \geq 0, \quad \lambda \leq 0, \quad \lambda g(\mathbf{d}) = 0 & \text{in } \Sigma. \end{cases} \quad (4.1)$$

Note that, as in Chapter 5, the Lagrange multiplier λ represents the contact force, which must be negative. For any positive function γ , the contact conditions (4.1)₂ can be reformulated in terms of the following non-linear relation (see, e.g., [Curnier and Alart \(1988\)](#)):

$$\lambda = \frac{1}{\gamma} [\gamma \lambda + g(\mathbf{d})]_{\mathbb{R}^-}, \quad (4.2)$$

where $[\cdot]_{\mathbb{R}^-}$ stands for the projection onto \mathbb{R}^- .

As in Chapter 2, we consider $\mathbf{W} \in [H_0^1(\Sigma)]^d$ as the admissible displacement space. The variational formulation of (4.1)₁ yields

$$\rho^s \varepsilon (\partial_t \dot{\mathbf{d}}, \mathbf{w}) + a^s(\mathbf{d}, \mathbf{w}) - \int_{\Sigma} \lambda \mathbf{n}_{\Sigma(t)} \cdot \mathbf{w} = \int_{\Sigma} \mathbf{T} \cdot \mathbf{w}$$

for all $\mathbf{w} \in \mathbf{W}$. Furthermore, one applies an additional constraint on the system (see [Mlika et al. \(2017\)](#)), by requiring that the differential contact forces on the opposite surfaces are balanced (viz., Newton's law), which yields the new relation

$$\rho^s \varepsilon (\partial_t \dot{\mathbf{d}}, \mathbf{w}) + a^s(\mathbf{d}, \mathbf{w}) - \frac{1}{2} \int_{\Sigma} \lambda \mathbf{n}_{\Sigma(t)} \cdot (\mathbf{w} - \mathbf{w}(\phi_t^{-1} \circ \pi \circ \phi_t)) = \int_{\Sigma} \mathbf{T} \cdot \mathbf{w} \quad (4.3)$$

for all $\mathbf{w} \in \mathbf{W}$.

4.2.2 Fluid-structure-contact model

Considering the notations introduced at the beginning of this section and the solid model with contact described above, the fluid-structure-contact interaction model reads

as follows: find the fluid velocity and pressure $\mathbf{u} : \Omega^f(t) \times \mathbb{R}^+ \rightarrow \mathbb{R}^d$, $p : \Omega(t)^f \times \mathbb{R}^+ \rightarrow \mathbb{R}$, the solid displacement and velocity $\mathbf{d} : \Sigma \times \mathbb{R}^+ \rightarrow \mathbb{R}^d$, $\dot{\mathbf{d}} : \Sigma \times \mathbb{R}^+ \rightarrow \mathbb{R}^d$, such that for all $t \in \mathbb{R}^+$, we have

- Fluid problem:

$$\begin{cases} \rho^f (\partial_t \mathbf{u} + \mathbf{u} \cdot \nabla \mathbf{u}) - \operatorname{div} \boldsymbol{\sigma}(\mathbf{u}, p) = \mathbf{0} & \text{in } \Omega^f(t), \\ \operatorname{div} \mathbf{u} = 0 & \text{in } \Omega^f(t), \\ \mathbf{u} = \mathbf{0} & \text{on } \Gamma, \end{cases} \quad (4.4)$$

- Solid problem with contact:

$$\begin{cases} \rho^s \varepsilon \partial_t \dot{\mathbf{d}} + \mathbf{L}(\mathbf{d}) - \lambda \mathbf{n}_{\Sigma(t)} = \mathbf{T} & \text{on } \Sigma, \\ g_\varepsilon(\mathbf{d}) \geq 0, \quad \lambda \leq 0, \quad \lambda g_\varepsilon(\mathbf{d}) = 0 & \text{on } \Sigma, \\ \dot{\mathbf{d}} = \partial_t \mathbf{d} & \text{on } \Sigma, \end{cases} \quad (4.5)$$

- Fluid-structure coupling conditions:

$$\begin{cases} \phi = \mathbf{I}_\Sigma + \mathbf{d}, \quad \Sigma(t) = \phi_t(\Sigma), \quad \Omega^f(t) = \Omega^f \setminus \Sigma(t), \\ \mathbf{u} = \dot{\mathbf{d}} \circ \phi_t^{-1} & \text{on } \Sigma(t), \\ \int_\Sigma \mathbf{T} \cdot \mathbf{w} = - \int_{\Sigma(t)} \llbracket \boldsymbol{\sigma}(\mathbf{u}, p) \mathbf{n} \rrbracket \cdot \mathbf{w} \circ \phi_t^{-1}, \quad \forall \mathbf{w} : \Sigma \rightarrow \mathbb{R}^d, \end{cases} \quad (4.6)$$

with the initial conditions $\mathbf{u}(0) = \mathbf{u}_0$, $\mathbf{d}(0) = \mathbf{d}_0$ and $\dot{\mathbf{d}}(0) = \dot{\mathbf{d}}_0$. In the solid problem we consider a relaxed contact formulation (see Section 1.2.4), hence the contact conditions (4.5)₂ employs the relaxed gap function $g_\varepsilon : \Sigma \rightarrow \mathbb{R}$, namely:

$$g_\varepsilon(\mathbf{x}) \stackrel{\text{def}}{=} g(\mathbf{x}) - \varepsilon,$$

for all $\mathbf{x} \in \Sigma_i \subset \Sigma$ and $\varepsilon > 0$ is a small parameter. Note that the kinematic and dynamic interface coupling conditions in (4.6) depend on the considered interface and the sided-restrictions to each physical region separated by the structure. The jump and average operators (2.1) across Σ , are now defined according for each interface Σ_i , $i = 1, 2, 3$.

4.3 Numerical methods

This section is devoted to the discretization of the coupled problem (4.4)-(4.6). We will mainly focus to the discretization via the Nitsche-XFEM method, but for the purpose of completeness, we will briefly recall the key components of the fitted mesh ALE and fictitious domain numerical methods, used in Section 4.4 for comparison. The common factor between the methods is the approximation of the solid problem with contact, which will be addressed separately. In the following, we denote with $\tau > 0$ the time-step discretization parameter, $t_n \stackrel{\text{def}}{=} n\tau$ where $n \in \mathbb{N}$ and with $\partial_\tau x^n \stackrel{\text{def}}{=} \frac{1}{\tau}(x^n - x^{n-1})$ the first

order backward difference. As in Chapter 2, we consider to following functional spaces for the solution of the fluid subproblem, namely $\mathbf{V} \stackrel{\text{def}}{=} [H_{\Gamma}^1(\Omega)]^d$ for the fluid velocity and $Q \stackrel{\text{def}}{=} L_0^2(\Omega)$ for the fluid pressure.

4.3.1 Solid contact approximation via penalty

For the discretization of problem (4.1), we consider a relaxed (see Section 1.2.4) penalty version of (4.3). Let be $\{\mathcal{T}_h^s\}_{0 < h < 1}$ a family of quasi-uniform triangulations of $\Sigma = \Sigma_1 \cup \Sigma_2$. We consider the standard space of continuous piecewise affine functions:

$$X_h^s \stackrel{\text{def}}{=} \{v_h \in C^0(\bar{\Sigma}) \mid v_h|_K \in \mathbb{P}_1(K), \quad \forall K \in \mathcal{T}_h^s\}. \quad (4.7)$$

Hence, we define the discrete space for the solid displacement and velocity approximations as $\mathbf{W}_h = [X_h^s]^d \cap \mathbf{W}$. The penalty approach consists in taking

$$\gamma = \frac{\gamma_C E \varepsilon}{h^2}, \quad \gamma_C > 0,$$

and by neglecting the term $\gamma \lambda$ in (4.2). This enables the elimination of λ , which yields the following numerical method in terms of primal variables only:

$$\rho^s \varepsilon (\partial_\tau \dot{\mathbf{d}}_h^n, \mathbf{w}_h) + a^s(\mathbf{d}_h^n, \mathbf{w}_h) - \frac{\gamma_C E \varepsilon}{2h^2} \int_{\Sigma} [g_{\varepsilon_h}(\mathbf{d}_h^n)]_{\mathbb{R}^-} \cdot \llbracket \mathbf{w}_h \rrbracket = \int_{\Sigma} \mathbf{T} \cdot \mathbf{w}_h \quad (4.8)$$

for all $\mathbf{w}_h \in \mathbf{W}_h$ and with the notations

$$g_{\varepsilon_h}(\mathbf{d}_h^n) \stackrel{\text{def}}{=} (\boldsymbol{\pi}(\boldsymbol{\phi}_h^n) - \boldsymbol{\phi}_h^n) \cdot \mathbf{n}_{\Sigma^n} - \varepsilon_h,$$

$$\llbracket \mathbf{w}_h \rrbracket \stackrel{\text{def}}{=} \mathbf{w}_h - \mathbf{w}_h \left((\boldsymbol{\phi}_h^n)^{-1} \circ \boldsymbol{\pi} \circ \boldsymbol{\phi}_h^n \right)$$

and where ε_h denotes the contact relaxation parameter. The contact term associated to (4.8) is evaluated locally at each quadrature point. For the derivation of the corresponding tangent term we refer to [Poulios and Renard \(2015\)](#).

Remark 4.3.1. *Note that we could invoke the relation (4.1) to get*

$$\lambda = (\rho^s \varepsilon \partial_t \dot{\mathbf{d}} + \mathbf{L}(\mathbf{d}) - \mathbf{T}) \cdot \mathbf{n}_{\Sigma(t)}$$

and then use (4.2) to eliminate the Lagrange multiplier in (4.3), by setting

$$\lambda = \frac{1}{\gamma} \left[\gamma (\rho^s \varepsilon \partial_t \dot{\mathbf{d}} + \mathbf{L}(\mathbf{d}) - \mathbf{T}) \cdot \mathbf{n}_{\Sigma(t)} + g(\mathbf{d}) \right]_{\mathbb{R}^-}.$$

This is the basis of the consistent Galerkin least-squares method for the obstacle problem reported in [Burman et al. \(2018\)](#).

4.3.2 Unfitted mesh Nitsche-XFEM method

In this section, we focus on the extension of the Nitsche-XFEM discretization technique to the case of contact with multiple immersed thin-walled solids. As already pointed out in Section 4.1, the basic idea of XFEM is to reproduce inside the discrete spaces the eventual singularities of the solution. Considering a single immersed structure (see Figure 4.3(a)), the only discontinuity lies across the interface Σ . In this case, the discretization procedure proposed by Alauzet et al. (2016) is able to reproduce the singularity within the discrete spaces. Similarly, the method covers the situation in which multiple structures are considered without contact (they do not intersect the same fluid element). This situation is showed in Figure 4.3(b). Whereas, if contact is allowed, two approaching solids can reach the same fluid element. As a result, two discontinuities, one for each interface, need to be incorporated within the fluid discrete spaces (see Figure 4.3(c)). In the next paragraphs

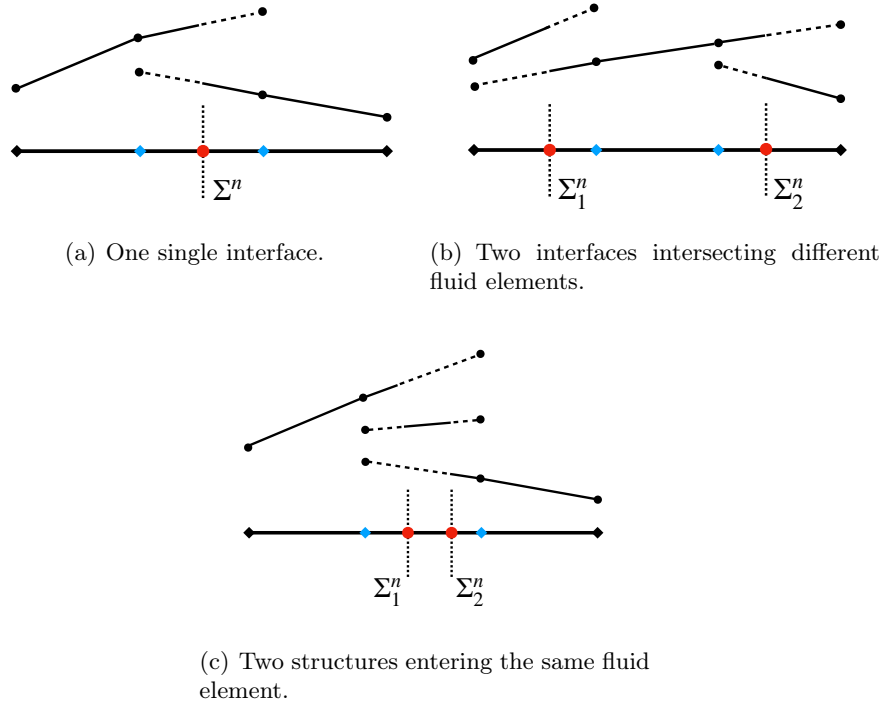


Figure 4.3: One-dimensional illustration of the different interface locations and associated physical discontinuities.

we extend the approach proposed in Alauzet et al. (2016) to this situation. We recall that, for simplicity, a relaxed contact condition is considered. Hence, even in the case of contact, a thin layer of fluid remains between the two contacting structures.

For sake of simplification, we assume that both Ω^f and Σ are polyhedral. For a given displacement $\mathbf{d}_h^n \in \mathbf{W}_h$, we define the interface position, at time level n , as $\Sigma^n \stackrel{\text{def}}{=} \phi_h^{n-1}(\Sigma)$, hence, for each interface $\Sigma_i^n \stackrel{\text{def}}{=} \phi_h^{n-1}(\Sigma_i)$. We further recall that $\Sigma^n = \Sigma_1^n \cup \Sigma_2^n$.

Additionally, the physical fluid domain is

$$\Omega^{f,n} \stackrel{\text{def}}{=} \Omega^f \setminus \Sigma^n$$

and therefore, $\Omega^{f,n} = \Omega_1^{f,n} \cup \Omega_2^{f,n} \cup \Omega_3^{f,n}$, where each $\Omega_i^{f,n}$ is the i -th physical fluid region.

We introduce three families of quasi-uniform triangulations $\{\mathcal{T}_{h,i}^n\}_{0 < h < 1}$, $i = 1, 2, 3$, starting from a family $\{\mathcal{T}_h^n\}_{0 < h < 1}$ of quasi-uniform triangulations of $\overline{\Omega^{f,n}}$. Each $\mathcal{T}_{h,i}^n$ is obtained as the collection of elements of \mathcal{T}_h^n that cover each region $\Omega_i^{f,n}$, separated by Σ_i^n , $i = 1, 2$. Thus, $\mathcal{T}_{h,i}^n$ covers the i -th fluid region $\Omega_i^{f,n}$. Each generated mesh $\mathcal{T}_{h,i}^n$ is fitted to the exterior boundary Γ_i but not to \mathcal{T}_h^s . An example of this setting is shown in Figure 4.4. Note that the triangulation composed by $\bigcup_{i=1,2,3} (K \in \mathcal{T}_{h,i}^n)$ is a conforming triangulation of the whole fluid domain $\Omega^f(t)$. Furthermore, for each fluid element K , such that $K \in \bigcup_{i,j} (\mathcal{T}_{h,i}^n \cap \mathcal{T}_{h,j}^n)$, we can distinguish two situations:

- K belongs only to one couple of fluid triangulations (see, for instance, the yellow and blue elements in Figure 4.4(b));
- K belongs to all fluid triangulations, namely $K \in \mathcal{T}_{h,1}^n \cap \mathcal{T}_{h,2}^n \cap \mathcal{T}_{h,3}^n$ (see, for instance, the grey elements in Figure 4.4(b)).

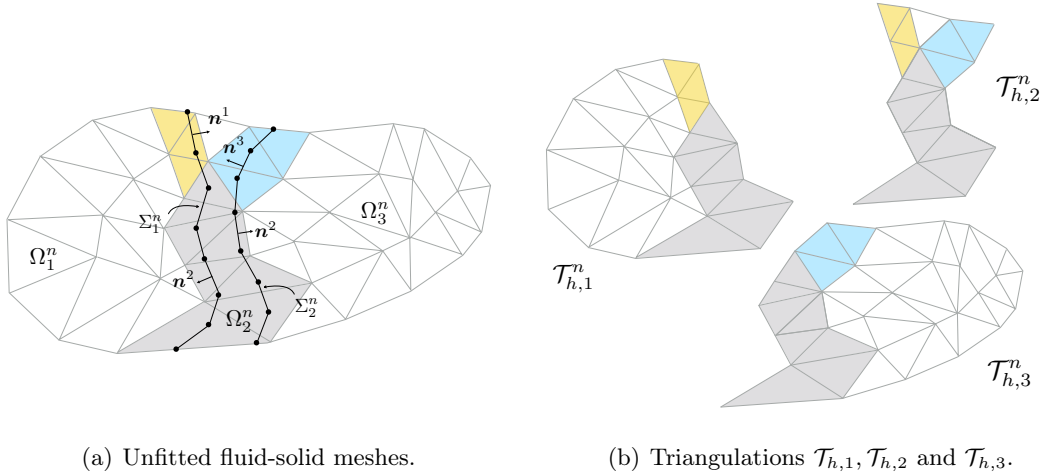


Figure 4.4: The overlapping region between $\mathcal{T}_{h,1}^n$, $\mathcal{T}_{h,2}^n$ and $\mathcal{T}_{h,3}^n$ is colored in grey, between $\mathcal{T}_{h,1}^n$ and $\mathcal{T}_{h,2}^n$ in yellow and between $\mathcal{T}_{h,2}^n$ and $\mathcal{T}_{h,3}^n$ is blue.

We denote by $\Omega_{h,i}^n$ the domain covered by $\mathcal{T}_{h,i}^n$,

$$\Omega_{h,i}^n \stackrel{\text{def}}{=} \text{int} \left(\bigcup_{K \in \mathcal{T}_{h,i}^n} K \right).$$

Let now introduce the following spaces of continuous piecewise affine functions, for $i = 1, 2, 3$:

$$X_{h,i}^n \stackrel{\text{def}}{=} \left\{ v_h \in C^0(\overline{\Omega_{h,i}^n}) \mid v_h|_K \in \mathbb{P}_1(K), \quad \forall K \in \mathcal{T}_{h,i}^n \right\}.$$

Associated with $X_{h,i}$ we define the spaces

$$\mathbf{V}_{h,i}^n \stackrel{\text{def}}{=} [X_{h,i}^n]^2 \cap \mathbf{V}^n, \quad Q_{h,i}^n \stackrel{\text{def}}{=} X_{h,i}^n \cap Q^n.$$

For the approximation of the fluid velocity and pressure, we will consider the following discrete product spaces

$$\mathbf{V}_h^n \stackrel{\text{def}}{=} \mathbf{V}_{h,1}^n \times \mathbf{V}_{h,2}^n \times \mathbf{V}_{h,3}^n, \quad Q_h^n \stackrel{\text{def}}{=} Q_{h,1}^n \times Q_{h,2}^n \times Q_{h,3}^n,$$

which guarantee that interfacial (strong and weak) discontinuities are included in the discrete approximation of both the fluid velocity and pressure, also in case two structures intersect the same fluid element. We will denote by $\mathbf{u}_{h,i}^n$ and $p_{h,i}^n$, with $i = 1, 2, 3$, the unknowns defined in each domain $\Omega_{h,i}^n$. We recall that the fluid trilinear form is given by the following expression

$$\begin{aligned} a_h^f(\mathbf{z}_h; (\mathbf{u}_h, p_h), (\mathbf{v}_h, q_h)) &\stackrel{\text{def}}{=} c_h^n(\mathbf{z}_h, \mathbf{u}_h, \mathbf{v}_h) + a^f((\mathbf{u}_h, p_h), (\mathbf{v}_h, q_h)) \\ &\quad + s_{v,h}^n(\mathbf{z}_h; \mathbf{u}_h, \mathbf{v}_h) + s_{p,h}^n(\mathbf{z}_h; p_h, q_h) + g_h^n(\mathbf{u}_h, \mathbf{v}_h), \end{aligned}$$

with the fluid discrete bi-linear form

$$a^f((\mathbf{u}_h, p_h), (\mathbf{v}_h, q_h)) \stackrel{\text{def}}{=} 2\mu(\boldsymbol{\epsilon}(\mathbf{u}_h), \boldsymbol{\epsilon}(\mathbf{v}_h))_{\Omega^{f,n}} - (p_h, \nabla \cdot \mathbf{v}_h)_{\Omega^{f,n}} + (q_h, \nabla \cdot \mathbf{u}_h)_{\Omega^{f,n}}$$

and the convective term by

$$\begin{aligned} c_h^n(\mathbf{z}_h, \mathbf{u}_h, \mathbf{v}_h) &\stackrel{\text{def}}{=} \rho^f(\mathbf{z}_h \cdot \nabla \mathbf{u}_h, \mathbf{v}_h)_{\Omega^{f,n}} + \frac{\rho^f}{2}((\text{div } \mathbf{z}_h) \mathbf{u}_h, \mathbf{v}_h)_{\Omega^{f,n}} \\ &\quad - \rho^f(\{\{\mathbf{z}_h\}\} \cdot \mathbf{n} \llbracket \mathbf{u}_h \rrbracket, \{\{\mathbf{v}_h\}\})_{\Sigma^n} - \frac{\rho^f}{2}(\llbracket \mathbf{z}_h \cdot \mathbf{n} \rrbracket, \{\{\mathbf{u}_h \cdot \mathbf{v}_h\}\})_{\Sigma^n}, \end{aligned}$$

where the jump and average operators are defined in Section 4.2.2. Terms $s_{v,h}^n$ and $s_{p,h}^n$ correspond to the CIP stabilization contributions (see Section 2.3.2 and [Burman and Fernández \(2007\)](#)), namely,

$$\begin{aligned} s_{v,h}^n(\mathbf{z}_h; \mathbf{u}_h, \mathbf{v}_h) &\stackrel{\text{def}}{=} \gamma_v h^2 \sum_{i=1}^3 \sum_{F \in \mathcal{F}_{h,i}^n} \xi(\text{Re}_F(\mathbf{z}_h)) \|\mathbf{z}_h \cdot \mathbf{n}\|_{L^\infty(F)} (\llbracket \nabla \mathbf{u}_h \rrbracket_F, \llbracket \nabla \mathbf{v}_h \rrbracket_F)_F, \\ s_{p,h}^n(\mathbf{z}_h; p_h, q_h) &\stackrel{\text{def}}{=} \gamma_p h^2 \sum_{i=1}^3 \sum_{F \in \mathcal{F}_{h,i}^n} \frac{\xi(\text{Re}_F(\mathbf{z}_h))}{\|\mathbf{z}_h\|_{L^\infty(F)}} (\llbracket \nabla p_h \rrbracket_F, \llbracket \nabla q_h \rrbracket_F)_F, \end{aligned}$$

where $\mathcal{F}_{h,i}^n$ denotes the set of interior edges ($d = 2$) or faces ($d = 3$) of $\mathcal{T}_{h,i}^n$, with $i = 1, 2, 3$, $\gamma_p, \gamma_v > 0$ are user-defined parameters, $\text{Re}_F(\mathbf{z}_h) \stackrel{\text{def}}{=} \rho^f \|\mathbf{z}_h\|_{L^\infty(F)} h \mu^{-1}$ denotes the local Reynolds number and $\xi(x) \stackrel{\text{def}}{=} \min\{1, x\}$. Finally, term g_h^n corresponds to the ghost-

penalty operator, given by

$$g_h^n(\mathbf{u}_h, \mathbf{v}_h) \stackrel{\text{def}}{=} \gamma_g \mu h \sum_{j=1}^2 \sum_{i=0}^1 \sum_{F \in \mathcal{F}_{i+j,h}^{\Sigma_j^n}} (\llbracket \nabla \mathbf{u}_{i+j,h} \rrbracket_F, \llbracket \nabla \mathbf{v}_{i+j,h} \rrbracket_F)_F,$$

where $\mathcal{F}_{k,h}^{\Sigma_j^n}$ denotes the set of interior edges or faces of the elements of $\mathcal{T}_{h,k}^n$, $k = 1, 2, 3$, intersected by Σ_j^n , $j = 1, 2$.

Algorithm 4.1 Nitsche-XFEM scheme.

For $n \geq 1$:

1. Interface update: $\phi_h^{n-1} = \mathbf{I}_\Sigma + \mathbf{d}_h^{n-1}$, $\Sigma^n = \phi_h^{n-1}(\Sigma)$, $\Omega^{f,n} = \Omega^f \setminus \Sigma^n$
2. Find $(\mathbf{u}_h^n, p_h^n, \mathbf{d}_h^n) \in \mathbf{V}_h^n \times Q_h^n \times \mathbf{W}_h$, such that $\dot{\mathbf{d}}_h^n = \partial_\tau \mathbf{d}_h^n$ and

$$\begin{aligned} & \rho^f (\partial_\tau \mathbf{u}_h^n, \mathbf{v}_h)_{\Omega^{f,n}} + a_h^f(\mathbf{u}_h^{n-1}; (\mathbf{u}_h^n, p_h^n), (\mathbf{v}_h, q_h)) + \rho^s \varepsilon (\partial_\tau \dot{\mathbf{d}}_h^n, \mathbf{w}_h)_\Sigma + a_h^s(\mathbf{d}_h^n, \mathbf{w}_h) \\ & - \frac{\gamma_C E \varepsilon}{2h^2} \int_\Sigma [g_{\varepsilon_h}(\mathbf{d}_h^n)]_{\mathbb{R}^-} \cdot \llbracket \mathbf{w}_h \rrbracket - \sum_{j=1}^2 \sum_{i=0}^1 (\boldsymbol{\sigma}(\mathbf{u}_{h,i+j}^n, p_{h,i+j}^n) \mathbf{n}_{i+j}, \mathbf{v}_{h,i+j} - \mathbf{w}_h)_{\Sigma^n} \\ & - \sum_{j=1}^2 \sum_{i=0}^1 (\mathbf{u}_{h,i+j}^n - \dot{\mathbf{d}}_h^n, \boldsymbol{\sigma}(\mathbf{v}_{h,i+j}, -q_{h,i+j})) \mathbf{n}_{i+j} \Big|_{\Sigma^n} \\ & + \frac{\gamma \mu}{h} \sum_{j=1}^2 \sum_{i=0}^1 (\mathbf{u}_{h,i+j}^n - \dot{\mathbf{d}}_h^n, \mathbf{v}_{h,i+j} - \mathbf{w}_h)_{\Sigma^n} = 0 \end{aligned}$$

for all $(\mathbf{v}_h, q_h, \mathbf{w}_h) \in \mathbf{V}_h^n \times Q_h^n \times \mathbf{W}_h$

The resulting numerical method is detailed in Algorithm 4.1. Note that the weak imposition of the interface coupling conditions (4.6) are now defined considering the physical domain on each side of every interface.

Remark 4.3.2. *In this chapter, we have assumed that the thin-walled solids have no boundaries in the interior part of the fluid domain, so that $\Omega^{f,n}$ is fully separated in different regions. The present approach can be generalized the case of partially intersected fluid domains by considering the tip treatment strategy proposed in Section 6.2.2 of Chapter 6. Note that the strategy proposed in Alauzet et al. (2016) cannot cover this situation.*

4.3.2.1 Intersection algorithm

For a full discussion on the 2D meshes intersection algorithm we refer to Landajuela (2016) and Alauzet et al. (2016). Here, we recall the salient points and we highlight the modifications necessary to consider multiple structures, possibly in contact, with Algorithm 4.1. The fundamental idea of the intersection algorithm is practically unchanged.

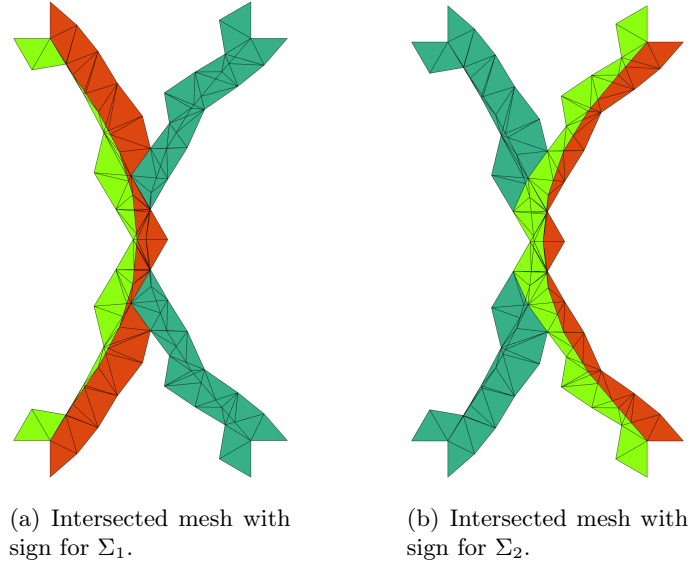


Figure 4.5: Marked intersected fluid mesh for the bottom interface Σ_1 (a) and for the top interface Σ_2 (b). Both interfaces have downward normal. Green color corresponds to left side, red to right.

The main modifications concern the definition of the physical domain within the intersected mesh (the mesh generated by all the sub-elements). We recall that the main phases of the algorithm are the following:

1. Localization and insertion of solid meshes vertices inside the fluid mesh;
2. Insertion of solid edges, one at a time.

Once the insertion procedure has been completed, we update all the data structures necessary for the duplication and integration over cut elements. In particular, we need to know which are the physical regions for each cut element, hence, we label as *LEFT*, the fluid sub-elements towards which the structure normal is pointing in, and *RIGHT* the others. Note that the side is defined with respect to each structure, therefore, all the fluid sub-elements are labeled with regard to every structure. We require the knowledge of which fluid element is intersected by each structure and if a sub-element is on the left or the right of every structure. An example is shown in Figure 4.5. See that the sub-elements are signed with respect to each interface, Σ_1^n Fig.(a) Σ_2^n (b). Note that not all the elements are signed, (dark green in Figure 4.5). In fact, we have a signed partition of the cut elements for each interface and the elements, which are intersected from both interfaces, have two sign patterns.

4.3.2.2 Element duplication

In this section we describe the proposed element duplication procedure, which is carried out exploiting the information stored at the end of the intersection algorithm of

Section 4.3.2.1. Each overlapping triangulation $\mathcal{T}_{h,i}^n$, $i = 1, 2, 3$, is generated by duplicating the elements of the intersected fluid element, starting from a conforming (background) mesh of $\Omega^{f,n}$. For each fluid elements K , intersected by $\Sigma^n = \Sigma_1^n \cup \Sigma_2^n \cup \Sigma_3^n$, we can identify two or more separated regions. We will refer to the *physical* part of a triangulation as the restriction of $\mathcal{T}_{h,i}^n$ on $\Omega_i^{f,n}$, $i = 1, 2, 3$. Its complementary part is called *nonphysical* or *fictitious*. Let consider the situation shown in Figure 4.6, in which we have three triangles

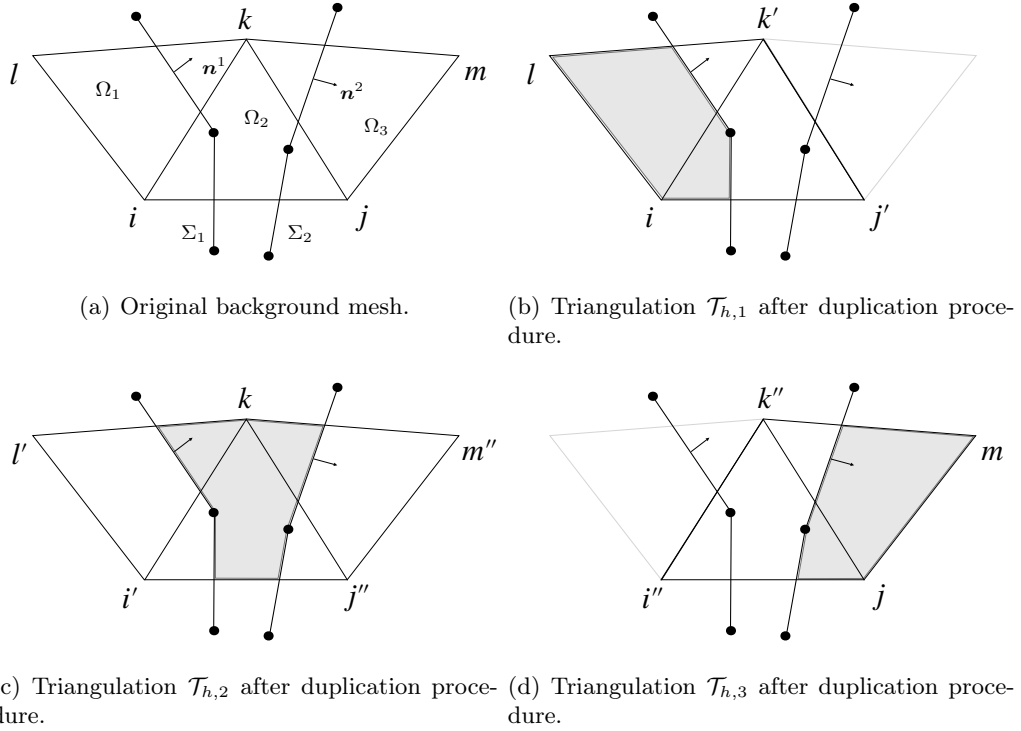


Figure 4.6: Duplication procedure. The fluid *physical* domains are Ω_1, Ω_2 and Ω_3 , and the interfaces are Σ_1 and Σ_2 .

with vertices $\{i, j, k\}$, $\{i, k, l\}$ and $\{j, l, k\}$. We show in Figure 4.6(a) the original background mesh. Note that nodes i, l are *physical* for $\Omega_1^{f,n}$, k is *physical* for $\Omega_2^{f,n}$ and j, m for $\Omega_3^{f,n}$.

Each interface introduces a new level of vertices duplication. For instance, the vertices of the fluid elements intersected by Σ_1^n will form the duplication *Level I*. The vertices duplicated due to Σ_2^n yield a second level of duplication, *Level II*. We will identify the duplicated nodes of *Level I* by \cdot' and the duplicates node of *Level II* (coming the Σ_2^n) by \cdot'' . The levels of vertex duplication for the example of Figure 4.6 are show in Table 4.1. For each element K intersected by Σ^n , we can have two scenarios:

1. K is intersected only by one structure, so that Σ^n divides K into two regions. In this case, we build two identical copies of K , namely K_1 and K_2 , associated to each region;
2. K is intersected by more than one interface. In this case, Σ^n divides K in three

regions. We define three identical copies of K , namely, K_1 , K_2 and K_3 . Each of them represents a *physical* region.

Let now describe the building strategy for triangulations $\mathcal{T}_{h,i}^n$, with $i = 1, 2, 3$, i.e., how the nodes for the generated copies are selected. The original vertices are always kept on the *physical* side of the triangulation, while the *unphysical* nodes are selected as follows:

- For $K \in \mathcal{T}_{h,1}^n$: we select as *unphysical* nodes the duplicated vertices belonging to *Level I*.
- For $K \in \mathcal{T}_{h,2}^n$: we choose as *unphysical* vertices the duplicated nodes belonging to *Level I*, when still available (if they are not used to build $\mathcal{T}_{h,1}^n$), otherwise, we select the nodes of *Level II*.
- For $K \in \mathcal{T}_{h,3}^n$: we select as *unphysical* the duplicated nodes belonging to *Level II*.

<i>Original</i>	i	j	k	l	m
<i>Level I</i>	i'	j'	k'	l'	-
<i>Level II</i>	i''	j''	k''	-	m''

Table 4.1: Levels of duplication for example of Figure 4.6

We now apply this procedure in the example of Figure 4.6. Let consider $K = \{i, k, l\}$. This element is intersected only form Σ_1^n , therefore we will create two copies of it, namely $\{i, k, l\}$ and $\{i', k', l'\}$. Note that we have used the duplicated nodes of *Level I*. At the end of the duplication procedure we will get $K_1 = \{i, k', l\}$ and $K_2 = \{i', k, l'\}$. (see Figure 4.6(b) and (c)). Similarly for $K = \{j, m, k\}$, except that is intersected only by Σ_2^n , therefore we will use the duplicated vertices of *Level II*. Finally, we have $K_1 = \{j, m, k''\}$ and $K_2 = \{j'', m'', k\}$. (see Figure 4.6(d) and (c)).

Let now consider, $K = \{i, j, k\}$. It is intersected by both Σ_1^n and Σ_2^n . We hence build three copies of K , namely K_1 , K_2 and K_3 . In order to construct K_1 we keep i as *physical* and we select the available nodes starting form *Level I*. Vertices j' and k' are not used yet, hence we obtain $K_1 = \{i, j', k'\}$ (Figure 4.6(b)). For K_2 we fix k as *physical* and we select i' and j'' as *unphysical*, since j' has already been used (see Figure 4.6(c)). At last, K_3 will be $K_3 = \{i'', j, k''\}$ (Figure 4.6(d)).

At the end of this process, we have, three independent meshes $\mathcal{T}_{h,1}^n$, $\mathcal{T}_{h,2}^n$ and $\mathcal{T}_{h,3}^n$ covering $\Omega_1^{f,n}$, $\Omega_2^{f,n}$ and $\Omega_3^{f,n}$, respectively. The duplicated elements are designed in such a way that the correct connectivity of the meshes is guaranteed. Hence, we preserve the continuity on each *physical* side of the duplicated elements with the rest of the fluid *physical* domain.

4.3.2.3 Integration with moving domains

As mentioned in Section 2.3.2, Algorithm 4.1 involves integrals with functions defined on spaces generated form time-dependent triangulations. Therefore, products of functions

that might be discontinuous at different locations in the same element. When the discontinuities are located in different elements, regardless the number of structures considered, the quadrature is performed in a standard fashion by treating separately each discontinuity. In fact, we store also the previous intersected meshes and the necessary informations. In case we have different discontinuities within the same element, this inconvenience is solved by shifting the discontinuity at time t^{n-1} to the structure location at time t^n (see Alauzet et al. (2016); Fries and Zilian (2009)). Note that an alternative strategy could have been considered as follows. When the number of discontinuities located inside an element at t^n and t^{n-1} is different, we denote by t^{k-} the sub-triangulation with less discontinuities and with t^{k+} the other one. Finally, the discontinuity at time t^{k-} is shifted to the structure location at time t^{k+} .

4.3.3 Fitted mesh ALE method

The purpose of this section is to recall the basic ingredients of the fitted mesh ALE-Lagrangian numerical scheme, starting from the coupled problem (4.4)-(4.6), described in Section 4.2. This scheme will be only used for comparison purposes in Section 4.4. Let begin by recalling that we consider a bijective map \mathcal{A} , such that $\mathcal{A} : \widehat{\Omega}^f \times \mathbb{R}^+ \rightarrow \Omega^f(t)$. We also parametrize the moving fluid domain by a one-to-one mapping introduce $\mathcal{A}_t \stackrel{\text{def}}{=} \mathcal{A}(\cdot, t)$.

We consider a fitted meshes based discretization, i.e., the fluid and solid meshes matches at the interface Σ . We consider a family of triangulations of $\{\mathcal{T}_h^f\}_{0 < h < 1}$ of the initial fluid domain Ω^f which are fitted to the family of triangulations $\{\mathcal{T}_h^s\}_{0 < h < 1}$ of the reference solid domain Σ . For the discrete spaces, we consider the standard Lagrange space of continuous piecewise affine functions, namely

$$X_h^f \stackrel{\text{def}}{=} \left\{ v_h \in C^0(\overline{\Omega^f}) \mid v_h|_K \in \mathbb{P}_1(K), \quad \forall K \in \mathcal{T}_h^f \right\}, \quad (4.9)$$

Then, we consider for the approximation of the fluid velocity $\mathbf{V}_h = [X_h^f]^d \cap \mathbf{V}$. For the fluid pressure space, we allow the pressure to be discontinuous across Σ , by considering piece-wise affine functions but continuous on each fluid domain, Ω_i , $i = \{1, 2, 3\}$. We achieve this objective by duplicating the fluid degrees of freedom belonging to Σ only for the pressure approximation. The geometric non-linearities are treated, once again, in an explicit fashion. Therefore, for a given solid displacement $\mathbf{d}_h^{n-1} \in \mathbf{W}_h$, we define the ALE map

$$\mathcal{A}_h^n = \mathbf{I}_{\widehat{\Omega}^f} + \mathbf{d}_h^{f,n},$$

where $\mathbf{d}_h^{f,n}$ is defined as $\mathbf{d}_h^{f,n} = \mathcal{L}_h(\mathbf{d}_h^{n-1})$.

Considering an overall backward Euler time-stepping and a strong coupling between fluid and solid sub-problems, the fitted meshes based discretization of problem (4.4)-(4.6) is detailed in Algorithm 4.2.

Algorithm 4.2 Fitted mesh ALE scheme.

For $n \geq 1$,

1. Fluid mesh update:

$$\mathbf{d}_h^{f,n} = \mathcal{L}_h(\mathbf{d}_h^{n-1}), \quad \mathbf{w}_h^n = \partial_\tau \mathbf{d}_h^{f,n}, \quad \mathcal{A}_h^n = \mathbf{I}_\Omega + \mathbf{d}_h^{f,n}, \quad \Omega_h^n = \mathcal{A}_h^n(\Omega).$$

2. Find $(\hat{\mathbf{u}}_h^n, \hat{p}_h^n, \mathbf{d}_h^n) \in \mathbf{V}_h \times Q_h \times \mathbf{W}_h$, with $\dot{\mathbf{d}}_h = \partial_\tau \mathbf{d}_h^n$ and $\hat{\mathbf{u}}_h^n|_\Sigma = \dot{\mathbf{d}}_h^n$, such that

$$\begin{aligned} & \frac{\rho^f}{\tau} (\mathbf{u}_h^n, \mathbf{v}_h)_{\Omega_h^n} - \frac{\rho^f}{\tau} (\mathbf{u}_h^{n-1}, \mathbf{v}_h)_{\Omega_h^{n-1}} - \rho^f ((\nabla \cdot \mathbf{w}_h^n) \mathbf{u}_h^n, \mathbf{v}_h)_{\Omega_h^n} \\ & + a_{\Omega_h^n}^f(\mathbf{u}_h^{n-1} - \mathbf{w}_h^n; (\mathbf{u}_h^n, p_h^n), (\mathbf{v}_h, q_h)) + \rho^s \varepsilon (\partial_\tau \dot{\mathbf{d}}_h^n, \mathbf{y}_h)_\Sigma \\ & + a_h^s(\mathbf{d}_h^n, \mathbf{y}_h) - \frac{\gamma_{\text{CE}} E \varepsilon}{2h^2} \int_\Sigma [g_{\varepsilon_h}(\mathbf{d}_h^n)]_{\mathbb{R}^-} \cdot \llbracket \mathbf{w}_h \rrbracket = 0, \end{aligned}$$

for all $(\hat{\mathbf{v}}_h, \hat{q}_h, \mathbf{y}_h) \in \mathbf{V}_h \times Q_h \times \mathbf{W}_h$, with $\mathbf{v}_h|_\Sigma = \mathbf{y}_h$.

In Algorithm 4.2, we have considered the following fluid discrete bilinear form

$$\begin{aligned} a_{\Omega_h^n}^f(\mathbf{z}_h; (\mathbf{u}_h, p_h), (\mathbf{v}_h, q_h)) & \stackrel{\text{def}}{=} c_h^n(\mathbf{z}_h; \mathbf{u}_h, \mathbf{v}_h) + 2\mu (\boldsymbol{\epsilon}(\mathbf{u}_h), \boldsymbol{\epsilon}(\mathbf{v}_h))_{\Omega_h^n} \\ & - (p_h, \nabla \cdot \mathbf{v}_h)_{\Omega_h^n} + (q_h, \nabla \cdot \mathbf{u}_h)_{\Omega_h^n} \\ & + s_{\Omega_h^n}(\mathbf{z}_h; \mathbf{u}_h, \mathbf{v}_h), \end{aligned}$$

with the convective trilinear form defined as

$$c_h^n(\mathbf{z}_h; \mathbf{u}_h, \mathbf{v}_h) \stackrel{\text{def}}{=} (\mathbf{z}_h \cdot \nabla \mathbf{u}_h, \mathbf{v}_h)_{\Omega_h^n} + \frac{\rho^f}{2} ((\nabla \cdot \mathbf{z}_h) \mathbf{u}_h, \mathbf{v}_h)_{\Omega_h^n}$$

and, since the couple velocity/pressure discrete spaces fails to satisfy the inf-sup condition we consider the SUPG/PSPG $s_{\Omega_h^n}$ stabilization (see, e.g., [Tezduyar \(1992\)](#)), as follows,

$$\begin{aligned} s_{\Omega_h^n}(\mathbf{z}_h; \mathbf{u}_h, \mathbf{v}_h) & \stackrel{\text{def}}{=} \sum_{K \in \mathcal{T}_h^n} \int_K \delta_h \left(\rho^f (\mathbf{z}_h \cdot \nabla) \mathbf{u}_h + \nabla p_h \right) \cdot \left(\rho^f (\mathbf{z}_h \cdot \nabla) \mathbf{v}_h + \nabla q_h \right), \\ \delta_h & \stackrel{\text{def}}{=} \lambda_M \left(\rho^f \sqrt{\frac{4}{\tau^2} + \frac{16\mu^2}{h^4(\rho^f)^2} + \frac{4|\mathbf{z}_h|^2}{h^2}} \right)^{-1}, \end{aligned} \tag{4.10}$$

with $\lambda_M > 0$ user-defined parameter.

Remark 4.3.3. *Algorithm 4.2 involves a motion of the fluid domain mesh and the efficiency of the method is strongly connected to the effectiveness of the lifting operator \mathcal{L}_h . The lifting operator has the objective of correctly deforming the fluid mesh while maintaining a reasonable elements quality. This becomes challenging and cumbersome in case of large displacement and when topological changes (e.g., contact) are considered. In the*

numerical experiments of Section 4.4, we consider the non-linear lifting operator introduced in Landajuela et al. (2017) which is an incremental variant of the approach reported in Stein et al. (2003). The core concept of the technique is to locally increase the stiffness of small elements in order to avoid the distortion of the mesh elements.

4.3.4 Unfitted mesh Fictitious Domain method

In the following Section, we will recall a discrete version of problem (4.4)-(4.6) based on FD method. Let consider two families of triangulations $\{\mathcal{T}_h^f\}_{0 < h < 1}$ and $\{\mathcal{T}_h^s\}_{0 < h < 1}$ of, respectively, Ω^f and Σ . The mesh \mathcal{T}_h^f is fitted to the exterior boundary but, possibly, not fitted to the solid mesh \mathcal{T}_h^s .

We consider the following space discretization. Let X_h^f and X_h^s be the standard spaces of piecewise continuous affine functions, given by (4.9). For the approximations of the fluid velocity and pressure we introduce the following spaces:

$$\mathbf{V}_h = [X_h^f]^d \cap \mathbf{V} \quad \text{and} \quad Q_h = X_h^f \cap Q.$$

Note that, in this case, the pressure and velocity spaces are both globally continuous. Considering an overall backward Euler scheme for the time discretization, the strongly coupled approximation with fictitious domain of problem (4.4)-(4.6) reads as follows:

For $n \geq 1$,

1. Interface update:

$$\phi_h^n = \mathbf{I}_\Sigma + \mathbf{d}_h^{n-1}, \quad \Sigma_h^n = \phi_h^n(\Sigma), \quad \Omega_h^n = \Omega^f \setminus \Sigma_h^n. \quad (4.11)$$

2. Find $(\mathbf{u}_h^n, p_h^n, \boldsymbol{\lambda}_h^n, \mathbf{d}_h^n) \in \mathbf{V}_h \times Q_h \times \boldsymbol{\Lambda}_h \times \mathbf{W}_h$, with $\dot{\mathbf{d}}_h = \partial_\tau \mathbf{d}_h^n$, such that

$$\begin{cases} \rho^f (\partial_\tau \mathbf{u}_h^n, \mathbf{v}_h)_{\Omega^f} + a_{\Omega, h}^f(\mathbf{u}_h^{n-1}; (\mathbf{u}_h^n, p_h^n), (\mathbf{v}_h, q_h)) \\ + \rho^s \varepsilon (\partial_\tau \dot{\mathbf{d}}_h^n, \mathbf{w}_h)_\Sigma + a^s(\mathbf{d}_h^n, \mathbf{w}_h) - \frac{\gamma_C E \varepsilon}{2h^2} \int_\Sigma [g_{\varepsilon_h}(\mathbf{d}_h^n)]_{\mathbb{R}^-} \cdot \llbracket \mathbf{w}_h \rrbracket \\ + b_h(\boldsymbol{\lambda}_h^n, \mathbf{v}_h \circ \phi_h^n - \mathbf{y}_h) - b_h(\boldsymbol{\mu}_h, \mathbf{u}_h^n \circ \phi_h^n - \dot{\mathbf{d}}_h^n) = 0, \end{cases} \quad (4.12)$$

for all $(\mathbf{v}_h, q_h, \boldsymbol{\mu}_h, \mathbf{w}_h) \in \mathbf{V}_h \times Q_h \times \boldsymbol{\Lambda}_h \times \mathbf{W}_h$.

Here, the kinematic constraint is treated in a weak fashion via Lagrange multipliers, with the discrete bilinear form $b_h : \boldsymbol{\Lambda}_h \times [C^0(\Sigma)]^d \rightarrow \mathbb{R}$, given by

$$b_h(\boldsymbol{\mu}_h, \mathbf{z}) \stackrel{\text{def}}{=} \sum_{i=1}^{N_h^s} \boldsymbol{\mu}_i \cdot \mathbf{z}(\mathbf{x}_i^s),$$

where $\boldsymbol{\Lambda}_h$ denotes the Lagrange multiplier space, namely,

$$\boldsymbol{\Lambda}_h = \left\{ \boldsymbol{\mu}_h = \sum_{i=1}^{N_h^s} \boldsymbol{\mu}_i \delta_{\mathbf{x}_i^s} \mid \boldsymbol{\mu}_i \in \mathbb{R}^d, \quad \forall i \in \{1, \dots, N_h^s\} \right\}$$

and $\{\mathbf{x}_i^s\}_{i=1}^{N_h^s}$ denotes the points of the triangulation \mathcal{T}_h^s and $\delta_{\mathbf{x}_i^s}$ stands for the Dirac's measure at point \mathbf{x}_i^s . Additionally we have considered the following notations,

$$\begin{aligned} a_{\Omega^f}^f(\mathbf{z}_h; (\mathbf{u}_h, p_h), (\mathbf{v}_h, q_h)) &\stackrel{\text{def}}{=} c_h(\mathbf{z}_h; \mathbf{u}_h, \mathbf{v}_h) + 2\mu(\boldsymbol{\epsilon}(\mathbf{u}_h), \boldsymbol{\epsilon}(\mathbf{v}_h))_{\Omega^f} \\ &\quad - (p_h, \boldsymbol{\nabla} \cdot \mathbf{v}_h)_{\Omega^f} + (q_h, \boldsymbol{\nabla} \cdot \mathbf{u}_h)_{\Omega^f} \\ &\quad + s_{\Omega^f}(\mathbf{z}_h; \mathbf{u}_h, \mathbf{v}_h), \end{aligned}$$

and convective trilinear form

$$c_h(\mathbf{z}_h; \mathbf{u}_h, \mathbf{v}_h) \stackrel{\text{def}}{=} (\mathbf{z}_h \cdot \boldsymbol{\nabla} \mathbf{u}_h, \mathbf{v}_h)_{\Omega^f} + \frac{\rho^f}{2} ((\boldsymbol{\nabla} \cdot \mathbf{z}_h) \mathbf{u}_h, \mathbf{v}_h)_{\Omega^f}.$$

The SUPG/PSPG and *grad-div* stabilizations (see, e.g., [Tezduyar \(1992\)](#)), are considered in order to treat the instabilities associated to the inf-sup incompatibility of the fluid discrete spaces, namely

$$\begin{aligned} s_{\Omega_h^n, h}(\mathbf{z}_h; \mathbf{u}_h, \mathbf{v}_h) &\stackrel{\text{def}}{=} \sum_{K \in \mathcal{T}_h^f} \int_K \frac{\lambda_C h^2}{\delta_h} (\boldsymbol{\nabla} \cdot \mathbf{u}_h) (\boldsymbol{\nabla} \cdot \mathbf{v}_h) \\ &\quad + \sum_{K \in \mathcal{T}_h^f} \int_K \delta_h \left(\rho^f (\mathbf{z}_h \cdot \boldsymbol{\nabla}) \mathbf{u}_h + \boldsymbol{\nabla} p_h \right) \cdot \left(\rho^f (\mathbf{z}_h \cdot \boldsymbol{\nabla}) \mathbf{v}_h + \boldsymbol{\nabla} q_h \right), \quad (4.13) \\ \delta_h &\stackrel{\text{def}}{=} \lambda_M \left(\rho^f \sqrt{\frac{4}{\tau^2} + \frac{16\mu^2}{h^4(\rho^f)^2} + \frac{4|\mathbf{z}_h|^2}{h^2}} \right)^{-1}, \end{aligned}$$

with $\lambda_M, \lambda_C > 0$ user-defined parameters. Note that the pressure approximation is continuous, so that in order to enhance mass conservation across the interface we consider the approach by (see, e.g., [Kamensky et al. \(2015\)](#)) which consists in boosting the grad-div stabilization in a vicinity of the interface. Note that this improved mass conservation is obtained at expense of a perturbation of the conditioning of the fluid system. Concretely, the stabilization parameter in (4.13) are modified in a neighborhood ω_h^n of the interface Σ_h^n , typically two layers of fluid elements on each side, as follows:

$$\lambda_C = 1 \quad \text{in} \quad \Omega^f, \quad \lambda_M = \begin{cases} 1 & \text{in} \quad \Omega^f \setminus \omega_h^n, \\ \varepsilon_M & \text{in} \quad \omega_h^n, \end{cases}$$

with $0 < \varepsilon_M \ll 1$ a user-defined parameter.

In the numerical experiments of Section 4.4, we consider the alternative fictitious domain method reported in Algorithm 4.3, where we introduce the *fluid-to-solid* Lagrange interpolation operator $\mathbf{B}_h : [C^0(\Sigma)]^d \rightarrow \mathbf{W}_h$.

The main advantages of this scheme, with respect to the strongly coupled problem (4.11) (4.12), are the fact that it is loosely coupled and it does not introduce additional unknown in the fluid problem, by giving an explicit expression for the Lagrange multiplier. This is achieved by applying mass lumping in the solid. Note that the solid inertia and the fluid are implicitly coupled in (4.14), which guarantees added-mass stability.

Algorithm 4.3 Loosely coupled FD scheme (from Boilevin-Kayl et al. (2019a))

For $n \geq 2$,

1. Interface update: $\phi_h^n = \mathbf{I}_\Sigma + \mathbf{d}_h^{n-1}$.
2. Fluid step: find $(\mathbf{u}_h^n, p_h^n) \in \mathbf{V}_h \times Q_h$, such that

$$\begin{aligned} & \rho^f (\partial_\tau \mathbf{u}_h^n, \mathbf{v}_h)_{\Omega^f} + a_h^f(\mathbf{u}_h^{n-1}; (\mathbf{u}_h^n, p_h^n), (\mathbf{v}_h, q_h)) \\ & \quad + \frac{\rho^s \varepsilon}{\tau} (\mathbf{B}_h(\mathbf{u}_h^n \circ \phi_h^n), \mathbf{B}_h(\mathbf{v}_h \circ \phi_h^n))_{\Sigma, h} \\ & = \frac{\rho^s \varepsilon}{\tau} (2\dot{\mathbf{d}}_h^{n-1} - \dot{\mathbf{d}}_h^{n-2}, \mathbf{B}_h(\mathbf{v}_h \circ \phi_h^n))_{\Sigma, h} - b_h(\boldsymbol{\lambda}_h^{n-1}, \mathbf{B}_h(\mathbf{v}_h \circ \phi_h^n)), \end{aligned} \quad (4.14)$$

for all $(\mathbf{v}_h, q_h) \in \mathbf{V}_h \times Q_h$.

3. Evaluate fluid load: find $\boldsymbol{\lambda}_h^n \in \boldsymbol{\Lambda}_h$, such that

$$b_h(\boldsymbol{\lambda}_h^n, \mathbf{w}_h) = \frac{\rho^s \varepsilon}{\tau} (\mathbf{B}_h(\mathbf{u}_h^n \circ \phi_h^n) - 2\dot{\mathbf{d}}_h^{n-1} + \dot{\mathbf{d}}_h^{n-2}, \mathbf{w}_h)_{\Sigma, h} + b_h(\boldsymbol{\lambda}_h^{n-1}, \mathbf{w}_h), \quad (4.15)$$

for all $\mathbf{w}_h \in \mathbf{W}_h$.

4. Solid step: find $\mathbf{d}_h^n \in \mathbf{W}_h$, with $\dot{\mathbf{d}}_h^n = \partial_\tau \mathbf{d}_h^n$, such that

$$\rho^s \varepsilon (\partial_\tau \dot{\mathbf{d}}_h^n, \mathbf{w}_h)_{\Sigma, h} + a^s(\mathbf{d}_h^n, \mathbf{w}_h) - \frac{\gamma_C E \varepsilon}{2h^2} \int_\Sigma [g_{\varepsilon_h}(\mathbf{d}_h^n)]_{\mathbb{R}^-} \cdot \llbracket \mathbf{w}_h \rrbracket = b_h(\boldsymbol{\lambda}_h^n, \mathbf{w}_h), \quad (4.16)$$

for all $\mathbf{w}_h \in \mathbf{W}_h$.

4.4 Numerical experiments

The purpose of this section is to illustrate the performance of the Nitsche-XFEM method for fluid-structure-contact interaction with multiple immersed structures (Algorithm 4.1), introduced in Section 4.3.2, in a 2D numerical example. To this end, we compare the numerical solution provided by Algorithm 4.1 with those of Algorithms 4.2 and 4.3. We recall that we express the units in the CGS system. In Algorithm 4.1, we select the Nitsche's penalty parameter as $\gamma = 100$ and $\gamma_v = \gamma_p = 10^{-2}$; in Algorithm 4.2 we consider $\lambda_M = 1$, while in Algorithm 4.3 we set $\lambda_C = 0.1$, $\lambda_M = 1$ and $\varepsilon_M = 10^4$. In the following, a non-linear Reissner–Mindlin beam model is considered for the solid. Its spatial approximation is based on linear MITC (Mixed Interpolation of Tensorial Components) elements, involving two displacements and one rotation as degrees of freedom per node in the increments (see, e.g., Bathe (1996)).

We consider a cross-shaped fluid domain and two idealized closed vertical valves in the horizontal branches. The considered geometry is displayed in Figure 4.7. The fluid domain bounding box is $[0, 1.25] \times [0, 1.5]$. The solids reference configurations are, respectively, $\Sigma_1 = 0.5 \times [0.5, 1]$ and $\Sigma_2 = 0.75 \times [0.5, 1]$.

Regarding the fluid boundary conditions, a zero traction is enforced on Γ_{out} and a

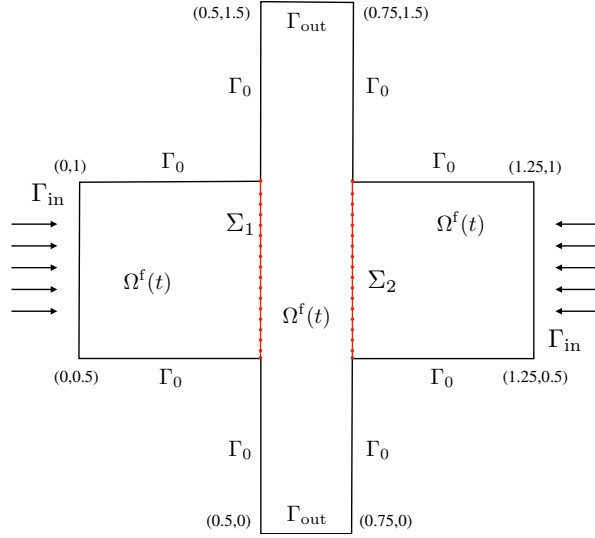


Figure 4.7: Geometric configuration of two idealized closed valves Σ_1 and Σ_2 immersed in a cross shape domain Ω^f .

time-dependent traction is imposed on Γ_{in} in terms of a sinusoidal time-dependent pressure $p_{\text{in}}(t)$, namely,

$$p_{\text{in}}(t) = 1.3 \cdot 10^4 \cdot \sin(2\pi t), \quad \forall t > 0.$$

Additionally, a no-slip boundary condition is prescribed on Γ_0 . The solids, Σ_1 and Σ_2 are clamped at their endpoints, hence the displacement, on both directions, and the rotations are set to zero.

The considered physical parameters for the fluid are $\rho^f = 1$ and $\mu = 0.035$. For the solid, we have $\rho^s = 1.2$, the Young's modulus $E = 7.5 \cdot 10^5$, thickness $\varepsilon = 0.0212$ and Poisson's ratio $\nu = 0.4$. The time-step is $\tau = 10^{-3}$ and the final time is $T = 1$, while for the contact gap we consider $\varepsilon_h = 5 \cdot 10^{-3}$ and $\gamma_C = 2 \cdot 10^{-3}$. The space discretization parameter is selected as $h \approx 0.02$ for Algorithm 4.1 and Algorithm 4.2, with the only difference that the fluid and solid meshes are fitted in Algorithm 4.2. For Algorithm 4.3, we consider the same space discretization for the fluid mesh, while, to overcome leaking issues, we use a finer solid mesh. The unstructured unfitted fluid mesh is composed by 5210 triangles, while for the fitted by 5362. The solid meshes contain, respectively, 52 edges for Algorithm 4.1-4.2 and 100 for Algorithm 4.3.

We first discuss the results of Algorithm 4.1. Figure 4.8 shows the structures location at different time instants. As the inlet pressure increases, the solids start to bend one towards the other. At $t = 0.25$ we reach the maximum positive pressure at the inlet, therefore the structures are at their minimum distance and they get into contact (see Figure 4.8(a)). After $t = 0.25$, the pressure decreases reaching zero at $t = 0.5$ (Figure 4.8(b)). At $t = 0.75$ the inlet pressure reaches the negative minimum and the structure are at their maximum distance, as shown in Figure 4.8(c). Afterward, the pressure increases and the solids approach again reaching the final state at $t = 1$ (see Figure 4.8(d)). Note that the solids move symmetrically, due to the underlying symmetry of the problem.

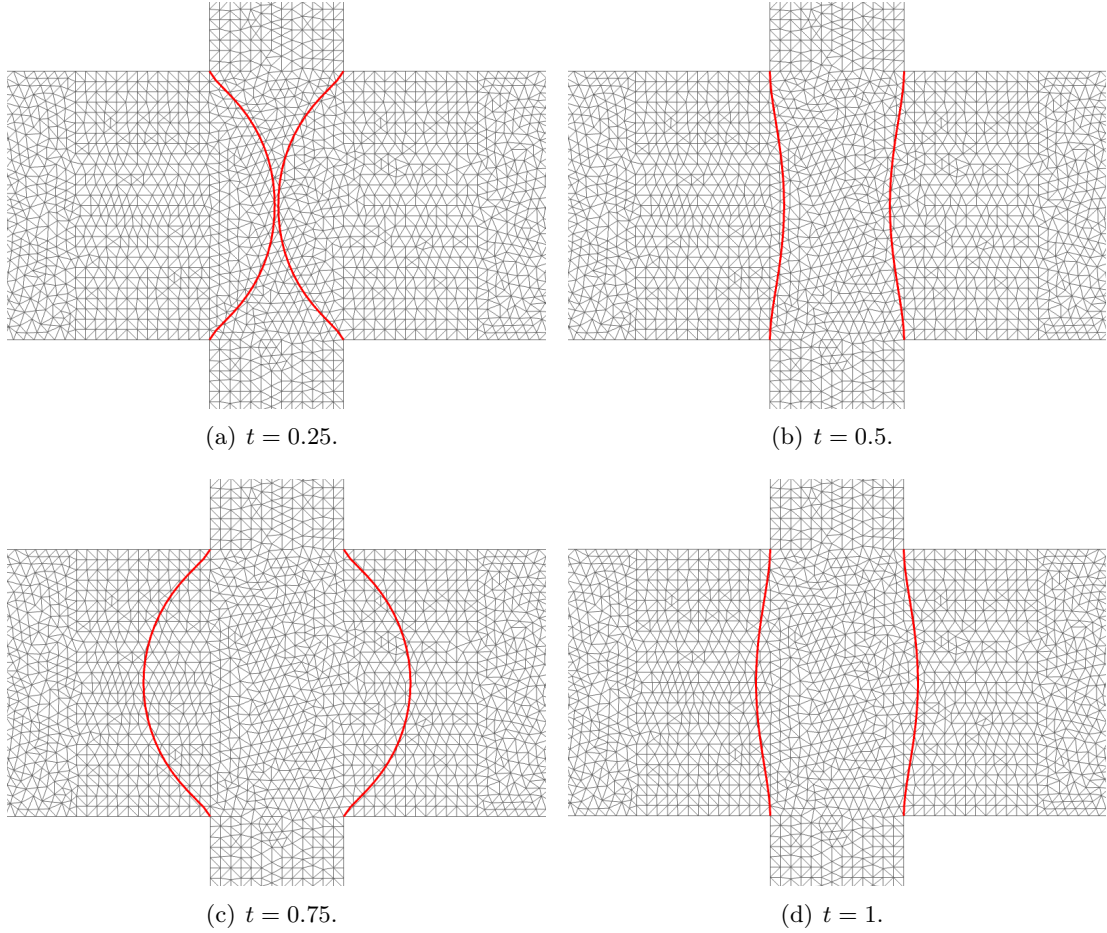


Figure 4.8: Deformed solid configurations at different time instants obtained with Algorithm 4.1.

At $t = 0.25$ the solids get into contact and cut the same fluid elements. In Figure 4.9(a), we highlight the fluid elements intersected by both structures. It can be noticed that, a small gap (smaller than the element size) remains between the structures, since we consider a relaxed contact approximation. We show in Figure 4.9(b) the effect of the duplication procedure described in Section 4.3.2.2. The elements highlighted in Figure 4.9(a) are duplicated twice as shown in Figure 4.9(b), the first in green and the second in red.

For illustration purposes, we display in Figure 4.10 some snapshots of the pressure elevation corresponding to the time instants of Figure 4.8. At each instant, the pressure jumps across the two interfaces are well captured. Figure 4.11 provides the corresponding fluid velocity magnitudes. When the structures start to approach, they squeeze the fluid in the middle channel, creating a flow in direction of Γ_{out} , until the structures stop at contact. Note that the fluid velocity is very low during contact (see Figure 4.11 (a)). Afterward, they move away and the flow is restored (see Figure 4.11 (b)). At that moment, the fluid enters from Γ_{out} . When the minimum pressure is reached at $t = 0.75$, the structures velocity is very low and the fluid is at rest (see Figure 4.11 (c)), until move towards the

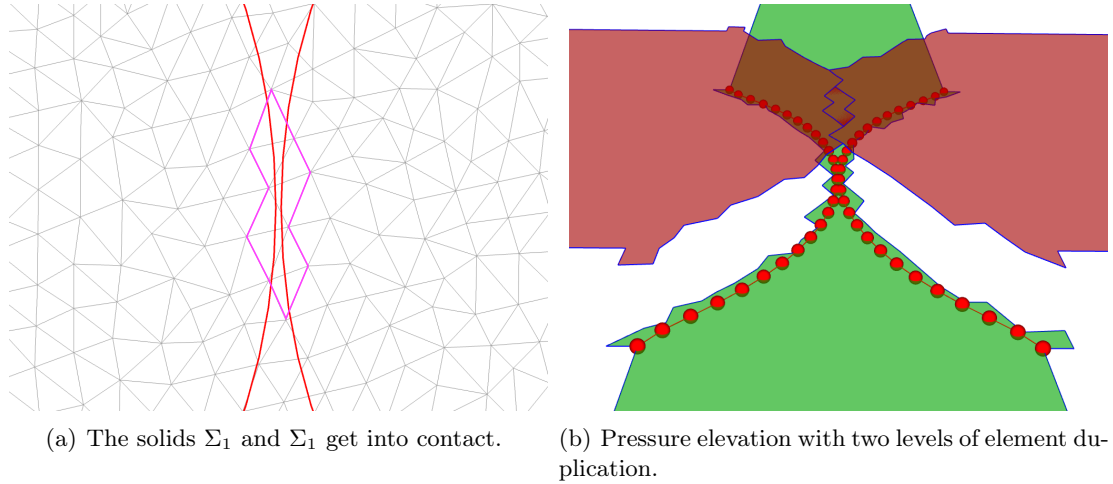


Figure 4.9: Zoom on the structures at contact, $t = 0.25$. The fluid elements highlighted in (a) are triplicated in (b), where the three copies of the elements are visible.

central channel, pushing again the fluid across Γ_{out} .

We now compare the results of Algorithm 4.1 with those obtained with Algorithms 4.2 and 4.3. Since we are mostly interested on the contact phenomenon, we focus our attention at $t = 0.25$. We show in Figure 4.12 the pressure elevations at $t = 0.25$ obtained with the three numerical methods. A very good agreement is visible between the solutions obtained with Algorithm 4.1 and Algorithm 4.2. The pressure is discontinuous and they well represent the exact pressure jump across the interface. Algorithm 4.3 provides a reasonable continuous approximation with a sharp gradient. Note however, that the gap between the two solids is larger when compared with those provided by Algorithms 4.1 and 4.2. In fact, in contrast to Algorithms 4.1-4.2, solid contact is not detected with Algorithm 4.3 from $t = 0.178$ until $t = 0.325$ and a layer of one or more fluid elements remains in between the two solids. This might be a consequence of: (i) a locking effect of the penalized grad-div term; or (ii) the leaking induced by the Robin treatment of the kinematic condition. The last point is illustrated in Figure 4.13, where we report the velocity magnitudes obtained with the three numerical methods. Note that spurious velocities are visible for Algorithm 4.3 (Figure 4.13(b)).

Figure 4.14 reports the deformed configurations of the solids and fluid meshes at $t = 0.25$. As a consequence of the fitted nature of Algorithm 4.2, the fluid elements between the structures are squeezed (see Figure 4.14(a)). This seems to not perturb the quality of the numerical solution in this example, indeed, Algorithms 4.1-4.2 show very small gaps (see Figure 4.14(c)). On the contrary, contact is not activated with Algorithm 4.3, which is visible in Figure 4.14(b) with larger gap.

We conclude this section with a space-time refinement study, by taking, $(h, \tau) \in \{0.04 \cdot 2^{-i}, 2 \cdot 10^{-3} \cdot 2^{-i}\}_{i=0}^2$. We recall that for Algorithm 4.3 we consider a finer solid mesh, typically taking twice the number of nodes with respect to Algorithms 4.1-4.2. The contact gap $\varepsilon_h = \varepsilon_h(h)$ is selected accordingly as $\varepsilon_h \in \{0.01 \cdot 2^{-i}\}_{i=0}^2$. We report in Figure 4.15

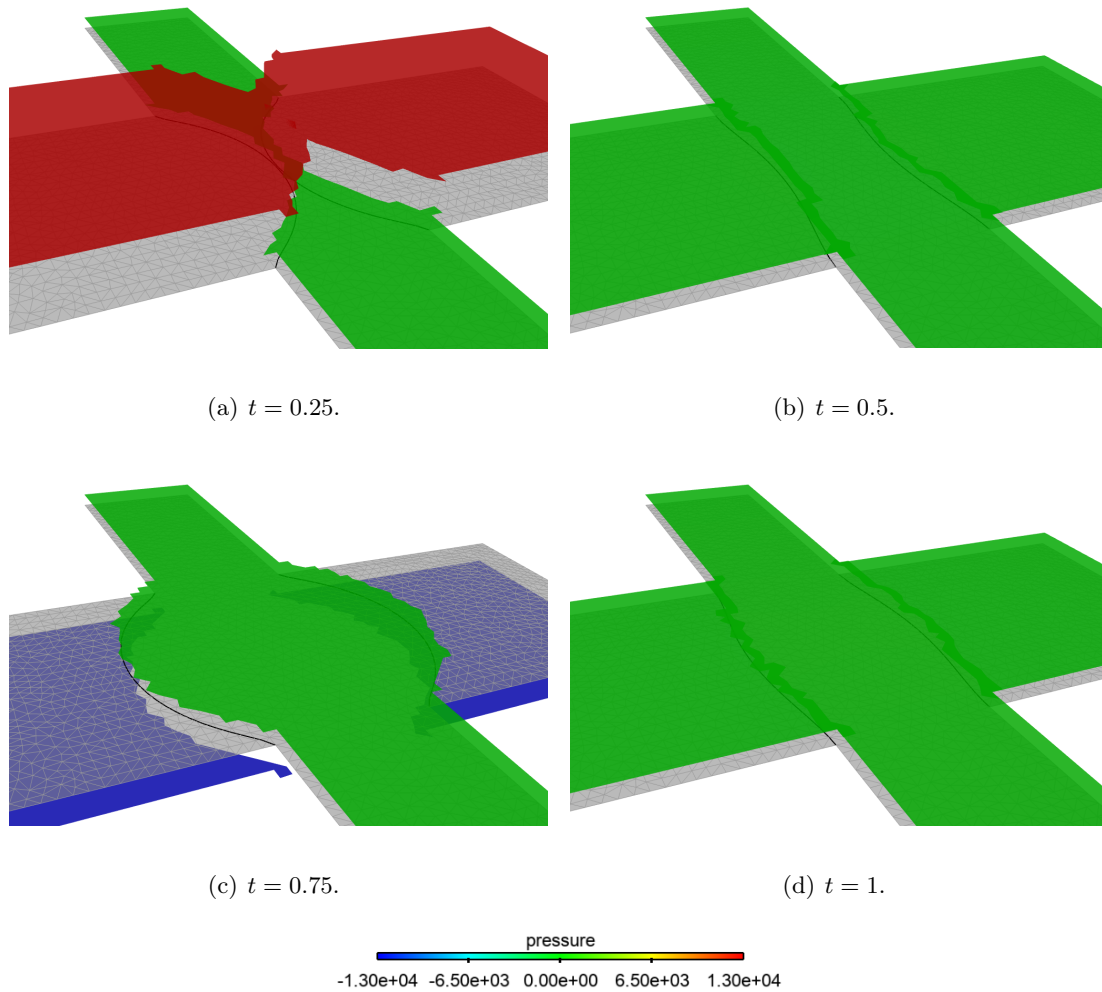


Figure 4.10: Pressure elevation at different time instants of the solution obtained with Algorithm 4.1.

the time history of the x -displacement at the middle left solid node. As previously noted, the very good agreement between Algorithms 4.1 and 4.2 is clearly visible. Figure 4.15 shows a convergent behavior of the approximations provided by Algorithm 4.3 towards those of Algorithms 4.1 and 4.2. Figure 4.15 points out that in Algorithms 4.1 and 4.2 the solids get into contact. This is not the case of Algorithm 4.3, even with the finest grid. Finally, we display in Figure 4.16 the velocity magnitude of the solution obtained via Algorithm 4.3 with the finest discretization. The spurious velocity are still present, but they reduce with refinement.

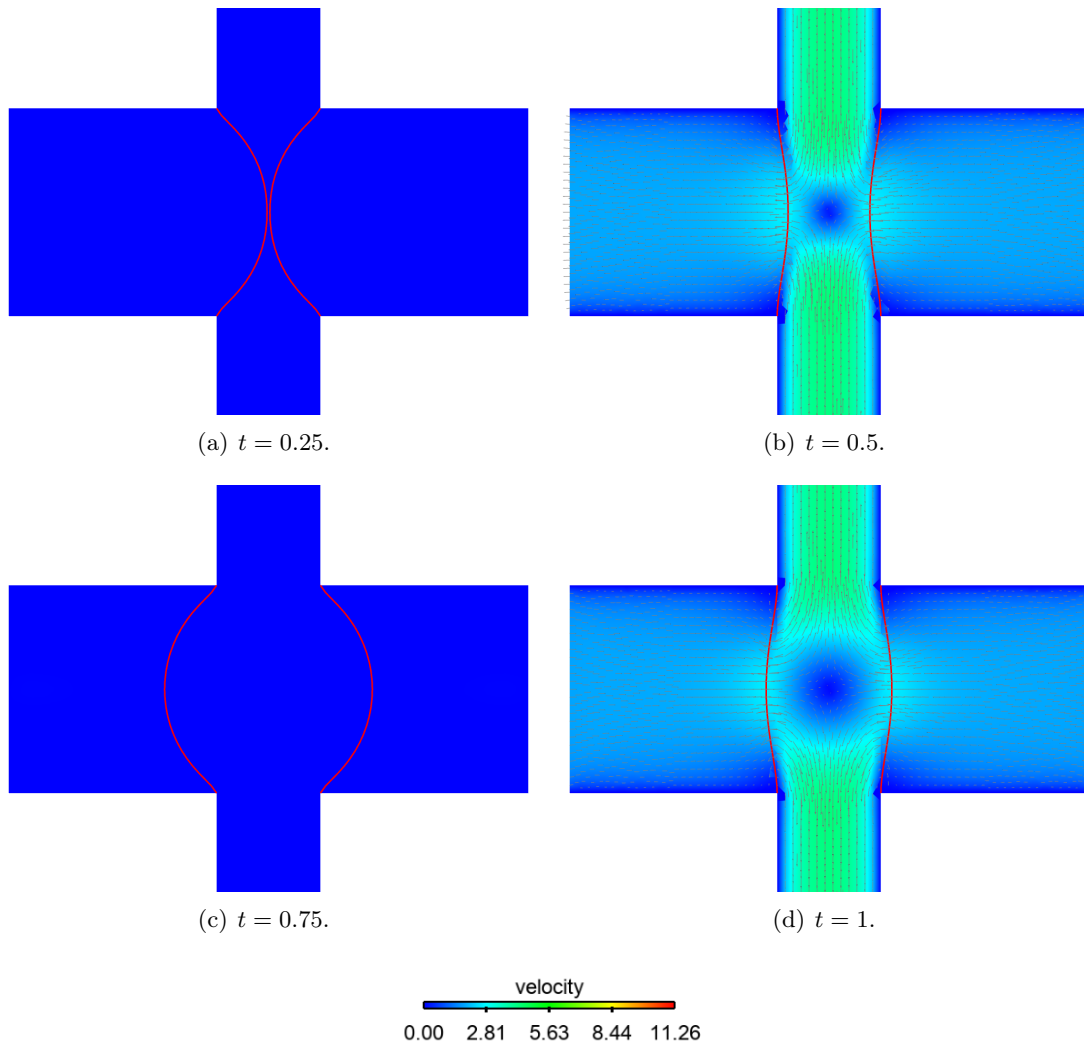


Figure 4.11: Velocity magnitude obtained with Algorithm 4.1.

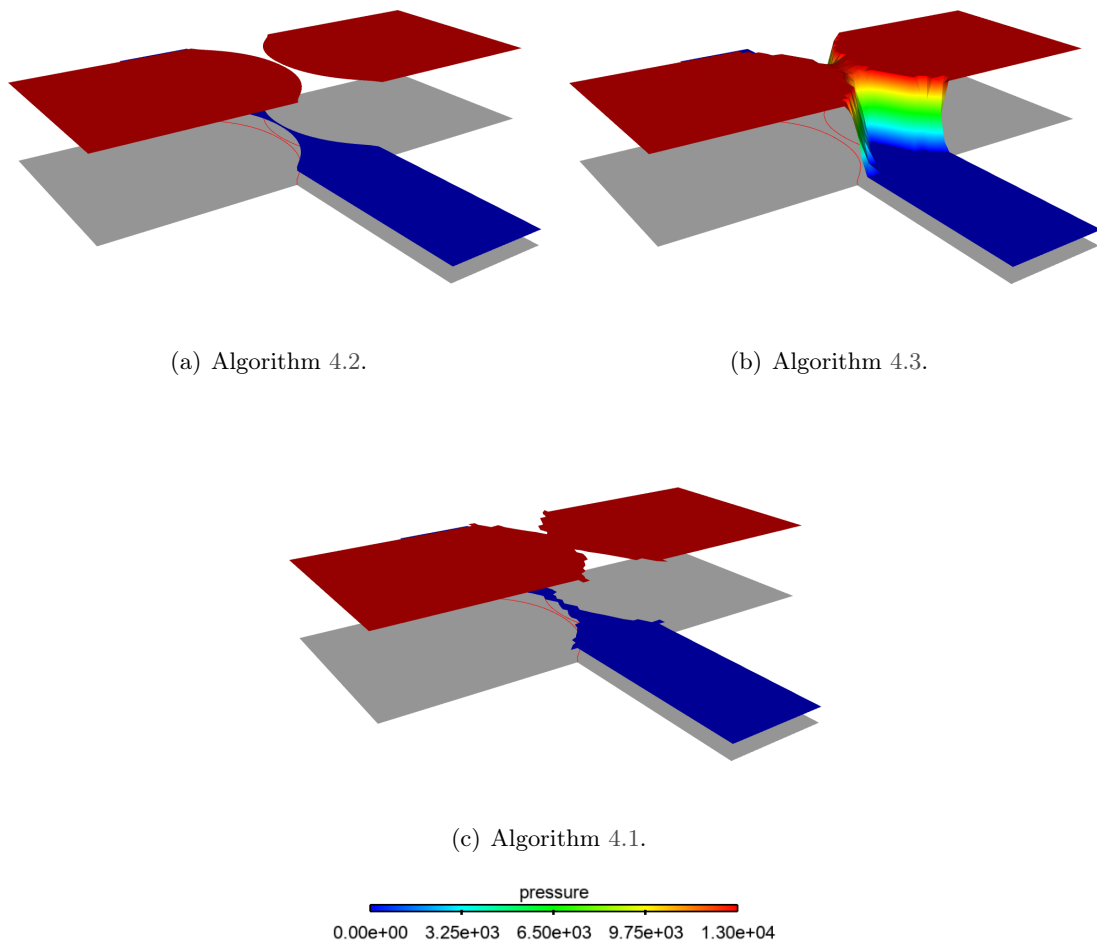


Figure 4.12: Pressure elevation at $t = 0.25$ obtained with the three considered numerical methods.

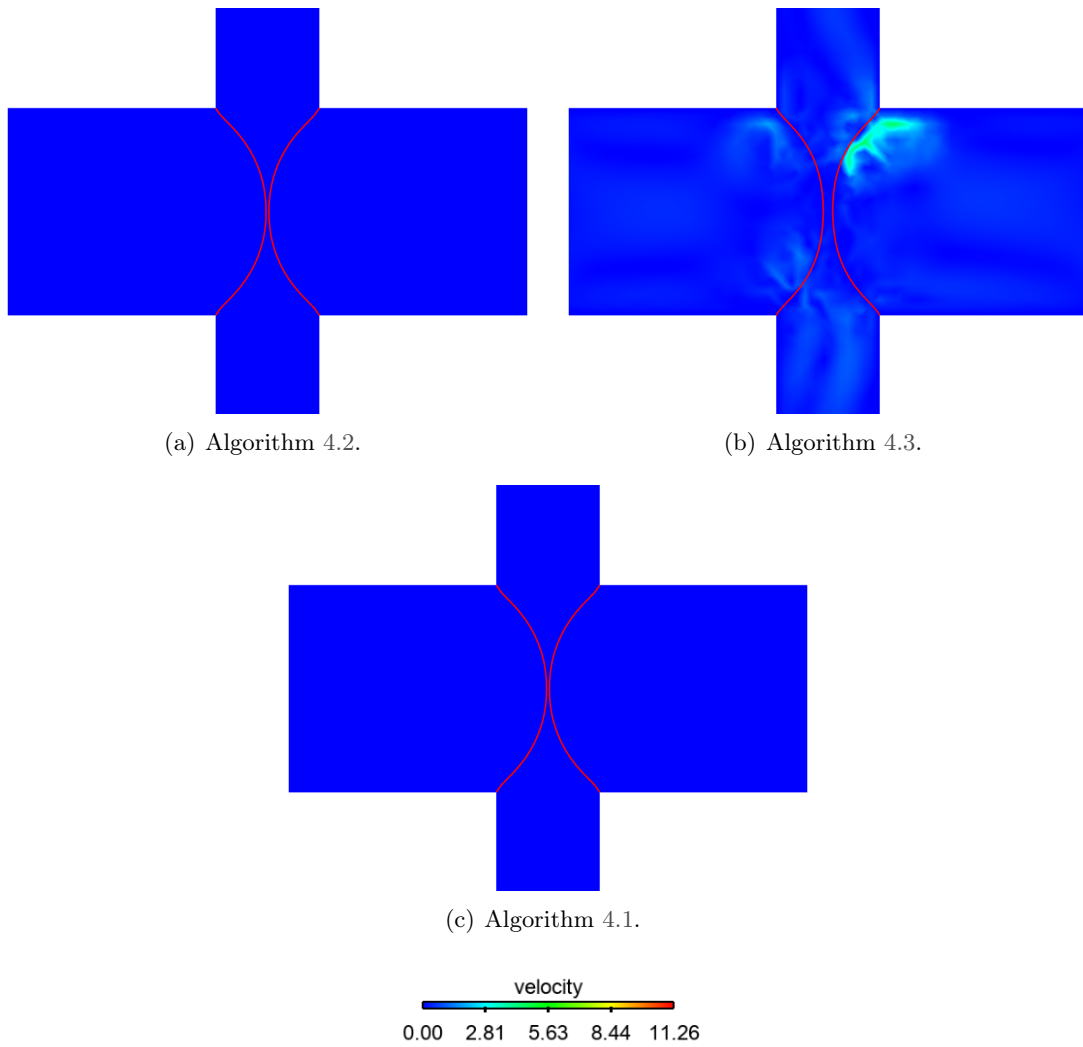
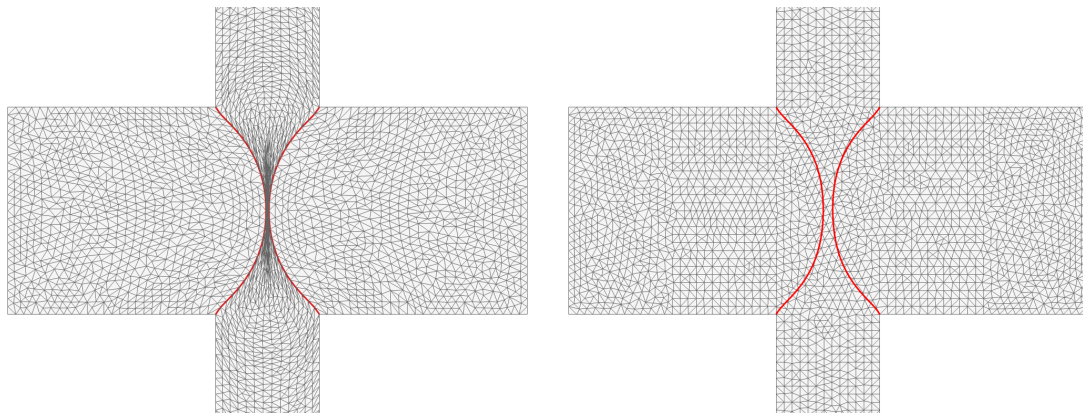
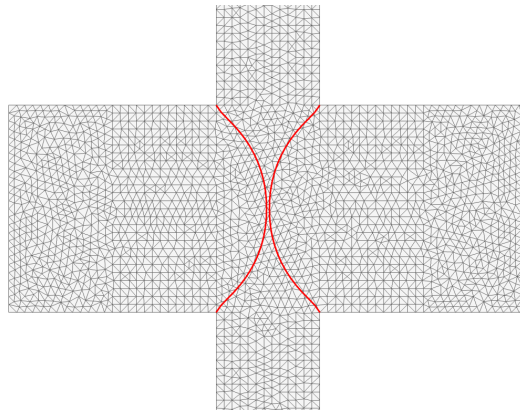


Figure 4.13: Velocity magnitude at $t = 0.25$ obtained with the three considered numerical methods.



(a) Algorithm 4.2.

(b) Algorithm 4.3.



(c) Algorithm 4.1.

Figure 4.14: Deformed structures at $t = 0.25$, obtained with the three numerical methods.

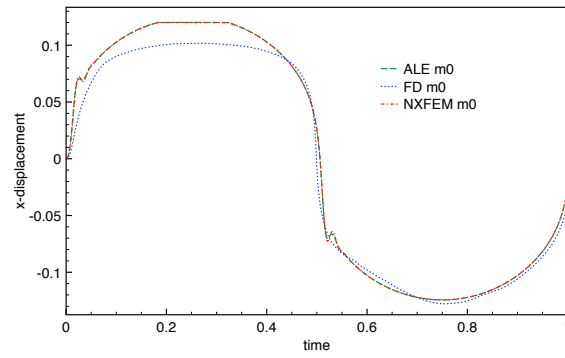
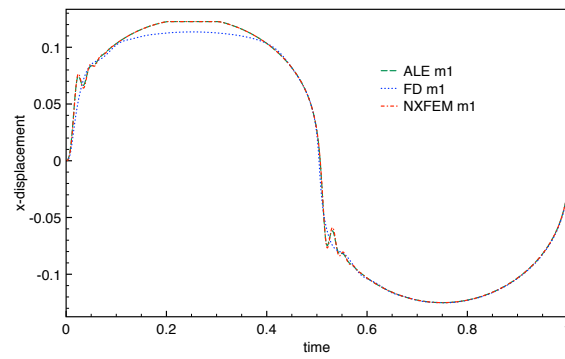
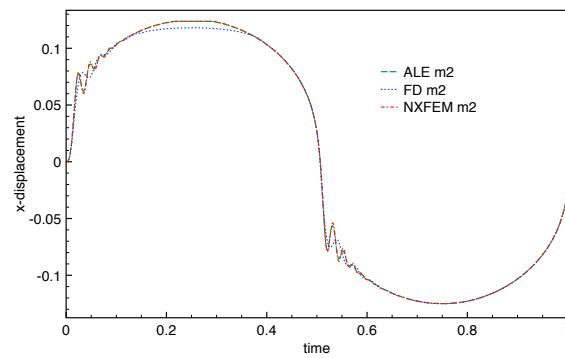
(a) $i = 0$.(b) $i = 1$.(c) $i = 2$.

Figure 4.15: Time history of the x -displacement at the middle structure point of the left structure, for different levels of space-time refinement.

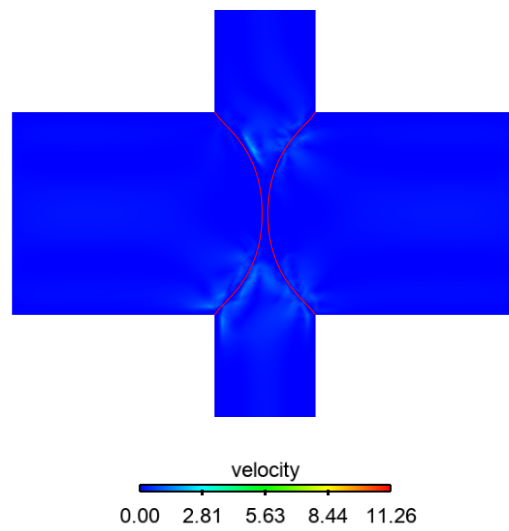


Figure 4.16: Velocity magnitude at $t = 0.25$ obtained with Algorithm 4.3 and $(h, \tau) = (0.01, 5 \cdot 10^{-4})$.

4.5 Conclusion

In this chapter, we have presented a new numerical method, based on unfitted mesh and Nitsche-XFEM framework, for the approximation of fluid-structure-contact interaction problems with immersed thin-walled solids. The introduced method extends the Nitsche-XFEM approximation from [Alauzet et al. \(2016\)](#) to the case of contact with multiple structures. The main features of the method can be summarized as follows:

- Consistent spacial approximation through the Nitsche-XFEM framework using a relaxed contact formulation;
- Ad hoc intersection and duplication strategies guarantee consistency and correctness of the overlapping meshes.

The Nitsche-XFEM method for contact is compared with fitted ALE and unfitted FD methods. Similar results are observed with Nitsche-XFEM and ALE methods, while FD suffers of no-collision and spurious velocity, particularly for the coarsest approximations. The main drawback of the presented methodology is that an additional duplication level complicates the computer implementation and major intrusive modifications were necessary within the existent fluid solver. Ongoing work concerns the extension to partially intersected fluid domain using the fictitious solid method proposed in Chapter 6, as well as the extension to 3D.

A mechanically consistent fluid-structure-contact interaction model

In this chapter we introduce a mixed dimensional fluid-structure-contact coupling model, in which we include a thin-walled porous layer, in order to model surface asperities. The thin-walled porous layer introduces tangential creeping flow along the boundary and allows for the modelling of boundary flow due to surface roughness, giving physical sense to the fluid stresses at contact and bringing mechanical consistency at contact and release. Numerical examples are reported for both Stokes'-Darcy coupling alone, as well as fluid-structure-Darcy-contact at the porous boundary layer.

Some of the results of this chapter have been reported in:

- E. Burman, M. A. Fernández, S. Frei, and F. M. Gerosa. **3D-2D Stokes-Darcy coupling for the modelling of seepage with an application to fluid-structure interaction with contact.** *Chapter 20 of F. J. Vermolen, C. Vuik (eds.), Numerical Mathematics and Advanced Applications ENUMATH 2019, Lecture Notes in Computational Science and Engineering, Vol. 139, 2020.* DOI: 10.1007/978-3-030-55874-1_20. Available online: <https://hal.inria.fr/hal-02417042>.

Contents

5.1 Introduction	122
5.2 Mathematical models	123
5.2.1 Darcy model with porous interface	123
5.2.2 Coupled Stokes and thin-walled Darcy model	126
5.2.3 Relaxed contact condition	128
5.2.4 Coupled fluid-structure-porous interaction model with contact	130
5.2.5 Numerical approximation	132
5.3 Numerical experiments	136
5.3.1 Reservoirs connected via porous layer	136
5.3.2 Idealized valve with contact	138
5.4 Conclusions	150

5.1 Introduction

Building a consistent fluid-structure-contact interaction numerical method is an highly complicate and challenging problem. As introduced in Section 1.2.4, between the typical numerical contact approaches, we can distinguish *real* and *relaxed* contact approximations. Both approximations suffer of consistency loss, at contact for the relaxed approximation and at release for the realistic one. In fact, in the relaxed approximation, the solid is simultaneously in contact and coupled with the fluid, which results in an incorrect balance of stresses (breaking the Newton's third law).

Contrarily to dry contact, when fluid-structure-contact is considered, the fluid serves as link between the contacting bodies, allowing stresses exchange even before contact. In fact, the fluid between the contacting bodies severely impacts the contact dynamics (for instance, the pulsating blood flow pilots the closure and opening of heart valves). It has recently been observed by several authors [Ager et al. \(2019a\)](#), [Burman et al. \(2020a\)](#) that the consistent modelling of fluid-structure interaction with contact requires a fluid model, in particular a pressure, also in the contact zone. Indeed, some seepage is expected to occur due to permeability of the contacting bodies or their surface roughness. Otherwise there is no continuous mechanism for the release of contact and non-physical voids can occur.

For instance, [Ager et al. \(2019b\)](#) propose to include the modelling of fluid stress in the contact zone, by an extension approach coupled with some compatibility conditions on the intersection between fluid-solid interface and solid-solid region.

Similar ideas were introduced in [Burman et al. \(2020a\)](#), but for computational reasons. Indeed, in the latter reference an elastic body immersed in a fluid enters in contact with a rigid wall and to allow for a consistent numerical modelling, the permeability of the wall is relaxed. This motivates the introduction of an artificial porous medium whose permeability goes to zero with the mesh-size.

In addition, it is ambiguous if the Navier-Stokes equations are still a valid model and numerics suffer of the no-collision paradox, when smooth solids are considered, with no-slip conditions for both contacting wall and fluid-structure coupling, see e.g. [Hillairet \(2007\)](#); [Hesla \(2004\)](#); [Hillairet and Takahashi \(2009\)](#); [Burman et al. \(2020a\)](#). A no-contact result in fluid-structure interaction with a thin-walled solid and no-slip condition is proven in [Grandmont and Hillairet \(2016\)](#). Alternative approaches consist in taking a slip or Navier-slip condition on both contacting wall and in the interface coupling (see, e.g., [Gérard-Varet et al. \(2015\)](#); [Burman et al. \(2020a\)](#); [Bălilescu et al. \(2017\)](#)). In [Gérard-Varet and Hillairet \(2010\)](#); [Davis et al. \(2003\)](#), authors study mathematically the roughness-induced effect on the collision process, showing that as soon as the surface asperities are considered, contact can occur.

However, an exact resolution of the surface asperities is impractical. [Ager et al. \(2019a\)](#) proposes to introduce a poroelastic model to describe the surface roughness and the flow near the contact wall. Since the poroelastic layer is an averaged representation between the fluid and the solid description, including this model into a fluid-structure-contact interaction problem, solves the issue related to consistency loss.

Nevertheless, they do consider a realistic contact approximation, hence, the problem

related to topology changes, such as, active switch between fluid-porous, fluid-solid and solid-porous interface coupling, isolated fluid region which are artifact of the non smoothness of the interfaces at discrete level and difficult implementation, are still present.

In this chapter, we propose to overcome this issues by considering a relaxed contact formulation and a reduced order thin-walled Darcy model for the thin porous domain, neglecting the porous deformation. Such approach is enough to account physical effect as fluid pressure between the contacting bodies, partially solving the problem of the rupture of the Newton's third law, because it gives physical sens to the fluid stresses that are sent to the structure at contact. The derivation of the reduced Darcy model, is inspired from the work of [Martin et al. \(2005\)](#), in which they introduce a reduced model for flow in fractures, considered as interfaces between sub-domains.

The rest of the chapter is organized as follows. In Section 5.2 we describe the mathematical models, in particular, the thin-walled Darcy model is introduced in Section 5.2.1, via an averaging approach across the thickness. Then, in Section 5.2.2, we describe the continuous coupled Stokes'-Darcy model. In Section 5.2.3, we present the relaxed contact model and in Section 5.2.4 the coupled fluid-structure-porous interaction model with contact. Section 5.2.5 is dedicated to the description of the numerical approximation of the fluid-structure-porous-contact interaction model. We illustrate numerically the models in Section 5.3, in the case of reservoirs coupling, only involving fluid and porous layer (Section 5.3.1), afterward the fluid-structure-porous contact model in Section 5.3.2. Finally, a summary of the conclusions is given in Section 5.4.

5.2 Mathematical models

In the following section, we will introduce the fundamental models necessary to define to full fluid-structure-contact model with a thin-walled Darcy interface. We will begin by describing the reduced order model for the porous interface, modeled via the Darcy equation. Afterward, before introducing the complete FSI model with contact, we explore the coupling of an incompressible fluid and the thin-walled porous layer. Such model can be seen as an intermediate step to the complete model, since we will consider a relaxed contact formulation, hence, the only coupling interface conditions appearing will be fluid-structure and fluid-porous.

5.2.1 Darcy model with porous interface

We present the reduced order Darcy model defined on the mid-surface interface of the porous domain Ω_p , based in the work of [Martin et al. \(2005\)](#) for fractures. The filtration of an incompressible fluid through a porous medium is often described by the Darcy's law. This mathematical relationship provides the simplest linear relation between velocity and pressure in porous medium under the physically reasonable assumption that fluid flows are usually very slow and all the inertial and non-linear terms may be neglected. Groundwater flows could be treated microscopically by the laws of hydrodynamics. However, the seepage path is tortuous and it branches into a multitude of ramifications. Darcy's law avoids the severe difficulties of modeling a microscopic picture via homogenization. In fact, it

describes an homogenized flow velocity, the Darcy velocity u_l , through a given cross section of the porous medium, rather than the true fluid velocity. We consider a Darcy flow model in a thin-walled domain $\Omega_p = \Sigma_1 \times (-\frac{\varepsilon_p}{2}, \frac{\varepsilon_p}{2}) \in \mathbb{R}^d$ for $d = 2, 3$, with mid-surface Σ_1 .

$$\begin{cases} \nabla \cdot \mathbf{u}_l = 0 & \text{in } \Omega_p, \\ \mathbf{u}_l + K \nabla p_l = 0 & \text{in } \Omega_p, \end{cases} \quad (5.1)$$

where u_l denotes the Darcy velocity, p_l the Darcy pressure and K is a symmetric positive definite and bounded tensor $K = (K_{ij})_{i,j=1,\dots,d}$, $K_{ij} \in L^\infty(\Omega_p)$, $K_{ij} > 0$, $K_{ij} = K_{ji}$, called hydraulic conductivity tensor, which depends on the properties of the fluid as well as on the characteristics of the porous medium. Suitable boundary condition will be included afterward. Let \mathbf{n} be the unit normal vector of the mid-surface Σ_1 that points towards the exterior boundary γ_+ and $\boldsymbol{\tau}$ the corresponding tangential parts (see Figure 5.1). In order to derive the Darcy reduced order model on the mid-surface interface, we proceed by averaging the Darcy equation across the thickness, i.e., along the line segments $[\mathbf{s} - \frac{\varepsilon_p}{2}\mathbf{n}, \mathbf{s} + \frac{\varepsilon_p}{2}\mathbf{n}]$, $\mathbf{s} \in \Sigma_1$ normal to Σ_1 .

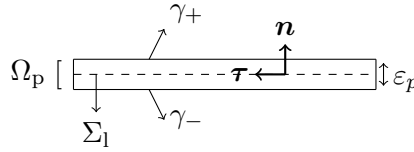


Figure 5.1: Porous geometric configuration

We first decompose the unknown and the differential operators using the curvilinear system defined by the tangential and normal vectors to the mid-surface Σ_1 , i.e., $\mathbf{x}(s, t) = s\boldsymbol{\tau} + t\mathbf{n}$. This yields the following decomposition for the velocity

$$\mathbf{u}_l = \mathbf{u}_{l,\tau} + \mathbf{u}_{l,n},$$

with $\mathbf{u}_{l,\tau} = u_{l,\tau}\boldsymbol{\tau}$ and $\mathbf{u}_{l,n} = u_{l,n}\mathbf{n}$. Let denote with ∇_τ and div_τ respectively the tangential gradient and divergence operator and with ∇_n and div_n the normal gradient and divergence operator.

Averaging the conservation equation

Using the above notation we may rewrite the divergence operator as

$$\text{div } \mathbf{u}_l = \text{div}_\tau u_{l,\tau} + \text{div}_n u_{l,n} \quad \text{in } \Omega_p.$$

We can rewrite (5.1)₁ as

$$\text{div}_\tau u_{l,\tau} + \text{div}_n u_{l,n} = 0 \quad \text{in } \Omega_p.$$

Then, integrating the mass conservation equation across the thickness we obtain

$$\operatorname{div}_\tau \int_{-\frac{\varepsilon_p}{2}}^{\frac{\varepsilon_p}{2}} u_{l,\tau} \, dt + u_{l,n}|_{\gamma_+} - u_{l,n}|_{\gamma_-} = 0 \quad \text{in } \Sigma_1.$$

By introducing the following notation for the averaged tangential velocity

$$U_l \stackrel{\text{def}}{=} \int_{-\frac{\varepsilon_p}{2}}^{\frac{\varepsilon_p}{2}} u_{l,\tau} \, dt,$$

we finally get

$$\operatorname{div}_\tau U_l = -u_{l,n}|_{\gamma_+} + u_{l,n}|_{\gamma_-} \quad \text{in } \Sigma_1. \quad (5.2)$$

The averaged conservation equation remains a mass conservation equation for the averaged tangential Darcy velocity but with an additional source term representing the flow penetrating into the porous medium from the adjacent domains.

Averaging Darcy's law

Using the same approach we can decompose the Darcy's equation (5.1)₂ as

$$\begin{aligned} u_{l,\tau} + K_\tau \nabla_\tau p_l &= 0 \quad \text{in } \Omega_p, \\ u_{l,n} + K_n \nabla_n p_l &= 0 \quad \text{in } \Omega_p, \end{aligned} \quad (5.3)$$

where, K_n and K_τ are decompositions of K , such that $K_n \stackrel{\text{def}}{=} \mathbf{n}^T K \mathbf{n}$ and $K_\tau \stackrel{\text{def}}{=} \boldsymbol{\tau}^T K \boldsymbol{\tau}$. Let assume that K_τ is constant along the segment $[s - \frac{\varepsilon_p}{2} \mathbf{n}, s + \frac{\varepsilon_p}{2} \mathbf{n}]$. Afterward, by integrating the first equation of (5.3) across the thickness we get

$$U_l + \varepsilon_p K_\tau \nabla_\tau P_l = \quad \text{in } \Sigma_1. \quad (5.4)$$

where we have used the averaged pressure across the thickness, defined as:

$$P_l \stackrel{\text{def}}{=} \frac{1}{\varepsilon_p} \int_{-\frac{\varepsilon_p}{2}}^{\frac{\varepsilon_p}{2}} p_l \, dt.$$

Hence, by averaging the Darcy's equation, we obtain again a Darcy's law for the averaged pressure and tangential velocity defined on the $(d-1)$ -dimensional domain Σ_1 . Afterward, combining (5.2) and (5.4) we get the following equation for the averaged pressure

$$-\nabla_\tau \cdot (\varepsilon_p K_\tau \nabla_\tau P_l) = u_{l,n}|_{\gamma_-} - u_{l,n}|_{\gamma_+} \quad \text{in } \Sigma_1. \quad (5.5)$$

We retrieve, similarly to (5.2), a mass conservation equation with a source term representing the flow entering from the domains adjacent to Σ_1 . The remaining equation involving the normal component (5.3)₂ is now used to impose the boundary conditions.

The integration of (5.3)₂ across the thickness yields:

$$\int_{-\frac{\varepsilon_p}{2}}^{\frac{\varepsilon_p}{2}} u_{l,n} dt + K_n (p_l|_{\gamma_+} - p_l|_{\gamma_-}) = 0 \quad \text{in } \Sigma_1. \quad (5.6)$$

The first integral of (5.6) can be approximated using a trapezoidal approximation rule,

$$\int_{-\frac{\varepsilon_p}{2}}^{\frac{\varepsilon_p}{2}} u_{l,n} dt \approx \frac{\varepsilon_p}{2} (u_{l,n}|_{\gamma_+} + u_{l,n}|_{\gamma_-}),$$

so that

$$\frac{\varepsilon_p}{2} (u_{l,n}|_{\gamma_+} + u_{l,n}|_{\gamma_-}) + K_n (p_l|_{\gamma_+} - p_l|_{\gamma_-}) = 0 \quad \text{in } \Sigma_1. \quad (5.7)$$

To close the system, we introduce the following additional modeling assumption for the averaged pressure, supposing that P_l is also the average of the pressures on the boundaries γ_+ and γ_- :

$$P_l \approx \frac{1}{2} (p_l|_{\gamma_+} + p_l|_{\gamma_-}) \quad \text{in } \Sigma_1. \quad (5.8)$$

The relations (5.7) and (5.8) can be used to eliminate $p_l|_{\gamma_+}$, which yields

$$2P_l - p_l|_{\gamma_-} = p_l|_{\gamma_-} - \frac{\varepsilon_p K_n^{-1}}{2} (u_{l,n}|_{\gamma_+} + u_{l,n}|_{\gamma_-}) \quad \text{in } \Sigma_1$$

and gives the following expression for the unknown pressure $p_l|_{\gamma_+}$:

$$p_l|_{\gamma_-} = P_l + \frac{\varepsilon_p K_n^{-1}}{4} (u_{l,n}|_{\gamma_+} + u_{l,n}|_{\gamma_-}) \quad \text{in } \Sigma_1. \quad (5.9)$$

To summarize, we are look for P_l solution of (5.5) and coupled to the external medium via (5.9). Hence, the final $d - 1$ -reduced interface porous model is given by:

$$\begin{cases} -\nabla_\tau \cdot (\varepsilon_p K_\tau \nabla_\tau P_l) = u_{l,n}|_{\gamma_-} - u_{l,n}|_{\gamma_+} & \text{in } \Sigma_1, \\ p_l|_{\gamma_-} = P_l + \frac{\varepsilon_p K_n^{-1}}{4} (u_{l,n}|_{\gamma_+} + u_{l,n}|_{\gamma_-}) & \text{in } \Sigma_1. \end{cases} \quad (5.10)$$

5.2.2 Coupled Stokes and thin-walled Darcy model

Before to introduce the full FSI model with contact and porous interface, let considered the model in which we coupled the fluid with a thin-walled porous layer. The Darcy interface, Σ_1 , coincides with a part of the fluid domain Ω^f . Note that, the Darcy problem can be seen as a non local boundary condition problem for the fluid, in which classic boundary conditions are replaced by the porous problem. Additionally, \mathbf{n} and $\boldsymbol{\tau}$ are respectively, the normal and tangent vector on Σ_1 . The geometric configuration is shown in Figure 5.2. In the following, \mathbf{u} denotes the fluid velocity, u_n and u_τ its normal and tangential components, p the fluid pressure.

We will represent the normal and tangential component of the Cauchy stress tensor,

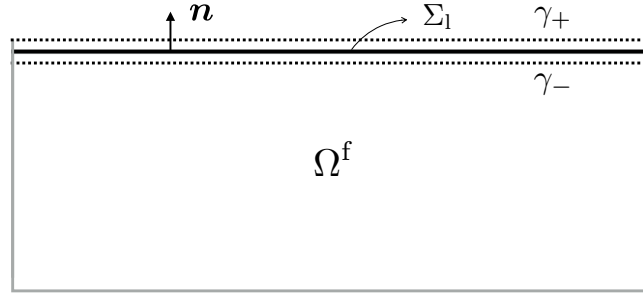


Figure 5.2: Geometric configuration of the coupled Stokes-thin-walled Darcy model.

by

$$\sigma_{nn} = \mathbf{n}^T \boldsymbol{\sigma}(\mathbf{u}, p) \mathbf{n} \quad \text{and} \quad \sigma_{n\tau} = \boldsymbol{\tau}^T \boldsymbol{\sigma}(\mathbf{u}, p) \mathbf{n}.$$

We consider the case in which a Stokes flow model is coupled to the Darcy system (5.10) on γ_- . The problem reads as follow: Find the fluid velocity and pressure $\mathbf{u} : \Omega^f \times \mathbb{R}^+ \rightarrow \mathbb{R}^d$, $p : \Omega^f \times \mathbb{R}^+ \rightarrow \mathbb{R}$, and the Darcy porous pressure $P_l : \Sigma_1 \times \mathbb{R}^+ \rightarrow \mathbb{R}$, such that, for all $t \in \mathbb{R}^+$, the following equations are satisfied

$$\begin{cases} \rho^f \partial_t \mathbf{u} - \mu \Delta \mathbf{u} + \nabla p = 0 & \text{in } \Omega^f, \\ \nabla \cdot \mathbf{u} = 0 & \text{in } \Omega^f, \end{cases} \quad (5.11)$$

$$\begin{cases} -\nabla_\tau \cdot (\varepsilon_p K_\tau \nabla_\tau P_l) = u_{l,n}|_{\gamma_-} - u_{l,n}|_{\gamma_+} & \text{in } \Sigma_1, \\ p_l|_{\gamma_-} = P_l + \frac{\varepsilon_p K_n^{-1}}{4} (u_{l,n}|_{\gamma_+} + u_{l,n}|_{\gamma_-}) & \text{in } \Sigma_1, \end{cases} \quad (5.12)$$

with interface coupling conditions

$$\begin{cases} u_n = u_{l,n} & \text{on } \gamma_-, \\ \sigma_{nn} = -p_l & \text{on } \gamma_-, \\ \sigma_{n\tau} = -\frac{\alpha}{\sqrt{K_\tau \varepsilon_p}} u_\tau & \text{on } \gamma_-. \end{cases} \quad (5.13)$$

Condition (5.13)₁ imposes the continuity of normal velocity. It should be observed that, in contrast to the situation of only fluid, the normal fluid velocity on γ_- is not zero, as the fluid can enter the porous layer. The second condition corresponds to the balance of stresses between fluid and porous layer at the interface γ_- . The latter condition in (5.13) corresponds to the so-called Beavers-Joseph-Saffmann condition (see, e.g., [Beavers and Joseph \(1967\)](#); [Saffman \(1971\)](#); [Mikelic and Jäger \(2000\)](#)). Beavers and Joseph, in [Beavers and Joseph \(1967\)](#), state that, a no-slip condition on a permeable boundary is physical only if the true fluid velocity is considered in the porous medium. The presence of a boundary layer at the permeable wall is modeled by introducing a slip velocity, proportional to the shear rate, at the permeable boundary. Note that the condition for the tangential stresses corresponds to a Navier-slip boundary condition for the fluid. The appropriate choice of the parameter α depends on the application. In the case in which γ_- corresponds to

a symmetry boundary within a larger fluid domain, where contact can take place, for instance between two contacting valves, it is appropriate to set $\alpha = 0$ (pure slip). If the porous layer is, however, placed at a rigid wall, the Beavers-Joseph-Saffmann condition with $\alpha > 0$ is more appropriate. The parameter α depends on the structure of the porous layer. Values $0.01 < \alpha < 5$ have been suggested in [Nield et al. \(2006\)](#)).

Moreover, in the upper outer porous boundary γ_+ we assume the wall to be not permeable, hence, we enforce zero normal velocity,

$$u_{l,n} = 0 \quad \text{on} \quad \gamma_+. \quad (5.14)$$

Owing to (5.13) and (5.14), relation (5.12), becomes

$$\left\{ \begin{array}{ll} -\nabla_\tau \cdot (\varepsilon_p K_\tau \nabla_\tau P_l) = u_n & \text{on} \quad \Sigma_1, \\ \sigma_{nn} = -P_l - \frac{\varepsilon_p}{4 K_n} u_n & \text{on} \quad \Sigma_1, \\ \sigma_{n\tau} = -\frac{\alpha}{\sqrt{K_\tau \varepsilon_p}} u_\tau & \text{on} \quad \Sigma_1. \end{array} \right. \quad (5.15)$$

We will use the following functional spaces definitions. Let $\mathbf{V} \stackrel{\text{def}}{=} [H_{\Gamma^f}^1(\Omega^f)]^d$ and $Q \stackrel{\text{def}}{=} L_0^2(\Omega^f)$ be the fluid velocity and pressure functional spaces, respectively. For the porous functional space we denote with $\mathbf{S} \stackrel{\text{def}}{=} L_0^2(\Sigma_1)$ the space for the Darcy pressure. The weak form of the linear coupled problem (5.11) and (5.15) reads as follows:

for $t > 0$, find $(\mathbf{u}(t), p(t), P_l(t)) \in \mathbf{V} \times Q \times \mathbf{S}$ such that

$$\left\{ \begin{array}{l} \rho^f (\partial_t \mathbf{u}, \mathbf{v})_{\Omega^f} + \mu (\nabla \mathbf{u}, \nabla \mathbf{v})_{\Omega^f} - (p, \text{div} \mathbf{v})_{\Omega^f} + (q, \text{div} \mathbf{u})_{\Omega^f} \\ \quad + (P_l, \mathbf{v} \cdot \mathbf{n})_{\Sigma_1} + \frac{\varepsilon_p}{4 K_n} (u_n, \mathbf{v} \cdot \mathbf{n})_{\Sigma_1} + \left(\frac{\alpha}{\sqrt{K_\tau \varepsilon_p}} u_\tau, \mathbf{v} \cdot \boldsymbol{\tau} \right)_{\Sigma_1} = 0, \\ (\varepsilon_p K_\tau \nabla_\tau P_l, \nabla_\tau q_l)_{\Sigma_1} - (u_n, q_l)_{\Sigma_1} = 0, \end{array} \right. \quad (5.16)$$

for all $(\mathbf{v}, q, q_l) \in \mathbf{V} \times Q \times \mathbf{S}$.

Before introducing the fluid-structure-porous coupled problem, let us make a few more comments. Taking $\varepsilon_p K_\tau \rightarrow 0$, we are forcing the fluid normal velocity to be zero on Σ_1 , $\varepsilon_p / K_n \rightarrow 0$ correspond to the case in which we remove the porous model on Σ_1 . Regarding the Beavers-Joseph-Saffmann condition, by taking $\alpha / \sqrt{\varepsilon_p K_\tau} \rightarrow 0$ we get free tangential fluid stresses on Σ_1 , while if $\alpha / \sqrt{\varepsilon_p K_\tau} \rightarrow \infty$ we force the fluid tangential velocity to be zero. Hence, in the limit $K_n, K_\tau \rightarrow 0$, the coupling conditions turn into a Navier-slip boundary condition for the fluid on Σ_1 .

5.2.3 Relaxed contact condition

In the following section, we will consider that contact can occur between the solid and the porous layer, namely $\Sigma(t)$ can come into contact with Σ_1 . We begin by introducing the considered contact model without fluid-structure-porous interaction. We denote by $\Sigma \subset \mathbb{R}^d$, with $d = 2$, the reference configuration of the solid mid-surface and the solid

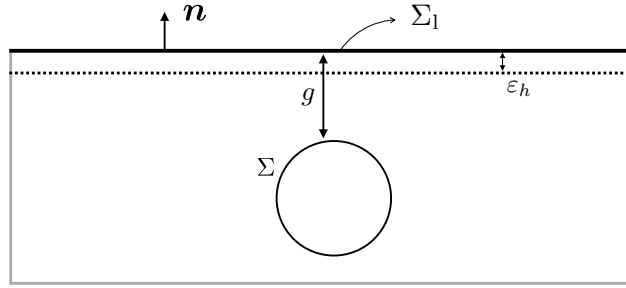


Figure 5.3: Geometric configuration of the relaxed contact situation.

elastic behavior is specified by an abstract operator \mathbf{L} .

We will consider unilateral frictionless contact law. Usually, two exclusive status *gap* or *contact* are classically formulated by imposing an impermeability condition, a compression condition and a complementary condition. In this case the solid $\Sigma(t)$ cannot penetrate into the porous medium Σ_1 via the contact conditions

$$\begin{cases} \rho^s \varepsilon \partial_t \dot{\mathbf{d}} + \mathbf{L}(\mathbf{d}) - \lambda \mathbf{n} = 0 & \text{on } \Sigma, \\ \mathbf{d} \cdot \mathbf{n} - g \leq 0, \quad \lambda \leq 0, \quad \lambda(\mathbf{d} \cdot \mathbf{n} - g) = 0 & \text{on } \Sigma. \end{cases} \quad (5.17)$$

Here, g denotes the gap function defined as the initial distance (see Figure 5.3), in the normal direction of a point on Σ to the wall Σ_1 and λ represents the contact force along \mathbf{n} , which can be seen as the Lagrange multiplier associated to the no-penetration condition. The first inequality in (5.17)₂ ensures that the solid can not pass through Σ_1 , the second inequality describes that the normal stress is zero (in the absence of contact) or negative (during contact) and the third condition is a complementarity condition that guarantees that at least one of the inequalities is “active”. During contact state we have that $\mathbf{d} \cdot \mathbf{n} - g = 0$ and $\lambda < 0$, while $\lambda = 0$ if $\mathbf{d} \cdot \mathbf{n} - g < 0$.

Following [Alart and Curnier \(1991\)](#); [Chouly and Hild \(2013\)](#), these conditions can be reformulated in an single equality as

$$\lambda = -\gamma_C [\mathbf{d} \cdot \mathbf{n} - g - \gamma_C^{-1} \lambda]_+ \quad \text{on } \Sigma,$$

for arbitrary $\gamma_C > 0$, where the notation $[\cdot]_+$ stands for the projection onto \mathbb{R}^+ .

In order to avoid the implementation issues of exact contact, a standard approach consists in relaxing the contact condition (5.17)₂, by introducing a small (mesh dependent) fictitious gap $\varepsilon_h = \varepsilon_h(h) > 0$, and $g_\varepsilon \stackrel{\text{def}}{=} g - \varepsilon_h$ ([Burman et al. \(2020a\)](#)) as follows:

$$\mathbf{d} \cdot \mathbf{n} - g_\varepsilon \leq 0, \quad \lambda \leq 0, \quad \lambda(\mathbf{d} \cdot \mathbf{n} - g_\varepsilon) = 0 \quad \text{on } \Sigma,$$

or, equivalently,

$$\lambda = -\gamma_C [\mathbf{d} \cdot \mathbf{n} - g_\varepsilon - \gamma_C^{-1} \lambda]_+ \quad \text{on } \Sigma. \quad (5.18)$$

In other words, the no-penetration condition is imposed at ε_h -distance from the porous

layer Σ_1 .

5.2.4 Coupled fluid-structure-porous interaction model with contact

In this section, we introduce and derive the fully coupled fluid-structure-porous interaction model with contact. We combine a similar fluid-porous coupled model described in Section 5.2.2 (where the fluid is described by the Navier-Stokes equations) and the solid problem (possibly non-linear beam or shell solid models) with the relaxed contact formulation of Section 5.2.3. The result is a fluid-structure-contact model, in which we add the thin-walled porous interface as boundary condition for the fluid problem. Due to the relaxation in the contact condition, the porous interface is only visible from the fluid side. No direct interaction occurs between the solid and the porous models.

Let $\Omega^f(t) \subset \mathbb{R}^d$ be the complete domain of interest with boundary $\partial\Omega \stackrel{\text{def}}{=} \Gamma \cup \Sigma_1$, where Σ_1 denotes the part of fluid boundary where contact might take place and where the thin-walled porous layer is considered. The fluid-structure interface is denoted by $\Sigma(t)$ and the solid reference configurations by Σ .

The structure is allowed to move within the domain Ω^f . The current position of the interface $\Sigma(t)$ is described in terms of a deformation map $\phi : \Sigma \times \mathbb{R}^+ \rightarrow \mathbb{R}^d$ such that $\Sigma(t) = \phi(\Sigma, t)$, with $\phi \stackrel{\text{def}}{=} \mathbf{I}_\Sigma + \mathbf{d}$ and where \mathbf{d} denotes the solid displacement. To simplify the notation we will refer to $\phi_t \stackrel{\text{def}}{=} \phi(\cdot, t)$, so that we can also write $\Sigma(t) = \phi_t(\Sigma)$. The fluid domain is time-dependent, namely $\Omega^f(t) \stackrel{\text{def}}{=} \Omega \setminus \Sigma(t) \subset \mathbb{R}^d$ with boundary $\partial\Omega^f(t) = \Sigma(t) \cup \Gamma \cup \Sigma_1$. The geometric configuration is shown in Figure 5.4.

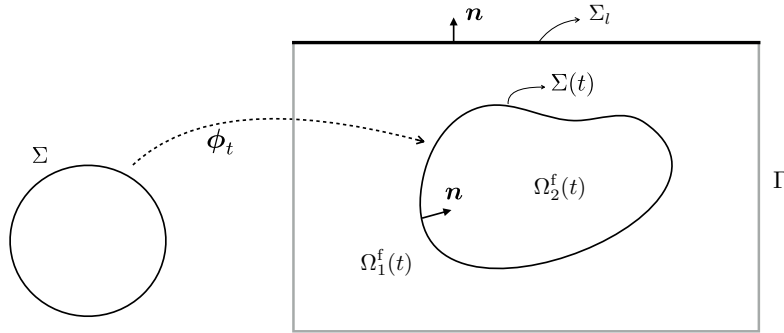


Figure 5.4: Geometric configuration of the fluid domain, the immersed solid and the thin-walled porous interface.

The solid domain divides $\Omega^f(t)$ into two sub-domains $\Omega^f(t) = \Omega_1^f(t) \cup \Omega_2^f(t)$, with respective unit normals $\mathbf{n}_1 \stackrel{\text{def}}{=} \mathbf{n}$ and $\mathbf{n}_2 \stackrel{\text{def}}{=} -\mathbf{n}$, as shown in Figure 5.4. The normal unit vector \mathbf{n} is given by the orientation of the surface $\Sigma(t)$. For a given field f defined in Ω (possibly discontinuous across the interface), we can define the sided-restrictions, jump and average operators defined in Chapter 2.

Let consider an incompressible viscous fluid governed by the Navier-Stokes equations in $\Omega^f(t)$ and either a beam or shell solid model (specified by an abstract operator \mathbf{L}). The fluid-structure-contact with thin-walled porous interaction model reads as follows: Find

the fluid velocity and pressure $\mathbf{u} : \Omega^f(t) \times \mathbb{R}^+ \rightarrow \mathbb{R}^d$, $p : \Omega(t)^f \times \mathbb{R}^+ \rightarrow \mathbb{R}$, the solid displacement and velocity $\mathbf{d} : \Sigma \times \mathbb{R}^+ \rightarrow \mathbb{R}^d$, $\dot{\mathbf{d}} : \Sigma \times \mathbb{R}^+ \rightarrow \mathbb{R}^d$, the Darcy porous pressure $P_l : \Sigma_1 \times \mathbb{R}^+ \rightarrow \mathbb{R}$ and the Lagrange multiplier $\lambda : \Sigma \times \mathbb{R}^+ \rightarrow \mathbb{R}$, such that for all $t \in \mathbb{R}^+$, the following equations are satisfied

- Fluid problem

$$\begin{cases} \rho^f (\partial_t \mathbf{u} + \mathbf{u} \cdot \nabla \mathbf{u}) - \operatorname{div} \boldsymbol{\sigma}(\mathbf{u}, p) = \mathbf{0} & \text{in } \Omega^f(t), \\ \operatorname{div} \mathbf{u} = 0 & \text{in } \Omega^f(t), \\ \mathbf{u} = \mathbf{0} & \text{on } \Gamma, \end{cases} \quad (5.19)$$

- Solid problem:

$$\begin{cases} \rho^s \varepsilon \partial_t \dot{\mathbf{d}} + \mathbf{L}(\mathbf{d}) - \lambda \mathbf{n} = \mathbf{T} & \text{on } \Sigma, \\ \dot{\mathbf{d}} = \partial_t \mathbf{d} & \text{on } \Sigma, \\ \mathbf{d} = \mathbf{0} & \text{on } \partial \Sigma \cap \Gamma, \end{cases} \quad (5.20)$$

- Contact conditions:

$$\mathbf{d} \cdot \mathbf{n} - g_\varepsilon \leq 0, \quad \lambda \leq 0, \quad \lambda(\mathbf{d} \cdot \mathbf{n} - g_\varepsilon) = 0 \quad \text{on } \Sigma, \quad (5.21)$$

- Porous interface problem:

$$\begin{cases} -\nabla_\tau \cdot (\varepsilon_p K_\tau \nabla_\tau P_l) = u_{l,n} & \text{on } \Sigma_1, \\ \varepsilon_p K_\tau \tau \cdot \nabla_\tau P_l = 0 & \text{on } \partial \Sigma_1, \end{cases} \quad (5.22)$$

- Fluid-structure coupling conditions

$$\begin{cases} \phi = \mathbf{I}_\Sigma + \mathbf{d}, \quad \Sigma(t) = \phi_t(\Sigma), \quad \Omega^f(t) = \Omega^f \setminus \Sigma(t), \\ \mathbf{u} = \dot{\mathbf{d}} \circ \phi_t^{-1} & \text{on } \Sigma(t), \\ \int_\Sigma \mathbf{T} \cdot \mathbf{w} = - \int_{\Sigma(t)} \llbracket \boldsymbol{\sigma}(\mathbf{u}, p) \mathbf{n} \rrbracket \cdot \mathbf{w} \circ \phi_t^{-1}, \quad \forall \mathbf{w} : \Sigma \rightarrow \mathbb{R}^d, \end{cases} \quad (5.23)$$

- Fluid-porous coupling conditions

$$\begin{cases} u_n = u_{l,n} & \text{on } \Sigma_1, \\ \sigma_{nn} = -P_l - \frac{\varepsilon_p}{4 K_n} u_n & \text{on } \Sigma_1, \\ \sigma_{n\tau} = -\frac{\alpha}{\sqrt{K_\tau \varepsilon_p}} u_\tau & \text{on } \Sigma_1. \end{cases} \quad (5.24)$$

The relations in (5.23) enforce, respectively, the geometrical compatibility, the kinematic and the dynamic coupling at the interface between the fluid and the solid. It should be noted that the no-penetration condition in (5.21) is already imposed at an ε -distance

to the porous layer Σ_1 . This modeling simplification circumvents most of the numerical difficulties associated with the topological change in the fluid domain induced by the exact contact condition (i.e., with $\varepsilon = 0$), such as switching between the contact and the fluid-solid interface and the presence of isolated small fluid regions (see Ager et al. (2019a)). This avoids switches in the variational formulation, which would be necessary in the transition between fluid-structure and fluid-porous interaction (Burman et al. (2020b)). On the other hand, the solid perceives indirectly the presence of the porous layer through the fluid stresses and velocity during contact. Moreover, it also facilitates the explicit treatment of the geometric condition in the fluid-structure coupling.

In the fluid-structure-porous-contact interaction model (5.19)-(5.24), a very thin fluid layer always remains between the solid and the porous medium during contact. Owing to the relations (5.24), the behavior of the fluid confined in the contact layer is expected to be very close to the one of the porous fluid. Indeed, this is a consequence of the kinematic-dynamic relations (5.24)_{1,2}, which are enforced both during and in absence of contact. As a result, all the kinematic and dynamic relations acting on the solid during contact have a physical meaning, which guarantees the mechanical consistency of the proposed fluid-structure-porous-contact interaction model.

More precisely, the solid Lagrange multiplier for the no-penetration condition will formally assume the form

$$\begin{aligned}\lambda &= \left(\rho^s \varepsilon \partial_t \dot{\mathbf{d}} + \mathbf{L}(\mathbf{d}) \right) \cdot \mathbf{n} + \llbracket \sigma_{nn} \rrbracket \\ &\approx \left(\rho^s \varepsilon \partial_t \dot{\mathbf{d}} + \mathbf{L}(\mathbf{d}) \right) \cdot \mathbf{n} + \sigma_p \circ \pi - \sigma_{nn} \Big|_2 \quad \text{on } \Sigma,\end{aligned}$$

where π indicates a (closest-point) projection from $\Sigma(t)$ to Σ_1 and the porous stresses σ_p denotes $\sigma_p \stackrel{\text{def}}{=} -P_l - \frac{\varepsilon_p}{4K_n} u_n$. Hence, this porous-contact approach gives physical meaning to the stresses generated in the infinitesimal fluid layer, in contrast to the relaxed contact formulation in Burman et al. (2020a), where the fluid stresses did not allow for a direct physical interpretation.

Remark 5.2.1 (Seepage). *The proposed fluid-structure-porous-contact interaction model allows for seepage in the sense that fluid can flow through the porous layer Σ_1 , for example to connect a cavity in the central part of the contact surface with the exterior fluid. These could emerge when the impact of the structure happens in the lateral parts of the structure first or when contact of the solid is released in a central part of the contact surface only. This is an important aspect in the modelling of fluid-structure-contact interaction, as otherwise unphysical configurations might result. If no seepage along Σ_1 is allowed, a vacuum would emerge between Σ and Σ_1 . While one could argue that this paradox is already circumvented by using the relaxed contact conditions, we note that only the porous layer gives a physical meaning to the fluid filling the infinitesimal contact layer.*

5.2.5 Numerical approximation

In this section, we introduce a consistent unfitted mesh spatial approximation of problem (5.19)-(5.24). We consider a fitted approximation for the fluid-porous interface, while

for the fluid-solid coupling, the unfitted spatial discretization described in Chapter 2. We recall here the most salient features, and complete the description adding the porous and contact discretization. Regarding time-discretization, we use a backward Euler time-stepping scheme. We denote by $\tau > 0$ the time-step length, $t_n \stackrel{\text{def}}{=} n\tau$ for $n \in \mathbb{N}$, and by $\partial_\tau x^n \stackrel{\text{def}}{=} \frac{1}{\tau} (x^n - x^{n-1})$ the first-order backward difference. The fluid fields (\mathbf{u}^n, p^n) will hence be approximated with triangulations of Ω^f , which are independent of Σ . To this purpose, it is important to note that the velocity gradient $\nabla \mathbf{u}^n$ and the pressure p^n are possibly discontinuous across $\Sigma(t)$. The contact conditions (5.21) are approximated via penalty method, considering the same discretization strategy of Section 2.4.2.

Let be $\{\mathcal{T}_h^s\}_{0 < h < 1}$ a family of triangulations of Σ . We then consider the standard space of continuous piecewise affine functions:

$$X_h^s \stackrel{\text{def}}{=} \{v_h \in C^0(\bar{\Sigma}) \mid v_h|_K \in \mathbb{P}_1(K), \quad \forall K \in \mathcal{T}_h^s\}.$$

The discrete space for the solid displacement and velocity approximations is hence defined as $\mathbf{W}_h = [X_h^s]^d \cap \mathbf{W}$, where $\mathbf{W} = [H^1(\Sigma)]_0^d$ denotes the space of admissible displacements. Given a discrete displacement approximation $\mathbf{d}_h^n \in \mathbf{W}_h$, we define by ϕ_h^n its associated deformation map as $\phi_h^n \stackrel{\text{def}}{=} \mathbf{I}_\Sigma + \mathbf{d}_h^n$. This map characterizes the current interface position, at time level n , as $\Sigma^n \stackrel{\text{def}}{=} \phi_h^n(\Sigma)$. We hence propose to explicitly update the physical fluid domain as

$$\Omega^{f,n} \stackrel{\text{def}}{=} \Omega^f \setminus \Sigma^{n-1},$$

allowing the geometrical non-linearity to vanish. For the fluid discrete spaces, we introduce a family of meshes $\{\mathcal{T}_h^n\}_{0 < h < 1}$, fitted to the exterior boundary $\Gamma \cup \Sigma_1$ but not to \mathcal{T}_h^s . Afterward, we define two family of meshes $\{\mathcal{T}_{h,i}^n\}_{0 < h < 1}$, $i = 1, 2$, where each $\mathcal{T}_{h,i}^n \subset \mathcal{T}_h^n$ covers the i -th fluid region $\Omega_i^{f,n}$ defined by Σ^n . Furthermore for every element $K \in \mathcal{T}_{h,1}^n \cap \mathcal{T}_{h,2}^n$ we assume that $K \cap \Sigma^n \neq \emptyset$. We denote by $\Omega_{h,i}^n$ the domain covered by $\mathcal{T}_{h,i}^n$, viz.,

$$\Omega_{h,i}^n \stackrel{\text{def}}{=} \text{int} \left(\bigcup_{K \in \mathcal{T}_{h,i}^n} K \right).$$

For $i = 1, 2$, we can hence introduce the following spaces of continuous piecewise affine functions:

$$X_{h,i}^n \stackrel{\text{def}}{=} \left\{ v_h \in C^0(\bar{\Omega}_{h,i}^n) \mid v_h|_K \in \mathbb{P}_1(K), \quad \forall K \in \mathcal{T}_{h,i}^n \right\}.$$

Associated with $X_{h,i}$ we define the spaces

$$\mathbf{V}_{h,i}^n \stackrel{\text{def}}{=} [X_{h,i}^n]^2 \cap [H_\Gamma^1(\Omega^{f,n})]^2, \quad Q_{h,i}^n \stackrel{\text{def}}{=} X_{h,i}^n \cap L^2(\Omega^{f,n})_0.$$

For the approximation of the fluid velocity and pressure we will consider the following discrete product spaces

$$\mathbf{V}_h^n \stackrel{\text{def}}{=} \mathbf{V}_{h,1}^n \times \mathbf{V}_{h,2}^n, \quad Q_h^n \stackrel{\text{def}}{=} Q_{h,1}^n \times Q_{h,2}^n, \quad (5.25)$$

which guarantee that interfacial (strong and weak) discontinuities are included in the discrete approximation of both the fluid velocity and pressure. Indeed, the functions

of (5.25) are continuous in the physical fluid domain $\Omega^{f,n}$ but discontinuous across the interface Σ^n . Since the discrete pair \mathbf{V}_h^n/Q_h^n is not inf-sup stable, we consider a symmetric stabilization operator, such as, the one given by Continuous Interior Penalty method (see [Burman and Hansbo \(2006\)](#)) over the whole computational domain:

$$s_h^n(p_h, q_h) \stackrel{\text{def}}{=} \frac{\gamma_p h^3}{\mu} \sum_{i=1}^2 \sum_{F \in \mathcal{F}_{h,i}} (\llbracket \nabla p_h \rrbracket_F, \llbracket \nabla q_h \rrbracket_F)_F,$$

where $\mathcal{F}_{h,i}$ denotes the set of interior edges or faces of $\mathcal{T}_{h,i}$. Finally, we introduce the fluid discrete form

$$\begin{aligned} a_h^{f,n}(w_h; (\mathbf{u}_h, p_h), (\mathbf{v}_h, q_h)) &\stackrel{\text{def}}{=} 2\mu(\boldsymbol{\epsilon}(\mathbf{u}_h), \boldsymbol{\epsilon}(\mathbf{v}_h))_{\Omega^{f,n}} + (w_h \cdot \nabla \mathbf{u}_h, \mathbf{v}_h)_{\Omega^{f,n}} - (p_h, \text{div } \mathbf{v}_h)_{\Omega^{f,n}} \\ &\quad + (\text{div } \mathbf{u}_h, q_h)_{\Omega^{f,n}} + s_h(p_h, q_h) + g_h(\mathbf{u}_h, \mathbf{v}_h), \end{aligned}$$

where the ghost-penalty operator is given by (see [Burman \(2010\)](#))

$$g_h^n(\mathbf{u}_h, \mathbf{v}_h) \stackrel{\text{def}}{=} \gamma_g \mu h \sum_{i=1}^2 \sum_{F \in \mathcal{F}_{i,h}^\Sigma} (\llbracket \nabla \mathbf{u}_{i,h} \rrbracket_F, \llbracket \nabla \mathbf{v}_{i,h} \rrbracket_F)_F$$

and where $\mathcal{F}_{i,h}^\Sigma$ denotes the set of interior edges or faces of the elements intersected by Σ^n . This operator guarantees robustness irrespectively to the way the interface is cutting the fluid mesh, by extending the coercivity of the viscous bi-linear form to the whole computational domain. In addition, we assume that a positive and symmetric elastic bi-linear form $a^s : \mathbf{W} \times \mathbf{W} \rightarrow \mathbb{R}$ corresponds to the solid elastic operator \mathbf{L} in case of a thin-walled solid.

For the approximation of the porous layer we consider a triangulation of Σ_1 which is fitted to the triangulation of Ω^f . We then consider the standard space of continuous piecewise affine functions:

$$X_h^p \stackrel{\text{def}}{=} \{v_h \in C^0(\overline{\Sigma_1}) \mid v_h|_K \in \mathbb{P}_1(K), \quad \forall K \in \mathcal{T}_h^p\}.$$

Finally, the following discrete space is considered for the approximation of the porous pressure

$$S_h \stackrel{\text{def}}{=} X_h^p.$$

The final ingredient towards the discretization of problem (5.19)-(5.24) is the contact treatment. Condition (5.18) can be embedded in an elegant way in the variational formulation using a Nitsche-based approach, see, e.g., [Burman et al. \(2020a\)](#), [Chouly and Hild \(2013\)](#) and [Chouly et al. \(2015\)](#). The Lagrange multiplier is eliminated using the definition of stresses jump on $\Sigma(t)$ and integrated consistently into the variational fluid-structure formulation via Nitsche's method. Unfortunately, for thin structure this approach involves an additional difficulty, i.e., the normal solid traction on the mid-surface is typically not available. Other possible approaches are penalty methods, where the set of inequalities associated to contact is replaced with a non-linear equation that approxi-

mates them. These methods are easy to implement, but nevertheless consistency is lost, as a small amount of penetration, controlled by the penalty parameter, is allowed. This penalty parameter needs to be chosen carefully. Indeed, when the penalty parameter gets smaller to improve the approximation of contact conditions, the discrete problem gets stiffer and ill-conditioned (see Chouly et al. (2017)). The penalty formulation is obtained as a simplification of (5.18), by taking $\gamma_C \approx \gamma_c h^{-2}$ and neglecting the $\gamma_C^{-1} \lambda$ term, namely,

$$\frac{\gamma_c E \varepsilon}{h^2} ([\mathbf{d}_h^n \cdot \mathbf{n} - g + \varepsilon_h]_+, \mathbf{w}_h)_{\Sigma}, \quad (5.26)$$

where $\gamma_c > 0$ is a (dimensionless) user-defined parameter, $\varepsilon_h > 0$ is a contact tolerance, \mathbf{n} denotes the exterior unit normal to Σ_1 and $g : \Sigma \rightarrow \mathbb{R}^+$ refer to the gap function between Σ and Σ_1 . This approach is optimal in the case of thin-walled solids. Finally, this method is highly competitive in terms of computational costs compared to approaches using Lagrange multipliers and/or active-sets.

Algorithm 5.1 Strongly coupled scheme for the approximation of (5.19)-(5.24).

For $n \geq 1$:

1. Definition of the interface position:

$$\phi_h^{n-1} = \mathbf{I}_{\Sigma} + \mathbf{d}_h^{n-1}, \quad \Sigma^{n-1} = \phi_h^{n-1}(\Sigma), \quad \Omega^n = \Omega \setminus \Sigma^{n-1}.$$

2. Find $(\mathbf{u}_h^n, p_h^n, P_l^n, \dot{\mathbf{d}}_h^n, \mathbf{d}_h^n) \in \mathbf{V}_h^n \times Q_h^n \times S_h \times \mathbf{W}_h \times \mathbf{W}_h$, with $\dot{\mathbf{d}}_h^n = \partial_{\tau} \mathbf{d}_h^n$ and such that

$$\begin{aligned} & \rho^f (\partial_{\tau} \mathbf{u}_h^n, \mathbf{v}_h)_{\Omega^{f,n}} + a_h^{f,n}(\mathbf{u}_h^{n-1}; (\mathbf{u}_h^n, p_h^n), (\mathbf{v}_h, q_h)) + \rho^s \varepsilon (\partial_{\tau} \dot{\mathbf{d}}_h^n, \mathbf{w}_h)_{\Sigma} + a^s(\mathbf{d}_h^n, \mathbf{w}_h) \\ & - \sum_{i=1}^2 (\boldsymbol{\sigma}(\mathbf{u}_{h,i}^n, p_{h,i}^n) \mathbf{n}_i, \mathbf{v}_{h,i} - \mathbf{w}_h)_{\Sigma^n} - \sum_{i=1}^2 (\mathbf{u}_{h,i}^n - \dot{\mathbf{d}}_h^n, \boldsymbol{\sigma}(\mathbf{v}_{h,i}, -q_{h,i})) \mathbf{n}_i)_{\Sigma^n} \\ & + \frac{\gamma \mu}{h} \sum_{i=1}^2 (\mathbf{u}_{h,i}^n - \dot{\mathbf{d}}_h^n, \mathbf{v}_{h,i} - \mathbf{w}_h)_{\Sigma^n} + \frac{\gamma_c E \varepsilon}{h^2} ([\mathbf{d}_h^n \cdot \mathbf{n} - g_{\varepsilon}]_+, \mathbf{w}_h \cdot \mathbf{n})_{\Sigma} \\ & + (P_l^n, \mathbf{v}_h \cdot \mathbf{n})_{\Sigma_1} + \frac{\varepsilon_p}{4 K_n} (\mathbf{u}_h^n \cdot \mathbf{n}, \mathbf{v}_h \cdot \mathbf{n})_{\Sigma_1} + \left(\frac{\alpha}{\sqrt{K_{\tau} \varepsilon_p}} \mathbf{u}_h^n \cdot \boldsymbol{\tau}, \mathbf{v}_h \cdot \boldsymbol{\tau} \right)_{\Sigma_1} \\ & + (\varepsilon_p K_{\tau} \nabla_{\tau} P_l, \nabla_{\tau} q_l)_{\Sigma_1} - (\mathbf{u}_h^n \cdot \mathbf{n}, q_l)_{\Sigma_1} = 0 \end{aligned}$$

for all $(\mathbf{v}_h, q_h, \mathbf{w}_h, q_l) \in \mathbf{V}_h^n \times Q_h^n \times \mathbf{W}_h \times S_h$.

In summary, we report the resulting Nitsche-based XFEM approximation of (5.19)-(5.24) in Algorithm 5.1. Notice that the scheme is strongly coupled, no weakly coupled strategies are considered indeed.

Remark 5.2.2. *It is worth noting that, when contact occur between Σ and Σ_1 , the fluid element is duplicated. In that case, the porous layer is connected to the physical duplicated element of the fluid domain.*

Remark 5.2.3. *If the the interface has a boundary inside the fluid domain (the tip), we consider the construction of the fluid and solid spaces proposed in Alauzet et al. (2016). A virtual interface $\tilde{\Sigma}$ is introduced by connecting the interface tip with the fluid vertex opposite to the edge intersected by the interface and therefore the fluid domain is closed. Afterwards, we enforce the kinematic/dynamic continuity of the fluid on $\tilde{\Sigma}$ in a discontinuous Galerkin fashion (see, e.g., Di Pietro and Ern (2012) and Chapter 2 and 6). More precisely, the following terms are added into 5.1*

$$-\left(\{\{\sigma(\mathbf{u}_h^n, p_h^n)\}\mathbf{n}, \llbracket \mathbf{v}_h \rrbracket\}\right)_{\tilde{\Sigma}} - \left(\{\{\sigma(\mathbf{v}_h, -q_h)\}\mathbf{n}, \llbracket \mathbf{u}_h^n \rrbracket\}\right)_{\tilde{\Sigma}} + \frac{\gamma\mu}{h}(\llbracket \mathbf{u}_h^n \rrbracket, \llbracket \mathbf{v}_h \rrbracket)_{\tilde{\Sigma}}.$$

Remark 5.2.4 (Discretization of Stokes'-Darcy model). *A discrete version of the continuous Stokes'-Darcy model (5.16) can be easily derived, by considering standard discontinuous spaces of piecewise linear affine functions for both fluid and porous and a backward Euler time-stepping scheme.*

5.3 Numerical experiments

In this section, we present a series of numerical models which illustrate the capabilities of the models introduced in the previous sections. In the first numerical example we consider the mixed dimensional Stokes'-Darcy system showing how the porous layer can be used to connect two disconnected fluid reservoirs. Later on, we consider the example of the idealized valve test with contact of Section 2.4.2, but on the context of fluid-structure-porous interaction. The model developed here is for two or three-dimensional spaces. Though numerical results are given only in the two-dimensional case, they could be carried out for three-dimensional problems, but with extra difficulties illustrate in Chapter 6. In the following we will consider an approximation of the Beavers-Joseph-Saffmann condition for tangential stresses, in which we let $\alpha \rightarrow 0$. Hence, in order to allow the valve to slide, we consider zero-tangential traction on Σ_1 . Additionally, a Newton method is considered for solve the coupled problem with a partitioned approach. All the units are given in the CGS units system.

5.3.1 Reservoirs connected via porous layer

In this example, we consider two disconnected fluid reservoirs, connected through a thin-walled porous interface located on the bottom wall Σ_1 , as shown in Figure 5.5. The fluid domain Ω^f is shown in Figure 5.5 and Σ_1 is a segment with extremities $(0, 0)$ and $(2, 0)$.

Regarding the fluid boundary conditions, we impose a pressure drop across the two parts of the top boundary. A traction is imposed on $\Gamma_f^{N_1}$ in terms of a sinusoidal time-dependent pressure $p_{\text{in}}(t)$, namely,

$$p_{\text{in}}(t) = 5 \cdot \sin(2\pi t), \quad \forall t \in \mathbb{R}^+,$$

while a zero traction is enforced on $\Gamma_f^{N_2}$. Additionally, a no-slip boundary condition is

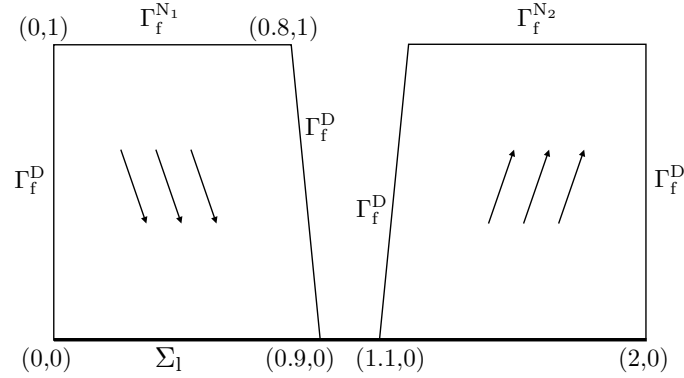


Figure 5.5: Geometrical configuration for the Stokes model with a thin-walled porous medium on the bottom wall.

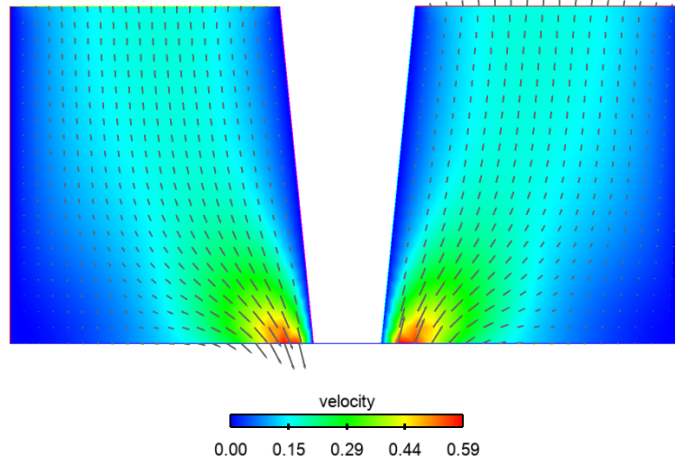


Figure 5.6: Snapshot of the fluid velocity.

enforce on Γ_f^D . The considered physical parameters are $\mu = 0.03$, $\rho^f = 1$, $\varepsilon_p = 0.01$ and $K_\tau = K_n = 1$.

The purpose of this example is to illustrate how the porous model is able to connect the fluid flow between the two containers. This can be clearly inferred from the results reported in Figure 5.6 and Figure 5.7 at $t = 0.25$, which, respectively, show a snapshot of the fluid velocity, the elevation of the fluid pressure and the associated porous pressure. As we can see, the fluid is entering into the porous layer from the left reservoir and leaving the porous interface into the right one. Further studies on the model parameters will be considered in the second numerical example.

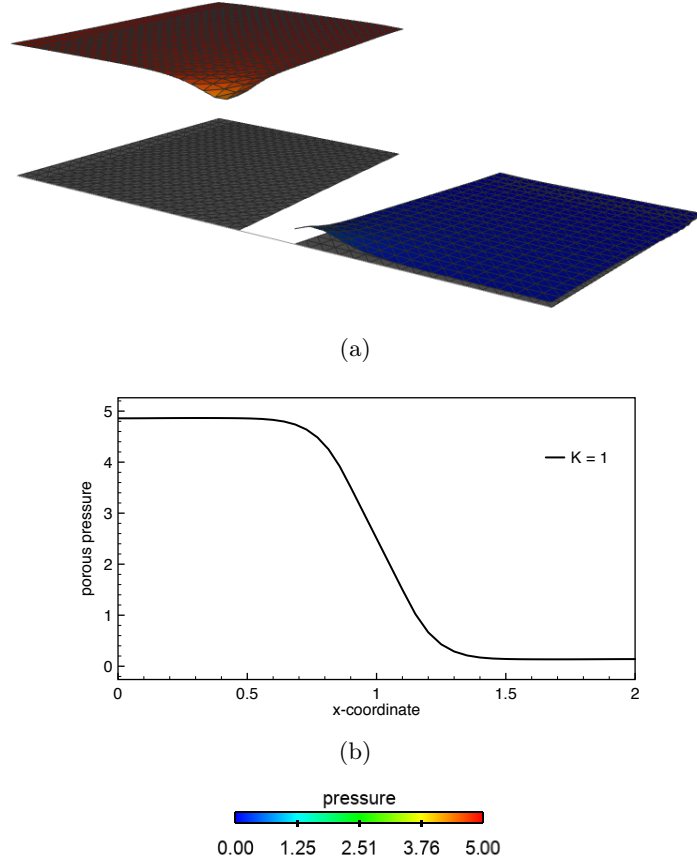


Figure 5.7: (a) Elevation of the fluid pressure, (b) Porous pressure.

5.3.2 Idealized valve with contact

This numerical example corresponds to the idealized valve test (see Section 2.4.2) with possible contact on the top wall, in which the porous interface is added on Σ_1 . The geometry is shown in Figure 5.8(a). The fluid domain is a rectangle $\Omega^f = [0, 8] \times [0, 0.805]$ and as reference configuration for the solid, Σ , we consider a curve segment of extreme $A = (4, 0)$ and $B = (5.112, 0.483)$, parametrized by the analytical function

$$y(x) = \frac{1}{2} \sqrt{1 - \frac{(x - 11/2)^2}{(3/2)^2}}, \quad x \in [4, 5.112].$$

The physical parameters used for the fluid in this test are $\rho^f = 1$, $\mu = 0.03$. While for the solid we have $\rho^s = 1.2$, $\varepsilon = 0.065$, the Young's modulus $E = 10^7$ and the Poisson's ratio $\nu = 0.4$. Regarding the porous medium, we consider $\varepsilon_p = 0.01$ and we explore the influence of the porous layer on the contact dynamics by changing the hydraulic conductivity parameters $K_\tau = K_n \in \{10^{-i}\}_{i=0}^3$ and by comparing it with the situation of simple wall on Σ_1 , where we enforce a symmetry condition.

Regarding the boundary condition, a no-slip condition is enforced on Γ_w , zero traction

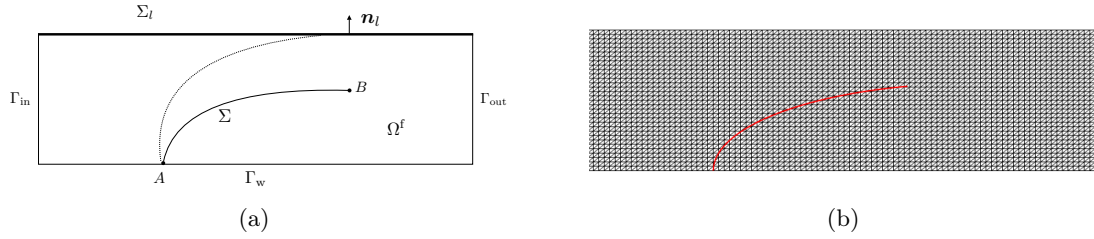


Figure 5.8: (a) Geometric configuration of the idealized valve with contact, (b) Zoom of the leaflet mesh and fluid mesh.

on the outflow boundary Γ_{out} and a traction condition is imposed on Γ_{in} in terms of the following time-dependent pressure:

$$p_{\text{in}}(t) = \begin{cases} -200 \operatorname{atanh}(100t) & \text{if } 0 < t < 0.7, \\ 200 & \text{if } t \geq 0.7. \end{cases}$$

The final time is $T = 1$ and it corresponds to one full valve oscillation cycle. The fluid and the solid are initially at rest and the beam is pinched at the bottom tip A . In this test, the solid is described by a non-linear Reissner–Mindlin curved beam model with a MITC spacial discretization. The ghost penalty parameter has been set to $\gamma_g = 1$ and the CIP stabilization parameters to $\gamma_v = \gamma_p = 10^{-2}$. In this particular case, the gap function is defined as the initial distance of a point on Σ to the wall Σ_1 in the direction of \mathbf{n}_l , namely $g = y_{\Sigma_1} - y(x)$. The contact parameters are given by $\varepsilon_h = 0.01$ and $\gamma_c = 5 \cdot 10^{-3}$ as in [Boilevin-Kayl et al. \(2019a\)](#). The relaxation parameter ε_h is chosen in such a way that the generated artificial gap is below h , typically $\varepsilon_h \approx h/2$. The penalty parameter γ_c (independent of h) is chosen to avoid penetration (i.e., not very small) and in such a way that the term (5.26) does not perturbs the convergence of the Newton solver in the solid (the operator $[\cdot]_+$ is not differentiable at 0).

The fluid mesh has 16384 triangles and the solid 50 edges. We have $h \approx 0.04$. The zoom on the both meshes is presented in Figure 5.8(b). The time discretization parameter is $\tau = 10^{-3}$ and the Nitsche parameter is set to $\gamma = 100$.

Let first consider the case in which we select $K_\tau = K_n = 10^{-3}$. We report in Figure 5.9 the velocity magnitude at two different instants. In Figure 5.9(a) is reported the approximation obtained at time $t = 0.6$. At this instant, the valve is in contact with the upper wall and the fluid velocity decreases globally as consequence of the closing. Contrarily to the idealized valve test without porous layer at the top wall, here, we allow the flow to enter the porous interface at contact. The fluid is transported, through the porous layer, from the right side of the domain, to the left side. At $t = 1$ the valve is open and far from Σ_1 , therefore the fluid flow is reestablished and the velocity increases in the channel. The same comparison is performed in Figures 5.10(a) and (b) for the pressure. We can see the high pressure jump when the valve is in contact with the wall (Figure 5.10(b)), while at $t = 1$ the discontinuity between the two sides of the interface is weaker (Figure 5.10(d)).

We now consider the case in which we insert a thin porous layer on the top contact

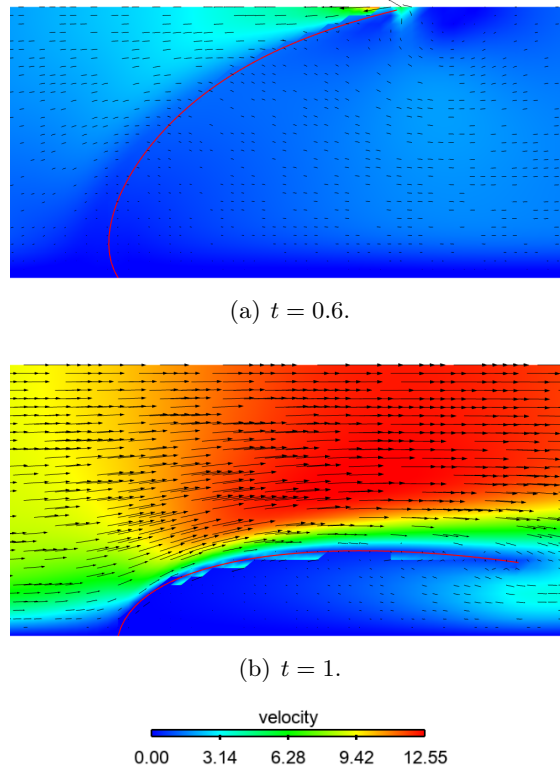


Figure 5.9: Velocity magnitude snapshots.

wall and investigate the impact of $K_\tau = K_n$ on the results. Figure 5.11 presents the time history of the horizontal, Figure 5.11 (a), and vertical displacement, Figure 5.11 (b), at the upper solid point B for different levels of conductivity. The non-penetration condition with the wall can be seen in Figure 5.11(b), whereas Figure 5.11(a) shows that the structure is sliding over the top wall. The interface is bouncing for all tests except the cases of $K_\tau = K_n = 1$ and 10^{-1} . In such cases, the structure reaches contact and the fluid flows abundantly into the porous layer, which prevents the release of contact. When the inlet pressure increases, the valve opens and the flow is restored. In all the other tests the interface is bouncing, but with a different reaction time, linked to the conductivity value. There is a slight difference in the first release time, but the more visible differences are on the second bounce. Both, the second contact instant and the final release, are considerably sensitive to the changing in $K_\tau = K_n$. Finally, let notice that taking $K_\tau \rightarrow 0$ and $K_n \rightarrow 0$ we converge to the situation of no porous layer on Σ_1 , as we can see in Figure 5.11.

Similar observations can be inferred from Figure 5.12 which shows the interface configuration at time $t = 0.25$ (during contact), $t = 0.45$ (after the first release) and $t = 1$ (when the flow is restored). We can see that for $K_\tau = K_n = 1$ and 10^{-1} the valve do not bounce, but they only release once the inlet pressure increases (see Fig. 5.12(c)). Decreasing the conductivity of the porous medium increases the structure sliding at contact (see Fig. 5.12(a)) and the bouncing force applied on the structure (see Fig. 5.12(b)).

Figure 5.13 displays the fluid pressure (continuous line) and the porous pressure

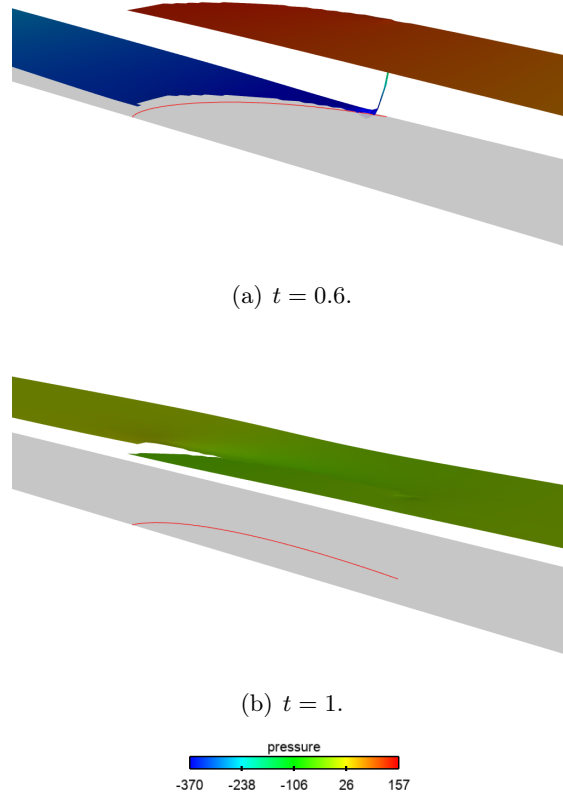


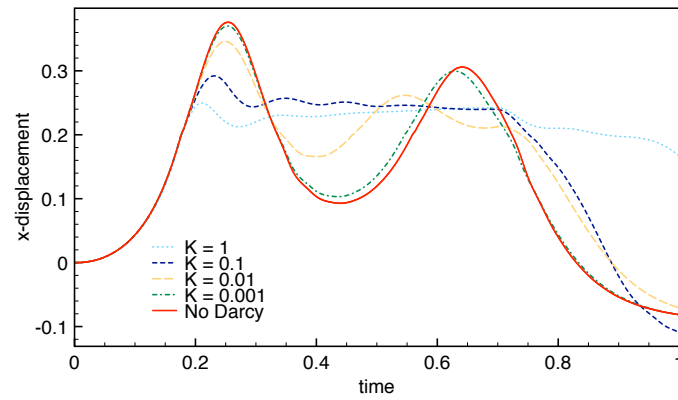
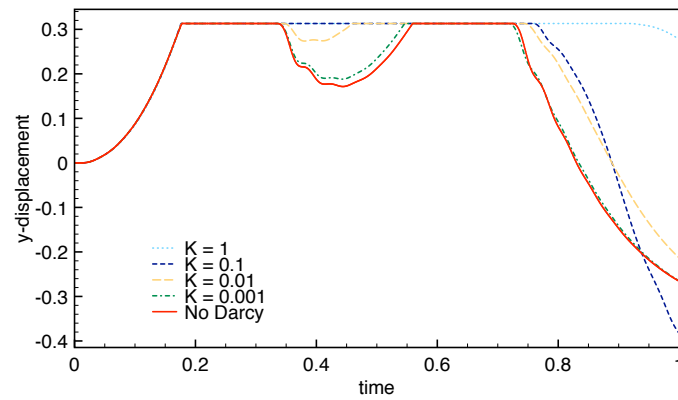
Figure 5.10: Pressure elevation snapshots.

(dashed line) at time $t = 0.25$ and $t = 0.45$. As expected, both pressures remain close. At time $t = 0.25$ the structure is in contact with the upper wall, therefore there is a high pressure gradient that decreases by increasing the conductivity.

Figure 5.14 shows the fluid x -velocity along the porous layer Σ_1 at two different instants. As we can see, the horizontal velocity is not zero also during contact as effect of the porous layer. As expected, the higher is the conductivity the greater the velocity magnitude is and a larger area of the porous layer is leaking or pushing fluid inside the domain. In Figure 5.15 we report the fluid y -velocity on Σ_1 . The effect are more localized near the contact area except for cases of $K = 1, 0.1$, where the porous layer is still leaking and entering also far from the contact area.

We now explore the results when variations on the porous thickness ε_p are considered. The porous hydraulic conductivity is taken $K_\tau = K_n = 10^{-3}$. We explore results for $\varepsilon_p \in \{10^{-i}\}_{i=1}^4$. The outcome is shown in Figure 5.16. For $\varepsilon_p \rightarrow 0$ the curves converge towards the results of no porous layer on the top wall.

No particular differences are visible at first contact between the structure and the upper wall. During contact, the horizontal velocity is lower for higher values of ε_p , therefore, the bouncing force is also lower. In addition, the higher is ε_p , the later is the first release, the lower is the rebound force and, consequently, the earlier is the second contact and release.

(a) x -displacement.(b) y -displacement.Figure 5.11: Time evolution of the x and y -displacement for the structure endpoint B .

For illustration purposes, we report in Figure 5.17 a zoom of the y -displacement between the first release and the second contact instants.

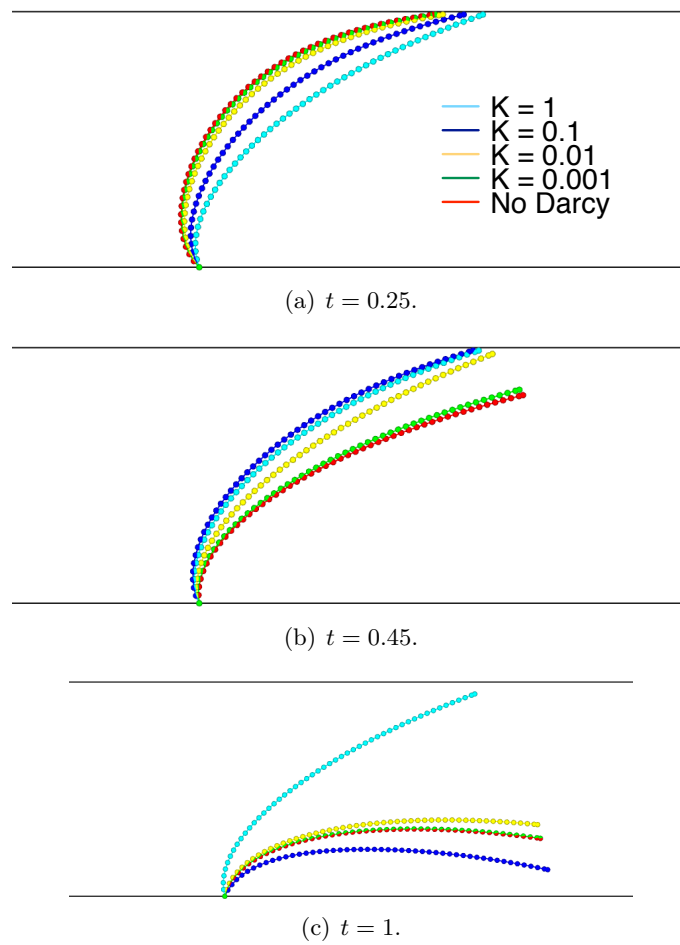


Figure 5.12: Interfaces location at time $t = 0.25$ (a), $t = 0.45$ (b) and $t = 1$ (c).

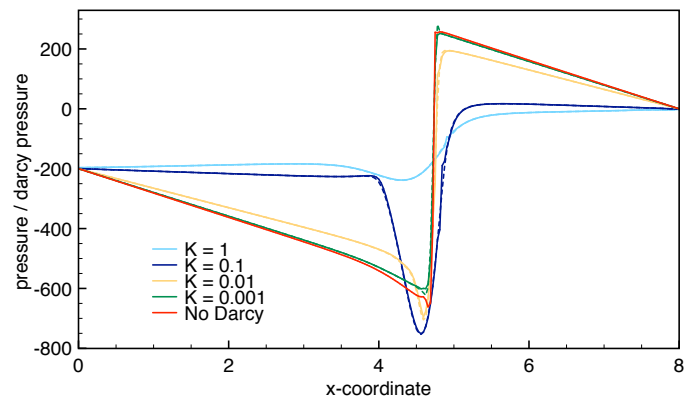
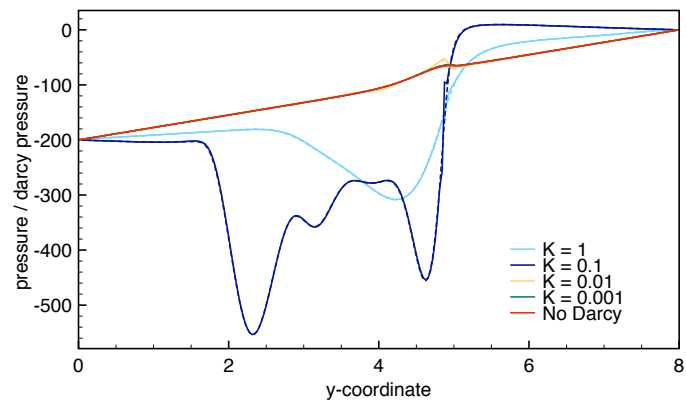
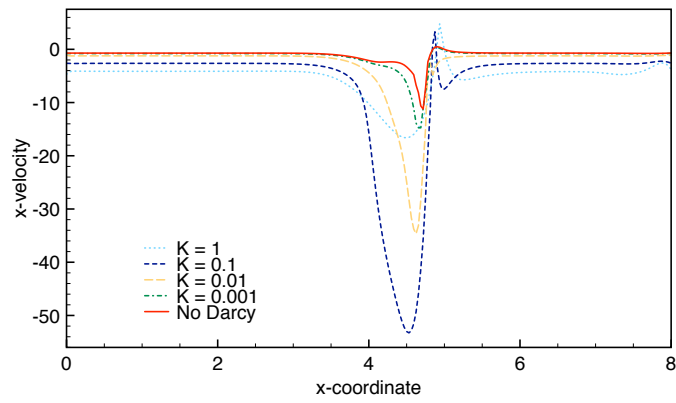
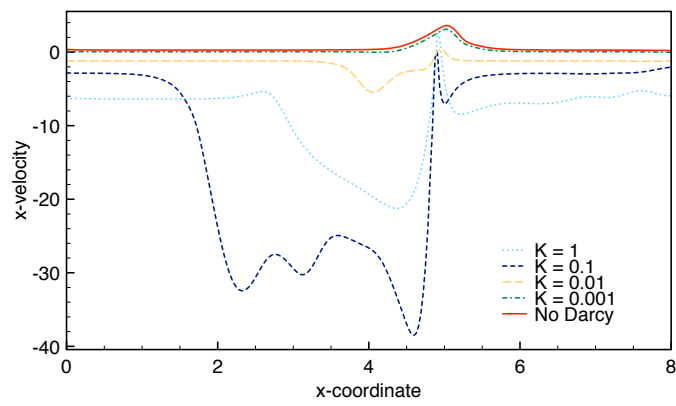
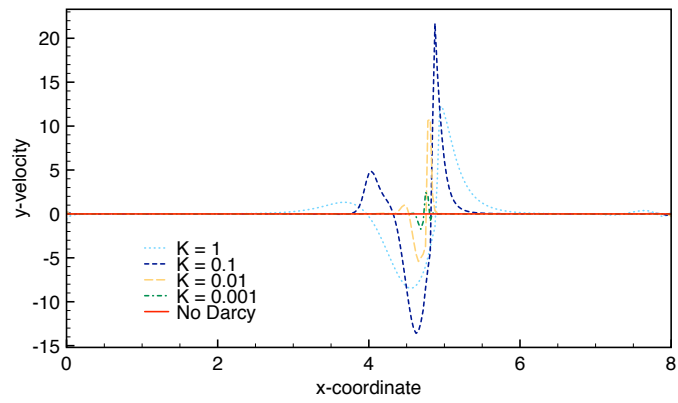
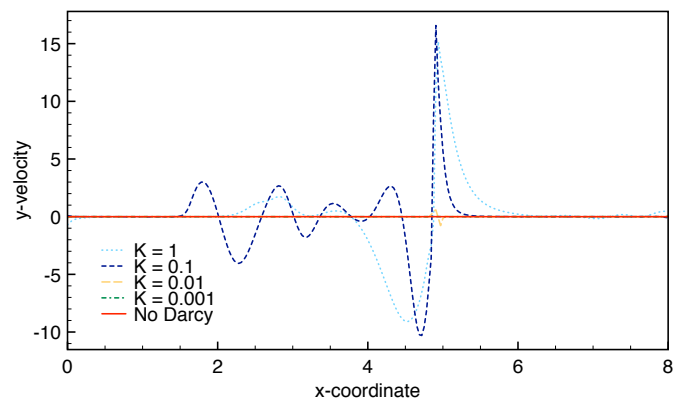
(a) $t = 0.25$.(b) $t = 0.45$.

Figure 5.13: Fluid pressure (continuous line) and porous pressure (dash line) on Σ_1 for different value of hydraulic conductivity at time $t = 0.25$ and $t = 0.45$.

(a) x-velocity at $t = 0.25$.(b) x-velocity at $t = 0.45$.Figure 5.14: Fluid velocity on Σ_1 .

(a) y-velocity at $t = 0.25$.(b) y-velocity at $t = 0.45$.Figure 5.15: Fluid velocity on Σ_1 .

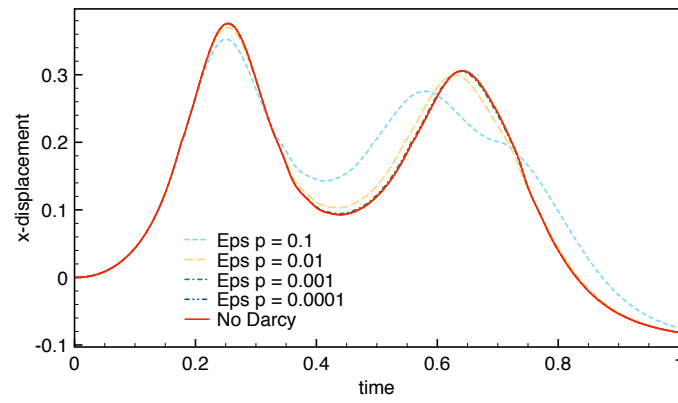
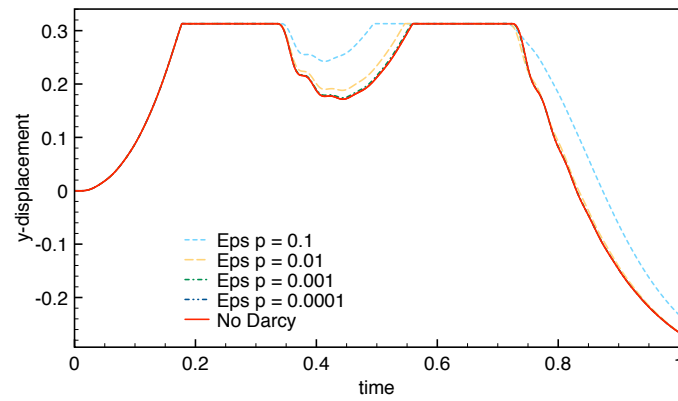
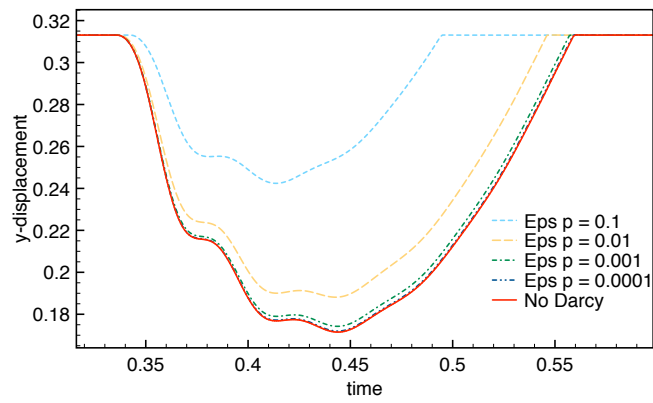
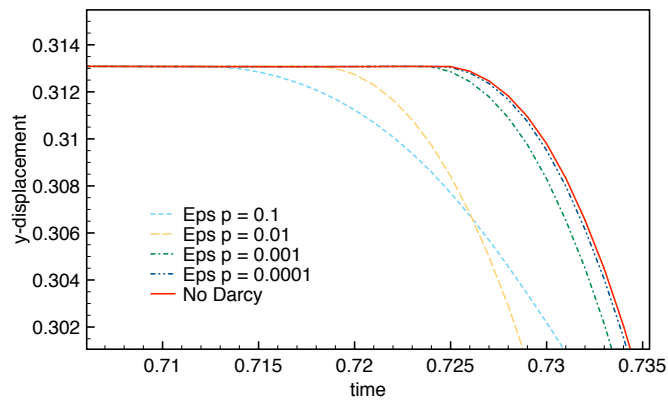
(a) x -displacement.(b) y -displacement.

Figure 5.16: Time evolution of the x -displacement (a) and y -displacement (b) for the structure endpoint B for different values of ϵ_p



(a) First release.



(b) Second release.

Figure 5.17: Time evolution of the y -displacement for the structure endpoint B , between first release and second contact (a) and after second release (b).

5.3.2.1 Space and time refinement

We explore the convergence behavior taking three levels of space and time refinement, namely $(\tau, h) \in \{2 \cdot 10^{-3} \cdot 2^{-i}, 0.07 \cdot 2^{-i}\}_{i=0}^2$. The coarser fluid and solid meshes are made of 5120 triangles and 26 segments, respectively. The middle meshes by 20480 triangles and 50 edges, while the finest by 81920 triangles and 102 segments. The porous conductivity is chosen $K_n = K_\tau = 10^{-3}$, and the contact relaxation parameter $\varepsilon_h = \varepsilon_h(h)$, chosen $\varepsilon_h \in \{0.02 \cdot 2^{-i}\}_{i=0}^2$.

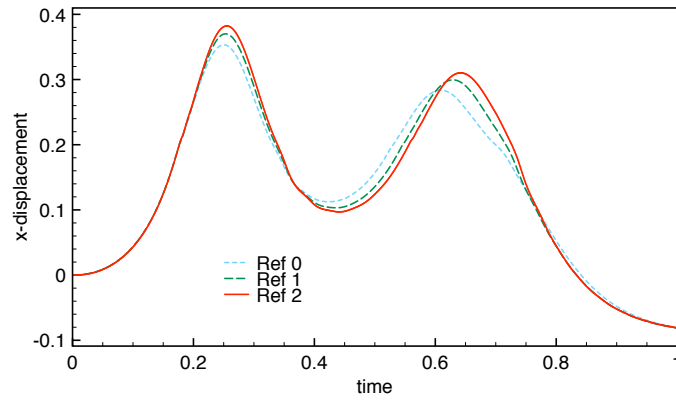
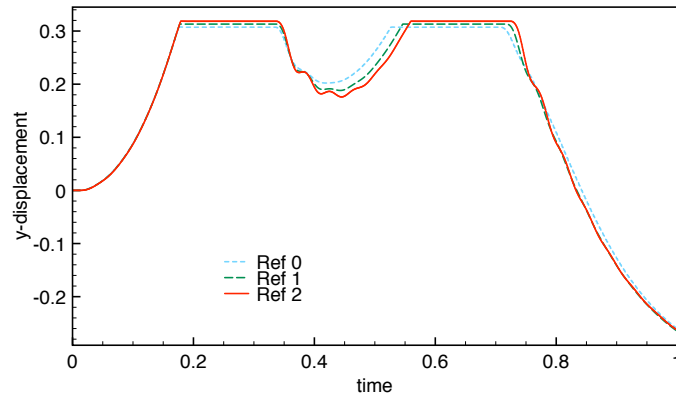
(a) x -displacement.(b) y -displacement.

Figure 5.18: Time evolution of the x -displacement (a) and y -displacement (b) for the structure endpoint B , with different levels of refinement.

We show in Figure 5.18 the results with these three refinement levels. We observe that the bouncing height is lower for the coarser mesh and that the intermediate level of refinement provides a reasonable approximation. We can also observe that, due to different contact relaxation parameters, contact and release occur at different instants and heights.

5.4 Conclusions

We have introduced a mechanically consistent fluid-structure-porous-contact interaction model, involving immersed thin-walled structures, thin-walled porous layer, on the contact surface, and a relaxed contact approximation. Physical enrichment is considered, by including surface roughness through a reduced order porous model on the contact interface, allowing seepage in the contact zone. The porous provides a mechanical justification for the relaxed contact approximation, giving a physical sense to the fluid stresses in the small layer of fluid remaining at contact. This relaxation is fundamental from the numerical point of view, since it does not introduce further non-linearities in the fluid-structure coupling, typical of the realistic contact formulation (where the FSI interface depends on the contact state). In fact, a relaxed contact approximation enables a fully partitioned solution of the fluid-structure-contact problem, i.e., contact does not perturb the FSI coupling and, hence, the solution procedure.

Extensions of this work can explore several directions. From the modeling point of view, the assessment of the model parameters is still an open issue. Experiments could assist for this purpose. Furthermore, the extension of the model to the case in which we consider a non rigid porous layer and contact with large displacement. Under such circumstances, additional difficulties related to geometrical non-linearities (concerning the fluid-porous coupling) have to be faced.

Part III

3D NUMERICAL SIMULATIONS

A 3D Nitsche-XFEM method for FSI with immersed thin-walled structures

In this chapter we formulate and implement the unfitted Nitsche-XFEM space semi-discretization presented in Chapter 2 to the three-dimensional case. For the temporal discretization, only the strongly coupled scheme is considered. Particular focus is made on the efficiency and robustness of the intersection algorithm, by avoiding to resort to black-box mesh generators. Note that the mathematical formulation of the method is the same as in two dimensions. A series of numerical examples in two and three dimensions, involving moving interfaces, with partially and fully intersected fluid domain, illustrate the performance of the proposed method.

Some of the results presented in this chapter have been reported in:

- F. Alauzet, D.C. Corti, M.A. Fernández, F.M. Gerosa. **A 3D Nitsche-XFEM method for immersed FSI with thin-walled solids.** *14th World Congress on Computational Mechanics (WCCM) ECCOMAS*, 2020 11–15 January 2021, Paris, France.

Contents

6.1	Introduction	154
6.2	The linear model	155
6.2.1	Space semi-discretization	156
6.2.2	Partially intersected fluid domain	159
6.2.3	Fully discrete scheme: time discretization	163
6.2.4	Intersection algorithm	163
6.2.5	Element duplication	171
6.2.6	Integration over cut elements	172
6.3	The non-linear model	175
6.4	Numerical experiments	176
6.4.1	Idealized closed valve	176
6.4.2	Vesicle in lid-driven cavity flow	180
6.4.3	Idealized open valve	187
6.5	Conclusion	194

6.1 Introduction

This chapter is devoted to the extension to three dimensions, of the numerical method for the mechanical interaction of an immersed thin-walled structure presented in [Alauzet et al. \(2016\)](#) and Chapter 2. We consider an Eulerian description for viscous fluid in a three-dimensional domain and a Lagrangian formulation for the immersed solid (see Section 1.2.3.1).

As already mentioned in the previous chapters, unfitted mesh formulations based on method like Immersed Boundary (see, e.g., [Peskin \(2002\)](#); [Kamensky et al. \(2015\)](#); [Sotiropoulos and Yang \(2014\)](#); [Griffith \(2012\)](#)) and Fictitious Domain (see, e.g., [Boffi and Gastaldi \(2017\)](#); [Astorino et al. \(2009b\)](#); [Baaijens \(2001\)](#)), are known to be inaccurate due to the continuous nature of the fluid approximation spaces at the interface between the fluid and the solid. One possible way to overcome this consistency issue is to combine a local XFEM duplication with a cut-FEM methodology and a weak imposition of the interface coupling.

A widely used implementation technique is to decompose the fluid intersected elements into sub-elements, conforming to an additional sub-division of the interface mesh. Even though this approach is extensively used in two dimensions, the extension to three dimensions is still a quite challenging problem (particularly for unstructured mesh). Additionally, when considering dynamic interfaces, there is the need to compute the intersection at each time iteration, hence, the algorithm has to be efficient and robust (with respect to how the structure mesh cuts the fluid mesh). Moreover, the sub-tetrahedralization without adding additional vertices, cannot be guaranteed, even for a simple polyhedron (see [Mayer et al. \(2009\)](#) and the references therein). A few 3D intersection and sub-tetrahedralization algorithms have been reported in the literature. For instance, we recall the work of [Mayer et al. \(2010\)](#), [Zonca et al. \(2018\)](#) and [Mayer et al. \(2009\)](#), the latter in the case of high-order XFEM implementation. Furthermore, [Massing et al. \(2013\)](#) presents only an algorithm to identify the intersecting elements and avoids sub-tetrahedralization, by considering a boundary representation of the bulk integrals. Finally, [Burman et al. \(2014\)](#) introduces an intersection based on a level-set methodology, in which the location of the boundary is given by the zero level set of a function.

The majority of those works relay on external meshing libraries for the elements sub-division, such as TetGen (see [Si \(2015\)](#)), with the purpose of building some constrained tetrahedralization. Contrarily, in the presented work, we will build an ad hoc intersection and sub-tetrahedralization algorithm. To summarize, with the aim of extending the Nitsche-XFEM method of [Alauzet et al. \(2016\)](#) to three dimensions, we require an intersection algorithm to locate the structure mesh within the fluid mesh, sub-tetrahedralize the fluid and solid intersected elements and which is efficient and robust with arbitrary fluid and solid unstructured meshes. Additionally, we will derive a duplication strategy able to preserve mesh connectivity and consistency, also with partially intersected fluid domain.

The rest of the chapter is organized as follows: Section 6.2 is devoted to the description of the linear coupled problem in the case of static interface. In particular, we will introduce in Section 6.2.1 the space semi-discretization, the partially intersected fluid domain

is addressed in Section 6.2.2. In Section 6.2.3 we introduce the fully discrete algorithm, Section 6.2.4 describes the intersection algorithm and Section 6.2.5 the duplication procedure, while in Section 6.2.6 we will address the problem of integrals over cut-elements. Section 6.3 concerns the extension to the method in the non-linear case. In Section 6.4 a series of three-dimensional numerical examples, involving moving interfaces and partially intersected fluid domain, illustrate the performance and robustness of the proposed method, by comparing with the two-dimensional solutions. Finally, Section 6.5 reports a summary of the conclusions for this chapter.

6.2 The linear model

We consider a linear coupled problem similar to the one introduced in Chapter 2, involving the Stokes system and a linear thin-walled solid problem in which the structure is immersed within the fluid and considered as static. The fluid domain is denoted by $\Omega^f \subset \mathbb{R}^3$ and the mid-surface of the structure is represented by the oriented manifold $\Sigma \subset \Omega^f$ of codimension 1 and unitary normal vector \mathbf{n} . For the time being, we will assume that Σ divides Ω^f into two open domains Ω_1 and Ω_2 (see Figure 2.1). We will address in Section 6.2.2 the more general case of partially intersected fluid domain Ω^f . We denote the outward unit normal to Ω_i on Σ by $\mathbf{n}_i, i = 1, 2$. Note that we choose Ω_1 and Ω_2 so that $\mathbf{n}_1 = \mathbf{n}$ and $\mathbf{n}_2 = -\mathbf{n}$. We define $\Gamma^f = \partial\Omega^f \setminus \Sigma$, and $\Gamma_i = \partial\Omega_i \setminus \Sigma$, with $i = 1, 2$. As already introduced in Section 2.2 we define the following definitions of side-restrictions, jumps and averaged, reported here for facilitate the reading. For a given continuous scalar or tensorial field f defined in Ω^f (possibly discontinuous across Σ) we define its sided-restrictions to Σ , noted by f_1 and f_2 , as

$$f_1(\mathbf{x}) \stackrel{\text{def}}{=} \lim_{\xi \rightarrow 0^+} f(\mathbf{x} + \xi \mathbf{n}_1), \quad f_2(\mathbf{x}) \stackrel{\text{def}}{=} \lim_{\xi \rightarrow 0^+} f(\mathbf{x} + \xi \mathbf{n}_2) \quad \forall \mathbf{x} \in \Sigma.$$

We also define the following jumps and average across the interface Σ :

$$\llbracket f \rrbracket \stackrel{\text{def}}{=} f_1 - f_2, \quad \llbracket f \mathbf{n} \rrbracket \stackrel{\text{def}}{=} f_1 \mathbf{n}_1 + f_2 \mathbf{n}_2, \quad \{\!\!\{ f \}\!\!\} \stackrel{\text{def}}{=} \frac{1}{2} (f_1 + f_2).$$

In this framework, the considered coupled problem reads as follow: find the fluid velocity and pressure $\mathbf{u} : \Omega^f \times \mathbb{R}^+ \rightarrow \mathbb{R}^3$, $p : \Omega^f \times \mathbb{R}^+ \rightarrow \mathbb{R}$, the solid displacement and velocity $\mathbf{d} : \Sigma \times \mathbb{R}^+ \rightarrow \mathbb{R}^3$, $\dot{\mathbf{d}} : \Sigma \times \mathbb{R}^+ \rightarrow \mathbb{R}^3$ such that for all $t \in \mathbb{R}^+$ we have

$$\begin{cases} \rho^f \partial_t \mathbf{u} - \text{div} \boldsymbol{\sigma}(\mathbf{u}, p) = \mathbf{0} & \text{in } \Omega_i \times \mathbb{R}^+, \quad i = 1, 2 \\ \text{div} \mathbf{u} = 0 & \text{in } \Omega_i \times \mathbb{R}^+, \quad i = 1, 2 \\ \mathbf{u} = \mathbf{0} & \text{on } \Gamma_i \times \mathbb{R}^+, \quad i = 1, 2 \end{cases} \quad (6.1)$$

$$\begin{cases} \rho^s \varepsilon \partial_t \dot{\mathbf{d}} + \mathbf{L} \mathbf{d} = \mathbf{T} & \text{in } \Sigma \times \mathbb{R}^+, \\ \dot{\mathbf{d}} = \partial_t \mathbf{d} & \text{in } \Sigma \times \mathbb{R}^+, \\ \mathbf{d} = \mathbf{0} & \text{on } \partial\Sigma \times \mathbb{R}^+, \end{cases} \quad (6.2)$$

$$\begin{cases} \mathbf{u}_1 = \mathbf{u}_2 = \dot{\mathbf{d}} & \text{on } \Sigma \times \mathbb{R}^+, \\ \mathbf{T} = -\llbracket \boldsymbol{\sigma}(\mathbf{u}, p) \mathbf{n} \rrbracket & \text{on } \Sigma \times \mathbb{R}^+ \end{cases} \quad (6.3)$$

complemented with standard initial conditions $\mathbf{u}(0) = \mathbf{u}_0$, $\mathbf{d}(0) = \mathbf{d}_0$ and $\dot{\mathbf{d}}(0) = \dot{\mathbf{d}}_0$. The standard Stokes bilinear forms are given by

$$a^f((\mathbf{u}, p), (\mathbf{v}, q)) \stackrel{\text{def}}{=} 2\mu(\boldsymbol{\epsilon}(\mathbf{u}), \boldsymbol{\epsilon}(\mathbf{v}))_{\Omega^f} - (p, \operatorname{div} \mathbf{v})_{\Omega^f} + (q, \operatorname{div} \mathbf{u})_{\Omega^f}$$

As in Section 2.2, the elastic bilinear form $a^s : \mathbf{W} \times \mathbf{W} \rightarrow \mathbb{R}$ will represent the weak form of the surface differential operator $\mathbf{L} : \mathbf{D}(\mathbf{L}) \subset [L^2(\Sigma)]^d \rightarrow [L^2(\Sigma)]^d$, namely

$$a^s(\mathbf{d}, \mathbf{w}) = (\mathbf{L}\mathbf{d}, \mathbf{w})_{\Sigma}$$

for all $\mathbf{d} \in \mathbf{D}(\mathbf{L})$ and $\mathbf{w} \in \mathbf{W}$. The weak form of the linear coupled problem (6.1)-(6.3) reads as follows: for $t > 0$, find $(\mathbf{u}(t), p(t), \mathbf{d}(t), \dot{\mathbf{d}}(t)) \in \mathbf{V} \times Q \times \mathbf{W} \times \mathbf{W}$ such that

$$\begin{cases} \mathbf{u}_1|_{\Sigma} = \mathbf{u}_2|_{\Sigma} = \dot{\mathbf{d}}, & \dot{\mathbf{d}} = \partial_t \mathbf{d} \\ \rho^f(\partial_t \mathbf{u}, \mathbf{v})_{\Omega^f} + a^f((\mathbf{u}, p), (\mathbf{v}, q)) + \rho^s \varepsilon(\partial_t \dot{\mathbf{d}}, \mathbf{w})_{\Sigma} + a^s(\mathbf{d}, \mathbf{w}) = 0. \end{cases}$$

6.2.1 Space semi-discretization

In the following Section we introduce the space semi-discretization. Since the three-dimensional mathematical formulation of the method is the same as in two dimensions, we will follow [Alauzet et al. \(2016\)](#). The discussion is similar to Section 2.2.2 since the discretization is independent from the dimension of the problem. As pointed out in Section 2.2, the thin-walled nature of the immersed solid introduces jumps on the fluid stresses (due to the dynamic coupling relation (6.3)₂), which, respectively, results in weak and strong discontinuities of the velocity and pressure fields.

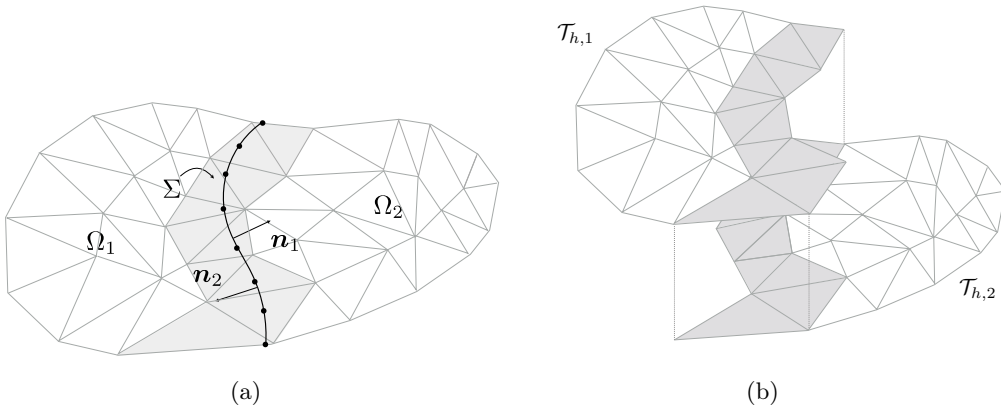


Figure 6.1: (a) Two-dimensional unfitted fluid-solid meshes (in gray the elements intersected by the structure Σ). (b) The triangulations $\mathcal{T}_{h,1}$ and $\mathcal{T}_{h,2}$ with the overlapping region in gray.

We propose to approximate the fluid velocity and pressure with triangulations of Ω^f which are independent of the interface Σ and we allow the discrete fluid solution to be possibly discontinuous by enriching the fluid elements that are intersected by the interface Σ , as shown in Figure 6.1 in two dimensions and the corresponding three-dimensional representation in Figure 6.2. This guarantees optimal convergence. In this framework we enforce the coupling conditions (6.3) by Nitsche's type mortaring as reported in Chapter 2.

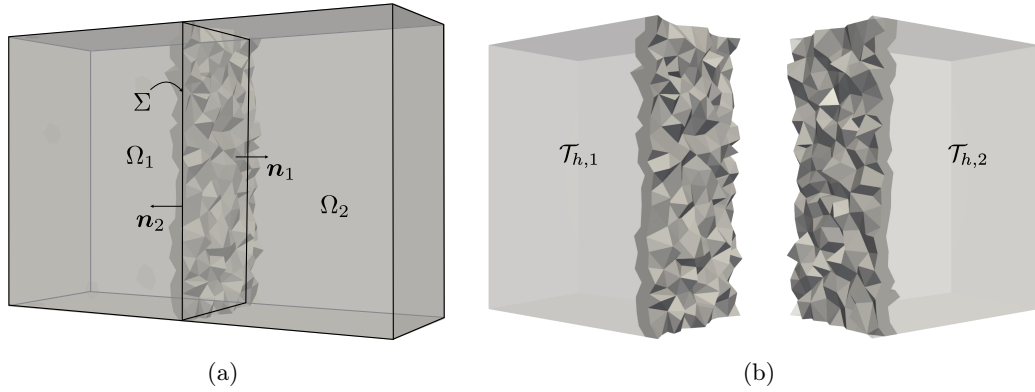


Figure 6.2: (a) Three-dimensional unfitted fluid-solid meshes (with the intersected fluid elements highlighted). (b) The triangulations $\mathcal{T}_{h,1}$ and $\mathcal{T}_{h,2}$ with the overlapping region in dark gray.

For sake of simplicity, we assume that both Ω^f and Σ are polyhedral. Let be $\{\mathcal{T}_h^s\}_{0 < h < 1}$ a family of quasi-uniform triangulations of Σ . We then consider the standard space of continuous piecewise affine functions:

$$X_h^s \stackrel{\text{def}}{=} \{v_h \in C^0(\overline{\Sigma}) \mid v_h|_K \in \mathbb{P}_1(K), \quad \forall K \in \mathcal{T}_h^s\}.$$

The discrete space for the solid displacement and velocity approximations is hence defined as $\mathbf{W}_h = [X_h^s]^3 \cap \mathbf{W}$.

For the fluid, we introduce two families of quasi-uniform tetrahedral meshes $\{\mathcal{T}_{h,i}\}_{0 < h < 1}$, $i = 1, 2$, where each $\mathcal{T}_{h,i}$ covers the i -th fluid region Ω_i^f separated by Σ . Each mesh $\mathcal{T}_{h,i}$ is fitted to the exterior boundary Γ_i but not to \mathcal{T}_h^s .

Moreover we assume that for every element $K \in \mathcal{T}_{h,1} \cap \mathcal{T}_{h,2}$ we have $K \cap \Sigma^n \neq \emptyset$. We denote by $\Omega_{h,i}$ the domain covered by $\mathcal{T}_{h,i}$,

$$\Omega_{h,i} \stackrel{\text{def}}{=} \text{int} \left(\cup_{K \in \mathcal{T}_{h,i}} K \right).$$

Note that the mesh composed by $\mathcal{T}_{h,1} \cup \mathcal{T}_{h,2}$ is a conforming mesh of the whole fluid domain Ω^f . For $i = 1, 2$, we can hence introduce the following spaces of continuous piecewise affine functions:

$$X_{h,i} \stackrel{\text{def}}{=} \{v_h \in C^0(\overline{\Omega_{h,i}}) \mid v_h|_K \in \mathbb{P}_1(K), \quad \forall K \in \mathcal{T}_{h,i}\},$$

Associated with $X_{h,i}$ we define the following spaces

$$\mathbf{V}_{h,i} \stackrel{\text{def}}{=} [X_{h,i}]^3 \cap [H_{\Gamma^f}^1(\Omega^f)]^3, \quad Q_{h,i} \stackrel{\text{def}}{=} X_{h,i} \cap L^2(\Omega^f)_0.$$

For the approximation of the fluid velocity and pressure we consider the following discrete product spaces

$$\mathbf{V}_h \stackrel{\text{def}}{=} \mathbf{V}_{h,1} \times \mathbf{V}_{h,2}, \quad Q_h \stackrel{\text{def}}{=} Q_{h,1} \times Q_{h,2}.$$

Note that interfacial strong and weak discontinuities are included these discrete approximation spaces. Since this choice of pressure and velocity approximation spaces do not satisfy the inf-sup condition we need a stabilization operator. For instance the symmetric stabilization operator given by the Continuous Interior Penalty method (see [Burman and Hansbo \(2006\)](#)):

$$s_h(p_h, q_h) = \frac{\gamma_p h^3}{\mu} \sum_{i=1}^2 \sum_{F \in \mathcal{F}_{h,i}} ([\nabla p_h]_F, [\nabla q_h]_F)_F,$$

where $\mathcal{F}_{h,i}$ denotes the set of interior faces of $\mathcal{T}_{h,i}$. Note that the stabilization operator acts on the whole computational domain.

Afterward, in order to guarantee robustness with respect to the way the interface is cutting the fluid domain, we consider the ghost-penalty stabilization operator $g_h : \mathbf{V}_h \times \mathbf{V}_h \rightarrow \mathbb{R}$ (see [Burman \(2010\)](#)) defined by

$$g_h(\mathbf{u}_h, \mathbf{v}_h) \stackrel{\text{def}}{=} \gamma_g \mu h \sum_{i=1}^2 \sum_{F \in \mathcal{F}_{i,h}^\Sigma} ([\nabla \mathbf{u}_{i,h}]_F, [\nabla \mathbf{v}_{i,h}]_F)_F$$

where $\gamma_g > 0$ is a user-defined parameter and $[\cdot]_F$ denotes the jump across the face F belonging to $\mathcal{F}_{i,h}^\Sigma$, the set of interior faces of the elements of $\mathcal{T}_{i,h}^f$ intersected by Σ , i.e., $F \in \mathcal{F}_{i,h}^\Sigma$ if there exist $K_1, K_2 \in \mathcal{T}_{i,h}^f$, with $K_1 \neq K_2$ and $K_1 \cap \Sigma \neq \emptyset$ or $K_2 \cap \Sigma \neq \emptyset$, such that $F = K_1 \cap K_2$. Hence, the total stabilization operator is given by

$$S_h((\mathbf{u}_h, p_h), (\mathbf{v}_h, q_h)) \stackrel{\text{def}}{=} s_h(q_h, q_h) + g_h(\mathbf{u}_h, \mathbf{v}_h)$$

with the associated semi-norm $|(\mathbf{v}_h, q_h)|_S \stackrel{\text{def}}{=} \sqrt{S_h((\mathbf{v}_h, p_h), (\mathbf{v}_h, q_h))}$. We can now introduce the fluid discrete bilinear form

$$a_h^f((\mathbf{u}_h, p_h), (\mathbf{v}_h, q_h)) \stackrel{\text{def}}{=} a^f((\mathbf{u}_h, p_h), (\mathbf{v}_h, q_h)) + S_h((\mathbf{u}_h, p_h), (\mathbf{v}_h, q_h))$$

and the space semi-discrete problem of (6.1)-(6.3) (from [Alauzet et al. \(2016\)](#)) as follows: for $t > 0$, find

$$\left(\mathbf{u}_h(t), p_h(t), \dot{\mathbf{d}}_h(t), \mathbf{d}_h(t) \right) \in \mathbf{V}_h \times Q_h \times \mathbf{W}_h \times \mathbf{W}_h$$

such that $\dot{\mathbf{d}}_h(t) = \partial_t \mathbf{d}_h(t)$ and

$$\left\{ \begin{array}{l} \rho^f (\partial_t \mathbf{u}_h, \mathbf{v}_h)_{\Omega^f} + a_h^f((\mathbf{u}_h, p_h), (\mathbf{v}_h, q_h)) + \rho^s \varepsilon (\partial_t \dot{\mathbf{d}}_h, \mathbf{w}_h)_{\Sigma} + a^s(\mathbf{d}_h, \mathbf{w}_h) \\ - \sum_{i=1}^2 (\boldsymbol{\sigma}(\mathbf{u}_{h,i}, p_{h,i}) \mathbf{n}_i, \mathbf{v}_{h,i} - \mathbf{w}_h)_{\Sigma} - \sum_{i=1}^2 (\mathbf{u}_{h,i} - \dot{\mathbf{d}}_h, \boldsymbol{\sigma}(\mathbf{v}_{h,i}, -q_{h,i}) \mathbf{n}_i)_{\Sigma} \\ + \frac{\gamma \mu}{h} \sum_{i=1}^2 (\mathbf{u}_{h,i} - \dot{\mathbf{d}}_h, \mathbf{v}_{h,i} - \mathbf{w}_h)_{\Sigma} = 0 \end{array} \right. \quad (6.4)$$

6.2.2 Partially intersected fluid domain

This section is focus on the generalization of the semi-discrete formulation 6.4 to the case in which the interface Σ only partially intersects the domain Ω^f , i.e. the structure has a boundary front (some boundary edges) inside Ω^f . We will introduce a procedure which aim to connect the fluid elements intersected by the solid boundary elements, with the rest of the fluid domain, and that will help the definition of the fluid discrete spaces. The two-dimensional connection strategy proposed in Alauzet et al. (2016) becomes inapplicable in three dimensions. For comparison and illustration purposes, we will first consider the two-dimensional case and recall the procedure proposed in Alauzet et al. (2016). In two dimensions we refer to the boundary solid vertex as *tip*, while in three dimensions the immersed boundary is identified as *front*. Additionally, we will name with *fluid tip elements* the fluid simplexes that are intersected by the solid boundary *tip* in 2D or the boundary *front* in 3D. The strategy is proposed in Alauzet et al. (2016) for the 2D case

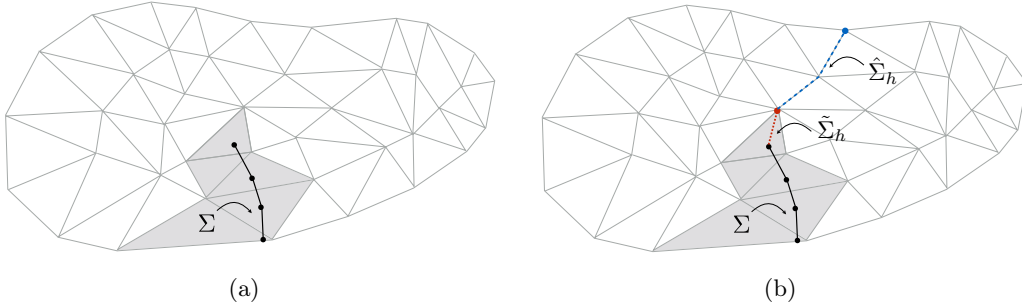


Figure 6.3: (a) Initial fluid and solid triangulations. (b) Virtual interface extension from Alauzet et al. (2016)

consists in introducing a virtual interface $\tilde{\Sigma}_h$ which closes the fluid domain within the cut element. The resulting fluid-fluid fictitious prolongation, shown in Figure 6.3, is defined in terms of the partition $\Sigma_h^{\text{tip}} = \tilde{\Sigma}_h \cup \hat{\Sigma}_h$ where:

- $\tilde{\Sigma}_h$ is the prolongation of the interface tip up to the fluid vertex which is opposite to the edge intersected by Σ ;
- $\hat{\Sigma}_h$ is arbitrary chosen, but aligned with the edges of the fluid mesh. It connects the fluid tip vertex with the fluid boundary.

We recall that, $\widehat{\Sigma}_h$ does not play any role in practice, it is only used as mathematical object to define the discrete spaces. As mentioned above, the extension of this strategy to three dimensions is not straightforward (a clear closing location of prolongation $\widetilde{\Sigma}_h$ is not available) and even less in the case of multiple structures (see Remark 4.3.2).

The main idea of the new approach is unchanged, we built a fictitious prolongation of Σ , namely Σ_h^{tip} , so that $\Sigma \cup \Sigma_h^{\text{tip}}$ divides Ω^f into two domains. The proposed approach

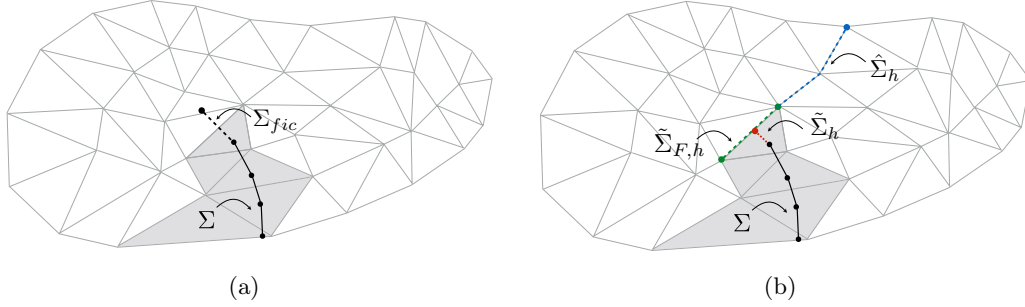


Figure 6.4: (a) Initial fluid and solid triangulation with the fictitious interface Σ_{fic} . (b) Virtual interface prolongation $\Sigma_h^{\text{tip}} = \widetilde{\Sigma}_h \cup \widetilde{\Sigma}_{F,h} \cup \widehat{\Sigma}_h$.

avoids any need of closure strategy in the *fluid tip elements*, by adding to the structure mesh Σ a fictitious extension Σ_{fic} (see Figure 6.4(a)), with the only function of helping defining the new solid prolongation $\widetilde{\Sigma}_h$. As shown in Figure 6.4 (for the two-dimensional version), the fluid-fluid fictitious prolongation Σ_h^{tip} is now defined as $\Sigma_h^{\text{tip}} = \widetilde{\Sigma}_h \cup \widetilde{\Sigma}_{F,h} \cup \widehat{\Sigma}_h$ where:

- $\widetilde{\Sigma}_h$: represents the intersection of the fictitious interface Σ_{fic} that belongs to the *fluid tip simplex*. Note that, contrarily to the approach proposed in Alauzet et al. (2016), the configuration of $\widetilde{\Sigma}_h$ is now arbitrary with respect to the fluid element;
- $\widetilde{\Sigma}_{F,h}$: stands for the edge or faces of the tip fluid element that are intersected by the fictitious interface Σ_{fic} (in two dimensions there is only one *tip edge*, while in three dimensions multiple faces can be considered as *tip faces*, see Figure 6.5);
- $\widehat{\Sigma}_h$: as in Alauzet et al. (2016), it is arbitrary chosen and aligned with the edges or faces of the fluid mesh connect with the tip edge or faces. It connects the fluid tip edge or faces with the fluid boundary.

We now proceed, as in Section 6.2.1, by introducing two overlapping meshes $\mathcal{T}_{i,h}^f, i = 1, 2$ (see Figure 6.6). Like in Alauzet et al. (2016), the overlap region reduces to the set of elements intersected by Σ . The fluid elements intersected only by the fictitious interface Σ_{fic} are not duplicated. The associated discrete spaces $X_{i,h}^f, i = 1, 2$, are then defined as in Section 6.2.1, while for the derivation of the velocity and pressure approximation spaces one last observation is necessary.

As a consequence of the duplication procedure, the generated fluid domains are disconnected across $\widehat{\Sigma}_h$ and $\widetilde{\Sigma}_{F,h}$. To overcome this issue Alauzet et al. (2016) proposes to

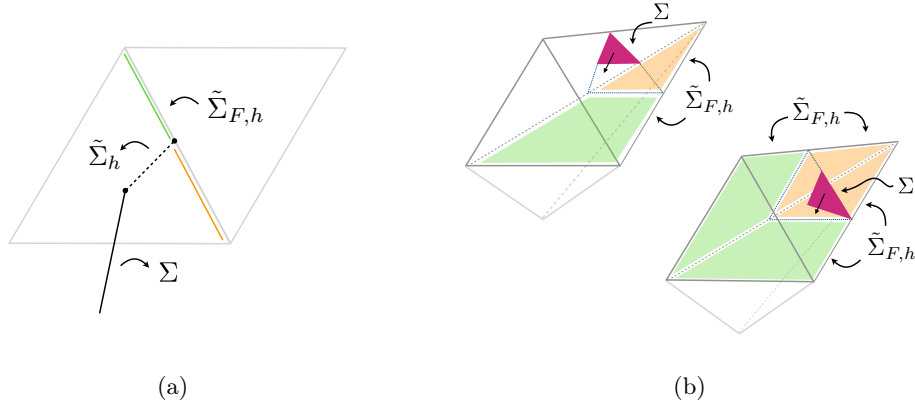


Figure 6.5: (a) two dimensions *tip edges*, (b) three dimensions *tip faces*.

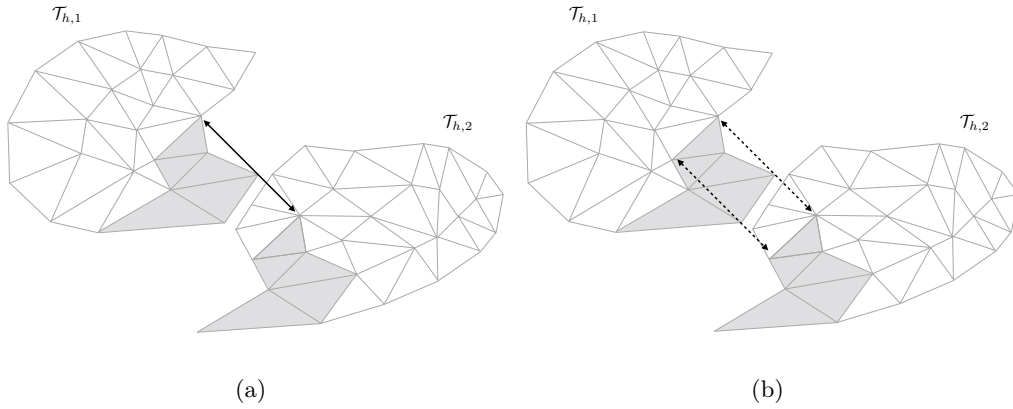


Figure 6.6: Two overlapping two-dimensional triangulations with partially intersected fluid domain. (a) Strong continuity imposed on the tip vertex (from Alauzet et al. (2016)) and (b) weak continuity imposed on the tip edges.

enforce strongly the continuity of the velocity and pressure across $\hat{\Sigma}_h$, in particular at the *tip vertex* (see Figure 6.6(a)). Contrarily, we propose to enforce weakly the continuity on $\tilde{\Sigma}_{F,h}$, between the physical part of the tip element and the rest of the fluid domain (see Figure 6.6(b)).

This new approach results in functions that are continuous in $\Omega_f \setminus (\Sigma \cup \tilde{\Sigma}_h \cup \tilde{\Sigma}_{F,h})$ and discontinuous across $\Sigma \cup \tilde{\Sigma}_h \cup \tilde{\Sigma}_{F,h}$. The fluid approximation spaces are hence defined as:

$$\mathbf{V}_h \stackrel{\text{def}}{=} \left\{ \mathbf{v}_h = (\mathbf{v}_{1,h}, \mathbf{v}_{2,h}) \in \mathbf{V}_{1,h} \times \mathbf{V}_{2,h} \mid \mathbf{v}_{1,h} = \mathbf{v}_{2,h} \text{ on } \hat{\Sigma}_h \right\}$$

$$Q_h \stackrel{\text{def}}{=} \left\{ q_h = (q_{1,h}, q_{2,h}) \in Q_{1,h} \times Q_{2,h} \mid q_{1,h} = q_{2,h} \text{ on } \hat{\Sigma}_h \right\}.$$

It should be noted that the solid fictitious region is introduced only to facilitate the treatment of the partially intersected fluid domains in three dimensions. The physical

interface Σ is the sole part of the fluid mesh which intervenes in the solid approximation and fluid-structure interaction coupling. The fictitious solid region Σ_{fic} is mechanically a slave of the solid interface Σ . In other words, a kinematic continuity is enforced, but no dynamic coupling is considered at the interface between the two regions. In practice, the uncoupling between the physical Σ and fictitious Σ_{fic} solid regions is performed at the algebraic level of the solid solver, during the elementary evaluations of the residual and tangent matrices. For the sake of clarity, we give here some details in the linear case. The finite element system over the whole solid computational domain has the following structure:

$$\begin{bmatrix} A_{PP} & A_{PI} & 0 \\ A_{IP} & A_{II} & A_{IF} \\ 0 & A_{FI} & A_{FF} \end{bmatrix} \begin{bmatrix} x_P \\ x_I \\ x_F \end{bmatrix} = \begin{bmatrix} b_P \\ b_I \\ b_F \end{bmatrix}, \quad (6.5)$$

where, the arrays x_P , x_F , x_I respectively denote the solid degrees of freedom in the physical region, fictitious region and interface between the two regions. The right-hand side arrays b_P , b_I and b_F stands for the algebraic counterpart of body forces and/or time-stepping terms. The fundamental idea consists in removing the coupling block A_{IF} in (6.5), which yields

$$\begin{bmatrix} A_{PP} & A_{PI} & 0 \\ A_{IP} & A_{II} & 0 \\ 0 & A_{FI} & A_{FF} \end{bmatrix} \begin{bmatrix} x_P \\ x_I \\ x_F \end{bmatrix} = \begin{bmatrix} b_P \\ b_I \\ \tilde{b}_F \end{bmatrix}, \quad (6.6)$$

where the fictitious right-hand side \tilde{b}_F does not contain anymore body forces related to the physical region, but only time-stepping terms. Note that, in this modified system, the physical degrees of freedom x_P and x_I are uncoupled from the fictitious degrees of freedom x_F . Indeed, the first two rows of (6.6) correspond to a solid problem in the physical region with homogeneous Neumann boundary conditions on the interface between the two regions. The last row of (6.6) is nothing but a solid problem in the fictitious region with Dirichlet conditions on the interface between the two regions (note that the prescribed Dirichlet data x_I is known from the first two rows of (6.6)). An illustration of this is given in Figure 6.7, for different external boundary conditions on the fictitious region. In this example, we impose a vertical volumetric force on the physical region Σ and different boundary conditions on the right extremity of Σ_{fic} , zero traction in 6.7(a) and zero displacement in 6.7(b). The displacement of Σ is clearly independent of the displacement of Σ_{fic} .

The fluid semi-discrete bilinear form in case of partially intersected fluid domain is hence redefined as: for $t > 0$, find

$$\left(\mathbf{u}_h(t), p_h(t), \dot{\mathbf{d}}_h(t), \mathbf{d}_h(t) \right) \in \mathbf{V}_h \times Q_h \times \mathbf{W}_h \times \mathbf{W}_h$$

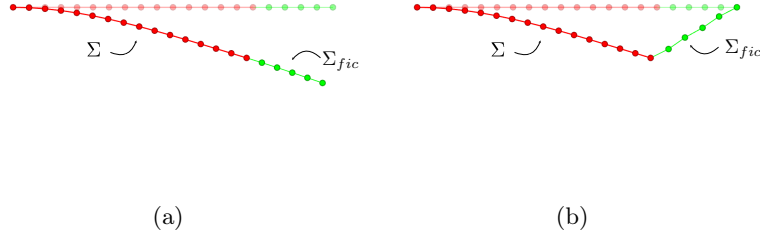


Figure 6.7: Illustration of the slave nature of Σ_{fic} with respect to Σ . The solid problem is solved in Σ_{fic} with different boundary conditions on its right extremity: (a) zero traction and (b) zero displacement.

such that $\dot{\mathbf{d}}_h(t) = \partial_t \mathbf{d}_h(t)$ and

$$\left\{ \begin{array}{l} \rho^f (\partial_t \mathbf{u}_h, \mathbf{v}_h)_{\Omega^f} + a_h^f((\mathbf{u}_h, p_h), (\mathbf{v}_h, q_h)) + \rho^s \varepsilon(\partial_t \dot{\mathbf{d}}_h, \mathbf{w}_h)_{\Sigma} + a^s(\mathbf{d}_h, \mathbf{w}_h) \\ - \sum_{i=1}^2 (\boldsymbol{\sigma}(\mathbf{u}_{h,i}, p_{h,i}) \mathbf{n}_i, \mathbf{v}_{h,i} - \mathbf{w}_h)_{\Sigma} - \sum_{i=1}^2 (\mathbf{u}_{h,i} - \dot{\mathbf{d}}_h, \boldsymbol{\sigma}(\mathbf{v}_{h,i}, -q_{h,i}) \mathbf{n}_i)_{\Sigma} \\ + \frac{\gamma \mu}{h} \sum_{i=1}^2 (\mathbf{u}_{h,i} - \dot{\mathbf{d}}_h, \mathbf{v}_{h,i} - \mathbf{w}_h)_{\Sigma} - (\{\{\boldsymbol{\sigma}(\mathbf{u}_h, p_h)\}\} \mathbf{n}, \llbracket \mathbf{v}_h \rrbracket)_{\tilde{\Sigma}_h \cup \tilde{\Sigma}_{F,h}} \\ - (\{\{\boldsymbol{\sigma}(\mathbf{v}_h, -q_h)\}\} \mathbf{n}, \llbracket \mathbf{u}_h \rrbracket)_{\tilde{\Sigma}_h \cup \tilde{\Sigma}_{F,h}} + \frac{\gamma \mu}{h} (\llbracket \mathbf{u}_h \rrbracket, \llbracket \mathbf{v}_h \rrbracket)_{\tilde{\Sigma}_h \cup \tilde{\Sigma}_{F,h}} = 0 \end{array} \right. \quad (6.7)$$

Remark 6.2.1. *It should be noted that the three additional terms act on the whole fluid-fluid fictitious interface $\tilde{\Sigma}_h \cup \tilde{\Sigma}_{F,h}$. The jumps and averages across the tip faces $\tilde{\Sigma}_{F,h}$ must be interpreted between the physical region of the tip fluid element and its respective opposite element in the fluid triangulation. We refer to Section 6.2.6 for further details about the integration onto sub-edges and sub-faces.*

6.2.3 Fully discrete scheme: time discretization

In what follows, we use the notation for the first-order backward difference introduced in Section 2.2.1. Considering an overall Backward Euler time-stepping and a strong coupling between fluid and solid problems, the discretization of the coupled problem (6.7) is given in Algorithm 6.1. Note that the only difference, with respect to Algorithm 2.2 in Chapter 2, concerns the DG terms, now acting on the interface prolongation $\tilde{\Sigma}_h$ and tip faces $\tilde{\Sigma}_{F,h}$.

6.2.4 Intersection algorithm

As pointed out earlier, the Nitsche-XFEM method requires a specific track of the interface inside the fluid mesh and the construction of sub-elements from cut elements, with the only purpose of numerical integration. A robust and computationally efficient

Algorithm 6.1 Linear strongly coupled scheme.

For $n \geq 1$: find $(\mathbf{u}_h^n, p_h^n, \dot{\mathbf{d}}_h^n, \mathbf{d}_h^n) \in \mathbf{V}_h \times Q_h \times \mathbf{W}_h \times \mathbf{W}_h$ with $\dot{\mathbf{d}}_h^n = \partial_\tau \mathbf{d}_h^n$ and such that

$$\begin{aligned} & \rho^f (\partial_\tau \mathbf{u}_h^n, \mathbf{v}_h)_{\Omega^f} + a_h^f((\mathbf{u}_h^n, p_h^n), (\mathbf{v}_h, q_h)) + \rho^s \varepsilon (\partial_\tau \dot{\mathbf{d}}_h^n, \mathbf{w}_h)_\Sigma + a^s(\mathbf{d}_h^n, \mathbf{w}_h) \\ & - \sum_{i=1}^2 (\boldsymbol{\sigma}(\mathbf{u}_{h,i}^n, p_{h,i}^n) \mathbf{n}_i, \mathbf{v}_{h,i} - \mathbf{w}_h)_\Sigma - \sum_{i=1}^2 (\mathbf{u}_{h,i}^n - \dot{\mathbf{d}}_h^n, \boldsymbol{\sigma}(\mathbf{v}_{h,i}, -q_{h,i})) \mathbf{n}_i)_\Sigma \\ & + \frac{\gamma\mu}{h} \sum_{i=1}^2 (\mathbf{u}_{h,i}^n - \dot{\mathbf{d}}_h^n, \mathbf{v}_{h,i} - \mathbf{w}_h)_\Sigma - (\{\{\boldsymbol{\sigma}(\mathbf{u}_h^n, p_h^n)\}\} \mathbf{n}, \llbracket \mathbf{v}_h \rrbracket)_{\tilde{\Sigma}_h \cup \tilde{\Sigma}_{F,h}} \\ & - (\{\{\boldsymbol{\sigma}(\mathbf{v}_h, -q_h)\}\} \mathbf{n}, \llbracket \mathbf{u}_h^n \rrbracket)_{\tilde{\Sigma}_h \cup \tilde{\Sigma}_{F,h}} + \frac{\gamma\mu}{h} (\llbracket \mathbf{u}_h^n \rrbracket, \llbracket \mathbf{v}_h \rrbracket)_{\tilde{\Sigma}_h \cup \tilde{\Sigma}_{F,h}} = 0 \end{aligned}$$

for all $(\mathbf{v}_h, q_h, \mathbf{w}_h) \in \mathbf{V}_h \times Q_h \times \mathbf{W}_h$.

intersection algorithm is a key component, especially when FSI problems with complex and deformable geometries are considered. These procedures are much more involving in 3D and, in particular, for arbitrary unstructured meshes. It should be noted that, no a priori notion exists regarding which fluid element is intersected from the solid mesh and vice versa. Additionally, for complex polyhedra, a subtetrahedralization cannot be guaranteed in 3D, without introducing additional vertices. Algorithms available in the literature often rely on external meshing libraries for the local subtetrahedralization. We refer, for instance, to [Zonca et al. \(2018\)](#); [Fries and Belytschko \(2010\)](#); [Mayer et al. \(2009\)](#), the latter in particular for three-dimensional higher-order XFEM-computations. An alternative approach to subtetrahedralization, based on a boundary representation of the integrals, is considered in [Massing et al. \(2013\)](#). At last, we refer to [Wang et al. \(2012\)](#) for the tracking of thin-walled immersed interface intersections.

In the following paragraphs, we will present a three-dimensional intersection algorithm for the localization of the thin-walled immersed solid mesh in the 3D fluid mesh and the subtetrahedralization of the intersected fluid elements (without resort to black-box meshing libraries). We recall that a triangulation \mathcal{T}_h of Ω of simplex K such that

$$\bar{\Omega} = \bigcup_{K \in \mathcal{T}_h} K$$

where $\bar{\Omega}$ is the closure of Ω , is called *conforming* if the non empty intersection F between two elements K_1, K_2 , namely $F = K_1 \cap K_2 \neq \emptyset$ with $K_1, K_2 \in \mathcal{T}_h$ and $K_1 \neq K_2$, is either a whole edge, face or a vertex of the triangulation. If this condition is not fulfilled the triangulation is called *non-conforming* (see, e.g. [Quarteroni and Quarteroni \(2009\)](#)). Another important features of the following algorithm is the notion of *geometry tolerance*. The *tolerance* is used in order to define the minimum distance between two separated nodes. Hence, if the distance between two nodes is smaller than the *tolerance*, they are merged into the same node. In the context of *conformal* meshes the notion of *tolerance* is global (unique for the whole mesh), while for *non-conformal* meshes the *tolerance* can be defined locally (it can be adapted on each element, i.e., we can have different tolerance in

each tetrahedra).

The two-dimensional intersection and sub-triangulation algorithm presented in [Alauzet et al. \(2016\)](#) was based on a *conformal* approach. Numerical experiments (already in two dimensions) show lack of robustness when the discretization parameter h_s of the solid mesh is considered significantly smaller than the one of the fluid mesh h_f . When moving to three dimensions, the corresponding conforming algorithm fails already with $h_s \approx h_f$, indeed invalid configurations are appearing (for instance tetrahedra generated from coplanar vertices). Adjusting (both increasing and reducing) the *geometry tolerance* can help to overcome these situations, but doing this globally (due to a conformity constraint) is unfeasible in practice. Consequently a *non-conformal* approach has been considered. A local notion of *tolerance* is considered in order to avoid eventual invalid configuration.

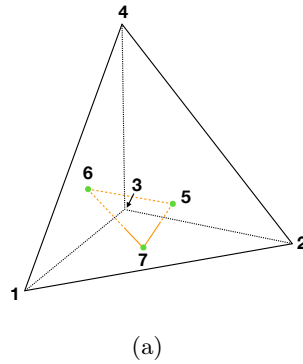


Figure 6.8: Initial configuration (fluid tetrahedron of vertices 1, 2, 3, 4 and structure triangle 5, 6, 7 partially intersecting the tetrahedron) and vertices localization. Solid vertex 5 is localized inside the tetrahedron, vertex 6 on the face, while vertex 7 is external.

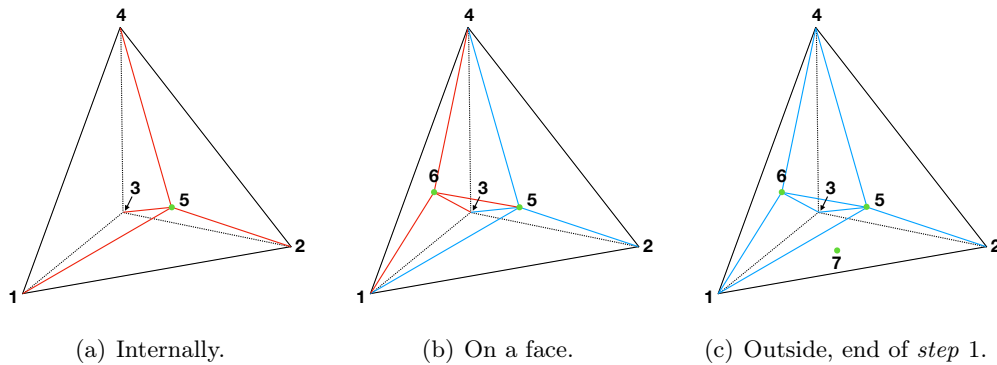


Figure 6.9: Insertion of solid vertices inside the tetrahedron (*step 1*).

The proposed algorithm proceeds as follows:

- We begin by localizing all the solid mesh vertices inside the fluid mesh. An example of initial configuration is showed in Figure 6.8. The localization is carried out using a barycentric coordinates based algorithm, which efficiently identifies the element of

the fluid mesh containing a given point (see, e.g., [Frey and George \(2007\)](#) or [Alauzet and Mehrenberger \(2010\)](#) for further details). We then define two lists of elements \mathcal{L}_1 and \mathcal{L}_2 . The first is the list of intersected fluid elements and the second contains the list of solid triangles intersecting a selected fluid tetrahedron. Thus, we will have a single list \mathcal{L}_1 and multiple lists \mathcal{L}_2 , one for each fluid intersected element (one list \mathcal{L}_2 for each element in \mathcal{L}_1). These lists are updated dynamically during the insertion algorithm described in the following steps.

- We continue by looping over the fluid elements contained in \mathcal{L}_1 . For each tetrahedron in \mathcal{L}_1 , we intersect, one by one, the solid elements contained in the \mathcal{L}_2 list of the selected fluid element. For each triangle, we begin by inserting in order vertices (*step 1*), edges (*step 2*) and face (*step 3*). From now on, we are working on each fluid element separately and we address with $K \in \mathcal{L}_1$ the selected tetrahedra and with $T \in \mathcal{L}_2$ its internal structure element. It should be point out that for efficiency a simple insertion operation is conducted, instead of complex vertex insertion operators (such as Delaunay kernel [Frey and George \(2000\)](#)). The core steps of the intersection algorithm are the following:

Vertex insertion (*step 1*): The vertices of T are localized inside K , using again a barycentric coordinates based algorithm. Once localized, the solid vertices are inserted into the fluid mesh. Five cases may arise (three of them being degenerated):

- ★ the point falls outside K , then nothing is done;
- ★ the point falls on a vertex of K , then nothing is done;
- ★ the point falls inside K , hence K is divided into four sub-tetrahedra;
- ★ the point falls on a face of K , then K is divided in three sub-tetrahedra;
- ★ the point falls on an edge of K , then K is divided in two sub-tetrahedra;

This steps are illustrated in Figure 6.9.

Edges insertion (*step 2*): Successively, we proceed by intersecting the structure edges into the local intersected mesh resulting from *step 1*, considering a partitioning algorithm (see, e.g., [George et al. \(2003\)](#) for a two-dimensional version). Each edge is treated one at a time. Its endpoints are vertices of the current (intersected) mesh thanks to *step 1*. Let AB be an edge of T . Starting from one of its endpoints, say A , we seek for the first current mesh edge or face intersected by AB . The intersection point P_1 is computed (see [Alauzet and Mehrenberger \(2010\)](#), Section 5 for details on the two-dimensional version) and inserted into the current local intersected mesh. P_1 is necessarily on a tetrahedron face (internally to the face or in one of its edges/vertices) and therefore we follow the same insertion strategy of *step 1*. At this stage the segment AP_1 has been added to the current local intersected mesh. Then, the process is pursued by seeking for the intersection between sub-edge P_1B and the current mesh faces/sub-faces, which will give a new intersection point P_2 and so on. If after n intersection steps the sub-edge P_nB belongs to the current mesh, the whole

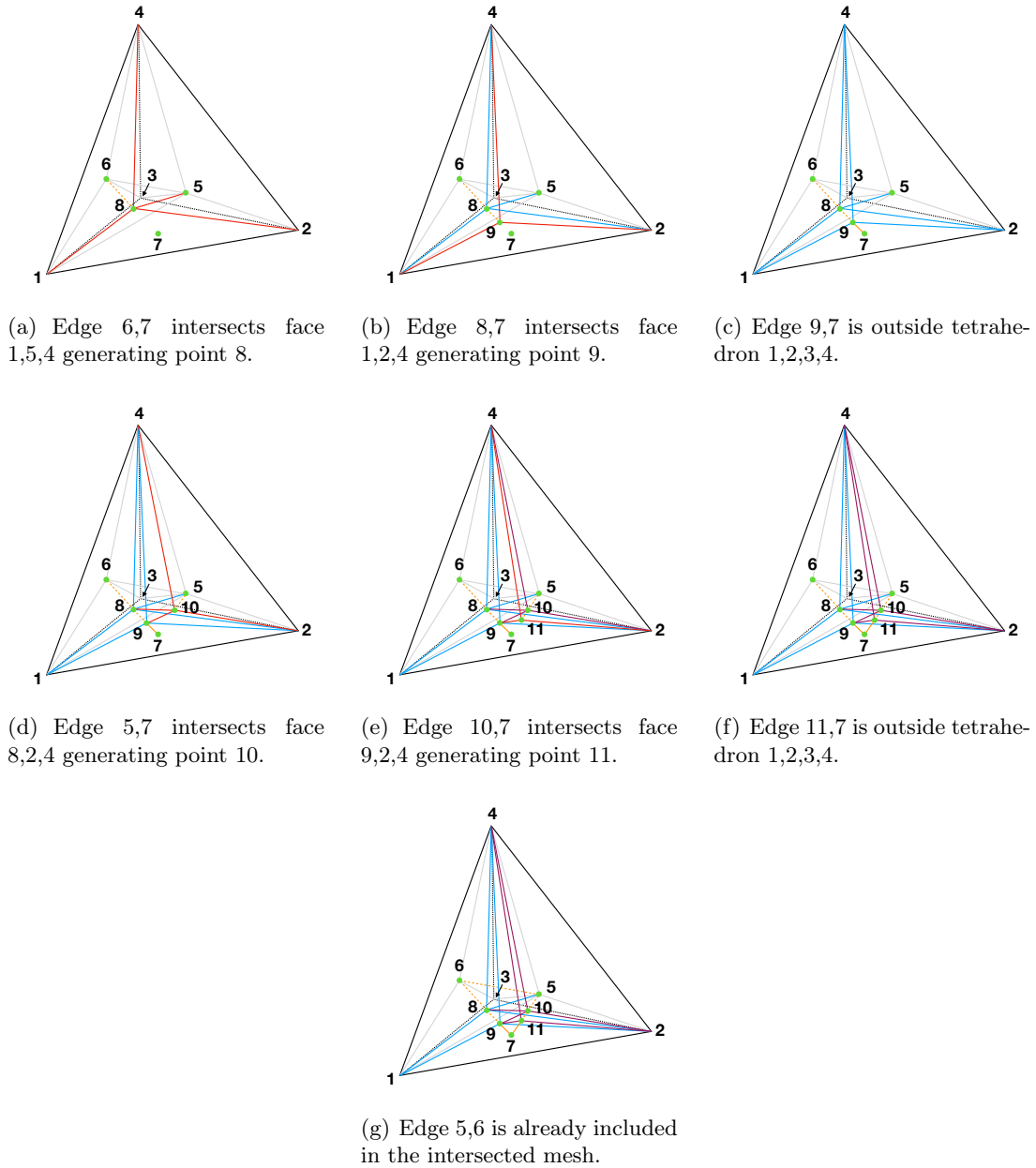


Figure 6.10: Insertion of the structure edges into the local intersected mesh resulting from *step 1*. Insertion of edges 6, 7 (a)-(c), edge 5, 7 (d)-(f) and edge 5, 6 (g).

solid edge AB has been inserted into this local mesh. Otherwise, if the sub-edge $P_n B$ lies outside the local mesh, this edge intersection is done. See Figure 6.10 for a detailed representation starting from configuration of Figure 6.9.

Face insertion (*step 3*): At this stage, we reconstruct the structure triangle (as union of its sub-elements) within the fluid intersected mesh. Thus, we search the structure sub-triangles among the fluid sub-faces. Let consider a face with

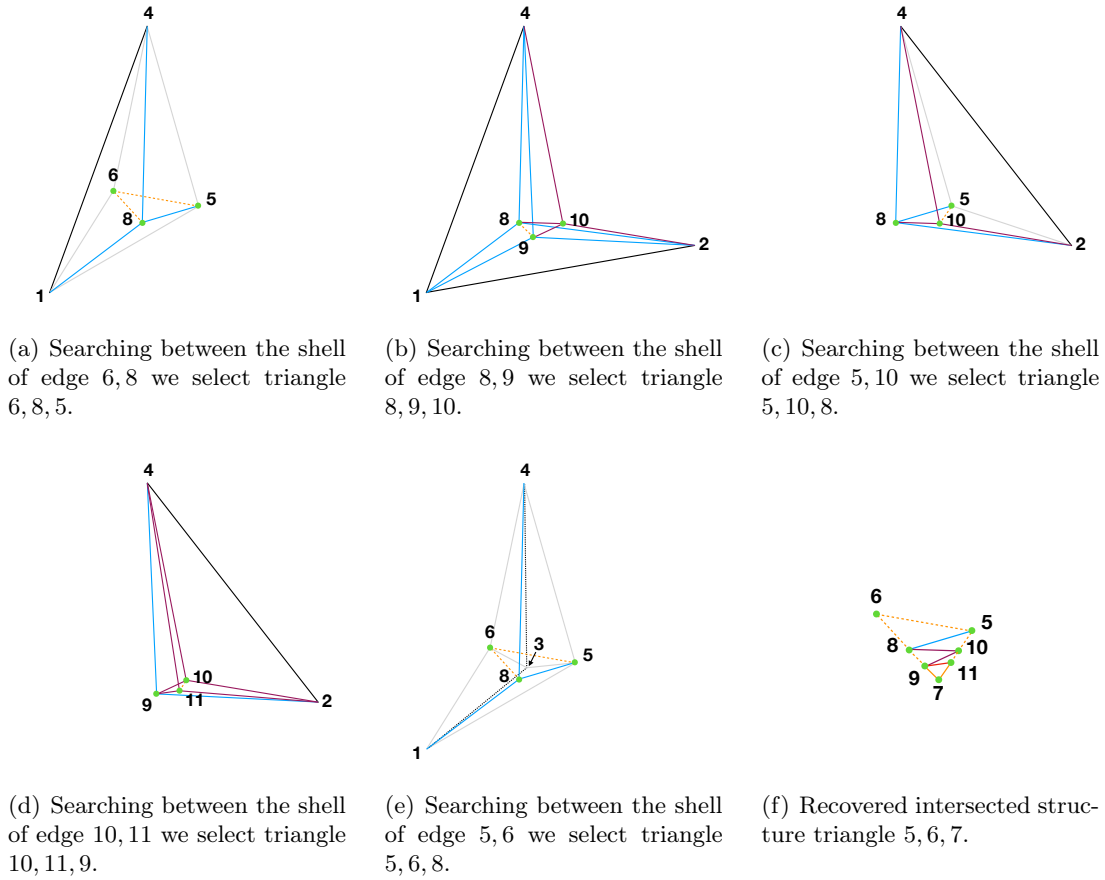


Figure 6.11: Insertion of structure face 5, 6, 7 and recovery of the interface from the intersected sub-faces.

vertices $\{A, B, C\}$, and $\{P_i\}_{i=1}^n$ the points on the edges of T generated by *step* 2, be \mathcal{I} the union of these vertices. Beginning from the first sub-edge AP_1 , we search between all the sub-tetrahedra belonging to its shell one with vertices $\{A, P_1, y\}$, with $y \in \mathcal{I}$. We report in Figure 6.11 these steps starting from configuration of Figure 6.10.

In case a sub-tetrahedra with aimed vertices is not detected, we still have to recover the surface, i.e. we loop on all the sub-tetrahedra belonging to its shell looking for an intersection between a fluid edge and the current interface. If we find it we insert the intersection point as in *step* 1. Figure 6.12 displays an example of the latter situation.

Completed the insertion of vertices, edges and face, before to continue a further control is needed: if the structure element T intersects the boundary face F of K , then the current solid triangle T is added to the \mathcal{L}_2 list of the neighbour fluid element with respect to F of the original mesh. In case the fluid opposite element is not already included into \mathcal{L}_1 , we add it. At this stage, we finish the intersection

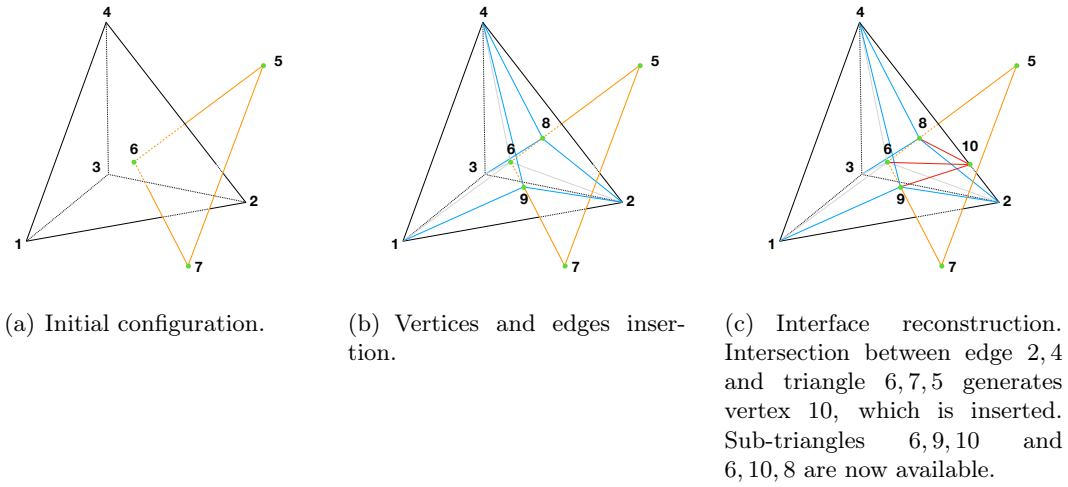


Figure 6.12: Reconstruction of structure sub-triangles after further solid triangle and fluid edges intersection.

between K and T and we pass to the next structure element in \mathcal{L}_2 .

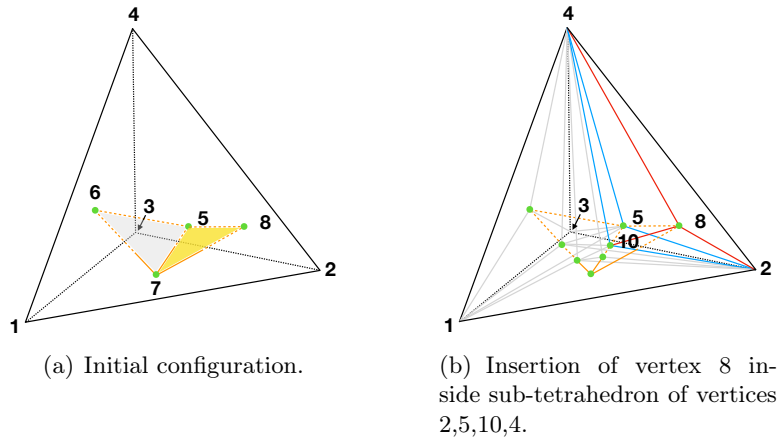


Figure 6.13: *Step 1* for solid triangle 8,5,7: insertion of solid vertices 8,5,7 inside tetrahedron $\{1,2,3,4\}$, which is already been intersected from the solid triangle $\{5,6,7\}$. Vertices 5 and 7 are already been inserted, vertex 8 is internal to the sub-tetrahedron $\{2,5,10,4\}$, hence, is divided in 4 sub-tetrahedra.

It should be noted that K could have already been intersected by another solid triangle, therefore *steps 1, 2, 3* can be conducted on sub-tetrahedra. For instance, in case of degenerated configurations in *steps 1* (solid vertex on a fluid face, edge or vertex) we also have to split the adjacent sub-tetrahedra. Concretely, if the solid vertex is on an edge we also split the corresponding shell elements (all sub-tetrahedra whose share the same edge), while if it is on a face we divide also the opposite sub-tetrahedra (if this exists, because it could be a boundary face). Figure 6.13 shows

an illustration of this circumstances.

- Once all the fluid elements have been intersected, we merge all the local intersected meshes into a global one. Additionally, the data structures needed for element duplication and integration (over cut elements) are updated accordingly. Regarding the latter, since for consistency only integration on the physical domain is considered, we need the notion of location of a sub-tetrahedron with respect to the interface. Considering that the structure is dividing the fluid element into two regions, we label as *LEFT*, the region towards which the structure normal is pointing in (hence, all its sub-elements), and *RIGHT* the other. The marking is starting from the sub-elements directly in contact with the structure, successively, the remaining sub-elements are marked by neighbor. Figure 6.14 illustrates a result of the presented algorithm.

Finally, it is worth recalling that the quality of the intersected mesh is definitely not a concern here, whose sole purpose is numerical quadrature in cut elements (not interpolation). Therefore, simple mesh validity suffices.

In the case of partially intersected fluid domain the algorithm remains unchanged, except for the following two steps:

1. the vertices belonging to the fictitious interface Σ_{fic} are not localized inside the fluid mesh. Therefore the fluid elements that contain only fictitious triangles are not included in the list of elements to be intersected (\mathcal{L}_1);
2. after the insertion of vertices, edges and face, if the structure element T intersects the boundary face F of K , but it belongs to the fictitious interface Σ_{fic} , we don't add it the list \mathcal{L}_2 of the opposite element (with respect to F).

Remark 6.2.2. *Following the same approach a similar non-conformal algorithm for two dimensions has been also implemented.*

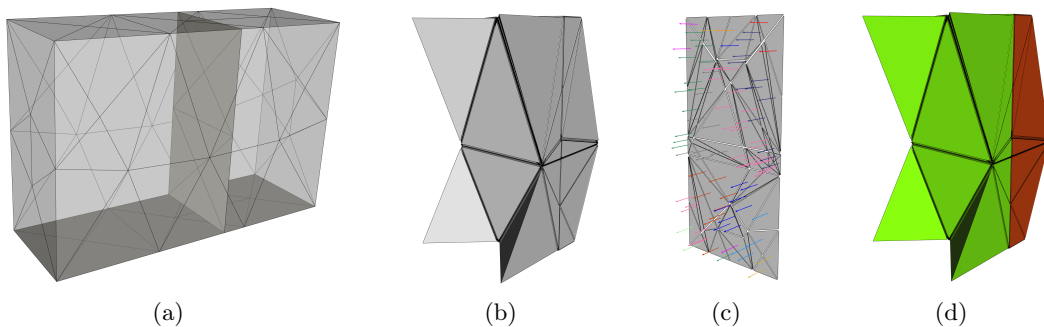


Figure 6.14: Example of intersected meshes. Initial configuration (a), intersected fluid mesh (b), Intersected solid mesh with sub-elements normals (c) and side colored fluid intersected mesh (*LEFT* sub-elements are colored in green and *RIGHT* sub-elements in red) (d).

6.2.5 Element duplication

The duplication procedure is carried out as following. The overlapping meshes $\mathcal{T}_{1,h}^f$ and $\mathcal{T}_{2,h}^f$ are created starting from a conforming triangulation \mathcal{T}_h^f of the whole fluid domain Ω^f and duplicating the elements that are intersected by the interface Σ . Using the information coming from the intersection algorithm described in Section 6.2.4, let

$$\mathcal{G}_h \stackrel{\text{def}}{=} \{K \in \mathcal{T}_h^f | K \cap \Sigma \neq \emptyset\}$$

be the subset of elements intersected by Σ . For each element $K \in \mathcal{G}_h$, with nodes $\{i, j, k, l\}$, we can identify two separated regions Ω_1 and Ω_2 , divided by the interface Σ ; we refer to Figure 6.15 for the details. In what follows, we will distinguish between *physical* and *nonphysical* domain. The former consists of the restriction of $\mathcal{T}_{i,h}^f$ on Ω_i , $i = 1, 2$, the latter contains the complementary part.

Let consider a duplication $\{i', j', k', l'\}$ of nodes $\{i, j, k, l\}$. In order to preserve the continuity between the physical adjacent duplicated elements, if a node has been already duplicated, we select the preexisting duplication as duplicated node. We define two identical copies of K , namely K_1 and K_2 , such that they will identify one of this regions. These new elements K_1, K_2 contains two parts, respectively *physical* (gray in Figure 6.15) and *nonphysical*, and they are defined such that if an original node $s \in \Omega_i \subseteq K$, $i = 1, 2$, then $s \in \mathcal{T}_{i,h}^f$. Concretely, the original nodes are kept on the physical part of the duplicated elements, i.e. they remains on each side of the interface. As a consequence, the respective duplicated nodes appears on the *nonphysical* side of each K_i , $i = 1, 2$.

Suppose that node l is in Ω_1 whereas i, j, k are in Ω_2 (see Figure 6.15). After the duplication process we have $l \in \mathcal{T}_{1,h}^f$ and its duplicated node $l' \in \mathcal{T}_{2,h}^f$, contrarily $i, j, k \in \Omega_2$, we have $i, j, k \in \mathcal{T}_{2,h}^f$ and $i', j', k' \in \mathcal{T}_{1,h}^f$ (see Figure 6.15).

To summarize, we build two copies of the intersected fluid elements, duplicating their nodes and keeping the original nodes on the physical side of each element. At the end of this process, we have, two independent meshes $\mathcal{T}_{1,h}^f$ and $\mathcal{T}_{2,h}^f$ covering Ω_1 and Ω_2 respectively, designed in such a way that the correct connectivity of the meshes is guaranteed.

In the case of a partially intersected fluid domain, the duplication procedure remains unchanged. In the work proposed by Alauzet et al. (2016), the duplication procedure for the tip element was conduced differently from the others fluid intersected elements and in such a way that, the continuity was strongly imposed on the fluid vertex where $\tilde{\Sigma}_h$ was closed (see Section 6.2.2). We propose to duplicate the tip fluid elements using the same duplication strategy as in the other elements. As a consequence, a lack of continuity appears, which is treated in a Discontinuous Galerkin (DG) fashion.

Suppose that tetrahedron $\{i, j, k, l\}$ is a tip element and its resulting duplicated elements are $\{i, j, k, l'\}$ and $\{i', j', k', l\}$ (see Figure 6.16). We first analyse the connection with the neighbours elements. Faces whose opposite element is also duplicated are well connected with the adjacent elements due to duplication process, for instance $\{i, k, l'\}$ and $\{j', l', k'\}$. Faces whose opposite element is not duplicated are not connected with the neighbour, (faces $\{i, l', j\}$ and $\{i', l, j'\}$ in Figure 6.16 are not connected with face $\{i, l, j\}$

of the below tetrahedron). Hence the need of DG treatment on this faces (called *tip faces*) in order to guarantee continuity.

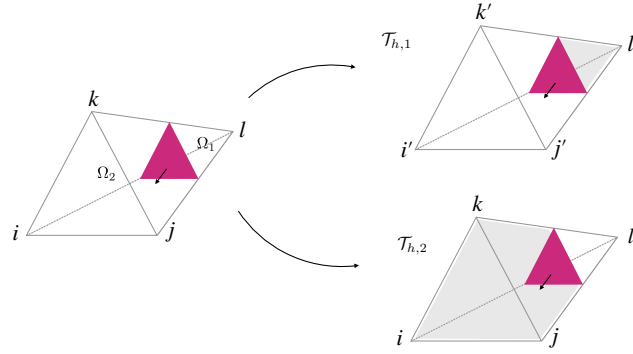


Figure 6.15: Duplication of tetrahedron $\{i, j, k, l\}$ (left) into $\{i, j, k, l'\}$ and $\{i', j', k', l\}$ (right).

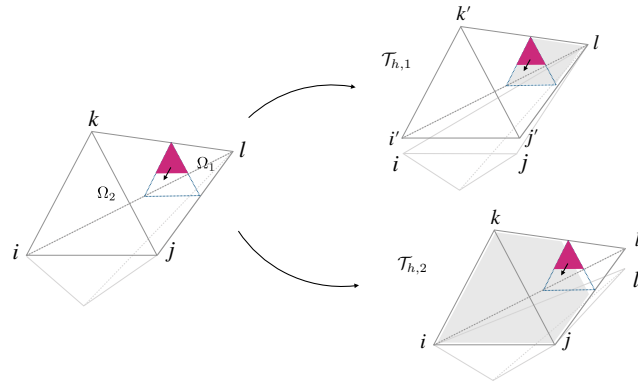


Figure 6.16: Duplication of tetrahedron $\{i, j, k, l\}$ containing a structure front (left). The resulting duplicated elements are $\{i, j, k, l'\}$ and $\{i', j', k', l\}$ (right). The below neighbour is included to show the loss of continuity on the bottom face.

6.2.6 Integration over cut elements

In the following paragraphs, we focus on the definition of the integration formulas over volume and surface sub-elements. These computation are needed for the evaluation of the fluid's bulk, Nitsche's interface and tip's faces DG terms.

The integration formulas are independent from the problem dimension, however the computations are involved in 3D. We refer to [Landajuela \(2016\)](#), for a complete derivation, while we will address only the salient aspects.

Let consider a tetrahedron K , which is fully intersected by the structure Σ and let $S = K \cap \Sigma$. The intersection algorithm described in 6.2.4 divides elements K and S into sub-elements $\{K_i\}_{i=1}^n$ and $\{S_i\}_{i=1}^m$. The reference elements are denoted with \widehat{K} and \widehat{S}

respectively for the fluid and the solid elements. To approximate these integrals, we will make use of the standard quadrature formulas over the reference elements, by combining them, with the transformations between sub-elements in the deformed configuration, sub-elements in the reference configuration and reference elements. Figure 6.17 shows the mappings that we will consider in the following.

Let first focus on integration over volume sub-elements. Let ϕ be a function defined in K . We assume that we are able to compute $\hat{\phi}(\hat{x}) = \phi(\mathbf{T}_{\hat{K} \rightarrow K}(\hat{x}))$. We define the gradient and the Jacobian of transformation $\mathbf{T}_{\hat{K} \rightarrow K}$ as follows:

$$\mathbf{F}_{\hat{K} \rightarrow K} \stackrel{\text{def}}{=} \nabla \mathbf{T}_{\hat{K} \rightarrow K}, \quad J_{\hat{K} \rightarrow K} \stackrel{\text{def}}{=} \det \mathbf{F}_{\hat{K} \rightarrow K}.$$

We denote the image of $K_i \subset K$ under the transformation $(\mathbf{T}_{\hat{K} \rightarrow K})^{-1}$ with $\tilde{K}_i \subset \hat{K}$, for $i \in \{1, \dots, n\}$. We consider also the mappings $\mathbf{T}_{\hat{K} \rightarrow \tilde{K}_i}$ from \hat{K} to \tilde{K}_i , with corresponding gradient and Jacobian $\mathbf{F}_{\hat{K} \rightarrow \tilde{K}_i}$ and $J_{\hat{K} \rightarrow \tilde{K}_i}$, for $i \in \{1, \dots, n\}$.

We may identify with $\{\hat{\xi}_l\}_{l=1}^{l_q}$ the quadrature points on \hat{K} and with $\{\hat{\omega}_l\}_{l=1}^{l_q}$ the corresponding quadrature weights. Using successively the change of variables $x = \mathbf{T}_{\hat{K} \rightarrow K}(\hat{x})$, $\tilde{x} = \mathbf{T}_{\hat{K} \rightarrow \tilde{K}_i}(\hat{\xi}_l)$, and considering an isoparametric approach with \mathbb{P}_1 finite elements, we have

$$\begin{aligned} \int_{K_i} \phi(x) dx &= \int_{\tilde{K}_i} \hat{\phi}(\tilde{x}) J_{\hat{K} \rightarrow K} d\tilde{x} \\ &= \int_{\hat{K}} \hat{\phi}(\mathbf{T}_{\hat{K} \rightarrow \tilde{K}_i}(\hat{x})) J_{\hat{K} \rightarrow K} J_{\hat{K} \rightarrow \tilde{K}_i} d\hat{x} \\ &\approx \sum_{l=1}^{l_q} \hat{\phi}(\mathbf{T}_{\hat{K} \rightarrow \tilde{K}_i}(\hat{\xi}_l)) J_{\hat{K} \rightarrow K} J_{\hat{K} \rightarrow \tilde{K}_i} \hat{\omega}_l. \end{aligned}$$

Thus, to approximate integrals over volume sub-elements we need to compute the

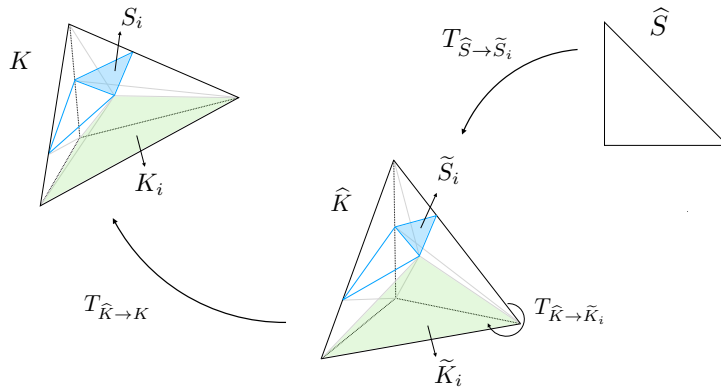


Figure 6.17: Mappings used to compute integrals over volume and surface sub-elements.

integration points $\mathbf{T}_{\hat{K} \rightarrow \tilde{K}_i}(\hat{\xi}_l) \in \tilde{K}_i$, evaluate $\hat{\phi}$ at these points and update the new

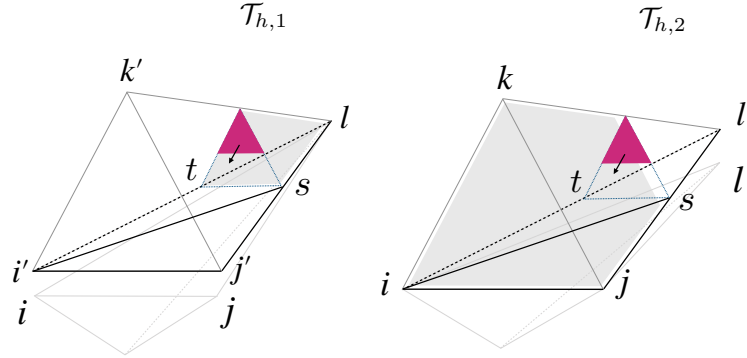


Figure 6.18: Integration over sub-faces in the case of partially intersected fluid domain.

quadrature weights $J_{\widehat{K} \rightarrow \widehat{K}_i} \widehat{\omega}_l$.

Let now consider the integration over interface sub-elements and faces sub-elements. As before, we first use the mapping from the reference volume elements \widehat{K} and, afterwards, the mapping from the reference surface element \widehat{S} . The image of S_i under the transformation $(\mathbf{T}_{\widehat{K} \rightarrow K})^{-1}$ is denoted by \widetilde{S}_i . In the same fashion as above, we consider the mapping $\mathbf{T}_{\widehat{S} \rightarrow \widetilde{S}_i}$ with the associated tensors gradient $\mathbf{F}_{\widehat{S} \rightarrow \widetilde{S}_i}$ and metric $\mathbf{a}_{\widehat{S} \rightarrow \widetilde{S}_i}$, given by

$$\mathbf{F}_{\widehat{S} \rightarrow \widetilde{S}_i} \stackrel{\text{def}}{=} \nabla \mathbf{T}_{\widehat{S} \rightarrow \widetilde{S}_i}, \quad \mathbf{a}_{\widehat{S} \rightarrow \widetilde{S}_i} \stackrel{\text{def}}{=} (\mathbf{F}_{\widehat{S} \rightarrow \widetilde{S}_i})^T \mathbf{F}_{\widehat{S} \rightarrow \widetilde{S}_i}.$$

Owing to the properties of the Piola transform and basics for differential geometry on the midsurface (see [Chapelle and Bathe \(2010\)](#); [Landajuela \(2016\)](#) and the references therein) and considering a \mathbb{P}_1 isoparametric approach, we may write:

$$\begin{aligned} \int_{S_i} \phi(x) dS &= \int_{\widetilde{S}_i} \phi(\mathbf{T}_{\widehat{K} \rightarrow K}(\tilde{\mathbf{x}})) J_{\widehat{K} \rightarrow K} \|(\mathbf{F}_{\widehat{K} \rightarrow K})^{-T} \tilde{\mathbf{n}}\| d\widetilde{S} \\ &= \int_{\widehat{S}} \widehat{\phi}(\mathbf{T}_{\widehat{S} \rightarrow \widetilde{S}_i}(\widehat{\mathbf{x}})) J_{\widehat{K} \rightarrow K} \|(\mathbf{F}_{\widehat{K} \rightarrow K})^{-T} \tilde{\mathbf{n}}\| \sqrt{\det \mathbf{a}_{\widehat{S} \rightarrow \widetilde{S}_i}} d\widehat{S} \\ &\approx \sum_{l=1}^{l_q^\partial} \widehat{\phi}(\mathbf{T}_{\widehat{S} \rightarrow \widetilde{S}_i}(\widehat{\xi}_l^\partial)) J_{\widehat{K} \rightarrow K} \|(\mathbf{F}_{\widehat{K} \rightarrow K})^{-T} \tilde{\mathbf{n}}\| \sqrt{\det \mathbf{a}_{\widehat{S} \rightarrow \widetilde{S}_i}} \widehat{\omega}_l^\partial \end{aligned}$$

where $\tilde{\mathbf{n}}$ is the normal to \widetilde{S}_i , $\widehat{\omega}_l^\partial$ and l_q^∂ are, respectively, the weights and quadrature points for the quadrature rule on \widehat{S} .

The above integration formula requires the computation of the new quadrature points $\mathbf{T}_{\widehat{S} \rightarrow \widetilde{S}_i}(\widehat{\xi}_l^\partial) \in \widetilde{S}_i$, the evaluation of $\widehat{\phi}$ at these points and the update the quadrature weights by $\|(\mathbf{F}_{\widehat{K} \rightarrow K})^{-T} \tilde{\mathbf{n}}\| \sqrt{\det \mathbf{a}_{\widehat{S} \rightarrow \widetilde{S}_i}} \widehat{\omega}_l^\partial$.

In case of partially intersected fluid domain, the above integration formulas are used

to compute the DG terms on $\tilde{\Sigma}_h$ and $\tilde{\Sigma}_{F,h}$. Terms acting on $\tilde{\Sigma}_h$ require integrals between the fluid tip elements and their duplicated elements. Contrarily, the DG terms acting on $\tilde{\Sigma}_{F,h}$ involve jumps and averages across the duplicated tip elements and their non duplicated neighbour. For consistency reason, these integrals are conducted only on the physical sub-faces of $\tilde{\Sigma}_{F,h}$ for each duplicated element. We show an example in Figure 6.18. In triangulation $\mathcal{T}_{1,h}$, we integrate only in sub-face $\{t, s, l\}$ between $\{i', j', l'k'\}$ and the opposite element, while in $\mathcal{T}_{2,h}$ we integrate on sub-faces $\{i, j, s\}$ and $\{i, s, t\}$.

6.3 The non-linear model

This section is devoted to the extension of the strongly coupled scheme given by Algorithm 6.1 to the case of non-linear fluid–structure interaction problems involving moving thin-walled structures immersed within an incompressible viscous fluid. For the geometric configurations and the numerical methods we refer to Section 2.3.

The only necessary observation concerns the partially intersected fluid domain. In fact, in such a case, the discrete tri-linear form associated to the fluid convective term becomes:

$$\begin{aligned} c^n(\mathbf{z}_h, \mathbf{u}_h, \mathbf{v}_h) &\stackrel{\text{def}}{=} \rho^f(\mathbf{z}_h \cdot \nabla \mathbf{u}_h, \mathbf{v}_h)_{\Omega^{f,n}} + \frac{\rho^f}{2}((\text{div} \mathbf{z}_h) \mathbf{u}_h, \mathbf{v}_h)_{\Omega^{f,n}} \\ &- \rho^f(\{\{\mathbf{z}_h\}\} \cdot \mathbf{n}[\mathbf{u}_h], \{\{\mathbf{v}_h\}\})_{\Sigma^n \cup \tilde{\Sigma}_h^n \cup \tilde{\Sigma}_{F,h}^n} - \frac{\rho^f}{2}([\mathbf{z}_h \cdot \mathbf{n}], \{\{\mathbf{u}_h \cdot \mathbf{v}_h\}\})_{\Sigma^n \cup \tilde{\Sigma}_h^n \cup \tilde{\Sigma}_{F,h}^n}. \end{aligned} \quad (6.8)$$

Hence, the Discontinuous Galerkin contributions of (6.8) have to be evaluated on the whole dynamic boundaries $\Sigma^n \cup \tilde{\Sigma}_h^n \cup \tilde{\Sigma}_{F,h}^n$, which are defined as in Section 6.2.2, but on the dynamic interface.

We now have all the ingredients to extend the numerical methods of Section 6.2 to the approximation of the non-linear coupled problem. By combining the explicit treatment of the geometric compatibility with the implicit coupling paradigm of Section 6.2.3 we get the solution procedure given in Algorithm 6.2.

Remark 6.3.1. *Due to the dynamic nature of problem, Algorithm 6.2 involves integrals of functions associated to different time levels, such as $(\mathbf{u}_h^{n-1}, \tilde{\mathbf{v}}_h)_{\Omega^{f,n}}$. At each iteration a new location of the structure is computed, together with a new subtetrahedralization. Hence, these integrals involve products of functions that might be discontinuous at different locations in the same element. We typically resolve this situation by locally shifting the discontinuity at time t^{n-1} at the structure location at time t^n (see also Alauzet et al. (2016); Fries and Zilian (2009) and Section 2.3).*

Algorithm 6.2 Non-linear strongly coupled scheme.For $n \geq 1$:

1. Interface update: $\phi_h^{n-1} = \mathbf{I}_\Sigma + \mathbf{d}_h^{n-1}$, $\Sigma_h^n = \phi_h^{n-1}(\Sigma)$, $\Omega^{f,n} = \Omega^f \setminus (\Sigma_h^n \cup \tilde{\Sigma}_h^n \cup \tilde{\Sigma}_{F,h}^n)$
2. Find $(\mathbf{u}_h^n, p_h^n, \dot{\mathbf{d}}_h^n, \mathbf{d}_h^n) \in \mathbf{V}_h^n \times Q_h^n \times \mathbf{W}_h \times \mathbf{W}_h$, such that $\dot{\mathbf{d}}_h^n = \partial_\tau \mathbf{d}_h^n$ and

$$\begin{aligned} & \rho^f (\partial_\tau \mathbf{u}_h^n, \mathbf{v}_h)_{\Omega^{f,n}} + a_h^f(\mathbf{u}_h^n; (\mathbf{u}_h^n, p_h^n), (\mathbf{v}_h, q_h)) + \rho^s \varepsilon (\partial_\tau \dot{\mathbf{d}}_h^n, \mathbf{w}_h)_\Sigma + a^s(\mathbf{d}_h^n, \mathbf{w}_h) \\ & - \sum_{i=1}^2 (\boldsymbol{\sigma}(\mathbf{u}_{h,i}^n, p_{h,i}^n) \mathbf{n}_i, \mathbf{v}_{h,i} - \mathbf{w}_h)_{\Sigma^n} - \sum_{i=1}^2 (\mathbf{u}_{h,i}^n - \dot{\mathbf{d}}_h^n, \boldsymbol{\sigma}(\mathbf{v}_{h,i}, -q_{h,i}) \mathbf{n}_i)_{\Sigma^n} \\ & + \frac{\gamma\mu}{h} \sum_{i=1}^2 (\mathbf{u}_{h,i}^n - \dot{\mathbf{d}}_h^n, \mathbf{v}_{h,i} - \mathbf{w}_h)_{\Sigma^n} - (\{\{\boldsymbol{\sigma}(\mathbf{u}_h^n, p_h^n)\}\} \mathbf{n}, \llbracket \mathbf{v}_h \rrbracket)_{\tilde{\Sigma}_h^n \cup \tilde{\Sigma}_{F,h}^n} \\ & - (\{\{\boldsymbol{\sigma}(\mathbf{v}_h, -q_h)\}\} \mathbf{n}, \llbracket \mathbf{u}_h^n \rrbracket)_{\tilde{\Sigma}_h^n \cup \tilde{\Sigma}_{F,h}^n} + \frac{\gamma\mu}{h} (\llbracket \mathbf{u}_h^n \rrbracket, \llbracket \mathbf{v}_h \rrbracket)_{\tilde{\Sigma}_h^n \cup \tilde{\Sigma}_{F,h}^n} = 0 \end{aligned}$$

for all $(\mathbf{v}_h, q_h, \mathbf{w}_h) \in \mathbf{V}_h^n \times Q_h^n \times \mathbf{W}_h$

6.4 Numerical experiments

In this section we present a numerical study which illustrates the performance of the proposed 3D Nitsche-XFEM solution algorithm. The method has been implemented in the FELiScE C++ finite element library (see team.inria.fr/commedia/software/felisce). Three different examples involving dynamic interfaces and both partially and fully intersected fluid domains are presented. Each of them is generated from a two dimensions example, which is then extruded along the third dimension. For validation purposes, we compare the original 2D solution to the 3D solution by exploiting the symmetry of the problem. Indeed, each 2D test is reproduced in 3D by enforcing a symmetry condition along \mathbf{e}_3 , namely the 3D solution is invariant on each plane with normal $\mathbf{n} = \mathbf{e}_3$. Along this section the user-defined parameters in Algorithm 6.2 are fixed to $\gamma_g = 1$, $\gamma_p = 10^{-2}$, $\gamma_v = 10^{-2}$, $\gamma = 100$. We remind that all the units are given in the CGS system. The beam and shell solid models are discretized in space by linear MITC2 elements and triangular MITC3 elements with 3 and 5 degrees of freedom per node in the increments, respectively.

6.4.1 Idealized closed valve

The first example reproduces the behavior of a closed valve under a pressure drop. This test case is a classical benchmark problem (see, e.g., [Kamensky et al. \(2015\)](#); [Van Loon et al. \(2004\)](#)) extensively tested with the two-dimensional version of Algorithm 6.2 in [Boilevin-Kayl et al. \(2019b\)](#); [Alauzet et al. \(2016\)](#).

The problem consists of an elastic shell clamped on its endpoints and immersed in a channel filled with an incompressible Newtonian fluid, as shown in Figure 6.19. The two dimensions fluid domain is given by the rectangle $\Omega = [0, 3] \times [0, 1]$, while for three dimensions we have $\Omega = [0, 3] \times [0, 1] \times [0, 0.2]$. The 2D reference solid configuration is the

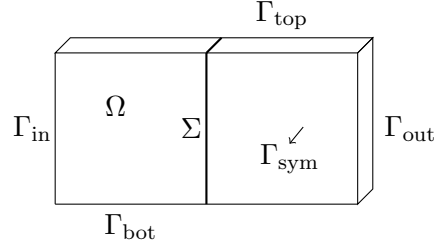


Figure 6.19: Geometric configuration and external boundary conditions.

segment with endpoints $(1.5, 0)$ and $(1.5, 1)$, while in 3D $\Sigma = \{1.5\} \times [0, 1] \times [0, 0.2]$.

As regards the boundary conditions for the fluid, a no-slip boundary condition is enforced on Γ_{top} and Γ_{bot} . A zero traction is enforced on the outer boundary Γ_{out} , while on Γ_{in} a traction is imposed in terms of the following negative time-dependent pressure function $p_{\text{in}}(t)$, given by:

$$p_{\text{in}}(t) = -10^5 \cdot \tanh(10t), \quad \forall t \in \mathbb{R}^+.$$

In addition, a symmetry condition, namely, $\mathbf{u} \cdot \mathbf{n} = 0$ and $\boldsymbol{\sigma}(\mathbf{u}, p)\mathbf{n} = \mathbf{0}$, is considered

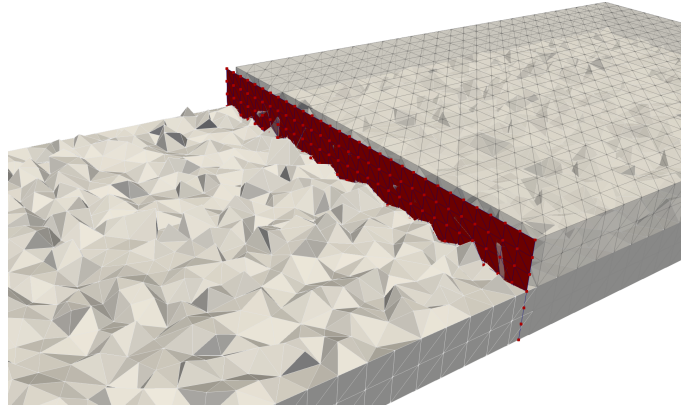


Figure 6.20: Fluid and solid meshes.

on Γ_{sym} in the three-dimensional case. Regarding the structure, it is fully clamped at its endpoints in two dimensions and on $\Gamma_{\text{top}} \cup \Gamma_{\text{bot}}$ in three dimensions. Additionally, a symmetry condition is considered on Γ_{sym} , namely $\mathbf{d} \cdot \mathbf{n}$ and $\mathbf{a} \cdot \mathbf{n}$, where \mathbf{a} denotes the director vector, are set to zero. Both fluid and solid are initially at rest.

The physical parameters for the fluid are $\rho^f = 1.0$ and $\mu = 0.035$. For the solid, we have $\rho^s = 1.1$, the Young's modulus $E = 7.5 \cdot 10^5$, $\varepsilon^s = 0.1$ and Poisson's ratio $\nu = 0.5$. The time-step is $\tau = 10^{-3}$ and the final time is $T = 1$.

The 3D fluid and solid meshes are shown in Figure 6.20. Both 2D and 3D meshes have a local size of $h \approx 0.05$. The fluid 2D mesh is composed of 2166 triangles, while the 3D mesh is made of 47181 tetrahedra. For the solid we consider a structure of 30

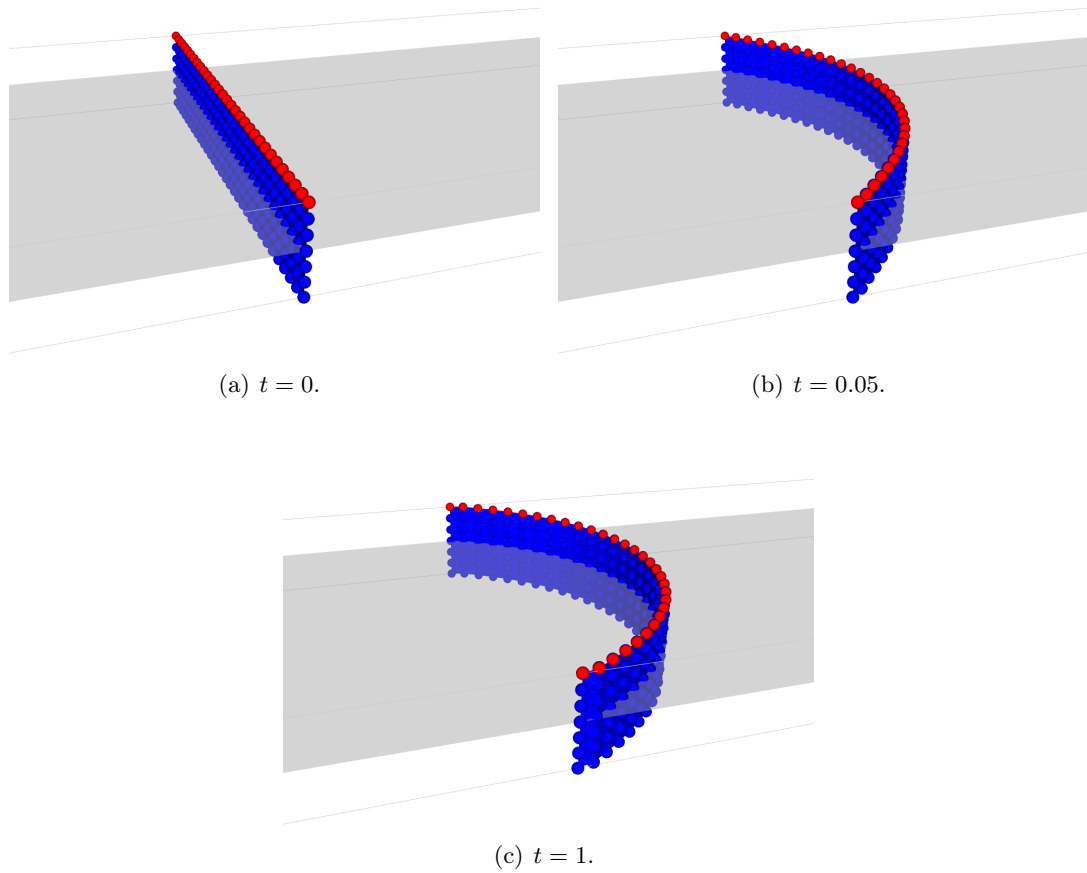


Figure 6.21: Deformed configurations in 2D (red dots) and 3D (blue) at different time instants.

segments in 2D and 360 triangles in 3D. As the prescribed pressure increases, the solid

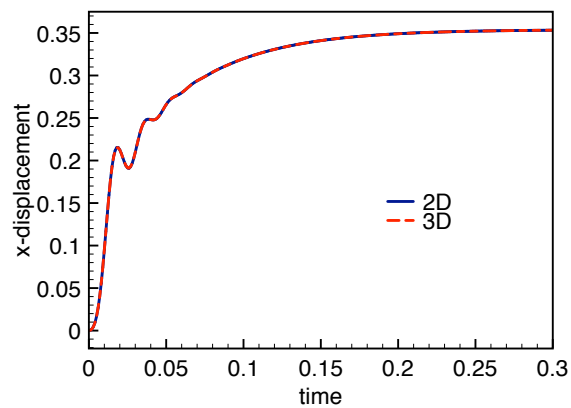
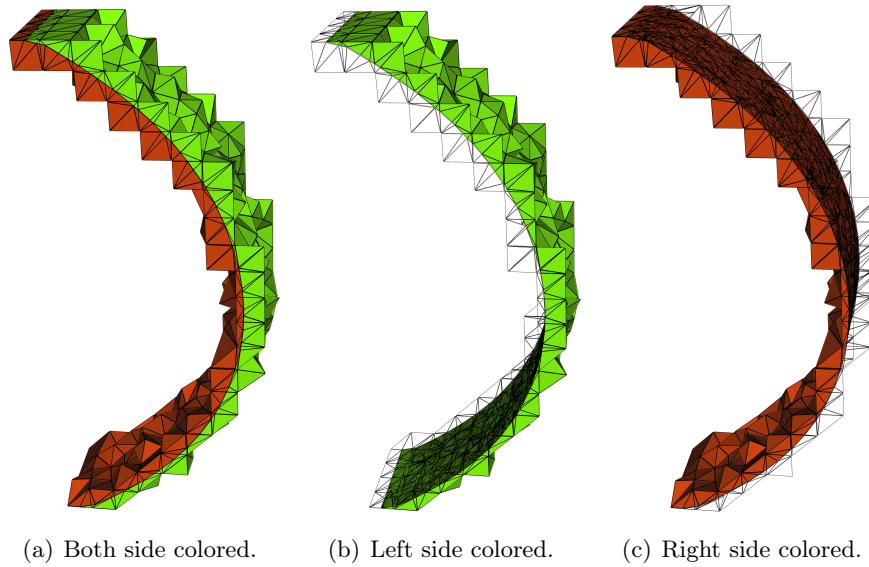
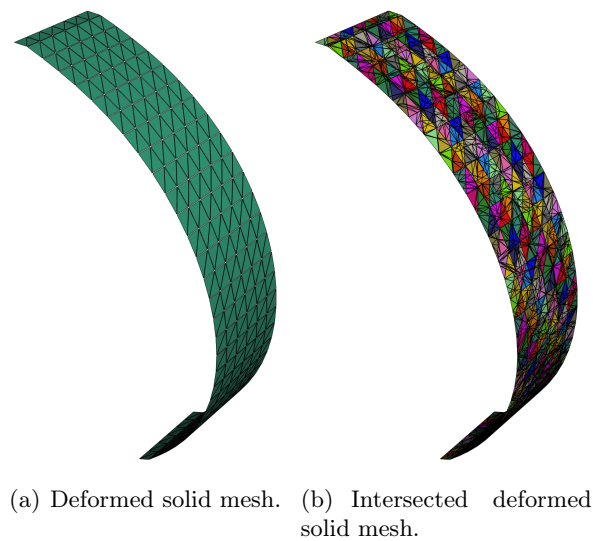


Figure 6.22: Solid x -displacement of the closed valve mid-point for the 2D-case and for the midpoint on the plane $z = 0$ for the 3D.

Figure 6.23: Fluid intersected mesh at $t = 1$.Figure 6.24: Deformed and intersected solid meshes at $t = 1$.

starts to bend. After a brief transition phase, the system reaches a steady state with a pressure jump across the interface. The fluid and solid velocities vanish and the pressure is a piecewise constant.

Some snapshots of the resulting deformed mesh at time $t = 0$, $t = 0.05$ and $t = 1$ are shown in Figure 6.21. We can observe that the 2D deformed configuration (red dots) and the 3D (blue) perfectly match. Already at $t = 0.3$, the structure has reached the stationary states.

Figure 6.22 reports a comparison of the time history of the solid x -displacement of the

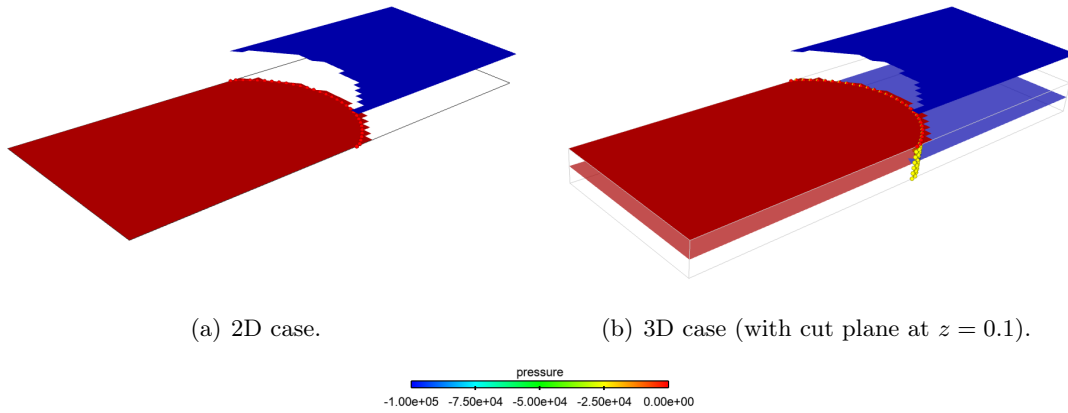


Figure 6.25: Snapshots of the pressure elevation at time $t = 1$.

closed-valve mid-point. Both results are practically indistinguishable.

For illustration purposes, Figure 6.23 and Figure 6.24 show the 3D intersected fluid and solid meshes respectively at the reached steady state. The fluid intersected mesh includes only the fluid elements that are cut by the structure. The two sides of the mesh are highlighted with different colors. It contains 16896 tetrahedra. As regards the solid, Figure 6.24(a) shows the deformed solid mesh, while Figure 6.24(b) shows the intersected mesh with its sub-elements (6805 triangles in this case).

For illustration purposes, pressure snapshots and elevations for two and three dimensions are reported in Figure 6.25. Both 2D and 3D Nitsche-XFEM methods get the correct pressure jump, $P_0 = -10^5$ on one side and zero on the other.

6.4.2 Vesicle in lid-driven cavity flow

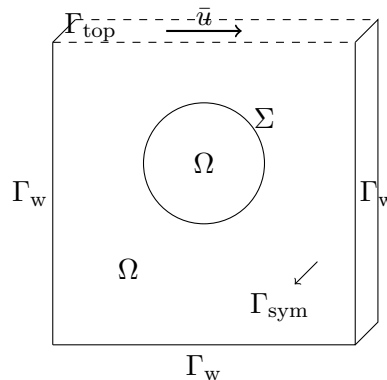


Figure 6.26: Geometric configuration and external boundary conditions in the 3D case.

As second example, we consider the lid-driven cavity test with an immersed elastic structure (see, e.g., [Roy et al. \(2013\)](#); [Wang and Zhang \(2010\)](#); [E Griffith \(2012\)](#); [Griffith](#)

and Luo (2017)).

In two dimensions the fluid domain Ω is given by the unit square $[0, 1] \times [0, 1]$. The reference solid configuration is a circle of center $(0.6, 0.5)$ and radius 0.2. In the three-dimensional case we have, $\Omega = [0, 1] \times [0, 1] \times [0, 0.2]$ and the reference solid configuration is an open right circular cylinder, with height 0.2 and each base is centered in $x_c = 0.6$, $y_c = 0.5$, as shown in Figure 6.26.

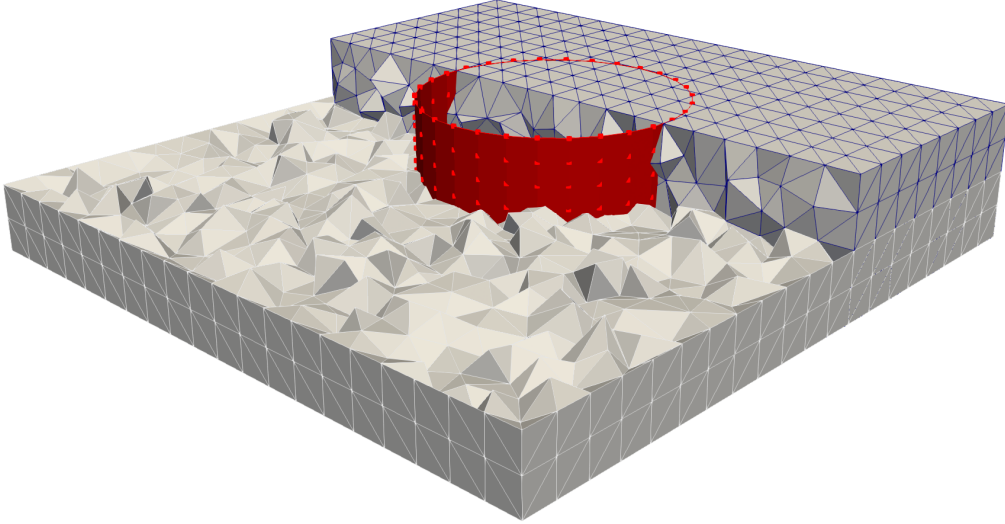


Figure 6.27: Fluid and solid meshes in 3D.

As regards the fluid boundary conditions, a no-slip boundary condition is enforced on Γ_w . A constant velocity $\bar{\mathbf{u}} = \mathbf{e}_1$ is prescribed on Γ_{top} . A symmetry condition is considered for both fluid and solid on Γ_{sym} , namely $\mathbf{u} \cdot \mathbf{n} = 0$, $\boldsymbol{\sigma}(\mathbf{u}, p)\mathbf{n} = \mathbf{0}$, $\mathbf{d} \cdot \mathbf{n} = 0$ and $\mathbf{a} \cdot \mathbf{n} = 0$. Finally, both fluid and solid are initially at rest.

The physical parameters used for the fluid in this test are $\rho^f = 100$, $\mu = 10$. For the solid we have $\rho^s = 100$, $\varepsilon = 0.0212$, the Young's modulus $E = 5.6 \cdot 10^3$ and Poisson's ratio $\nu = 0.4$. The time-step is $\tau = 5 \times 10^{-3}$ and the final time is $T = 10$.

As previously discussed in Section 2.4.3, since the fluid is entirely enclosed by Dirichlet-type boundary conditions, standard Dirichlet–Neumann partitioned solution procedures are not suitable for the resolution of this type of problems. Therefore an additional volumetric constraint on the solid velocity is enforced in Algorithm 6.2. We refer to Section 2.4.3 for extra details.

The 2D solution has been generated using a fluid mesh made of 800 triangles and a solid mesh of 29 segments. The three-dimensional fluid mesh is composed by 15830 tetrahedra, while the solid by 800 triangles. Figure 6.27 shows respectively the considered fluid and solid meshes. In both cases the space discretization parameter is $h \approx 0.05$.

As mentioned above, at each time step we need to evaluate the intersection between the two meshes and the subtetrahedralization of the fluid intersected elements. We show in Figure 6.28 the three-dimensional intersected fluid mesh at $t = 2.5$, where the two regions of the fluid domain are highlighted with different colors. The intersected mesh is

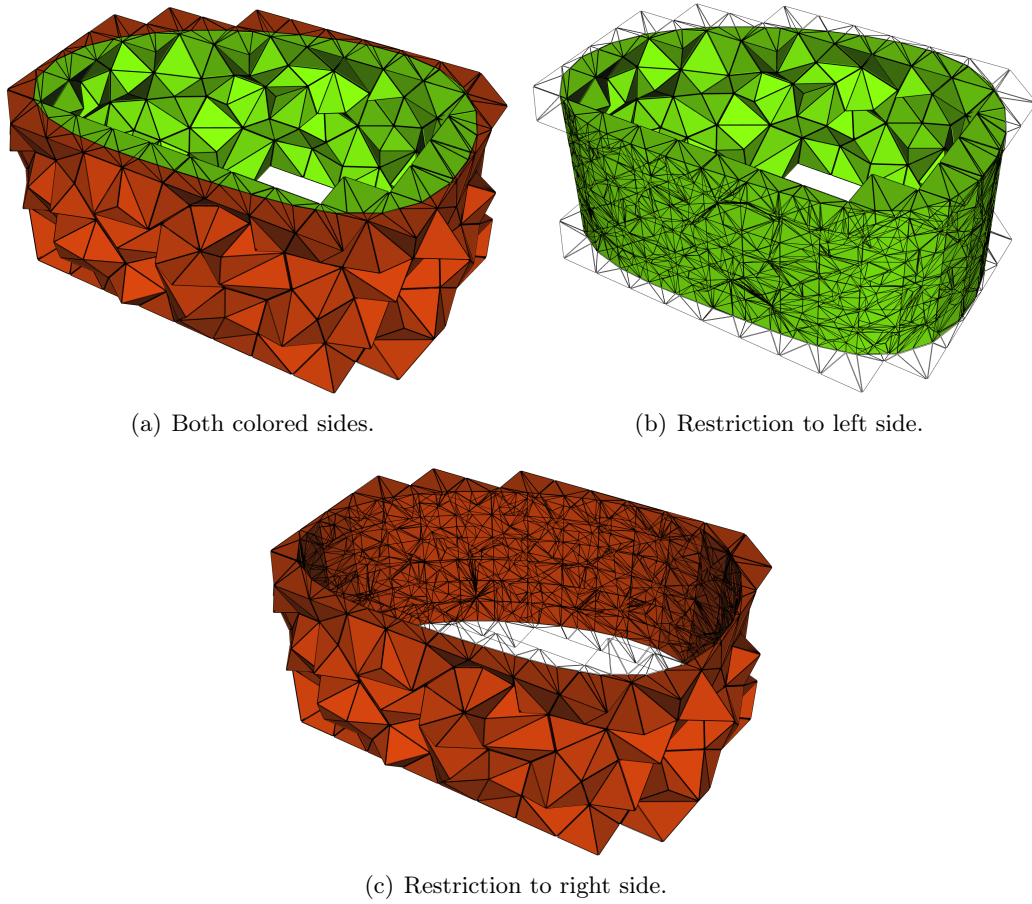


Figure 6.28: Fluid intersected mesh at $t = 2.5$.

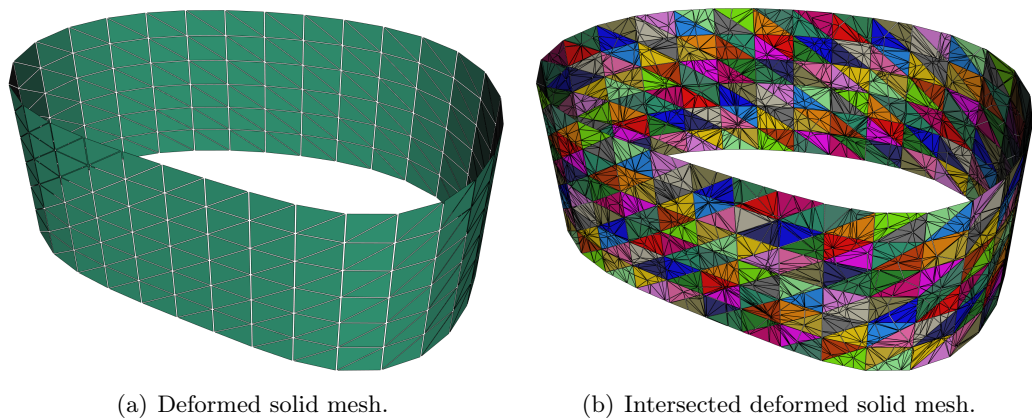


Figure 6.29: Deformed and intersected solid meshes at $t = 2.5$.

made of 17886 tetrahedra. Notice that we are starting from an initial fluid mesh of 15830 tetrahedra, i.e., we are generating an intersected mesh with more tetrahedra than the

original one. It should be noted that this induces additional computational cost (only) to the assembling phase, the price to pay when integrating over arbitrary polygons. Similarly for the structure intersected mesh. Figure 6.29(a) shows the deformed solid mesh at $t = 2.5$ and Figure 6.29(b) the corresponding intersected solid mesh, composed by 7222 triangles while the original were 360. Each color in Figure 6.29(b) characterizes an original solid triangle.

For illustration purposes, Figure 6.30 shows the snapshots of the fluid velocity magnitude for 2D and 3D tests. At $t = 2.5$, Figures 6.30(a) and (d), the vesicle is heading towards the moving upper region of the cavity, getting closer at $t = 5$, Figures 6.30(b) and (e). At $t = 7.5$, Figures 6.30(c) and (f), the vesicle has completed the first rotation around the initial position. Both results show present the same dynamics.

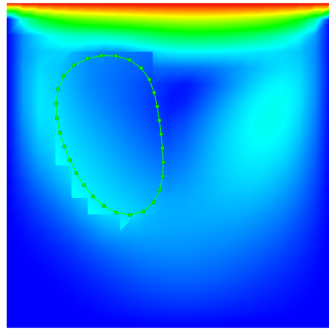
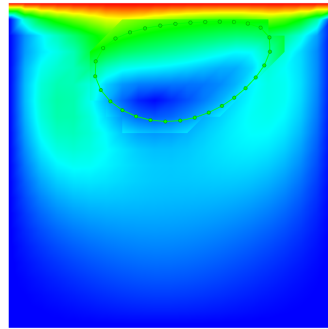
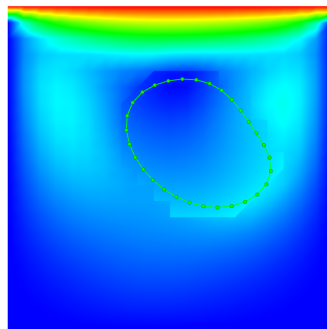
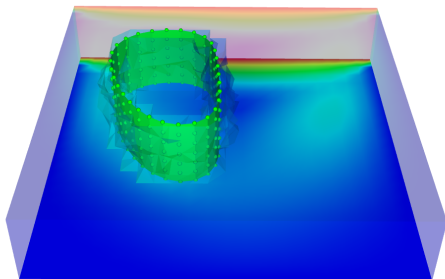
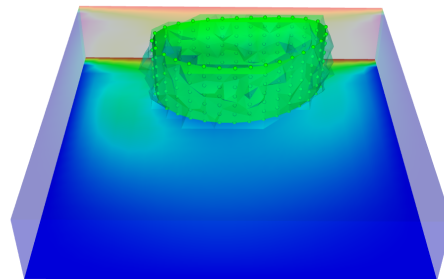
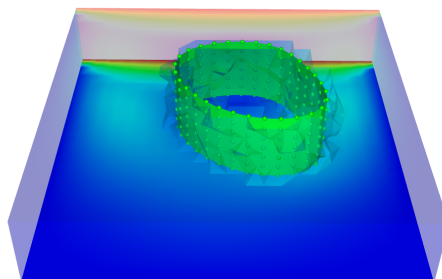
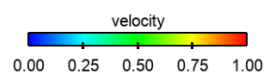
(a) $t = 2.5$.(b) $t = 5$.(c) $t = 7.5$.(d) $t = 2.5$.(e) $t = 5$.(f) $t = 7.5$.

Figure 6.30: Velocity magnitude snapshots in 2D ((a)-(c)) and 3D ((d)-(f)).

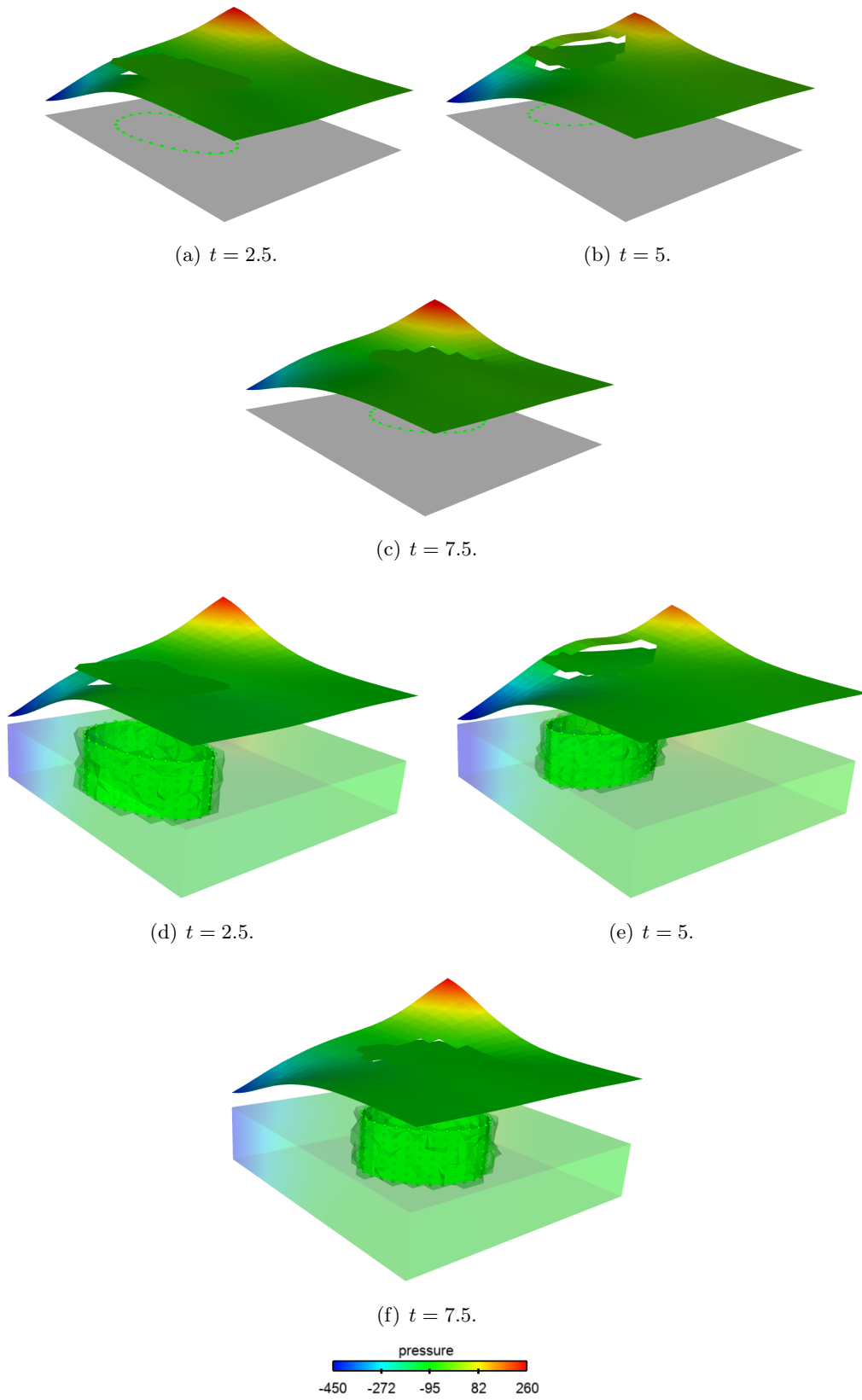


Figure 6.31: Pressure snapshots and elevation in 2D ((a)-(c)) and 3D ((d)-(f)).

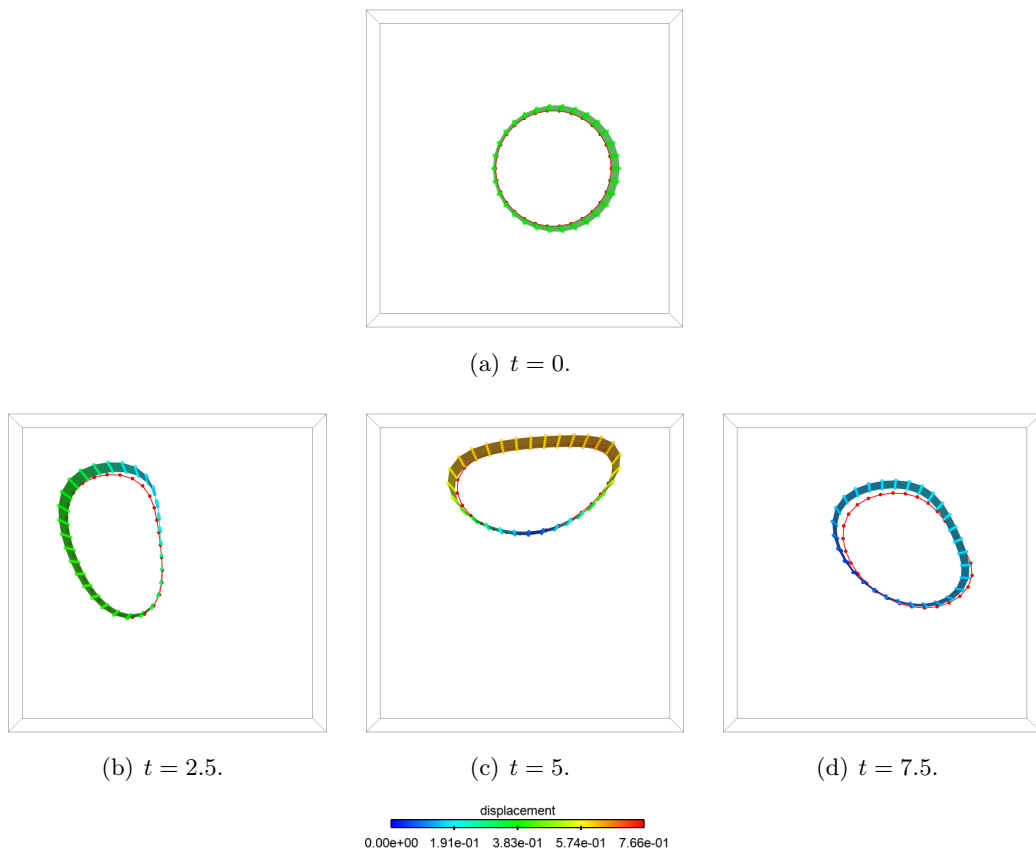


Figure 6.32: Overlapping of the actual solid location for two dimensions and three dimensions case at different time.

Similar observations can be made from Figure 6.31 which shows the pressure elevation of the whole fluid domain in 2D and of a cutting plane parallel to Γ_{sym} for the 3D test. As for the velocity, different time instants are considered. Both cases reproduce well the pressure jump across the moving interface $\Sigma(t)$.

In order to validate the implementation of the Nitsche-XFEM algorithm, an additional comparison is carried out. We show in Figure 6.32 the solid configuration at different time instants, namely $t = 0, 2.5, 5, 7.5$. Some differences can be observed between the 2D and 3D configurations at time $t = 7.5$. This can be due to the asymmetry of the fluid mesh. We can expect the solutions to get closer with space refinement.

In Figure 6.33 we present the trajectory of the vesicle rightmost vertex for the 2D case and the rightmost node on the plane $z = 0$ for the 3D case. The results with a coarser mesh are included in the figure, $h_c \approx 2h$ and $\tau_c = 2\tau$ (dashed line in Figure 6.33). Time markers have been depicted in order to facilitate the comparison of the results. The 3D test is able to capture the dynamics of the 2D case and as expected the 2D and 3D results draw closer with the finer mesh.

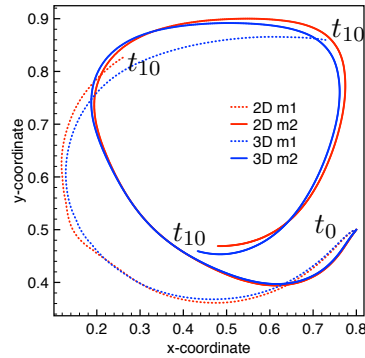


Figure 6.33: Comparison of trajectory of the extreme right node of the vesicle from $t = 0$ to $t = 10$ between 2D and 3D.

6.4.3 Idealized open valve

The last example simulates the behavior of an open valve, no contact is considered. Notice that in this case the structure has a boundary inside the fluid domain. Hence, the

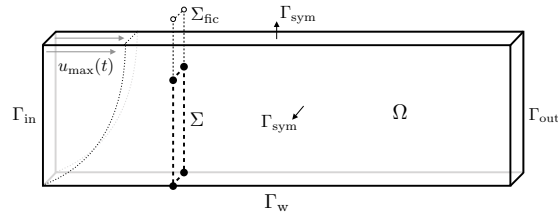


Figure 6.34: Geometric configuration of the 3D case.

front treatment proposed in Section 6.2.2 is considered. The 2D fluid domain is a rectangle

$\Omega = [0, 4] \times [0, 0.805]$, while the immersed solid reference configuration Σ is the straight segment AB , with $A = (2, 0)$ and $B = (2, 0.7)$. In three dimensions the fluid domain is $\Omega = [0, 4] \times [0, 0.805] \times [0, 0.2]$. For the structure we have $\Sigma = 2 \times [0, 0.7] \times [0, 0.2]$, and a fictitious interface $\Sigma_{\text{fic}} = 2 \times [0.7, 0.9] \times [0, 0.2]$. The considered geometry is shown in Figure 6.34.

The physical parameters used for the fluid in this test are $\rho^f = 100$, $\mu = 10$. While for the solid we have $\rho^s = 100$, $\varepsilon = 0.0212$, the Young's modulus $E = 5.6 \cdot 10^7$ and Poisson's ratio $\nu = 0.4$. Concerning the external boundary conditions for both 2D and 3D, no-slip

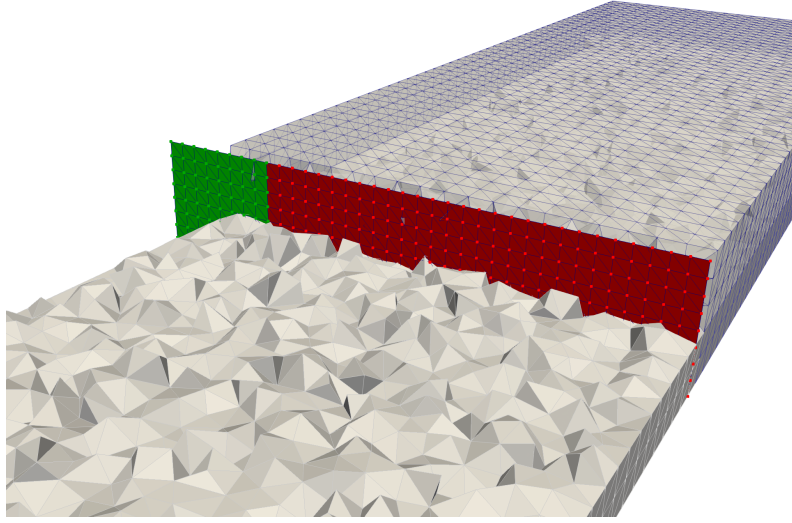


Figure 6.35: Fluid and solid meshes in 3D.

boundary condition is apply on Γ_w , a symmetry condition is imposed on Γ_{sym} ($\mathbf{u} \cdot \mathbf{n} = 0$ and $\boldsymbol{\sigma}(\mathbf{u}, p)\mathbf{n} = \mathbf{0}$), zero traction on Γ_{out} and finally, the following half parabolic profile is applied on Γ_{in} :

$$u_{\text{max}}(t) = 5(0.805)^2(\sin(2\pi t) + 1.1), \quad t \in \mathbb{R}^+.$$

In addition the solid is clamped at its bottom, namely rotation and displacement are set to zero. A further symmetry condition is considered for the 3D-structure on Γ_{sym} . Both fluid and solid are considered initially at rest.

The considered space discretization parameter is approximately $h \approx 0.04$. The two-dimensional solid mesh is made of 28 edges while the fluid unfitted mesh is made of 4000 triangles. For the 3D case, we consider an unstructured fluid mesh made of 102380 tetrahedra while the structure mesh is made of 576 triangles. Figure 6.35 shows the corresponding meshes. The physical structure is colored in red and the fictitious interface in green. The time-step is $\tau = 2 \times 10^{-3}$ and the final time is $T = 1$, which corresponds to one full oscillation cycle for the structure.

For illustration purposes, snapshots of the fluid velocity magnitude and the position of the interface, computed in two and three dimensions cases, are shown in Figure 6.36 at time $t = 0.3$, 0.75 and 1 respectively. For the 2D case we show a zoom of the fluid

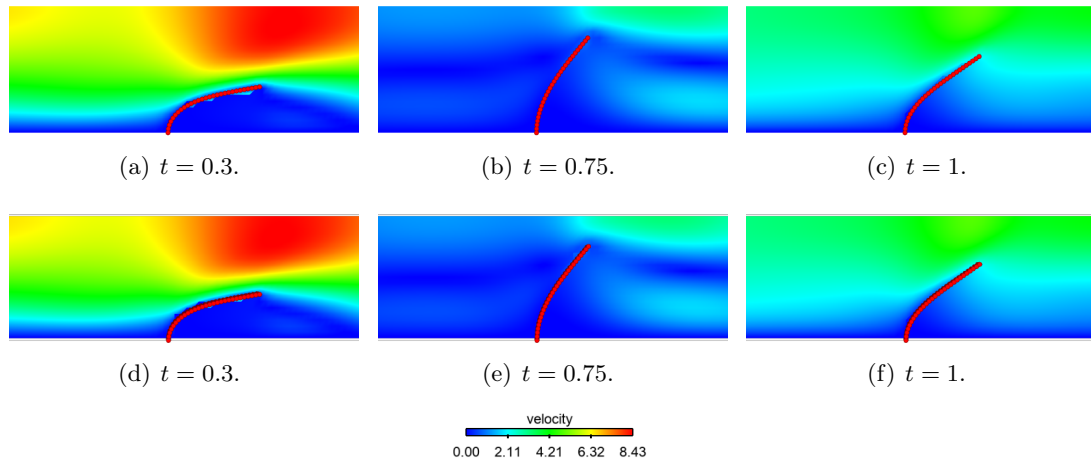


Figure 6.36: Snapshots of the fluid velocity magnitude at $t = 0.3$ (left column), $t = 0.75$ (center column) and $t = 1$. (right column) for both 2D (top row) and 3D (bottom row).

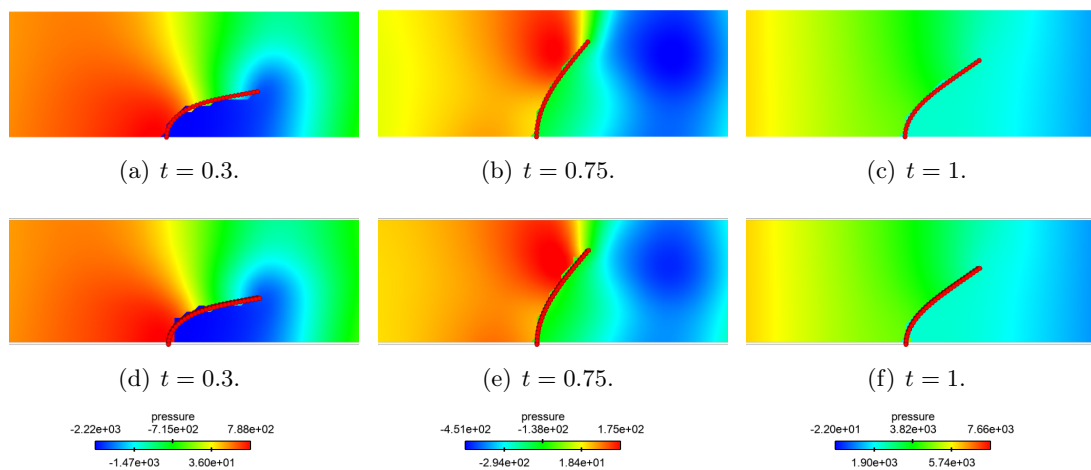
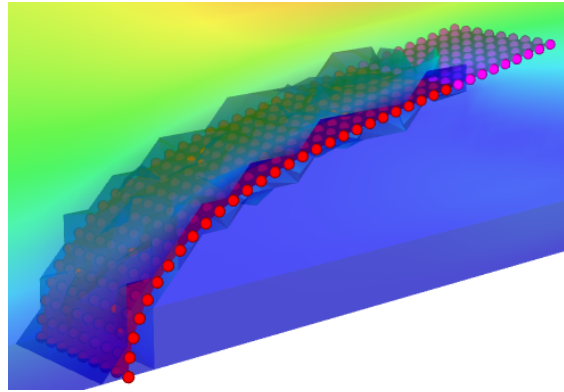
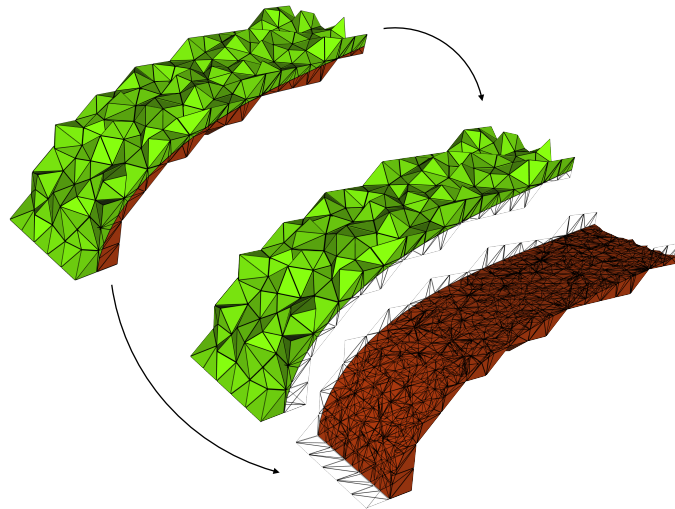


Figure 6.37: Snapshots of the fluid pressure at $t = 0.3$ (left column), $t = 0.75$ (center column) and $t = 1$. (right column) for both 2D (top row) and 3D (bottom row).

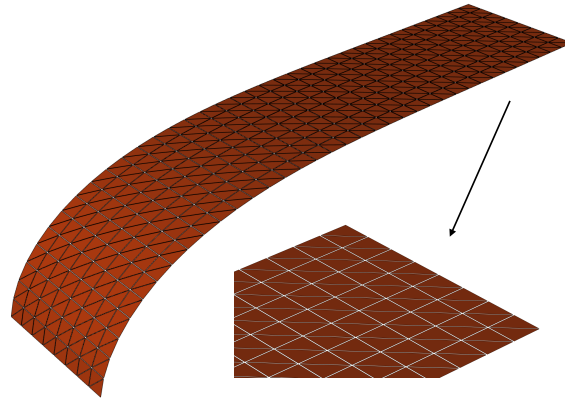
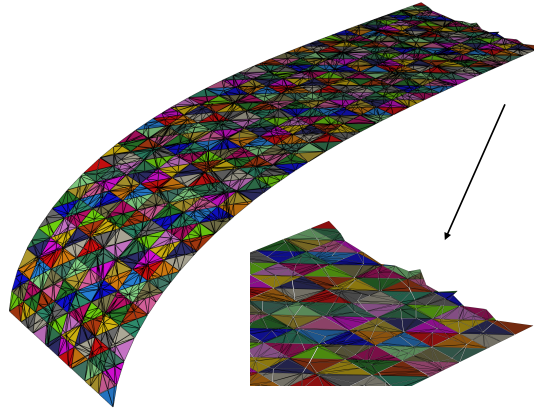


(a) Deformed solid mesh (Σ and Σ_{fic}).



(b) Intersected fluid mesh.

Figure 6.38: Deformed solid interface (physical and fictitious) immersed in the fluid channel (a) and the fluid intersected mesh with its restriction on each side of the interface (b) at $t = 0.3$.

(a) Deformed solid mesh $\Sigma(t)$.

(b) Intersected structure mesh

Figure 6.39: Deformed and intersected solid meshes at $t = 0.3$, both with a zoom on the immersed front solid boundary. Note that (a) contains only the physical interface $\Sigma(t)$ (the front is flat), while the front of (b) includes some sub-elements of Σ_{fic} .

domain near the deformed structure location, while for the three dimension case we plot the solution on a clipped plane, namely $z = 0.1$. A very good agreement is obtained for the two cases. Similarly, Figure 6.37 presents the snapshots of the pressure at three different time instants. No particular difference between the two cases is visible.

Additionally, we show in Figure 6.38(a) the three dimensions deformed structure interface with the fictitious part at $t = 0.3$. Across the physical structure, we can see the faces of the intersected fluid mesh. Notice that no tetrahedra around the fictitious interface are visible, they are not included into the fluid intersected mesh. In figure 6.38(b) we exhibit the fluid intersected mesh, highlighting the two side of the interface. The fluid intersected mesh is composed by 17879 tetrahedra.

Figure 6.39 reports the deformed structure mesh (a) and the corresponding intersected mesh, which contains 7415 triangles. A zoom of the immersed front boundary is displays for each mesh. The intersected structure mesh contains all the triangles of the original mesh (divided into sub-triangles) and the extra sub-triangles belonging initially to Σ_{fic}

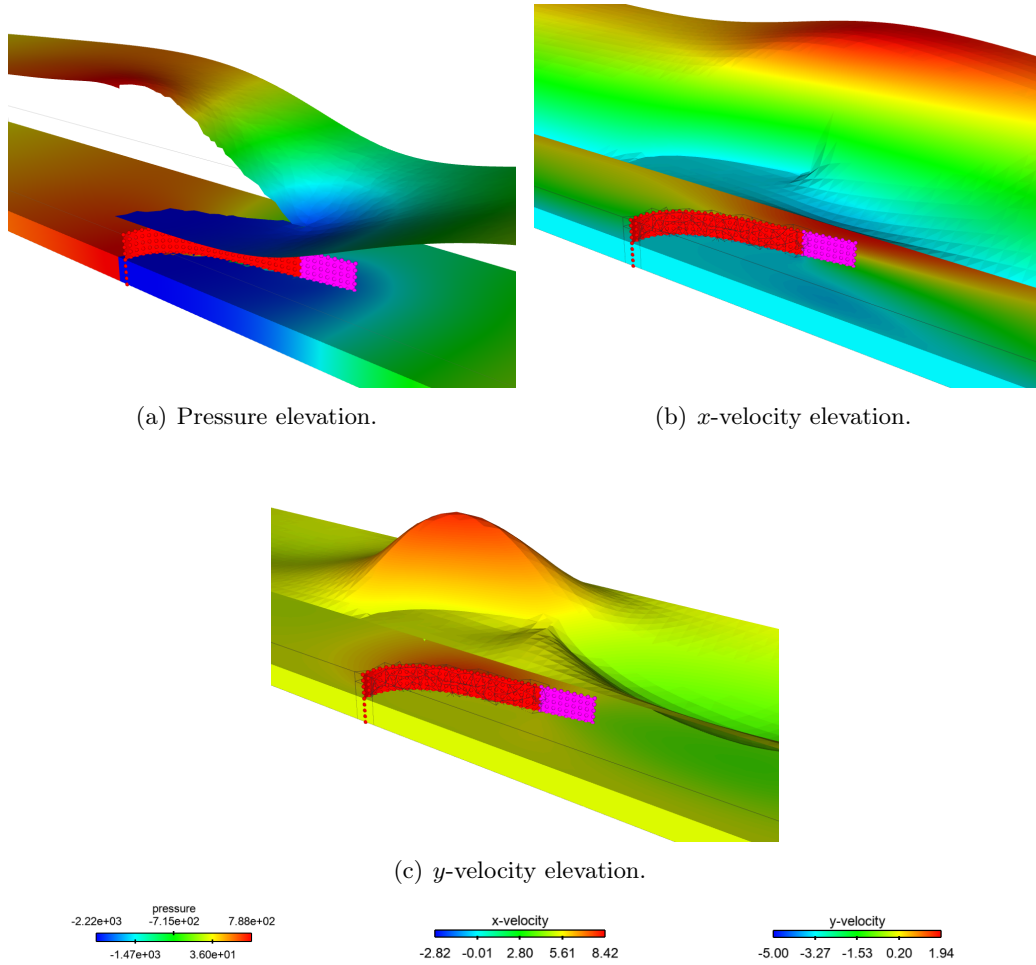


Figure 6.40: Snapshots of the fluid elevated pressure, x -velocity and y -velocity of a clipped plane $z = 0.1$, obtained in the 3D case, at $t = 0.3$.

which are necessary to close the structure front inside the fluid tip elements.

Figure 6.40(a) presents the pressure elevation for the cutting plane $z = 0.1$. The fictitious part of the structure is included with the purpose of highlighting that the pressure discontinuity is well captured across the physical interface, while it is continuous across the fictitious interface, i.e., the fictitious interface is totally imperceptible from both the fluid side as well as the solid side. Additionally, Figures 6.40(b) and (c) show respectively the elevation of the x - and y -component of the velocity. Each velocity component is continuous across Σ and also Σ_{fic} , but clearly no constraint on the velocity on Σ_{fic} are visible from the fluid side. The velocity z -component vanishes due to the symmetry of this problem.

For illustration purposes, we display in Figure 6.41 the solid configurations in both two and three dimensions with the displacement magnitude at different instants, namely $t = 0.3, 0.75$ and 1 . Once more, no notable differences are visible between the 2D and 3D solutions. Figure 6.42 reports the displacement history of the upper 2D-structure endpoint and the upper 3D-structure on the plane $z = 0$ as function of time, in terms of

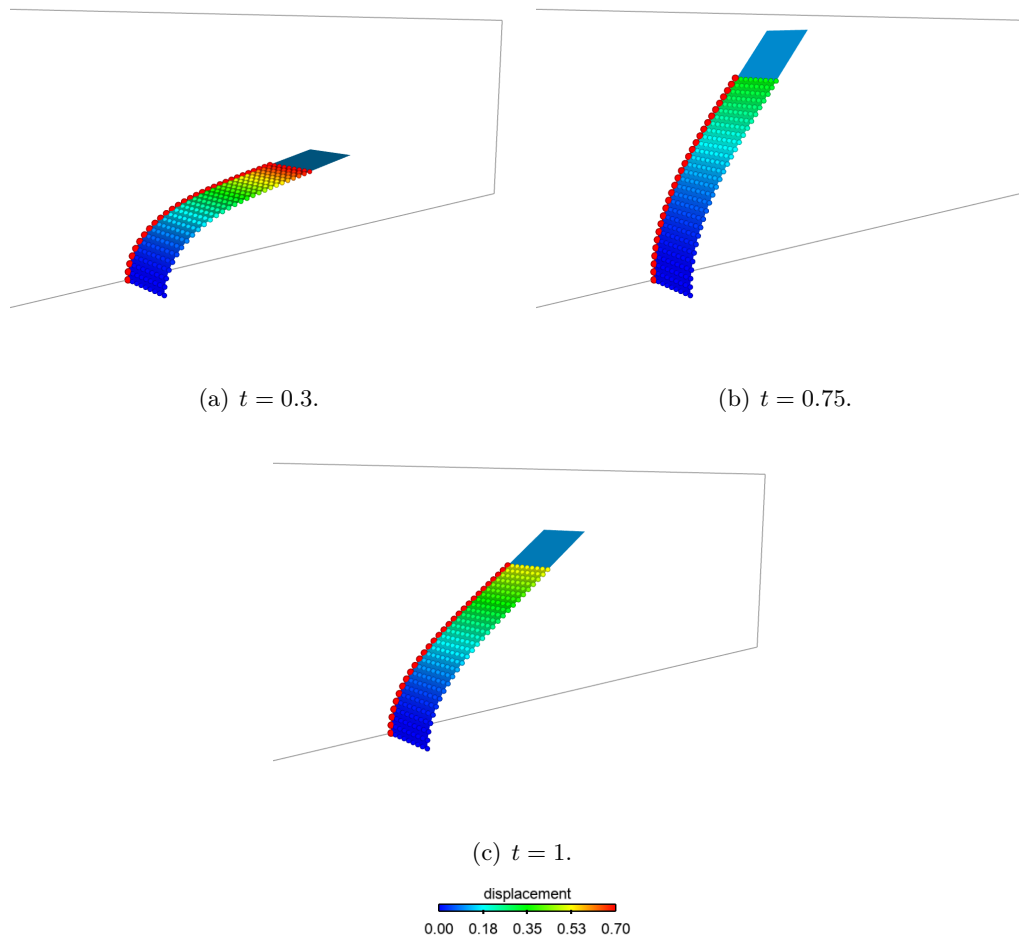


Figure 6.41: Representation of the actual structure location at three different instants. The 2D solution (in red) is superimposed to the 3D (colored by the solid displacement magnitude). The fictitious interface is displayed (colored in blue).

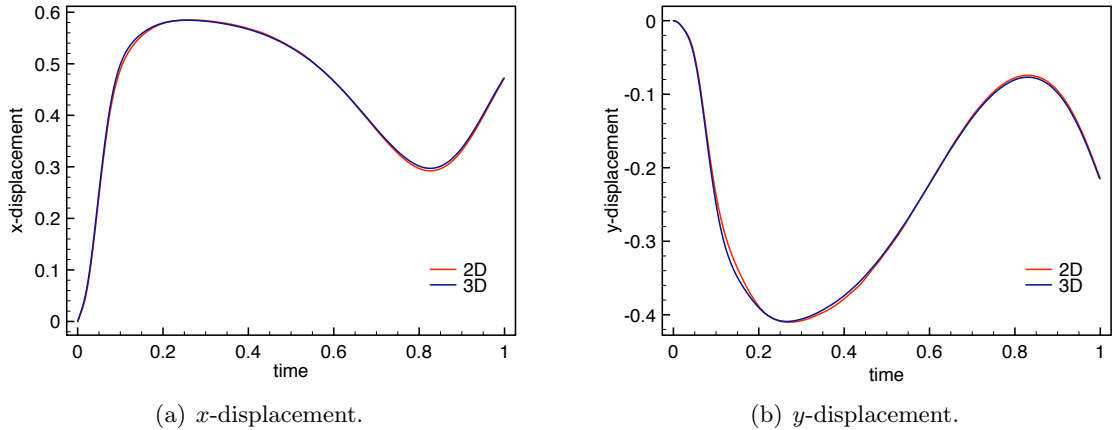


Figure 6.42: Displacement time history of the solid tip in 2D and the top node on the plane $z = 0$ in 3D.

x -displacement and y -displacement respectively. The 3D is able to reproduce very well the 2D dynamics even if small differences are visible. We expect this small mismatch to be reduced with space refinement.

6.5 Conclusion

In this chapter we have presented a three dimensional unfitted Nitsche-XFEM method for incompressible fluid-structure interaction problems involving thin-walled structures. The extension to three dimensions of XFEM/cut-FEM methods is still a quite challenging problem, specially because it requires a robust and efficient intersection algorithm. We recall that sub-tetrahedralization without adding additional vertices, cannot be guaranteed, even for a simple polyhedron (see e.g. Mayer et al. (2009)).

The key features of the presented model are the following:

- Nitsche-XFEM consistent treatment of the interface coupling based on an affine finite element approximation with local elements duplication;
- cut-FEM methodology is enabled owing to a robust and efficient intersection algorithm for general unstructured meshes, by localizing the solid mesh within the fluid mesh and subdividing in sub-tetrahedra the fluid intersected elements;
- partially intersected fluid domain are included in the model by adding a fictitious interface Σ_{fic} only with the purpose of helping to connect the fluid domain from the two side of the interface. In fact, the prolongation Σ_{fic} is a mechanical slave of the physical interface Σ .

The three-dimensional method is validated via a series of numerical examples, involving moving interfaces as well as partially intersected fluid domain. On going works attempt to show the efficiency of the discussed algorithm, by comparing with remeshing techniques.

Other future working directions can include, for instance, 3D contact with single and multiple structures (including the numerical method presented in Chapter 4).

GENERAL CONCLUSION AND
PERSPECTIVES

In this thesis we have considered the modeling and numerical approximation of fluid-structure interaction problems with immersed solids within the unfitted mesh Nitsche-XFEM framework.

In Part I, we have successfully avoided strong coupling without compromising stability and accuracy, introducing an unfitted mesh semi-implicit scheme, combining a fractional-step time-marching in the fluid with the consistent Nitsche-XFEM spatial discretization method. The numerical results of Chapter 2 have shown that, traditional accuracy issues of previous weakly coupled schemes with Nitsche's interface treatment (see [Astorino et al. \(2009a\)](#); [Alauzet et al. \(2016\)](#)) are circumvented through a consistent transfer of the fluid viscous stresses to the solid, even though subordinated to an additional CFL-like condition, linking the space discretization and the Nitsche's penalty parameters. In Chapter 3, we have derived an *a priori* error analysis, in the case of first and second order extrapolations in the kinematic coupling, showing a superior accuracy, with respect to the stabilized explicit scheme of [Burman and Fernández \(2014a\)](#), which suffers of stagnation phenomena when $\tau = \mathcal{O}(h)$. Additionally, numerical evidence indicates that the new semi-implicit algorithm and the strongly coupled (from [Burman and Fernández \(2014a\)](#)) deliver the same accuracy behavior.

The second part (Part II) of this thesis focused on fluid-structure-contact interaction problems. In Chapter 4, we have addressed the case of contact with multiple structures within the unfitted mesh Nitsche-XFEM framework. Consistency and correctness of the overlapping meshes are guaranteed also at contact, as a consequence of an additional duplication of the fluid elements intersected from different structures. A new duplication procedure has been developed and a numerical experiment (with low displacements), in which we compare the Nitsche-XFEM method with fitted ALE and unfitted FD methods, showed similar results between Nitsche-XFEM and ALE and the higher robustness of Nitsche-XFEM with respect to FD. In Chapter 5, we have presented a fluid-structure-porous-contact model, in which, mechanical consistency issues of the relaxed contact formulations are avoided. We have introduced a thin-walled porous layer, over the contacting surface, in order to model the solid asperities and give a physical meaning to the fluid stresses at contact.

Furthermore, in Part III, we have extended the Nitsche-XFEM unfitted mesh method of [Alauzet et al. \(2016\)](#) to three dimensions. The development of an intersection and sub-tetrahedralization algorithm is a crucial point for the effectiveness of the presented methodology. This is one of the main contributions of Chapter 6. Additionally, considering the case of partially intersected fluid domain, special treatment are included in the method, by adding a solid region which reduces the geometrical operations to the case of fully intersected domains. Numerical evidences have validated the 3D Nitsche-XFEM unfitted mesh method.

From the present work, several research directions can be explored:

- The implementation of the semi-implicit coupled scheme presented in Chapter 2 in

three-dimensions, considering the contributions of Chapter 6, in order to be able to handle complex and physiological simulation of heart valves.

- From the theoretical point of view, the extension of the stability and convergence analysis of Chapters 2, 3 to the case of curved and dynamic interfaces. Both subjects have not been particularly analyzed in the literature. We refer to [Lehrenfeld and Olshanskii \(2019\)](#) for stability and error analysis accounting also geometric errors, while for the study of parabolic problems with moving interfaces we refer to [Zunino \(2013\)](#). Additionally, further insight on the analysis in the case of second order time-discretization in both fluid and solid problem could be considered.
- The extension of the fluid-structure-contact interaction model of Chapter 4 to 3D and the case of partially intersected fluid domain, using the fictitious solid method proposed in Chapter 6. As regards partially intersected fluid domain, this is a promising approach, since the tip procedure reduces the operations to the case of fully intersected domains. Hence, by avoiding penetration also within the fictitious interface, we can apply the same strategy of Chapter 4.
- Regarding the fluid-structure-porous-contact model of Chapter 5, we can consider the extension of the model to the case in which we consider a non rigid porous layer, with large displacements.
- On going works are devoted to the comparison of the unfitted mesh Nitsche-XFEM based FSI-contact model of Chapter 4, with advanced moving meshes techniques, coupled with the ALE fitted approach (see, e.g., [Alauzet \(2014\)](#)) in the context of contact with large displacements.

References

- C. Ager, B. Schott, A. Vuong, A. Popp, and W. Wall. A consistent approach for fluid-structure-contact interaction based on a porous flow model for rough surface contact. *Int J Numer Methods Eng*, 119(13):1345–1378, 2019a.
- C. Ager, A. Seitz, and W. A. Wall. A consistent and versatile computational approach for general fluid-structure-contact interaction problems. *International Journal for Numerical Methods in Engineering*, 2019b.
- P. Alart and A. Curnier. A mixed formulation for frictional contact problems prone to Newton like solution methods. *Computer Methods in Applied Mechanics and Engineering*, 92(3):353–375, Nov. 1991. ISSN 0045-7825.
- F. Alauzet. A changing-topology moving mesh technique for large displacements. *Eng. Comput.*, 30(2):175–200, 2014.
- F. Alauzet and M. Mehrenberger. P1-conservative solution interpolation on unstructured triangular meshes. *International Journal for Numerical Methods in Engineering*, 84(13):1552–1588, 2010.
- F. Alauzet, B. Fabrèges, M. A. Fernández, and M. Landajuela. Nitsche-xfem for the coupling of an incompressible fluid with immersed thin-walled structures. *Computer Methods in Applied Mechanics and Engineering*, 301:300–335, 2016.
- M. Annese. *Time integration schemes for fluid-structure interaction problems: non-fitted FEMs for immersed thin structures*. PhD thesis, Università degli studi di Brescia, 2017.
- M. Annese, M. A. Fernández, and L. Gastaldi. Splitting schemes for a lagrange multiplier formulation of fsi with immersed thin-walled structure: stability and convergence analysis. (2020), arXiv:2007.04699.
- M. Astorino and C. Grandmont. Convergence analysis of a projection semi-implicit coupling scheme for fluid-structure interaction problems. *Numer. Math.*, 116:721–767, 2010.
- M. Astorino, F. Chouly, and M. A. Fernández. Robin based semi-implicit coupling in fluid-structure interaction: Stability analysis and numerics. *SIAM J. Sci. Comput.*, 31(6):4041–4065, 2009a.
- M. Astorino, J.-F. Gerbeau, O. Pantz, and K.-F. Traore. Fluid–structure interaction and multi-body contact: application to aortic valves. *Computer Methods in Applied Mechanics and Engineering*, 198(45-46):3603–3612, 2009b.
- F. P. Baaijens. A fictitious domain/mortar element method for fluid–structure interaction. *International Journal for Numerical Methods in Fluids*, 35(7):743–761, 2001.

- S. Badia, F. Nobile, and C. Vergara. Fluid–structure partitioned procedures based on robin transmission conditions. *Journal of Computational Physics*, 227(14):7027–7051, 2008a.
- S. Badia, A. Quaini, and A. Quarteroni. Splitting methods based on algebraic factorization for fluid-structure interaction. *SIAM J. Sci. Comput.*, 30(4):1778–1805, 2008b.
- S. Badia, A. Quaini, and A. Quarteroni. Modular vs. non-modular preconditioners for fluid–structure systems with large added-mass effect. *Computer Methods in Applied Mechanics and Engineering*, 197(49-50):4216–4232, 2008c.
- L. Bălilescu, J. San Martín, and T. Takahashi. Fluid-rigid structure interaction system with coulomb’s law. *SIAM Journal on Mathematical Analysis*, 49(6):4625–4657, 2017.
- K. Bathe. *Finite Element Procedures*. Prentice Hall, 1996.
- G. S. Beavers and D. D. Joseph. Boundary conditions at a naturally permeable wall. *Journal of fluid mechanics*, 30(1):197–207, 1967.
- R. Becker, E. Burman, and P. Hansbo. A nitsche extended finite element method for incompressible elasticity with discontinuous modulus of elasticity. *Computer Methods in Applied Mechanics and Engineering*, 198, 09 2009. doi: 10.1016/j.cma.2009.06.017.
- M. Bischoff, E. Ramm, and J. Irslinger. Models and finite elements for thin-walled structures. *Encyclopedia of Computational Mechanics Second Edition*, pages 1–86, 2018.
- D. Boffi and L. Gastaldi. A fictitious domain approach with lagrange multiplier for fluid-structure interactions. *Numerische Mathematik*, 135(3):711–732, 2017.
- D. Boffi, N. Cavallini, and L. Gastaldi. Finite element approach to immersed boundary method with different fluid and solid densities. *Math. Models Methods Appl. Sci.*, 21(12):2523–2550, 2011.
- D. Boffi, N. Cavallini, and L. Gastaldi. The finite element immersed boundary method with distributed lagrange multiplier. *SIAM Journal on Numerical Analysis*, 53(6):2584–2604, 2015.
- L. Boilevin-Kayl, M. A. Fernández, and J.-F. Gerbeau. A loosely coupled scheme for fictitious domain approximations of fluid-structure interaction problems with immersed thin-walled structures. *SIAM J. Sci. Comput.*, 41(2):B351–B374, 2019a.
- L. Boilevin-Kayl, M. A. Fernández, and J.-F. Gerbeau. Numerical methods for immersed fsi with thin-walled structures. *Computers & Fluids*, 179:744–763, 2019b.
- R. Boman and J.-P. Ponthot. Finite element simulation of lubricated contact in rolling using the arbitrary lagrangian–eulerian formulation. *Computer methods in applied mechanics and engineering*, 193(39-41):4323–4353, 2004.

- F. Brezzi and J. Pitkäranta. On the stabilization of finite element approximations of the Stokes equations. In *Efficient solutions of elliptic systems (Kiel, 1984)*, volume 10 of *Notes Numer. Fluid Mech.*, pages 11–19. Vieweg, 1984.
- M. Bukac and B. Muha. Stability and convergence analysis of the extensions of the kinematically coupled scheme for the fluid-structure interaction. *SIAM J. Numer. Anal.*, 54(5):3032–3061, 2016.
- M. Bukac, C. Canic, R. Glowinski, T. Tambaca, and A. Quaini. Fluid-structure interaction in blood flow capturing non-zero longitudinal structure displacement. *J. Comp. Phys.*, 235(0):515–541, 2013.
- E. Burman. Ghost penalty. *C. R. Math. Acad. Sci. Paris*, 348(21-22):1217–1220, 2010.
- E. Burman and M. Fernández. Continuous interior penalty finite element method for the time-dependent Navier-Stokes equations: space discretization and convergence. *Numer. Math.*, 107(1):39–77, 2007.
- E. Burman and M. Fernández. Stabilization of explicit coupling in fluid-structure interaction involving fluid incompressibility. *Comput. Methods Appl. Mech. Engrg.*, 198(5-8):766–784, 2009.
- E. Burman and M. Fernández. An unfitted Nitsche method for incompressible fluid-structure interaction using overlapping meshes. *Comput. Methods Appl. Mech. Engrg.*, 279:497–514, 2014a.
- E. Burman and M. Fernández. Explicit strategies for incompressible fluid-structure interaction problems: Nitsche type mortaring versus Robin-Robin coupling. *Int. J. Num. Meth. Engrg.*, 97(10):739–758, 2014b.
- E. Burman and P. Hansbo. Edge stabilization for the generalized stokes problem: A continuous interior penalty method. *Computer Methods in Applied Mechanics and Engineering*, 195:2393–2410, 04 2006. doi: 10.1016/j.cma.2005.05.009.
- E. Burman and P. Hansbo. Fictitious domain finite element methods using cut elements: II. A stabilized Nitsche method. *Appl. Numer. Math.*, 62(4):328–341, 2012.
- E. Burman and P. Hansbo. Fictitious domain methods using cut elements: III. A stabilized Nitsche method for Stokes’ problem. *ESAIM Math. Model. Numer. Anal.*, 48(3):859–874, 2014.
- E. Burman, M. Fernández, and P. Hansbo. Continuous interior penalty finite element method for Oseen’s equations. *SIAM J. Numer. Anal.*, 44(3):1248–1274, 2006.
- E. Burman, S. Claus, P. Hansbo, M. Larson, and A. Massing. CutFEM: Discretizing geometry and partial differential equations. *Int. J. Num. Meth. Engrg.*, 2014. doi: 10.1002/nme.4823. URL <http://dx.doi.org/10.1002/nme.4823>.

- E. Burman, A. Ern, and M. A. Fernández. Fractional-step methods and finite elements with symmetric stabilization for the transient Oseen problem. *ESAIM Math. Model. Numer. Anal.*, 51(2):487–507, 2017.
- E. Burman, P. Hansbo, and M. G. Larson. Augmented Lagrangian and Galerkin least-squares methods for membrane contact. *International Journal for Numerical Methods in Engineering*, 114(11):1179–1191, 2018.
- E. Burman, P. Hansbo, and M. G. Larson. Augmented lagrangian finite element methods for contact problems. *ESAIM: Mathematical Modelling and Numerical Analysis*, 53(1):173–195, 2019.
- E. Burman, M. A. Fernández, and S. Frei. A nitsche-based formulation for fluid-structure interactions with contact. *ESAIM: Mathematical Modelling and Numerical Analysis*, 54(2):531–564, 2020a.
- E. Burman, M. A. Fernández, S. Frei, and F. M. Gerosa. 3D-2D Stokes-Darcy coupling for the modelling of seepage with an application to fluid-structure interaction with contact. In *Chapter 20 of F. J. Vermolen, C. Vwik (eds.), Numerical Mathematics and Advanced Applications ENUMATH 2019, Lecture Notes in Computational Science and Engineering 139*, Paris, France, 2020b. doi: 10.1007/978-3-030-55874-1_20.
- P. Causin, J.-F. Gerbeau, and F. Nobile. Added-mass effect in the design of partitioned algorithms for fluid–structure problems. *Computer methods in applied mechanics and engineering*, 194(42-44):4506–4527, 2005.
- D. Chapelle and K. Bathe. *The Finite Element Analysis of Shells - Fundamentals*. Springer, 2011.
- D. Chapelle and K.-J. Bathe. *The finite element analysis of shells-fundamentals*. Springer Science & Business Media, 2010.
- D. Chapelle and A. Ferent. Modeling of the inclusion of a reinforcing sheet within a 3d medium. *Mathematical Models and Methods in Applied Sciences*, 13(04):573–595, 2003.
- F. Chouly and P. Hild. On convergence of the penalty method for unilateral contact problems. *Applied Numerical Mathematics*, 65, 04 2012. doi: 10.1016/j.apnum.2012.10.003.
- F. Chouly and P. Hild. A nitsche-based method for unilateral contact problems: numerical analysis. *SIAM Journal on Numerical Analysis*, 51(2):1295–1307, 2013.
- F. Chouly, P. Hild, and Y. Renard. Symmetric and non-symmetric variants of nitsche’s method for contact problems in elasticity: theory and numerical experiments. *Mathematics of Computation*, 84(293):1089–1112, 2015.
- F. Chouly, M. Fabre, P. Hild, R. Mlika, J. Pousin, and Y. Renard. An overview of recent results on nitsche’s method for contact problems. In *Geometrically unfitted finite element methods and applications*, pages 93–141. Springer, 2017.

- P. Ciarlet. *Mathematical elasticity. Vol. I*, volume 20 of *Studies in Mathematics and its Applications*. North-Holland, 1988.
- G.-H. Cottet, E. Maitre, and T. Milcent. Eulerian formulation and level set models for incompressible fluid-structure interaction. *ESAIM: Mathematical Modelling and Numerical Analysis*, 42(3):471–492, 2008.
- P. Crosetto, S. Deparis, G. Fourestey, and A. Quarteroni. Parallel algorithms for fluid-structure interaction problems in haemodynamics. *SIAM Journal on Scientific Computing*, 33(4):1598–1622, 2011.
- A. Curnier and P. Alart. A generalized Newton method for contact problems with friction. *J. Méc. Théor. Appl.*, 7(suppl. 1):67–82, 1988.
- R. H. Davis, Y. Zhao, K. P. Galvin, and H. J. Wilson. Solid–solid contacts due to surface roughness and their effects on suspension behaviour. *Philosophical Transactions of the Royal Society of London. Series A: Mathematical, Physical and Engineering Sciences*, 361(1806):871–894, 2003.
- J. De Hart, G. Peters, P. Schreurs, and F. Baaijens. A three-dimensional computational analysis of fluid-structure interaction in the aortic valve. *Journal of Biomechanics*, 36:103–112, 2003.
- D. Di Pietro and A. Ern. *Mathematical aspects of discontinuous Galerkin methods*, volume 69 of *Mathematics & Applications*. Springer, Heidelberg, 2012.
- N. Diniz dos Santos, J.-F. Gerbeau, and J.-F. Bourgat. A partitioned fluid-structure algorithm for elastic thin valves with contact. *Comput. Methods Appl. Mech. Engrg.*, 197(19-20):1750–1761, 2008.
- J. Donea, S. Giuliani, and J.-P. Halleux. An arbitrary lagrangian-eulerian finite element method for transient dynamic fluid-structure interactions. *Computer methods in applied mechanics and engineering*, 33(1-3):689–723, 1982.
- Q. Du, M. Gunzburger, L. Hou, and J. Lee. Semidiscrete finite element approximations of a linear fluid-structure interaction problem. *SIAM J. Numer. Anal.*, 42(1):1–29, 2004.
- B. E Griffith. On the volume conservation of the immersed boundary method. *Communications in Computational Physics*, 12, 08 2012. doi: 10.4208/cicp.120111.300911s.
- A. Ern and J.-L. Guermond. *Theory and Practice of Finite Elements*, volume 159 of *Applied Mathematical Sciences*. Springer, New York, 2004. doi: 10.1007/978-1-4757-4355-5. URL <http://books.google.fr/books?id=CCjm79FbJbcC>.
- L. C. Evans. Partial differential equations, ams. *Graduate Studies in Mathematics*, 19, 2002.
- M. Fernández. Coupling schemes for incompressible fluid-structure interaction: implicit, semi-implicit and explicit. *SĒMA J.*, (55):59–108, 2011.

- M. Fernández. Incremental displacement-correction schemes for incompressible fluid-structure interaction: stability and convergence analysis. *Numer. Math.*, 123(1):21–65, 2013.
- M. Fernández and M. Landajuela. Splitting schemes for incompressible fluid/thin-walled structure interaction with unfitted meshes. *C. R. Math. Acad. Sci. Paris*, 2015., 2015. DOI: 10.1016/j.crma.2015.04.003.
- M. Fernández and M. Moubachir. A Newton method using exact Jacobians for solving fluid-structure coupling. *Comp. & Struct.*, 83:127–142, 2005.
- M. Fernández and J. Mullaert. Convergence and error analysis for a class of splitting schemes in incompressible fluid-structure interaction. *IMA J. Numer. Anal.*, 36(4): 1748–1782, 2016.
- M. Fernández, J. Gerbeau, and C. Grandmont. A projection semi-implicit scheme for the coupling of an elastic structure with an incompressible fluid. *Int. J. Num. Meth. Engrg.*, 69(4):794–821, 2007.
- M. A. Fernández and M. Landajuela. Splitting schemes and unfitted-mesh methods for the coupling of an incompressible fluid with a thin-walled structure. *IMA J. Numer. Anal.*, 2019. doi: 10.1093/imanum/dry098.
- L. Formaggia, J. Gerbeau, F. Nobile, and A. Quarteroni. On the coupling of 3d and 1d navier-stokes equations for flow problems in compliant vessels. *Computer Methods in Applied Mechanics and Engineering*, 191:561–582, 12 2001. doi: 10.1016/S0045-7825(01)00302-4.
- L. Formaggia, A. Quarteroni, and A. Veneziani, editors. *Cardiovascular mathematics*, volume 1 of *MS&A. Modeling, Simulation and Applications*. Springer-Verlag Italia, Milan, 2009. Modeling and simulation of the circulatory system.
- C. Förster, W. Wall, and E. Ramm. Artificial added mass instabilities in sequential staggered coupling of nonlinear structures and incompressible viscous flows. *Comput. Methods Appl. Mech. Engrg.*, 196(7):1278–1293, 2007.
- S. Frei. *Eulerian finite element methods for interface problems and fluid-structure interactions*. PhD thesis, 2016.
- P. Frey and P. George. *Mesh generation. Application to finite elements*. Hermès Science Publ., Paris, Oxford, 2000.
- P. J. Frey and P.-L. George. *Mesh generation: application to finite elements*. Iste, 2007.
- T.-P. Fries and T. Belytschko. The extended/generalized finite element method: an overview of the method and its applications. *International journal for numerical methods in engineering*, 84(3):253–304, 2010.

- T.-P. Fries and A. Zilian. On time integration in the xfem. *International Journal for Numerical Methods in Engineering*, 79:69 – 93, 07 2009. doi: 10.1002/nme.2558.
- M. W. Gee, U. Küttler, and W. A. Wall. Truly monolithic algebraic multigrid for fluid–structure interaction. *International Journal for Numerical Methods in Engineering*, 85(8):987–1016, 2011.
- P.-L. George, H. Borouchaki, and E. Saltel. ‘ultimate’ robustness in meshing an arbitrary polyhedron. *International Journal for Numerical Methods in Engineering*, 58(7):1061–1089, 2003.
- D. Gérard-Varet and M. Hillairet. Regularity issues in the problem of fluid structure interaction. *Archive for rational mechanics and analysis*, 195(2):375–407, 2010.
- D. Gérard-Varet, M. Hillairet, and C. Wang. The influence of boundary conditions on the contact problem in a 3d navier–stokes flow. *Journal de Mathématiques Pures et Appliquées*, 103(1):1–38, 2015.
- A. Gerstenberger and W. Wall. An extended finite element method/Lagrange multiplier based approach for fluid-structure interaction. *Comput. Methods Appl. Mech. Engrg.*, 197(19-20):1699–1714, 2008a.
- A. Gerstenberger and W. A. Wall. An extended finite element method/lagrange multiplier based approach for fluid–structure interaction. *Computer Methods in Applied Mechanics and Engineering*, 197(19-20):1699–1714, 2008b.
- A. Gil, A. and Arranz Carreño, J. Bonet, and O. Hassan. An enhanced immersed structural potential method for fluid-structure interaction. *Journal of Computational Physics*, 250:178–205, 10 2013. doi: 10.1016/j.jcp.2013.05.011.
- R. Glowinski, T.-W. Pan, T. I. Hesla, and D. D. Joseph. A distributed lagrange multiplier/fictitious domain method for particulate flows. *International Journal of Multiphase Flow*, 25(5):755–794, 1999.
- C. Grandmont and M. Hillairet. Existence of global strong solutions to a beam–fluid interaction system. *Archive for Rational Mechanics and Analysis*, 220(3):1283–1333, 2016.
- B. Griffith and X. Luo. Hybrid finite difference/finite element immersed boundary method. *International Journal for Numerical Methods in Biomedical Engineering*, 33(12):e2888, 2017.
- B. E. Griffith. Immersed boundary model of aortic heart valve dynamics with physiological driving and loading conditions. *International Journal for Numerical Methods in Biomedical Engineering*, 28(3):317–345, 2012.
- J. L. Guermond, P. Mineev, and J. Shen. An overview of projection methods for incompressible flows. *Comput. Methods Appl. Mech. Engrg.*, 195(44-47):6011–6045, 2006.

- M. E. Gurtin. *An introduction to continuum mechanics*. Academic press, 1982.
- E. Hachem, S. Feghali, R. Codina, and T. Coupez. Immersed stress method for fluid-structure interaction using anisotropic mesh adaptation. *Internat. J. Numer. Methods Engrg.*, 94(9):805–825, 2013.
- J. Han and C. S. Peskin. Spontaneous oscillation and fluid–structure interaction of cilia. *Proceedings of the National Academy of Sciences*, 115(17):4417–4422, 2018.
- A. Hansbo and P. Hansbo. A finite element method for the simulation of strong and weak discontinuities in solid mechanics. *Comput. Methods Appl. Mech. Engrg.*, 193(33-35): 3523–3540, 2004.
- F. Hecht. New development in freefem++. *J. Numer. Math.*, 20(3-4):251–265, 2012. ISSN 1570-2820. URL <https://freefem.org/>.
- C. Hesch, A. Gil, A. Arranz Carreño, and J. Bonet. On continuum immersed strategies for fluid-structure interaction. *Computer Methods in Applied Mechanics and Engineering*, 247–248:51–64, 11 2012. doi: 10.1016/j.cma.2012.07.021.
- T. I. Hesla. *Collisions of smooth bodies in viscous fluids: A mathematical investigation*. PhD thesis, University of Minnesota, 2004.
- J. G. Heywood and R. Rannacher. Finite-element approximation of the nonstationary navier–stokes problem. part iv: Error analysis for second-order time discretization. *SIAM Journal on Numerical Analysis*, 27(2):353–384, 1990.
- M. Hillairet. Lack of collision between solid bodies in a 2d incompressible viscous flow. *Communications in Partial Differential Equations*, 32(9):1345–1371, 2007.
- M. Hillairet and T. Takahashi. Collisions in three-dimensional fluid structure interaction problems. *SIAM journal on mathematical analysis*, 40(6):2451–2477, 2009.
- G. Hou, J. Wang, and A. Layton. Numerical methods for fluid-structure interaction—a review. *Commun. Comput. Phys.*, 12(2):337–377, 2012. ISSN 1815-2406.
- C. Kadapa, W. Dettmer, and D. Perić. A stabilised immersed framework on hierarchical b-spline grids for fluid-flexible structure interaction with solid-solid contact. *Comput. Methods Appl. Mech. Engrg.*, 335:472–489, 2018.
- D. Kamensky, M.-C. Hsu, D. Schillinger, J. A. Evans, A. Aggarwal, Y. Bazilevs, M. S. Sacks, and T. J. Hughes. An immersogeometric variational framework for fluid–structure interaction: Application to bioprosthetic heart valves. *Computer methods in applied mechanics and engineering*, 284:1005–1053, 2015.
- W. Kim and H. Lee, I. Choi. A weak-coupling immersed boundary method for fluid–structure interaction with low density ratio of solid to fluid. *J. Comput. Phys.*, 359:296–311, 2018.

- U. Küttler, C. Förster, and W. A. Wall. A solution for the incompressibility dilemma in partitioned fluid–structure interaction with pure dirichlet fluid domains. *Computational Mechanics*, 38(4):417–429, Sep 2006.
- W. M. Lai, D. H. Rubin, D. Rubin, and E. Krempl. *Introduction to continuum mechanics*. Butterworth-Heinemann, 2009.
- M. Landajuela, M. Vidrascu, D. Chapelle, and M. A. Fernández. Coupling schemes for the fsi forward prediction challenge: comparative study and validation. *International journal for numerical methods in biomedical engineering*, 33(4):e2813, 2017.
- M. L. Landajuela. *Coupling schemes and unfitted mesh methods for fluid-structure interaction*. PhD thesis, 2016.
- K. Lau, V. Diaz, P. Scambler, and G. Burriesci. Mitral valve dynamics in structural and fluid–structure interaction models. *Medical engineering & physics*, 32(9):1057–1064, 2010.
- P. Le Tallec and J. Mouro. Fluid structure interaction with large structural displacements. *Comput. Meth. Appl. Mech. Engrg.*, 190:3039–3067, 2001.
- A. Legay, J. Chessa, and T. Belytschko. An eulerian–lagrangian method for fluid–structure interaction based on level sets. *Computer Methods in Applied Mechanics and Engineering*, 195(17-18):2070–2087, 2006.
- C. Lehrenfeld and M. Olshanskii. An eulerian finite element method for pdes in time-dependent domains. *ESAIM: Mathematical Modelling and Numerical Analysis*, 53(2): 585–614, 2019.
- Y. Liu and W. K. Liu. Rheology of red blood cell aggregation by computer simulation. *Journal of Computational Physics*, 220(1):139–154, 2006.
- V. Martin, J. Jaffré, and J. E. Roberts. Modeling fractures and barriers as interfaces for flow in porous media. *SIAM Journal on Scientific Computing*, 26(5):1667–1691, 2005.
- A. Massing, M. G. Larson, and A. Logg. Efficient implementation of finite element methods on nonmatching and overlapping meshes in three dimensions. *SIAM J. Sci. Comput.*, 35(1):C23–C47, 2013.
- U. M. Mayer, A. Gerstenberger, and W. A. Wall. Interface handling for three-dimensional higher-order xfem-computations in fluid–structure interaction. *International journal for numerical methods in engineering*, 79(7):846–869, 2009.
- U. M. Mayer, A. Popp, A. Gerstenberger, and W. A. Wall. 3d fluid–structure-contact interaction based on a combined xfem fsi and dual mortar contact approach. *Computational Mechanics*, 46(1):53–67, 2010.
- A. Mikelic and W. Jäger. On the interface boundary condition of beavers, joseph, and saffman. *SIAM J Appl Math*, 60(4):1111–1127, 2000.

- R. Mlika, Y. Renard, and F. Chouly. An unbiased Nitsche's formulation of large deformation frictional contact and self-contact. *Comput. Methods Appl. Mech. Engrg.*, 325:265–288, 2017.
- T. Nakata and H. Liu. A fluid–structure interaction model of insect flight with flexible wings. *Journal of Computational Physics*, 231(4):1822–1847, 2012.
- E. Newren, A. Fogelson, R. Guy, and R. Kirby. Unconditionally stable discretizations of the immersed boundary equations. *J. Comput. Phys.*, 222(2):702–719, 2007.
- D. Nield, A. Bejan, et al. *Convection in porous media*, volume 3. Springer, 2006.
- F. Nobile. Numerical approximation of fluid-structure interaction problems with application to haemodynamics. Technical report, EPFL, 2001.
- F. Nobile, M. Pozzoli, and C. Vergara. Time accurate partitioned algorithms for the solution of fluid–structure interaction problems in haemodynamics. *Computers & Fluids*, 86:470–482, 2013.
- C. S. Peskin. The immersed boundary method. *Acta numerica*, 11:479–517, 2002.
- L. Possenti, S. di Gregorio, F. M. Gerosa, G. Raimondi, G. Casagrande, M. L. Costantino, and P. Zunino. A computational model for microcirculation including fahraeus-lindqvist effect, plasma skimming and fluid exchange with the tissue interstitium. *International journal for numerical methods in biomedical engineering*, 35(3):e3165, 2019.
- K. Poullos and Y. Renard. An unconstrained integral approximation of large sliding frictional contact between deformable solids. *Computers & Structures*, 153:75–90, 2015.
- C. Pozrikidis. *Computational hydrodynamics of capsules and biological cells*. Chapman & Hall/CRC Mathematical and Computational Biology. CRC Press, 2010.
- A. Pries, T. W. Secomb, T. Gessner, M. Sperandio, J. Gross, and P. Gaehtgens. Resistance to blood flow in microvessels in vivo. *Circulation research*, 75(5):904–915, 1994.
- A. Quaini and A. Quarteroni. A semi-implicit approach for fluid-structure interaction based on an algebraic fractional step method. *Math. Models Methods Appl. Sci.*, 17(6):957–983, 2007.
- A. Quarteroni and S. Quarteroni. *Numerical models for differential problems*, volume 2. Springer, 2009.
- T. Richter. A fully Eulerian formulation for fluid–structure-interaction problems. *Journal of Computational Physics*, 233:227–240, 2013.
- T. Richter and T. Wick. Finite elements for fluid–structure interaction in ale and fully eulerian coordinates. *Computer Methods in Applied Mechanics and Engineering*, 199(41-44):2633–2642, 2010.

- A. Roshchenko, P. D. Minev, and W. H. Finlay. A time splitting fictitious domain algorithm for fluid–structure interaction problems (a fictitious domain algorithm for fsi). *Journal of Fluids and Structures*, 58:109–126, 2015.
- S. Roy, L. Heltai, and F. Costanzo. Benchmarking the immersed finite element method for fluid-structure interaction problems. *Computers and Mathematics with Applications*, 69, 06 2013. doi: 10.1016/j.camwa.2015.03.012.
- P. G. Saffman. On the boundary condition at the surface of a porous medium. *Studies Appl Math*, 50(2):93–101, 1971.
- S. Salsa. *Partial Differential Equations in Action: From Modelling to Theory*. Springer, Milan, 2009.
- T. Sawada and A. Tezuka. LLM and X-FEM based interface modeling of fluid-thin structure interactions on a non-interface-fitted mesh. *Comput. Mech.*, 48(3):319–332, 2011.
- R. Scholz. Numerical solution of the obstacle problem by the penalty method. *Computing*, 32:297–306, 12 1984. doi: 10.1007/BF02243774.
- H. Si. Tetgen, a delaunay-based quality tetrahedral mesh generator. *ACM Transactions on Mathematical Software (TOMS)*, 41(2):1–36, 2015.
- F. Sotiropoulos and X. Yang. Immersed boundary methods for simulating fluid–structure interaction. *Progress in Aerospace Sciences*, 65:1–21, 2014.
- J. H. Spühler, J. Jansson, N. Jansson, and J. Hoffman. 3d fluid-structure interaction simulation of aortic valves using a unified continuum ale fem model. *Frontiers in physiology*, 9:363, 2018.
- K. Stein, T. Tezduyar, and R. Benney. Mesh moving techniques for fluid-structure interactions with large displacements. *J. Appl. Mech.*, 70(1):58–63, 2003.
- K. Takizawa and T. E. Tezduyar. Computational methods for parachute fluid–structure interactions. *Archives of Computational Methods in Engineering*, 19(1):125–169, 2012.
- T. Tezduyar. Stabilized finite element formulations for incompressible flow computations. In *Advances in applied mechanics, Vol. 28*, volume 28 of *Adv. Appl. Mech.*, pages 1–44. Academic Press, Boston, MA, 1992.
- A. Toselli and O. Widlund. *Domain decomposition methods-algorithms and theory*, volume 34. Springer Science & Business Media, 2006.
- E. van Brummelen. Added mass effects of compressible and incompressible flows in fluid-structure interaction. *J. Appl. Mech.*, 76(2):021206–7, 2009.
- E. Van Brummelen. Partitioned iterative solution methods for fluid–structure interaction. *International Journal for Numerical Methods in Fluids*, 65(1-3):3–27, 2011.

- R. Van Loon, P. D. Anderson, J. De Hart, and F. P. Baaijens. A combined fictitious domain/adaptive meshing method for fluid–structure interaction in heart valves. *International Journal for Numerical Methods in Fluids*, 46(5):533–544, 2004.
- R. Van Loon, P. D. Anderson, F. P. Baaijens, and F. N. Van de Vosse. A three-dimensional fluid–structure interaction method for heart valve modelling. *Comptes Rendus Mecanique*, 333(12):856–866, 2005.
- K. Wang, J. Grétarsson, A. Main, and C. Farhat. Computational algorithms for tracking dynamic fluid–structure interfaces in embedded boundary methods. *International Journal for Numerical Methods in Fluids*, 70(4):515–535, 2012.
- X. Wang and L. Zhang. Interpolation functions in the immersed boundary and finite element methods. *Computational Mechanics*, 45:321–334, 03 2010. doi: 10.1007/s00466-009-0449-5.
- G. D. Weymouth, D. G. Dommermuth, K. Hendrickson, and D. K.-P. Yue. Advancements in cartesian-grid methods for computational ship hydrodynamics. 2006.
- T. Wick. Fluid-structure interactions using different mesh motion techniques. *Computers & Structures*, 89(13-14):1456–1467, 2011.
- T. Wick. Flapping and contact fsi computations with the fluid-solid interface-tracking/interface-capturing technique and mesh adaptivity. *Computational Mechanics*, 53, 10 2013. doi: 10.1007/s00466-013-0890-3.
- P. Wriggers and G. Zavarise. Computational contact mechanics. *Encyclopedia of computational mechanics*, 2004.
- A. Zilian and A. Legay. The enriched space–time finite element method (est) for simultaneous solution of fluid–structure interaction. *International Journal for Numerical Methods in Engineering*, 75(3):305–334, 2008.
- S. Zonca, C. Vergara, and L. Formaggia. An unfitted formulation for the interaction of an incompressible fluid with a thick structure via an xfem/dg approach. *SIAM Journal on Scientific Computing*, 40(1):B59–B84, 2018.
- S. Zonca, P. F. Antonietti, and C. Vergara. A polygonal discontinuous galerkin formulation for contact mechanics in fluid-structure interaction problems. 2020.
- P. Zunino. Analysis of backward Euler/extended finite element discretization of parabolic problems with moving interfaces. *Comput. Methods Appl. Mech. Engrg.*, 258:152–165, 2013.